DESIGN AND PERFORMANCE SIMULATION OF A HYBRID SOUNDING ROCKET

Seffat Mohammad Chowdhury

In fulfillment of the academic requirements for the degree of Master of Science in Mechanical Engineering, College of Agriculture, Engineering and Science, University of KwaZulu-Natal

December, 2012

Supervisor: Michael Brooks

Co-Supervisor: Jean-Francois Pitot de la Beaujardiere

Co-Supervisor: Professor Lance Roberts

ABSTRACT

Sounding rockets find applications in multiple fields of scientific research including meteorology, astronomy and microgravity. Indigenous sounding rocket technologies are absent on the African continent despite a potential market in the local aerospace industries. The UKZN Phoenix Sounding Rocket Programme was initiated to fill this void by developing inexpensive medium altitude sounding rocket modeling, design and manufacturing capacities. This dissertation describes the development of the Hybrid Rocket Performance Simulator (HYROPS) software tool and its application towards the structural design of the reusable, 10 km apogee capable Phoenix-1A hybrid sounding rocket, as part of the UKZN Phoenix programme. HYROPS is an integrated 6–Degree of Freedom (6-DOF) flight performance predictor for atmospheric and near-Earth spaceflight, geared towards single-staged and multi-staged hybrid sounding rockets. HYROPS is based on a generic kinematics and Newtonian dynamics core. Integrated with these are numerical methods for solving differential equations, Monte Carlo uncertainty modeling, genetic-algorithm driven design optimization, analytical vehicle structural modeling, a spherical, rotating geodetic model and a standard atmospheric model, forming a software framework for sounding rocket optimization and flight performance prediction. This framework was implemented within a graphical user interface, aiming for rapid input of model parameters, intuitive results visualization and efficient data handling. The HYROPS software was validated using flight data from various existing sounding rocket configurations and found satisfactory over a range of input conditions. An iterative process was employed in the aero-structural design of the 1 kg payload capable Phoenix-1A vehicle and CFD and FEA numerical techniques were used to verify its aerodynamic and thermo-structural performance. The design and integration of the Phoenix-1A's hybrid power-plant and onboard electromechanical systems for recovery parachute deployment and motor oxidizer flow control are also discussed. It was noted that use of HYROPS in the design loop led to improved materials selection and vehicle structural design processes. It was also found that a combination of suitable mathematical techniques, design know-how, human-interaction and numerical computational power are effective in overcoming the many coupled technical challenges present in the engineering of hybrid sounding rockets.

DECLARATION 1 - PLAGIARISM

I, Seffat Mohammad Chowdhury, declare that

1. The research reported in this dissertation, except where otherwise indicated, is my original research.

2. This dissertation has not been submitted for any degree of examination at any other university.

3. This dissertation does not contain other persons" data, pictures, graphs or other information, unless specifically acknowledged as being sourced from other persons.

4. This dissertation does not contain other persons" writing, unless specifically acknowledged as being sourced from other researchers. Where other written sources have been quoted, then
a. Their words have been re-written but the general information attributed to them has been referenced.
b. Where their exact words have been used, then their writing has been placed in italics and inside quotation marks, and referenced.

5. This thesis does not contain text, graphics, or tables copied and pasted from the Internet, unless specifically acknowledged, and the source being detailed in this thesis and in the References section.

Signed _____ Date _____

Seffat Mohammad Chowdhury

As the candidate's supervisor, I agree/do not agree to the submission of this thesis.

Signed _____ Date _____

Mr. Michael Brooks

As the candidate's co-supervisor, I agree/do not agree to the submission of this thesis.

Signed _____ Date _____

Mr. Jean-Francois Pitot de la Beaujardiere

As the candidate's co-supervisor, I agree/do not agree to the submission of this thesis.

Signed _____ Date _____

Prof. Lance Roberts

DECLARATION 2 – PUBLICATIONS

Brooks, M. J., Pitot de la Beaujardiere, J. P., Chowdhury, S. M., Genevieve, B. and Roberts, L., "Introduction to the UKZN Hybrid Sounding Rocket Program", Proceedings of the 46th AIAA/ASME/SAE/ASEE Joint Propulsion Conference & Exhibit, Nashville, TN, United States of America, 25-28 July 2010

Pitot de la Beaujardiere, J. P., Brooks, M. J., Genevieve, B., Chowdhury, S., M. and Roberts, L., W., "Sounding Rockets for Africa", Proceedings of the 1st South African Space Association Congress, Cape Town, South Africa, 7-9 October 2010

Chowdhury, S. M., Pitot de la Beaujardiere, J. P., Brooks, M. J. and Roberts, L. W., "An Integrated Six Degree-of-Freedom Trajectory Simulator for Hybrid Sounding Rockets", Proceedings of the 49th AIAA Aerospace Sciences Meeting, Orlando, FL, United States of America, 4-7 January 2011

Pitot de la Beaujardiere, J. P., Brooks, M. J., Chowdhury, S. M., Genevieve, B. and Roberts, L. W., "The Phoenix Hybrid Sounding Rocket Program: A Progress Report", Proceedings of the 47th AIAA/ASME/SAE/ASEE Joint Propulsion Conference & Exhibit, San Diego, CA, United States of America, 2011

Genevieve, B., Chowdhury, S. M., Brooks, M. J., Pitot de la Beaujardiere, J. P., Veale, K. and Roberts, L. W., "The Phoenix Sounding Rocket Program: A Progress Report 2012", Proceedings of the 48th Annual AIAA/ASME/SAE/ASEE Joint Propulsion Conference and Exhibit and 10th Annual International Energy Conversion Engineering Conference, Atlanta, GA, United States of America, 29 July – 1 August 2012

Signed _____ Date _____

Seffat Mohammad Chowdhury

ACKNOWLEDGEMENTS

To my parents and sister, whose patience, support and love have inspired what is best in me.

TABLE OF CONTENTS

NOMENCLATURE

Symbols

a	Speed of sound
	Component to x axis vehicle center of gravity shift
A	Aerodynamic reference area
	Principal x axis moment of inertia
	Fin aspect ratio
A_e	Nozzle exit area
A_P	Aerodynamic projected area
A_S	Apparent acceleration due to spherical Earth
$A_{CORIOLIS}$	Apparent acceleration due to Coriolis effect
A_{WET}	Airframe wetted area
b	Component to vehicle y axis center of gravity shift
B	Principal y axis moment of inertia
c	Component to vehicle z axis center of gravity shift
C	Aerodynamic coefficient
	Principal z axis moment of inertia
C_A	Axial force coefficient
C_D	Drag coefficient
C_{D_c}	Steady-state cross-flow drag coefficient on infinite cylinder
C_{D_F}	Skin friction drag coefficient
C_f	Skin friction coefficient
C_{fc}	Compressibility corrected skin friction coefficient
$C_{j_{x_i}}$	Aerodynamic dynamic derivative
C_l	Rolling moment
$C_{l(d)}$	Roll damping moment
$C_{l(f)}$	Roll forcing moment
C_L	Lift coefficient

C_m	Pitching moment coefficient
C_{m_α}	Pitching moment coefficient derivative due to angle of attack
C_{m_q}	Pitch damping coefficient derivative
C_n	Yawing moment coefficient
C_N	Normal force coefficient
C_{N_α}	Normal force coefficient derivative due to angle of attack
$C_{N_\alpha}^{F(B)}$	Fin-body interference normal force coefficient angle of attack derivative
C_r	Fin root chord
C_t	Fin tip chord
C_Y	Horizontal side force coefficient
C_Z	Vertical side force coefficient
D	Principal plane product of inertia
D_{eq}	Equivalent diameter
e	Orbital eccentricity
E	Weld efficiency factor
	Principal plane product of inertia
f	Derivative function
	Fluid external force
	Force
F	Thrust
	Principal plane product of inertia
$\overrightarrow{F_A}$	Aerodynamic force
F_{EXT}	External forces
F_I	Internal forces
$\overrightarrow{F_m}$	Propulsion force
F_{max}	Maximum thrust force
$F_x^m F_y^m F_z^m$	Body frame referenced propulsion forces
F_N^B	Body frame referenced normal aerodynamic force
F_X^B	Body frame referenced axial aerodynamic force
g	Gravitational acceleration

g_c	Crossover real-valued gene
$g_{p1} \; g_{p2}$	Parent genes
G	Universal gravitational constant
G_E	Shear modulus
h	Altitude
h_0	Atmospheric layer base altitude
$h_{jet-ceil}$	Jet stream ceiling altitude
$h_{jet-floor}$	Jet stream floor altitude
H	Angular momentum
i	Time step number
I	Moment of inertia tensor
I_G	Moment of inertia tensor about center of gravity
I_P	Moment of inertia tensor about arbitrary point
I_{XX}	Principal x axis moment of inertia
I_{XY}	Principal xy plane product of inertia
I_{XZ}	Principal xz plane product of inertia
I_{YY}	Principal y axis moment of inertia
I_{YZ}	Principal yz plane product of inertia
I_{ZZ}	Principal z axis moment of inertia
k	Ratio of specific heats
$(k_2 - k_1)$	Munk's apparent mass factor
K	Quaternion unity-magnitude correction gain
	Stiffness matrix
$K_1 K_2 K_3 K_4$	Runge-Kutta integrator intermediate derivatives
l	Aerodynamic reference length
L	Turbulence correlation length
L_{cg}	Fuselage segment to center of gravity longitudinal distance
L_g	Longitude
L_t	Latitude
m	Mass
$\dot{m}_e$	Motor mass flow rate

M	Mach number
	Mass of earth
M_{EXT}	External moments
$M^b_{F_x}\ M^b_{F_y}\ M^b_{F_z}$	Body frame propulsion moments
$M^B_X\ M^B_Y\ M^B_Z$	Body frame external moments
	Number of fins
N	Gaussian normal distribution function
	Number of stages
	Pressure
p	Body frame roll rate
	Linear momentum
p_0	Atmospheric layer base pressure
p_a	Atmospheric ambient pressure
p_e	Motor nozzle exit pressure
p_t	Earth rotation rate x component in body axes
	Pressure vessel internal pressure
P	Non-permuted input
	Orbital period
P_{MC}	Permuted Monte Carlo input
q	Body frame pitch rate
	Generic quaternion
$q_0\ q_1\ q_2\ q_3$	Quaternion components
q_t	Earth rotation rate y component in body axes
r	Body frame yaw rate
	Orbital radius
r_1	Fuselage segment forward radius
r_2	Fuselage segment aft radius
r_t	Earth rotation rate z component in body axes
	Fin root chord distance from vehicle axis
R	Center of mass
	Center of gravity

	Gas constant
$\mathcal{R}$	Uniformly distributed random number
R_e	Reynolds" number
R_S	Critical Reynolds" number
R_t	Radius of the Earth
s	Fin span
	Gradient wind speed
s_0	Gradient wind ground speed
S	Aerodynamic reference area
	Allowable pressure vessel tensile stress
t	Time
t_{flat}	Ramp thrust function time to sustained burn
t_i	Simulation time at beginning of integration step
t_{i+1}	Simulation time at end of integration step
$t_{ramp-down}$	Ramp thrust function total burn time
$t_{ramp-up}$	Ramp thrust function ramp-up transient duration
T	Atmospheric temperature
	Co-ordinate transformation matrix
T_0	Atmospheric layer base temperature
T_h	Temperature lapse rate
u	Body frame speed
v	Body frame speed
	Velocity
v_e	Motor nozzle exhaust velocity
V	Velocity
V_a	Aerodynamic velocity
V_{bs}	Volume of fuselage or body
V_B	Volume of fuselage or body segment
V_E	Eastward geographic velocity
V_f	Fin-flutter critical velocity
V_{jet}	Jet stream velocity

$V_{jet-max}$	Jet stream maximum velocity
V_k	Kinematic velocity
$\overrightarrow{\dot{V}_k}$	Kinematic acceleration vector
$\overrightarrow{\dot{V}_{k_R}}$	Launch rail projected kinematic acceleration vector
V_N	Northward geographic velocity
V_w	Wind velocity
V_Z	Downward geographic velocity
w	Turbulence spatial coordinate
	Body frame speed
x	Cartesian coordinate
x_0	Longitudinal fuselage location of flow separation
$x_1 x_2$	Dryden spectrum state variables
X	Kinematic vector quantity
	State vector
X_C	Center of pressure longitudinal location w. r. t. body moment center
X_P	Center of pressure longitudinal location
y	Cartesian coordinate
	Span-wise fin location
y_{MAC}	Span-wise location of fin mean aerodynamic chord
z	Cartesian coordinate
α	Angle of attack or incidence angle
	BLX parameter
α_T	Total angle of attack
$\alpha_x \alpha_y \alpha_z$	Transformation matrix rotation angles
β	Aerodynamic sideslip angle
	Prandtl compressibility correction factor
γ	Ratio of specific heats
δ	Fin cant angle
	Material deflection

ε_n	Nose tip included half angle	
η	Infinite cylinder to finite cylinder cross-flow drag ratio	
θ	Elevation angle	
θ_0	Launch elevation angle	
θ_m	Thrust misalignment angle	
ϑ	Fin mid-chord sweep angle	
κ	Fin aspect ratio	
λ	Quaternion deviation from unity	
μ	Viscosity	
	Random distribution mean	
ν	Viscosity	
ρ	Density	
ρ_0	Atmospheric layer base density	
σ	Tensile stress	
	Random distribution standard deviation	
σ_{jj}	Components of stress tensor	
σ_v	von-Mises equivalent yield stress	
τ	Turbulent gust velocity	
ϕ	Roll angle	
ϕ_a	Aerodynamic roll angle	
ϕ_m	Thrust misalignment rotational direction	
ψ	Azimuth angle	
ψ_0	Launch azimuth angle	
ψ_w	Wind direction (azimuth) angle	
$\bar{\omega}$	Turbulence spatial frequency	
Δt	Time step duration	
Φ	Orientation Euler angle triplet	
Φ_{zz}	Dryden spectral density function	
Ω	Angular velocity	
Ω_t	Earth angular velocity	

Superscripts

B	Body frame
I	Inertial frame
O	Earth-fixed frame

Subscripts

b	Body frame
i	Inertial frame
o	Earth-fixed frame

Abbreviations

6-DOF	Six Degree-of-Freedom
AMG	Algebraic Multi Grid
AMSL	Above Mean Sea Level
AOA	Angle of Attack
CAD	Computer Aided Design
CFD	Computational Fluid Dynamics
CFRP	Carbon Fiber Reinforced Polymer
CM	Center of Mass
CNC	Computer Numerical Control
CP	Center of Pressure
DATCOM	Data Compendium
DOS	Desktop Operating System
ESA	European Space Agency
FEA	Finite Element Analysis
FEM	Finite Element Method
FVM	Finite Volume Method
GSE	Ground Support Equipment

GFRP	Glass Fiber Reinforced Polymer
GPS	Global Positioning System
GUI	Graphical User Interface
HAZ	Heat Affected Zone
HTPB	Hydroxyl-Terminated Polybutadiene
IC	Integrated Circuit
INS	Inertial Navigation System
KML	Keyhole Markup Language
LEO	Low Earth Orbit
MCU	Microcontroller Unit
MEMS	Micro Electro Mechanical Systems
MOSFET	Metal Oxide Semiconductor Field Effect Transistor
NACA	National Advisory Committee on Aeronautics
NDT	Non-Destructive Testing
OTR	Overberg Test Range
PCB	Printed Circuit Board
PCD	Pitch Circle Diameter
PDE	Partial Differential Equation
PWM	Pulse Width Modulation
TRL	Technological Readiness Level

LIST OF FIGURES

CHAPTER 7

LIST OF TABLES

CHAPTER 1

Introduction

Rocket propulsion refers to the use of reaction forces from accelerating exhausted propellants to propel a vehicle according to the principle of conservation of momentum. Chemical rockets typically combust fuels in a confined combustion chamber to produce accelerating gaseous exhaust products which are used to generate a propulsion force by expansion through a nozzle. Whilst chemical rocket engines are by far the most common type, a variety of other processes may be used to generate exhaust matter and used for propulsion based on the same principle. A flying vehicle using any form of rocket motor for propulsion is simply referred to as a rocket. Rockets have been used for centuries as missiles in warfare and for recreational purposes in the form of fireworks. The development of mathematical theories for rocket motion in the late 19th and early 20th centuries and the subsequent invention of the liquid propellant chemical rocket have made the rocket the technological mainstay of human space exploration.

Rockets have often been designed specifically to deliver experimental payloads from the ground to a point at altitude. Such rockets are commonly referred to as 'sounding rockets' by virtue of their early role in taking atmospheric measurements or 'soundings'. Figure 1-1 displays some of the most commonly used sounding rockets developed and flown by NASA. The success of a sounding rocket mission is determined by the delivery of the payload to the intended altitude in a functional state followed by the recovery of the scientific information gathered by the payload. The engineering of a sounding rocket system is focused on achieving the greatest chances of flying successful missions. Sounding rocket technology has played an important role in the exploration of space. Functioning primarily as an intermediary technology between spacecraft and high altitude aircraft, sounding rockets have often served as stepping stones for orbital launch vehicle development programs. The relative simplicity and affordability of the sounding rocket makes it ideal for a wide variety of scientific missions ranging from the upper atmospheric to the near-space altitude regions. Sounding rockets are most often classified by the type of rocket propulsion system used. The vast majority of sounding rockets use chemical rocket motors. The three most common variants of chemical rocket motors use solid, liquid and hybrid fuels. Solid rocket motors use a solid-phase combination of fuel and oxidizer and liquid rocket motors use fuels and oxidizers both in the liquid phases. A third variant known as the hybrid rocket motor employs a solid fuel and a liquid oxidizer combination, or less frequently, a solid oxidizer and liquid fuel. Multi-stage sounding rockets employ a series of motors which are fired and subsequently discarded to assist in generating large accelerations, boosting

performance. Sounding rockets are also classified according to the number of stages and the type of motor used on each stage. These characteristic generally define the flight scope of a sounding rocket system and hence its potential application areas.

The overall altitude attained by a sounding rocket is primarily related to the acceleration levels produced by its propulsion system and opposed by its inertia. The external geometry of the vehicle induces aerodynamic forces and moments during atmospheric flight, significantly affecting performance. Great emphasis is often placed on an efficient aerodynamic design. A third flight performance determinant is the dynamic stability of the vehicle. The combination of an efficient propulsion system, an optimally aerodynamic geometry and stable dynamic characteristics lead to a robust, well performing sounding rocket.
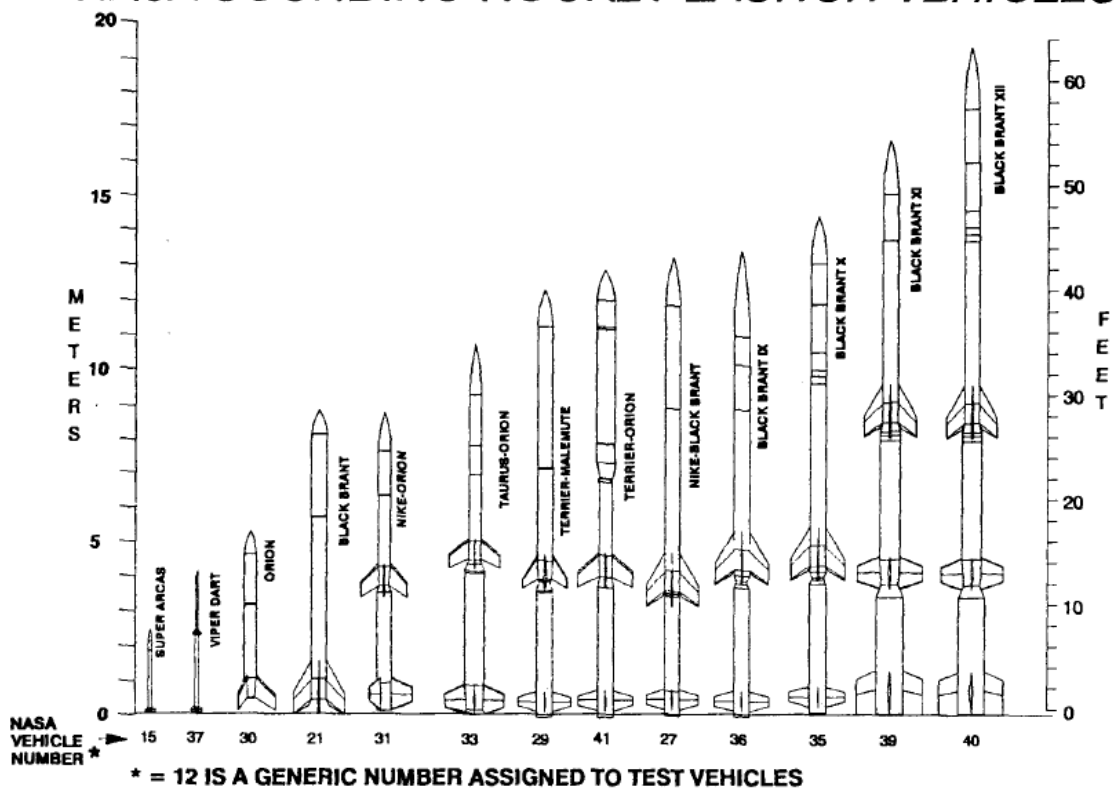
Figure 1-1: A collection of popular NASA Sounding Rockets [1]

All sounding rockets are comprised of three core subsystems: a propulsion system, an aero-structure and a payload. An array of engineering disciplines is involved in the simulation, design, manufacture and operation of a sounding rocket. Rockets motors are capable of imparting great acceleration to a flying vehicle, leading to various challenging operational

conditions. These include large stresses in the vehicle structure, significant thermal and shock loads as well as destabilizing dynamic effects arising from complex aerodynamic and mechanical interactions. The use of propellants at high pressures introduces the need for safe onboard pressure storage systems. In order to be useful, sounding rockets must also store and return measured scientific data reliably, requiring robust onboard electronic telemetry and avionics systems or some means of safe payload recovery. Actively guided sounding rockets require a dedicated navigation, guidance and actuation system. The performance of a sounding rocket strongly correlates with the ratio of propellant mass to vehicle empty mass hence conservation of weight in sounding rocket design is given high priority. The use of lightweight, high performance materials and their associated design and manufacturing expenses present a trade-off which benefits from constrained optimization studies for minimal cost. Additionally, ground support subsystems such as fueling equipment, launching mechanisms and transporting gear must be designed for compatibility with the vehicle. Each of these constituent subsystems cannot be designed separately. The design process involves selecting a general configuration for the vehicle and designing each subsystem to integrate successfully.

The flight performance of a rocket is not determined trivially as it is the result of complex interactions between the structural, propulsion and aerodynamic subsystems of the vehicle as well as the Earth and its atmosphere. A prediction of flight performance also requires dynamic mathematical models for the vehicle's propulsion system, physical geometry, inertial properties, aerodynamic characteristics and control signals. Models of the Earth's gravitation, geometry and atmosphere are needed to complete the simulation framework. The flight dynamics of the rigid sounding rocket are governed by the Newtonian momentum conservation differential equation, commonly known as Newton's second law. The complexity of the associated mathematical models often prohibits analytical solution. Therefore, the numerical solution of the Newtonian flight dynamics equation forms the core of the rocket flight performance prediction process. The quantification of inherent flight uncertainties through statistical methods is also necessary if the predictions are to be applied to real world launch scenarios. Sounding rockets also present the engineer with a highly coupled multi-disciplinary optimization problem (MDO) and this work intended to automate this optimization process.

Despite the engineering challenges inherently present, smaller sounding rockets have generated a steady level of research attention since the introduction of the hybrid rocket motor, as surveyed in Chapter 2 of this dissertation. Hybrid motors possess less mechanical complexity than liquid fueled rocket motors but display greater reliability and controllability than solid fueled rocket motors, placing them in a position potentially suited to reliable, low-cost sounding rocket applications. Hybrid motors are also attractive due to their relatively lower cost when

compared to liquid motors and their relatively high level of reusability when compared to solid rocket motors. Additionally, the controllability of the hybrid motor makes it suitable for university level research programs where it is highly desirable to use inherent safe systems, unlike large solid rocket motors. However, hybrid motors do introduce certain drawbacks from both liquid and solid fuel systems such as the presence of high pressure fuel tanks and high frequency pressure oscillations in the motor combustion chamber. A number of academic research programs have attempted to address these problems. Various governmental and commercial aerospace industries have also established hybrid rocket development programs.

At the time of writing, there is an emerging demand for suborbital sounding rocket technologies in South Africa from the meteorological and physics research communities. Academic and industrial research into artificial satellites in South Africa is already underway [2] and there is a foreseeable need for indigenous launch system in the next decade. The high cost of imported systems is also a driver for research into affordable locally developed aerospace solutions. The establishment of a national space agency is further indication that the South African aerospace industry is maturing [3].

The University of KwaZulu-Natal (UKZN) Phoenix-1A sounding rocket is the first of a series of sounding rockets planned under the UKZN Phoenix Hybrid Sounding Rocket Program. This program aims to fill the void in sounding rocket technologies in South Africa and seeks to contribute towards the establishment of an indigenous civilian South African space program. The Phoenix-1A sounding rocket is intended to probe and measure the feasibility of hybrid sounding rocket technologies in meeting the needs of the South African scientific and industrial communities. It also aims to develop much needed human capital in the local aerospace sector. This dissertation describes the engineering of the UKZN Phoenix-1A hybrid sounding rocket. The two major aspects of this work were the simulation and the design of the Phoenix-1A vehicle. The scope of this work excludes the modeling, design and testing of the vehicle's PV-1 flight weight hybrid rocket motor, which is the subject of a parallel research effort [4]. However, the integration of the vehicle and its motor and their combined functionality is included. Aspects of the vehicle which are integral to the functioning of the PV-1 motor, such as the nitrous oxide oxidizer tank and the actuation system for oxidizer flow control also fell within the scope of this dissertation. Figure 1-2 displays a cutaway view of the Phoenix-1A vehicle design, showing the major components.
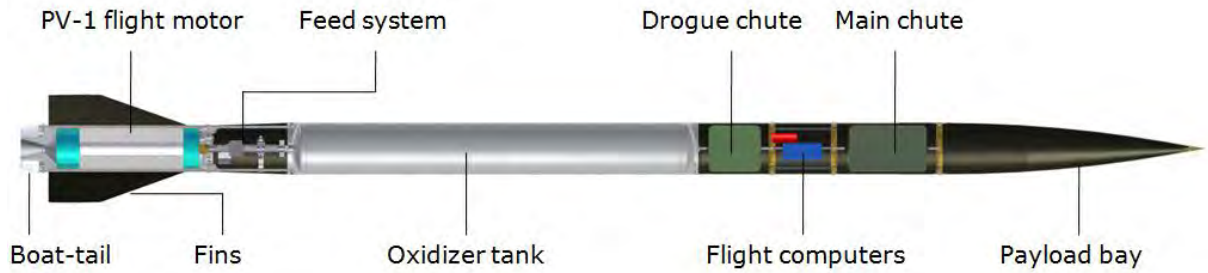
Figure 1-2: Cutaway CAD rendition of the UKZN Phoenix-1A hybrid sounding rocket design

The development of the Phoenix-1A sounding rocket was driven by predefined performance specifications. The first step in the design process was the development of a flight performance prediction software tool covering the operational scope of the Pheonix-1A. This software, named the Hybrid Rocket Performance Simulator (HYROPS), was specified to provide flight performance predictions and associated design aids for generic sounding rockets capable of reaching altitudes of 100 km above Earth's mean sea level. The scope of the tool included the modeling of the effects of uncertain flight conditions and the modeling of all dynamic phenomena which significantly alter the altitude performance of a sounding rocket. The tool was used iteratively to improve the Phoenix-1A design until it met its specifications. Whilst HYROPS is geared towards the investigation hybrid rocket technology, it is not restricted to hybrid sounding rockets alone. Despite the availability of various existing flight simulation tools, the development of the HYROPS software was independently undertaken with the following goals:

a) Implementation of an integrated, scalable and user-friendly tool geared strongly towards high altitude sounding rocket performance prediction with emphasis on hybrid propulsion

b) Development of an independent simulation framework which is free of international intellectual property restrictions and would be easily expanded to include launch vehicle configurations

c) Use of an optimal software architecture based on the computing resources available to the program

d) Use of the tool as a key feature of the Phoenix sounding rocket design iteration process, wherein it is used to predict the performance of a particular design iteration

The HYROPS tool is unique in its capacity to integrate six degree of freedom sounding rocket flight dynamics, multi-staging, geodetic modeling, uncertainty modeling, high-fidelity motor

performance modeling, aerodynamic performance prediction and multi-disciplinary design optimization functionalities into a single software framework. This effectively extends the current state of sounding rocket flight performance modeling and simulation research, thereby furthering the application scope of such tools. The tool is ultimately aimed at bridging the gap between existing sub-orbital rocket modeling software and dedicated orbital simulation codes. It also aims to make the design process more robust, efficient and user friendly by the integration of more novel design techniques such as genetic algorithms which inject a degree of artificial intelligence into the design process. Refer to Table 4-1 in Chapter 4 for a detailed comparison of HYROPS with existing high-power sub-orbital rocket simulation codes.

Chapter 2 of this dissertation contains a brief review of the current state of research regarding the performance simulation and design of sounding rockets, with emphasis on hybrid propulsion. Chapter 3 details the mathematical techniques used to model rocket flight performance and the various sounding rocket subsystem. A description of how these techniques are adapted for use in the HYROPS tool is also given. Chapter 4 describes the HYROPS software implementation, input and output interfaces, software architecture and also presents validation of HYROPS results against existing sounding rocket flight performance data. The implementation of the software included development of the requisite internal software architectures as well as the external interfaces which will enable it to be marketed as an independent software tool outside the objectives of the Phoenix program.

Based on the requirements of the program, the Phoenix-1A sounding rocket was specified to be a reusable single stage unguided suborbital hybrid sounding rocket. The following set of broad specifications defines the functionality of the Phoenix-1A.

1) Capacity to reach a nominal apogee altitude of at least 10 km above launch point
2) Delivery of a scientific payload weighing at least 1 kg to apogee
3) Capability to recover the payload over land and water
4) A high degree of component reusability
5) Inherently stable dynamic flight behavior
6) Integration with a dedicated hybrid rocket motor and ground support equipment

The development of the HYROPS tool and its use in the design of the Phoenix-1A sounding rocket formed part of an effort to independently acquire the technology and know-how required to reach high altitudes, including but not restricted to the edge of space, which is defined as an altitude of 100 km above mean sea level. The Phoenix-1A vehicle design process had several research objectives to this end.

a) Investigation of the suitability of hybrid rocket motors for powering medium to high altitude sounding rocket missions and possibly the upper stages of a future launch vehicle

b) Generation of human capital in the various areas of aerospace engineering and design, ground support equipment design, flight planning, launch execution, vehicle recovery and data analysis, all of which are relevant to a future launch capacity

c) Evaluation of the expenses incurred in the procurement and manufacture of a typical sounding rocket using the existing local industrial base and overcoming any practical challenges related to the availability of materials, manufacturing tools and test facilities

d) Development of an affordable local sounding rocket solution which may be used for frequent, inexpensive, mid-altitude meteorological soundings as well as for educational applications and the stimulation of public interest in the aerospace field

Chapter 6 of this dissertation presents the engineering analysis of the Phoenix-1A thermo-structural and aero-structural design problem and its solution in terms of material selection, geometric design, finite element analysis (FEA), manufacture and assembly. Chapter 7 describes the selection, design, software programming and integration of various supporting electromechanical systems used on the Phoenix-1A for flight control and vehicle recovery. Figure 1-3 shows how the various research areas of this dissertation lead to the design of the Phoenix-1A.
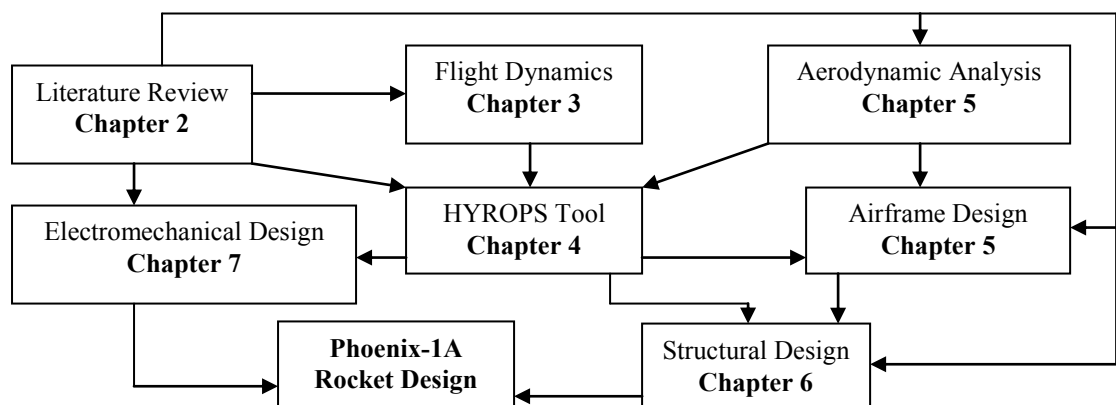
Figure 1-3: Dependency diagram from constituent research areas to sounding rocket design

This work has applied established engineering principles and methods in the simulation, design and manufacture of a small hybrid sounding rocket. It has been demonstrated that hybrid sounding rockets offer a potentially cost effective solution to the low to medium altitude sounding rocket needs of the South African aerospace industry. However, it is apparent that

further focused research is needed to develop this solution into a mature product that can be used to reliably fly missions and obtain experimental results with a short lead time. Chapter 8 presents the final conclusion from this work and also suggests areas where further research may be conducted.

CHAPTER 2

Literature Review

2.1 A Brief History of Sounding Rockets

Rockets have their origins in the invention of suitable propellants such as gunpowder, which took place in the early 1st millennium AD in the Far East. Gunpowder propelled projectiles were used by several civilizations including the Chinese, Mongols, Arabs and Indians. Military rocket technologies steadily progressed westwards, reaching Europe and the Americas in the 17th century. Several late 19th century scientists recognized the rocket's great potential to accelerate vehicles. Mathematicians such as Konstantin Tsiolkovsky demonstrated the rocket's capacity to escape the Earth's gravitational field and enter interplanetary space. Liquid propellants were identified as a more suitable fuel for rockets in the early 20th century. Several innovators are credited with proposing the conceptual design of the modern multi-stage rocket. These include Hermann Oberth, Konstantin Tsiolkovsky and Robert Esnault-Peltiere. Goddard was the first to build a rocket and demonstrate its flight potential. Nazi Germany was the first nation to produce liquid propellant rockets on an industrial scale. The German V2 liquid-rocket missiles were used during World War II and subsequently developed into the first sounding rockets in the post-war USA and USSR [5].

Widespread scientific use of sounding rockets began in the mid 1950's with the aim of collecting data from the upper atmosphere. These flights investigated the ionosphere and its effects on radio communication. A vast majority of the early sounding rockets used military surplus solid or liquid motors and employed multi-staging to achieve greater altitudes. Typical altitudes for these missions ranged from 50 km to 250 km. The 'space-race' between the USA and USSR led to the swift development of larger and more capable sounding rockets over the next decades. Often sounding rockets were used to test the performance of vehicle subsystems before a lunar or interplanetary space mission was attempted. Sounding rockets were also used heavily in meteorological studies, astronomical observations, microgravity research and the investigation of biological phenomena in space [5]. Sounding rockets continue to be used for research and educational purposes in many countries that do not possess extensive space programs.

2.2 A Brief Survey of Sounding Rocket Systems

In Europe, the European Space Agency (ESA) and the United Kingdom have undertaken independent sounding rocket research and development programs. These programs continue to run and have been historically aligned towards supporting their host countries respective atmospheric and near-space research programs. The same is true for the United States and Canada. Table 2-1 summarizes the salient characteristics for some prominent sounding rockets developed in the European Union whilst Table 2-2 presents similar data for vehicle developed in the North America.

Table 2-1: Some European sounding rockets [5]

Vehicle	Agent	Type	Payload (kg)	Apogee (km)	Stages	Spin (Hz)	Length (m)	Max. Acceleration (g)
Mini TEXUS	ESA	Solid	160	140	2	5	10	21
TEXUS	ESA	Solid	370	260	2	3/ 4	13	10
MASER	ESA	Solid	260	260	2	3/ 4	13	10
MAXUS	ESA	Solid	800	705	1	0.5	16.2	13
Skylark 12	UK	Solid	200	575	2	N/A	12.8	N/A

Table 2-2: Some North American sounding rockets [6]

Vehicle	Agent	Type	Payload (kg)	Apogee (km)	Stages	Length (m)	Max. Acceleration (g)	Max. Speed (m/s)
Aerobee 150	NASA	Solid/ Liquid	45	300	2	9.7	21	2250
Aerobee 100	NASA	Solid/ Liquid	19	126	2	7.8	15.2	1420
Black Brant V	Canada	Solid	272.2	250	1	5.3	N/A	N/A
Black Brant XII	Canada	Solid	113.4	1500	4	15	N/A	N/A

Over the last five decades, NASA in the United States has also used a large variety of combinations of military surplus boosters and existing sounding rocket motors in multi-stage sounding rocket configurations including the Nike series (Dart, Cajun, Asp and Apache varieties) and the Iris, Javelin, Arcas, Arcon, Jason, Exos, Skylark, Jaguar, Journeyman, Shot-

put and Strong-arm sounding rockets. Similarly, the USSR had also embarked on several extensive sounding rocket development and launch campaigns and an extensive listing of the vehicles developed is beyond the scope of this dissertation.

Generic sounding rocket research remains a key component of the aerospace sector human capital development initiatives being undertaken in many universities worldwide. Examples of such research programs involving solid rocket motor propulsion include those at Virginia Tech [7], Pennsylvania State University [8], Massachusetts Institute of Technology [9] and the program of the National Space Organization (NSPO) of Taiwan [10]. The ESRA competition remains an important driver in the development of sounding rocket human capital development in the United States, as evidenced by efforts from University of Washington ACES program [11] or the ERAU Pathfinder Heavy II [12] amateur entry. Amateur rocketry hobbyists have also contributed to sounding rocket research. A prominent example in the field of hybrid rocketry is the Delft University amateur rocketry club [13].

2.3 Current Research on Hybrid Sounding Rockets

Student rocketry programs have generated the largest number of hybrid sounding rocket development initiatives. Thus far, these programs have been limited to suborbital vehicles. The Purdue Hybrid Rocket Technology Demonstrator [14] is a university program aimed at developing general purpose hybrid sounding rockets capable of delivering payloads to 100 km. This program uses a hydrogen peroxide and HTPB hybrid fuel combination. Another such program is the 100 km Peregrine Sounding Rocket Project [15] undertaken by collaboration between Stanford University, NASA and the Space Propulsion Group (SPG), which focuses on nitrous oxide and paraffin wax propellants. These programs have integrated hybrid motor development with conventional rocket aero-structures to produce functional hybrid sounding rockets. The resulting vehicles have demonstrated that potentially inexpensive hybrid rocket motors may be operated safely on small rocket vehicles and launched from relatively low-cost ground support platforms. Tsohas [16] proposes staging three hybrid motors to form a small satellite launch vehicle capable of lofting research payloads to LEO. This concept is explored using a simple 'Delta-V' budget analysis code. A 6- DOF flight simulation code called *SORDS* is also part of that program. The Copenhagen Suborbital team is another example of an amateur association employing hybrid rocket motors in vehicles intended to fly suborbital payloads [17].

Hybrid rockets have also been proposed for commercial vehicles such as the Romanian HAAS orbital launcher [18] entry for the Google Lunar X Prize. The HAAS launcher uniquely reduces motor length by using annular oxidizer tanks placed around the motor combustion chamber. The

Virgin Galactic SpaceShipOne [19] vehicle is an example of a suborbital space-plane that has successfully used hybrid propulsion technology in winning the Ansari X-Prize competition. Table 2-3 summarizes the prominent hybrid sounding rocket research initiatives at the time of writing.

Table 2-3: Some ongoing hybrid sounding rocket research projects

Vehicle	Developer	Propellant Combination	Mission	Payload
Peregrine	Stanford University [15]	N_2O / Paraffin Wax	100 km Suborbital	Generic 5 kg
Small Satellite Launch Vehicle Project	Purdue University [16]	H_2O_2 / HTPB	Low Earth Orbit (LEO)	Generic 10 kg
HAAS	ARCA [18]	H_2O_2 / Bitumen	Lunar Mission	ELE Probe
Tycho Deep Space	Copenhagen Suborbital [17]	Liquid O_2 / Paraffin Wax	100 km Suborbital	Human Capsule
HERA	Matthias Grosse [20]	RFNA / LIR - 503	20 km Suborbital	N/A

2.4 Sounding Rocket Classification, Application Areas, Sub-systems and Technology Areas

Sounding Rockets may be classified by propulsion technology, staging characteristics, operating envelope and payload type. Propulsion technology is most commonly used as it often dictates the primary hardware subsystems needed. However, the targeted performance envelope of a sounding rocket is what drives the system cost, size and staging choices. Sounding rocket performance characteristics scale with cost and payload capacity in a relatively simple manner. In this work, the focus on hybrid rockets leaves less scope for comparing different propulsion techniques and involves a more thorough study of how performance is correlated to size, scale and cost. A brief review of some of the existing hybrid sounding rocket research programs provided in Table 2-3 reveals a range of payload application areas and altitude targets. Current research initiatives in the field also come from both academic and industrial researchers. This implies that hybrid sounding rocket research should not be focused on a single application area and that it is worthwhile to explore the solution space for technologies that may eventually be applied in the wider market, ranging from space-planes to orbital-launch vehicles.

The staging configuration of sounding rockets is another area where hybrid rocket technology is promising. Although not optimally suited to low altitude use, hybrid sounding rockets offer attractive options for the second or third stage of multi-stage high altitude vehicles or orbital launch vehicles. Their controllability is a distinct advantage over solid rocket motors, especially when viewed in combination with thrust-vectoring technologies.

In this work, research was not confined to any specific aspects of existing sounding rocket technologies, but rather aimed at selecting the best concept from the various technology areas applicable to each of the subsystems found in a sounding rocket. Table 2-4 presents lists of relevant technology areas which offer solutions applicable to the major subsystems found on sounding rockets.

Table 2-4: Unguided sounding rocket subsystems

Subsystem	Class of Vehicle	Key Technology Areas
Propulsion System	Chemical Rockets	Solid Rocket Motors, Liquid Rocket Motors, Hybrid Rocket Motors, Lightweight Pressure Vessels, Flow Control Systems, Temperature Regulation Systems, Thrust Vectoring
Recovery System	Reusable	Single Parachute, Dual Parachute, Para-foils, Streamers, Pyrotechnic Deployment, Non-Pyrotechnic Deployment
Payload System	All	Inertial Sensors, Rate Sensors, Barometric Sensors, Thermal Sensors, Micro Electro Mechanical Systems (MEMS)
External Airframe	All	Composite Materials, Aerodynamic Optimization, Aero-elasticity (Flutter reduction), High Temperature Materials, Control Surfaces
Avionics	Unguided Rockets	Embedded Processors, Custom Flight Computers, High Acceleration Resistant Circuitry, Miniature Camera Technologies, Radio Telemetry, Navigation (GPS, INS)
Aero-structures	All	Finite Element Analysis (FEA), High Specific Strength Materials, Shock Resistant Materials

Although relatively few researchers have addressed the integrated engineering and design of sounding rockets, a very concise summary of useful techniques and results from the various technology areas is presented in the United States military handbook for the design of aerodynamically stabilized free rockets [21]. Other amateur sources such as a model rocket recovery system design handbook [22] focus on specific subsystems but provide an unprecedented level of relevant details. Guidelines from these works were extensively used for the design of the Phoenix-1A vehicle.

CHAPTER 3

Sounding Rocket Flight Dynamics

3.1 Introduction

This chapter describes techniques used in the modeling and simulation of a sub-orbital multi-stage sounding rocket flight. The aim of sounding rocket flight simulation is to predict the flight performance of a sounding rocket design. Salient flight performance parameters may only be predicted by calculating the trajectory of the rocket's flight through space. The complex, nonlinear nature of the differential equations governing rocket flight dynamics does not allow for a general analytical solution. Therefore, a comprehensive model of rocket flight dynamics is developed using differential calculus. The resulting ordinary differential equations are then solved using numerical methods in a software program.

There are four general phases in the flight of a single-stage sub-orbital sounding rocket. In order, these are the launch phase, the boost phase, the coast phase and the descent phase as shown in Figure 3-1. Assuming the rocket starts from rest from a launch platform, the launch phase is the period prior to the rocket center-of-mass leaving the launch platform. It is typically the shortest flight phase and is characterized by the constrained motion of the rocket along the launching equipment. The boost phase is characterized by a rapid ascent under powered acceleration which lasts until motor burnout. This is followed by the coast phase, which is characterized by unpowered ascent under gravitational and/or aerodynamic deceleration until the maximum altitude (apogee) is reached. In the temporal vicinity of the apogee, the vehicle experiences a short period of low vertical velocity and an apparent absence of gravitational acceleration. At this time, the payload is typically used to gather scientific data or perform experiments. Thereafter, any suborbital vehicle will fall back to the earth, resulting in the descent phase. The descent phase velocity may be limited using a recovery system to allow for the safe recovery of the vehicle. The changes in geometry and aerodynamic properties incurred by the deployment of the recovery system take a certain amount time. This period may be considered as an addition flight phase termed the recovery deployment phase. If left to descend freely, the rocket will turn its nose over and descend under gravitational acceleration. A steady terminal descent velocity may be reached if the aerodynamic resistance forces balance the gravitational force. In this work, all the phases of flight are modeled within a single generic dynamic modeling framework.

Several parameters of a sounding rocket's trajectory are of interest to the sounding rocket designer. These parameters constitute the flight performance of a particular vehicle design. The maximum altitude attainable for a given payload mass (the apogee altitude) is perhaps of greatest significance. The down-range and cross-range landing impact distances are also critical from the safety and recovery perspectives. The maximum acceleration and Mach number attained by the vehicle are essential for adequate aerodynamic and structural design of the vehicle as well as its payload. The magnitudes of the aerodynamic lift drag and side forces are also relevant to vehicle structural design. In addition, the aerodynamic stability margin of the vehicle is dependent on the aerodynamic incidence angles encountered during flight. The times spent in each phase of flight are also desirable outputs from a simulation. In this work, the primary objective of the modeling and flight simulation process is the estimation of these flight performance parameters to an acceptable degree of accuracy.
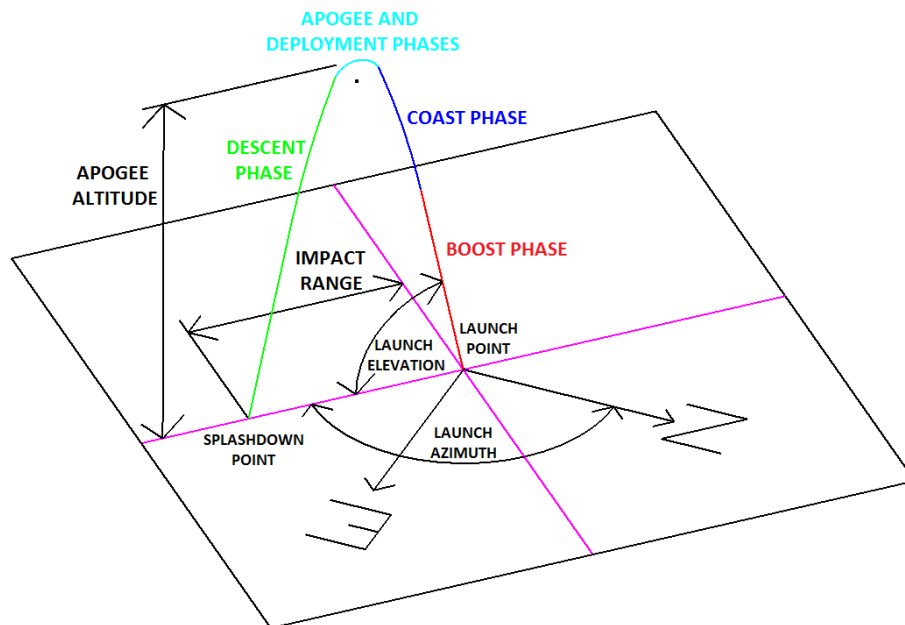
Figure 3-1 Ballistic trajectory flight phases of a single-stage ground-launched sounding rocket

Flying vehicles are complex assemblies of thousands of interacting parts which cannot be practically modeled in their full complexity. The dynamics of flight is also known to be governed by highly nonlinear differential equations, making it necessary to adopt a number of simplifying assumptions. A major simplification is derived by noting that sounding rockets are essentially rigid bodies. The position of a rigid body is well described by a single three-dimensional vector denoting the displacement of the body's center of mass from an inertial point of reference. The orientation of such a body is similarly described by the triplet of angles between the body's three mutually orthogonal reference axes and a similar of set of inertial reference axes. Simulations of aircraft motion are thus often characterized by the number of

degrees of freedom which are modeled. Often, during the initial phases of development, only the three translational degrees of freedom are modeled for simplicity, resulting in what are commonly known as 3-DOF models. Vehicles with onboard control must also model lateral orientations (pitch and yaw), resulting in more advanced 5-DOF simulation models. This work focuses on modeling the full six degrees of freedom (6-DOF) for sounding rocket flight to ensure generality and enable more detailed studies of dynamic effects due to manufacturing imperfections, uncertainties and winds.

3.2 A Brief Review of Published Works on Sounding Rocket Trajectory Simulation

The nature of the trajectories of rigid bodies through 3D Euclidean spaces has been studied extensively since the 17th century. Newton first formulated the basic laws of motion for rigid bodies. These laws may be applied directly to the simulation of a rocket provided that the vehicle is adequately described by a rigid body approximation. This is sufficiently true for most flying vehicles and hence methods from aircraft flight dynamics may be adapted for use on sounding rockets. Aerospace-oriented formulations for the atmospheric flight of aircraft are presented in detail by Boiffier [23], Zipfel [24], Etkin [25] and many others. The extension of Newton's laws for translational motion to the three angular degrees of freedom using Euler's equation lead to the classic 6-DOF equations used by virtually all high fidelity trajectory simulation codes.

As rocket propulsion technology was developed, the 6-DOF equations of motion were adapted for applications involving rocket trajectories. Seminal studies into rocket motion by Tsiolkovsky [26] led to the formulation of the well-known *ideal rocket equation* in 1903. This equation illustrated for the first time the potential offered by rocket propelled vehicles to reach great altitudes, opening up the way to space exploration. The advantages obtained by staging were also apparent from the ideal rocket equation. Subsequent research during and immediately after World War II led to the refinement of the rocket equation to account for atmospheric losses.

Both military and civilian developers of rocket systems have adapted the well-known 6-DOF formulations for terrestrial atmospheric flight into differential equations of motion for rocket trajectory prediction. A fairly recent work by Gorecki [27] illustrates the application of these equations of motion in the missile industry with emphasis on guidance and navigation. Very similar techniques are seen in the prediction of projectile trajectories by Khalil *et al* [28] who also include the Earth's rotation. Jenkins [29] presents a more generalized version of these formulations, accounting for both the rotation and spherical geometry of the Earth. A much earlier work by James [30] is evidence of the use of the classical flat, non-rotating Earth 6-DOF

equations of atmospheric flight in the design of sounding rockets. Another example of a more generic 6-DOF model is available from the BASIC program by McFarland [31] at NASA, which includes the Earth's rotation and spherical geometry. The numerical solution of the equations has been investigated in detail by Karbon [32] who found that Runge-Kutta solution techniques are satisfactory. Kti *et al* [33] have shown that analytical solutions may be used for preliminary performance studies for multi-stage rockets. These solutions do not capture the full complexity of rocket flight but are helpful in the initial design stage when major configuration decisions are made.

Uncertainty modeling using stochastic techniques has been applied to sounding rocket 6-DOF simulators. Saghafi and Khalilidelshad [34] used the Monte Carlo method for impact dispersion analysis.

The usefulness of a core 6-DOF simulator in furthering vehicle design has been investigated, but not in a comprehensively integrated manner. Early works on optimal rocket trajectories by Vinh [35] and Coburn [36] attempted to find analytical solutions to the simplified and idealized rocket trajectory. These solutions often lacked the sophistication required for real rockets due to their simplistic aerodynamic models. More advanced multidisciplinary design optimization (MDO) studies by Roshanian and Keshavarz [37] demonstrate that design iterations may be improved by using established optimization techniques such as the response surface method. Bayley [38] shows that a multi stage launch vehicle may be optimized using multi-objective genetic algorithms (MOGA). Similar results are derived for cost optimization of multi stage launch vehicles by Bairstow [39]. However, a fully coupled multi-disciplinary optimization framework is not presented in these works; rather the methods are restricted to a limited set of vehicle parameters.

3.3 Simplifying Assumptions

The scope of this work necessitates adoption of a number of simplifying assumptions. These assumptions make the process of sounding rocket flight simulation more efficient and its results more relevant. Sufficient generality and accuracy are maintained for the application areas intended for this work.

1) The center-of-mass of the Earth is an inertial point
2) The Earth's mass is a known constant
3) The Earth is a spherical planet
4) The Earth's geometric center coincides with its center-of-mass

5) The Earth rotates about its North-South axis with a known, constant angular velocity

6) The vehicle is a rigid body and its internal forces sum to zero

7) The mass of the vehicle is negligible in comparison to that of the Earth

8) The airframe possesses tetragonal (cruciform) symmetry with respect to its longitudinal axis

9) The airframe possesses no geometric control surfaces to manipulate its aerodynamics

10) Atmospheric properties vary with altitude alone

11) The mean wind vector field is a known, steady function of altitude and geographic location

12) Air is an ideal gas

13) The atmospheric temperature derivative with respect to altitude is piecewise constant

14) The Earth's gravitational acceleration is a function of altitude and latitude alone

15) The gravitational effects of all bodies except the Earth are negligible

16) The vehicle launches off of a frictionless, motionless, perfectly rigid launch rail

17) The parachute-payload combination is a rigid body of revolution about the body x-axis

18) The parachute canopy possesses hemispherical shell geometry with rigid shroud lines

3.4 Coordinate Frames

Coordinate frames are used to define the domain of a flight simulation and measure spatial quantities therein. To be meaningful, a rocket's six degrees of freedom must be referred to an inertial co-ordinate frame. It is convenient to adopt the center-of-mass of the Earth as the origin of the *inertial frame* for terrestrial flight dynamics. The inertial frame can be assumed to be Galilean as the Earth's motion around the Sun and its interaction with other planets negligibly affects the dynamics of sounding rocket flight. In this work, the orientations of the inertial frame's axes are assumed to be fixed towards some astronomical reference points. The dynamic effect of the daily rotation of the Earth is then manifested through 'apparent' Coriolis acceleration terms and not explicitly modeled by as this necessitates use of a separate non-inertial frame which would rotate with the Earth's surface. The x axis and y axis of the inertial frame lie on the Earth's equatorial plane whilst the z axis is oriented parallel to the Earth's polar axis. Figure 3-2 shows the relations between the inertial, Earth-fixed and body frames for a terrestrial simulation of rocket flight. Note that for geographic referencing, longitude is measured frame from a reference point such as the Greenwich meridian but the axes of the Inertial frame do not rotate daily with the reference meridian. Quantities expressed in the inertial frame are superscripted by I.
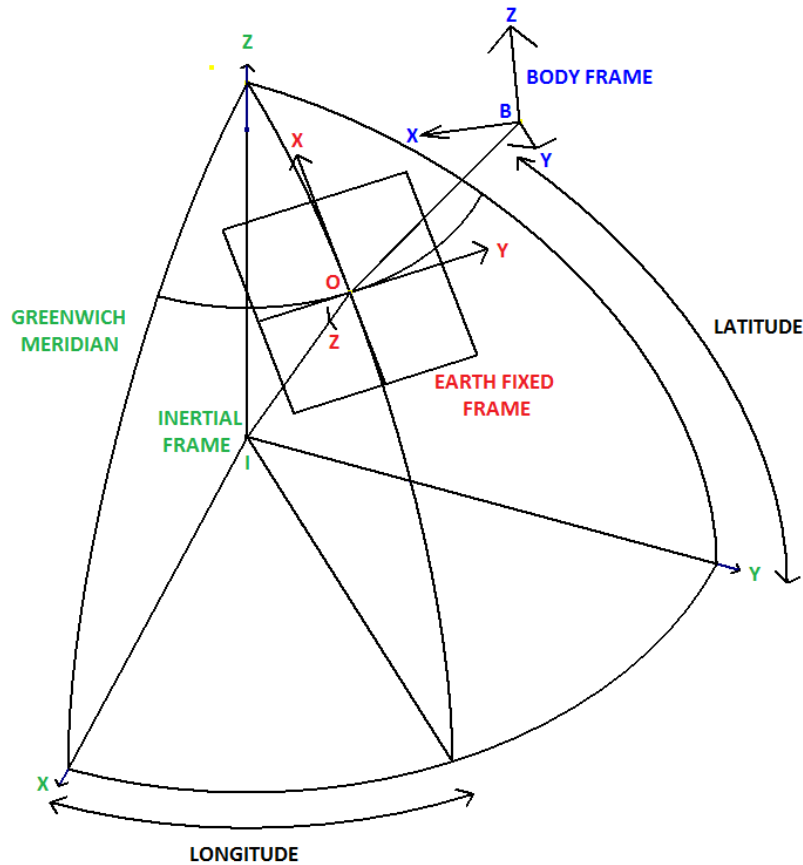
Figure 3-2: The inertial, Earth-fixed and body frames in relation to each other.

The formulations of dynamic and kinematic relations used for rocket flight simulation give rise to several other co-ordinate frames. Prominent amongst these are the *body frame* and *Earth-fixed frame*. An *aerodynamic frame* is also required to co-ordinate aerodynamic forces and moments that act on the vehicle during atmospheric flight.

The origin of the body frame is the mass center of the sounding rocket and its axes are oriented using the vehicle's aerodynamic geometry. By convention, the x axis of the body frame points towards the nose of a rocket and is parallel to the idealized thrust vector produced by the rocket motor (Figure 3-3). If the x axis is regarded as the frontal 'nose-tail' direction, the y axis points to the right and the z axis vertically downwards when the rocket lies parallel to the surface of the Earth based on a right hand co-ordinate system. Quantities in the body frame are superscripted by B. The body coordinate system has vehicle angular velocity components p, q and r about it's x, y and z axes respectively. The corresponding vehicle linear velocity components are denoted u, v and w.
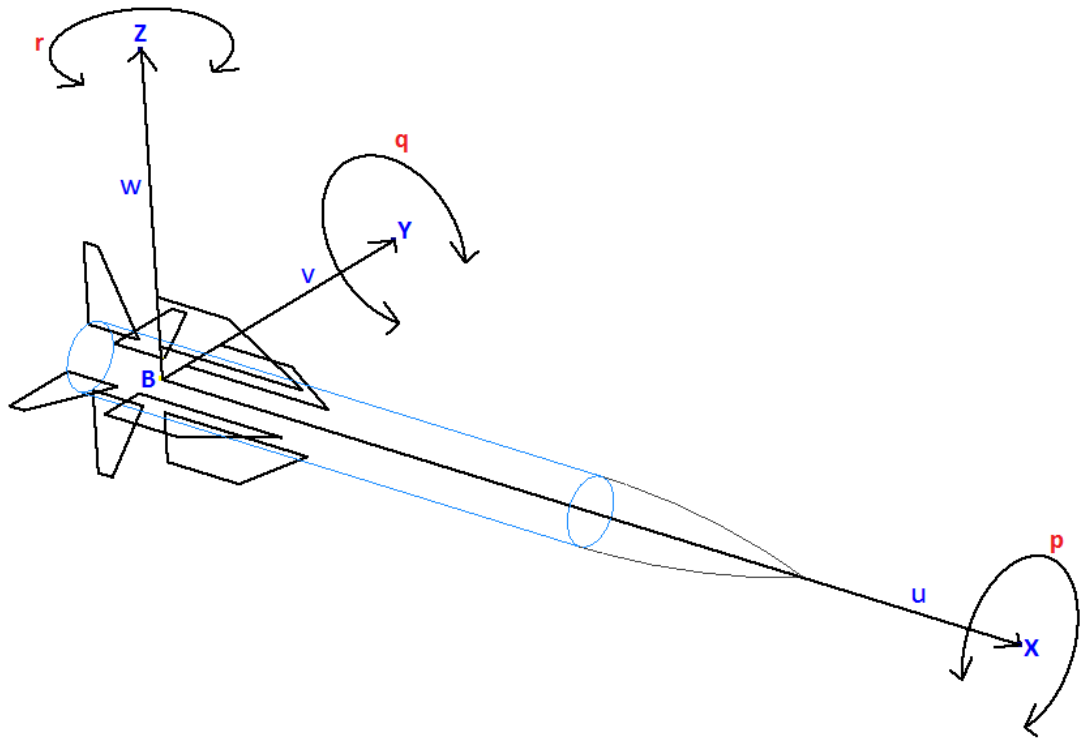
Figure 3-3: The body frame and its vehicle angular and linear velocity components

The Earth-fixed frame is defined with its origin at a fixed geographic location on the surface of the Earth. Its axes are oriented so that the z axis points towards the Earth's mass center and the x axis and y axis point towards geographic North and East respectively. Note that the Earth-fixed frame rotates with the Earth's surface daily and hence its orientation with respect to the inertial frame is not fixed. However, the latitude of the origin of the Earth-fixed frame is constant with respect to the inertial frame. Quantities expressed in the Earth-fixed frame are superscripted by O.

The aerodynamic frame is defined such that its x axis points towards the aerodynamic velocity of the rocket. The aerodynamic velocity is the velocity of the local atmosphere with respect to the center-of-mass of the vehicle. The aerodynamic frame x axis is thus oriented parallel to the aerodynamic drag force. Similarly, the y axis and z axis of the aerodynamic frame are oriented parallel to the aerodynamic side-force and lift-force respectively. This convention allows simpler evaluation and application of aerodynamic forces and moments. Quantities expressed in the aerodynamic frame are superscripted by A.

The meaningful interpretation of trajectory data requires representation in geographical co-ordinates. The geographical co-ordinate system is an adaptation of the spherical co-ordinate system used to represent position as a latitude, longitude and altitude triplet. Transformations

from the Cartesian inertial frame to the spherical geographic frame and vice versa are performed using trigonometric relations.

3.5 Coordinate Transformations

It is often necessary in the flight simulation process to evaluate a vector quantity in a Cartesian frame other than the frame in which it is originally defined. This mathematical tool to perform this is known as a co-ordinate transformation. If the origins of the source and destination frames are co-incident, a vector need only be rotated to change its reference from the source frame to the destination frame. The angles of rotation correspond to the angles between the corresponding axes of the two frames in question. Vector rotations correspond to multiplications by rotation matrices. Matrix multiplication may be used to combine the effects of multiple rotations around several axes into a single matrix known as a transformation matrix. A transformation matrix T_{ob} is defined to transform a vector X^b from a source frame b to a destination frame o, giving the transformed vector X^o (Eq. 3-1). The inverse of the same transformation matrix is used to transform a vector back from the destination frame to the source frame. Transformation matrices are orthogonal, implying that the inverse of a transformation matrix is equal to its transpose (Eq. 3-2). This property allows computationally inexpensive co-ordinate transformations without the need for matrix inversion. As matrix multiplication is non-commutative, the order of multiplication is relevant if multiple transformations are applied.

$$X^o = T_{ob}X^b \tag{3-1}$$

$$T_{ob} = T_{bo}^{-1} = T_{bo}^{T} \tag{3-2}$$

In n dimensional Cartesian spaces, transformation matrices are square matrices of size (n, n). Multiplications by transformation matrices do not change the magnitude of a vector. This property is used to correct for floating point errors by calculating and storing the magnitude of the vector before transformation and scaling the transformed vector to its original magnitude.

The three basic transformation matrices for rotation about the three orthogonal Cartesian coordinate axes are given by Eq. 3-3.

$$T_x(\alpha_x) = \begin{bmatrix} 1 & 0 & 0 \\ 0 & \cos\alpha_x & -\sin\alpha_x \\ 0 & \sin\alpha_x & \cos\alpha_x \end{bmatrix} \tag{3-3a}$$

$$T_y(\alpha_y) = \begin{bmatrix} \cos\alpha_y & 0 & \sin\alpha_y \\ 0 & 1 & 0 \\ -\sin\alpha_y & 0 & \cos\alpha_y \end{bmatrix} \qquad (3\text{-}3b)$$

$$T_z(\alpha_z) = \begin{bmatrix} \cos\alpha_z & -\sin\alpha_z & 0 \\ \sin\alpha_z & \cos\alpha_z & 0 \\ 0 & 0 & 1 \end{bmatrix} \qquad (3\text{-}3c)$$

The rotation represented by the Euler angle triplet $(\alpha_x \quad \alpha_y \quad \alpha_z)$ is obtained by successive multiplication by the matrices in Eq. 3-3 in the appropriately desired sequence. If the source and destination frames do not share a co-incident origin, a translation is applied to the vector in the source frame to refer it to the origin of the destination frame. Thereafter, the transformation matrices are applied in the correct sequence. Finally, the result is translated again to refer it back to the origin of the source frame

In order to correctly preserve vector directions, integration of vector variables must always be performed after the integrand vector is referred to the frame in which the sum vector is desired. Velocities are thus referred to the Earth-fixed frame or inertial frame before integration to obtain absolute position, depending on the frame in which the position is desired. The constant of integration in each case is the initial position of the vehicle.

3.6 Kinematic Positions, Velocities, Orientations, Angular Rates and Transformations

The position of the vehicle with respect to the inertial origin (Earth center-of-mass) is defined using a geographic coordinate system with latitude L_t, longitude L_g and an altitude h. The geographic coordinate system thus uses spherical coordinates with the latitude and longitude representing the angles about the Cartesian z and y axes respectively whilst the height or altitude is the coordinate along the radial dimension (Eq. 3-4).

$$X^I = \begin{pmatrix} L_g \\ L_t \\ h \end{pmatrix} \qquad (3\text{-}4)$$

An equivalent Cartesian position vector can be used to represent inertial position but this vector is of little significance to the Earth based observer and is not used during the simulation process except as a means of determining absolute altitude. This altitude is obtained by subtracting the local Earth radius R_t from the magnitude of the inertial position vector in Cartesian coordinates (Eq. 3-5).

$$h = |T_{IO}X^O| - R_t \tag{3-5}$$

The angular orientation of the vehicle body-frame x axis with respect to the Earth fixed frame x axis is simply referred to as the orientation of the vehicle. The orientation is most intuitively described by an Euler angle triplet Φ^{OB}. The Euler angles about the Earth-fixed frame x, y and z axes are physically interpreted as the roll ϕ, pitch θ and yaw ψ angles respectively (Eq. 3-6).

$$\Phi^{OB} = \begin{pmatrix} \phi \\ \theta \\ \psi \end{pmatrix} \tag{3-6}$$

The order in which the rotations about the individual axes are applied is important. The convention followed is the Euler 3-2-1 where the z axis Euler angle rotation (yaw) is applied first followed by the y axis Euler angle (pitch) and finally the x axis Euler angle (roll). Figure 3-4 diagrammatically describes this transformation in a right handed coordinate system.
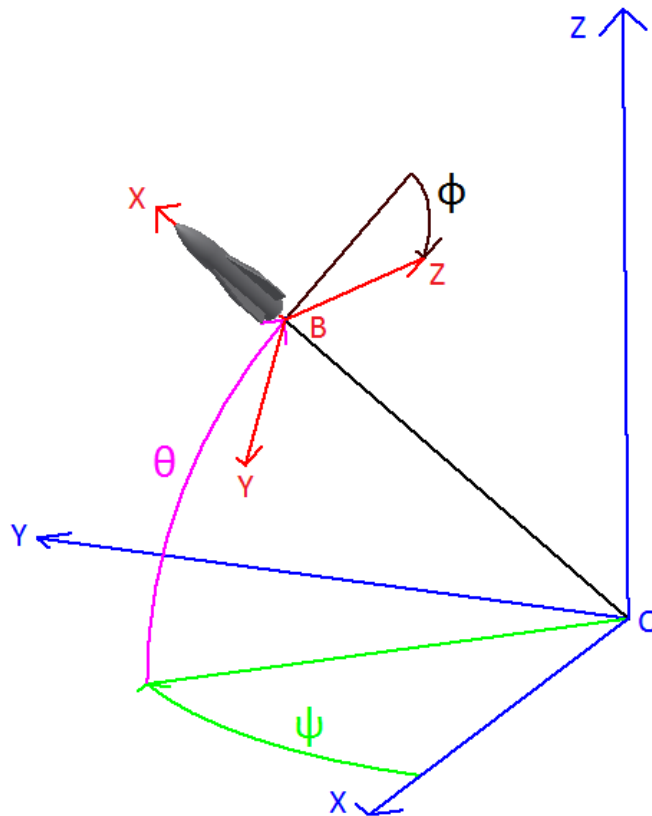
Figure 3-4: The orientation Euler angles applied to transform from the Earth fixed frame to the body frame. The rotations must be applied successively in the order shown.

Several velocities are defined to describe a sounding rocket's dynamics relative to the various measurement frames meaningfully. In this work, the vehicle experiences rotational and translational motion whilst the atmosphere experiences linear motion. In addition, points on the Earth's surface experience arcing motion around the polar axis.

The velocity of the origin of the body frame with respect to the origin of the Earth-fixed frame is known as the kinematic velocity V_k. The kinematic velocity is thus the time rate of change of the vector OB from the Earth-fixed frame origin O to the body frame origin B. This quantity also represents the velocity of the center-of-mass of the vehicle with respect to a fixed point on the ground and hence it is also commonly known as the ground velocity. By definition, the x component and y component of the kinematic velocity are the speeds in the Northerly V_N and Easterly V_E directions respectively. The z component of the kinematic velocity V_Z represents the rate of change of altitude and is positive downward when a right handed coordinate system is used (Eq. 3-7). The differentiation in Eq. 3-7 must be performed in the Earth-fixed frame.

$$V_k = \frac{d\overrightarrow{OB}}{dt} = \begin{pmatrix} V_N \\ V_E \\ V_Z \end{pmatrix} \tag{3-7}$$

The inertial velocity is the velocity of the vehicle center-of-mass with respect to the origin of the inertial frame. The inertial velocity expressed in the Earth-fixed frame V_I^O is obtained by accounting for the effects of the Earth's spherical shape and daily rotation rate Ω_t, representing the most general motion of a terrestrial vehicle (Eq. 3-8). The inertial velocity in the inertial frame V_I^I is simply obtained by multiplying V_I^O by the Earth-fixed frame to inertial frame transformation matrix T_{IO} (See Eq. 3-13)

$$V_I^O = \begin{pmatrix} V_N \\ V_E + \Omega_t(R_t + h)\cos(L_t) \\ -V_Z \end{pmatrix} \tag{3-8}$$

The evaluation of aerodynamic effects requires the definition of the aerodynamic velocity V_a. The aerodynamic velocity is the relative velocity of the local atmosphere with respect to the vehicle center-of-mass. The wind velocity V_w is defined as the local atmospheric velocity relative to the Earth-fixed frame origin. The kinematic velocity thus equals the sum of the wind velocity and the aerodynamic velocity (Eq. 3-9). Wind velocities are always referred to the Earth-fixed frame.

$$V_k = V_a + V_w \tag{3-9}$$

The components of the body frame referenced kinematic velocity V^B are often used to calculate aerodynamic incidence angles. They are assigned specific symbols for convenience. In contrast to the kinematic velocity, the body frame velocity x, y and z components denote speeds in the forward u, rightward v and upward w directions respectively when measured relative to the vehicle center-of-mass (Eq. 3-10).

$$V^B = \begin{pmatrix} u \\ v \\ w \end{pmatrix} \tag{3-10}$$

The derivative of the vehicle's orientation is the kinematic angular velocity Ω_k^b, defined as the rate of change of the orientation of the body frame with respect to the Earth-fixed frame, expressed in the body frame. By convention, its x, y and z components are denoted p, q and r respectively (Eq. 3-11).

$$\Omega_k^b = \begin{pmatrix} p_k^b \\ q_k^b \\ r_k^b \end{pmatrix} = \begin{pmatrix} p \\ q \\ r \end{pmatrix} \tag{3-11}$$

The angular velocity of the Earth Ω_{OI}^b contributes to the inertial angular velocity of the vehicle. It is expressed in the body-frame as in Eq. 3-12 and has components p_t, q_t and r_t about the x, y and z axes respectively.

$$\Omega_{OI}^b = \Omega_t \begin{pmatrix} \cos(L_t) \\ 0 \\ -\sin(L_t) \end{pmatrix} = \begin{pmatrix} p_t \\ q_t \\ r_t \end{pmatrix} \tag{3-12}$$

Having defined the kinematic positions and velocities, two transformations and their inverses are common in the kinematic modeling of sounding rocket flight. The first is the transformation from the body frame to the Earth-fixed frame, denoted by T_{OB} (Eq. 3-13). The second is the transformation from the Earth-fixed frame to the inertial frame, denoted by T_{IO} (Eq. 3-14). The transformation T_{OB} is a function of the body frame orientation triplet composed of Euler angles whilst T_{IO} is a function of the vehicle latitude and longitude, the Earth's daily angular rotation rate and flight time t.

$$T_{BO}$$
$$= \begin{bmatrix} \cos\theta\cos\psi & -\cos\theta\sin\psi & \sin\theta \\ \sin\phi\sin\theta\cos\psi + \cos\phi\sin\psi & -\sin\phi\sin\theta\sin\psi + \cos\phi\cos\psi & -\sin\phi\cos\theta \\ -\cos\phi\sin\theta\cos\psi + \sin\phi\sin\psi & \cos\phi\sin\theta\sin\psi + \sin\phi\cos\psi & \cos\phi\cos\theta \end{bmatrix}$$
$$\tag{3-13}$$

$$T_{IO} = \begin{bmatrix} -\sin(L_t)\cos(L_g + \Omega_t t) & \sin(L_g + \Omega_t t) & -\cos(L_t)\cos(L_g + \Omega_t t) \\ \sin(L_t)\sin(L_g + \Omega_t t) & \cos(L_g + \Omega_t t) & \cos(L_t)\sin(L_g + \Omega_t t) \\ \cos(L_t) & 0 & -\sin(L_t) \end{bmatrix} \tag{3-14}$$

3.7 State Variables

Simulations of dynamic systems predict the evolution of systemic state variables. A set of state variables describe completely the time varying aspects of a simulated system. A state vector X is defined to contain these variables (Eq. 3-15). The state vector at a given simulation time encapsulates all variables necessary to predict the state vector at a later simulation time. A sufficient set of state variables is not unique. In this work, state variables are chosen so as to convey maximal intuitive flight performance information whilst aiming to minimize computational and storage requirements.

$$X = \begin{bmatrix} L_g \\ L_t \\ h \\ \phi \\ \theta \\ \psi \\ u \\ v \\ w \\ p \\ q \\ r \end{bmatrix} \tag{3-15}$$

A freely flying rigid rocket possesses three translational and three rotational degrees of freedom. These describe the location and orientation of the vehicle at a given instant, referred to an inertial co-ordinate frame. The time history of these variables and their derivatives defines the vehicle's trajectory and is the solution to the flight dynamics problem. The first derivatives of the location and orientation define the vehicle's linear and angular velocities respectively. In turn, the derivatives of the linear and angular velocities are the linear and angular accelerations, respectively. There are several other variables that must be known to completely describe the state of the vehicle at any time. These include the aerodynamic incidence angles, free-stream Mach number, vehicle Reynolds number, mass, center-of-mass and center-of-pressure. Auxiliary velocities such as the aerodynamic velocity are also of interest.

3.8 Newtonian Dynamics

The governing equation in Newtonian flight dynamics is Newton's 2nd Law, embodying the principle of conservation of momentum where the momentum is denoted p and the speed v. Newton's 2nd Law states that the sum of external efforts F_{EXT} acting on a body of mass m is equal to product of its inertia and its acceleration. This differential equation of motion for linear

dynamics is applied by calculating the sum of external efforts and dividing by the body mass. In three dimensions, the resulting acceleration vector forms a vector second order ordinary differential equation. The solution of this differential equation produces the trajectory of the body through space. As with any ordinary differential equation in time, initial conditions must be supplied before a unique solution may be found. The initial state vector must be supplied by the user, embodying the launch conditions of the sounding rocket being simulated. In the application of the law to a rocket, the change in momentum of the exhausted propellant also needs to be accounted for separately as Newton's 2nd law is applicable only to constant mass systems. This effect is apparent when linear momentum is differentiated using the product rule in Eq. 3-16, leading to the second term $v\frac{dm}{dt}$, wherein it should be understood that the mass flow rate $\frac{dm}{dt}$ refers to the *propellant mass flow rate* and the velocity v is the *propellant exhaust velocity*.

The analogue of Eq. 3-16 in angular coordinates is Euler's Law (Eq. 3-17), stating that the sum of external moments M_{EXT} equals the product of the body moment-of-inertia I and angular acceleration. In this case, the angular momentum is denoted H and the angular velocity Ω. The linear and rotational degrees of freedom are treated separately. The calculation of the accelerations using Newton's and Euler's laws requires instantaneous knowledge of the external efforts and physical properties of the vehicle. The accurate calculation of these quantities is the major task in rocket flight dynamics. This process requires modeling of the vehicle structure, the vehicle propulsion system and the Earth and its atmosphere. The following sections describe the techniques used to model these systems based only on input information from the state vector.

$$\sum F_{EXT} = \frac{dp}{dt} = \frac{d(mv)}{dt} = m\frac{dv}{dt} + v\frac{dm}{dt} \qquad (3\text{-}16)$$

$$\sum M_{EXT} = \frac{dH}{dt} = \frac{d(I\Omega)}{dt} = I\frac{d\Omega}{dt} + \Omega\frac{dI}{dt} \qquad (3\text{-}17)$$

The use of rotating coordinate frames such as the body frame and Earth-fixed frame necessitates the use of the fundamental relation of dynamics (Eq. 3-18) for vector differentiation (which is also known as the Coriolis equation). This relation states that the inertial time derivative of a vector X observed from a rotating frame $\frac{dX^1}{dt}$ equals the sum of that vector's time derivative in the stationary frame $\frac{dX^0}{dt}$ and the cross product of the vector being differentiated and the angular velocity vector Ω_{10} of the rotating frame, relative to the inertial frame. The relation is most often

applied when formulating equations of motion in the body frame, which rotates relative to the Earth-fixed frame.

$$\frac{d\mathbf{X^1}}{dt} = \frac{d\mathbf{X^0}}{dt} + \mathbf{\Omega_{10}} \times \mathbf{X}$$

(3-18)

Dynamic effects due to the curvature and the rotation of the Earth must be included for accurate generation of trajectories that traverse more than one degree of the Earth's circumference (approximately 111.2 km of arc distance on the Earth's surface). The curvature of the Earth causes an apparent downward centripetal acceleration of the vehicle proportional to the square of the Earth-tangential component of the kinematic velocity. The Earth's daily rotation about its polar axis induces the Coriolis Effect. This effect is the apparent eastward or westward motion of objects that fly off the surface of the Earth in a northerly or southerly direction respectively. The Coriolis Effect results from the differential linear motion of the Earth's surface at various latitudes. Locations on the Equator experience maximum linear motion due to the Earth's rotation whilst the poles are stationary with respect to the Earth's mass center. Whilst a vehicle is in flight its linear velocity due to the angular motion of the Earth is dependent on its instantaneous latitude. The Coriolis Effect results in an 'apparent acceleration' term whose effect diminishes with increasing absolute latitude, known as the Coriolis acceleration. The effect of the Earth's curvature is also manifested as an additional 'apparent acceleration' term in the Newtonian formulation of the rocket dynamics equation. It is important to note that the Coriolis Effect is only observable from a rotating frame of reference, such as the Earth.

3.9 Quaternion Angular Representation for Rotational Dynamics

Euler angles are commonly used to represent orientation in orthogonal 3D space. The three angles of an Euler angle triplet represent three successive rotations about three corresponding mutually orthogonal axes in a specific order. Although highly intuitive, Euler angles display two important drawbacks. The first is the presence of inherent singularities at the 'poles' of the spherical domain of rotation about the body x and z axes, where the vehicle pitch angles reach $\pm$ 90°. A second disadvantage is the loss of a degree of freedom when two of the orthogonal axes of rotation are parallel, leading to a degenerate two-dimensional space of rotations. This phenomenon is known as gimbal lock.

A quaternion is a four dimensional vector quantity derived by extending the set of complex numbers $(q_0 + q_1\boldsymbol{i})$ with two extra imaginary dimensions, denoted $\boldsymbol{j}$ and $\boldsymbol{k}$, resulting in the quantity $\boldsymbol{q}$ defined by Eq. 3-19.

$$q = (q_0 + q_1 i + q_2 j + q_3 k) \qquad \text{(3-19)}$$

where q_0, q_1, q_2 and q_3 are real numbers. Quaternions are useful in the description of angular coordinates and rotational transformations in 3D due to the presence of an extra degree of freedom. This extra mathematical dimension eliminates all singularities as well as the gimbal lock effect. Quaternions may also be regarded as a combination of a vector and a scalar. Unit quaternions are characterized by the constraint in Eq. 3-20.

$$q_0^2 + q_1^2 + q_2^2 + q_3^2 = 1 \qquad \text{(3-20)}$$

It can be shown that the quaternion representation of a rotation described by an Euler angle triplet is given by Eq. 3-21.

$$
\begin{bmatrix} q_0 \\ q_1 \\ q_2 \\ q_3 \end{bmatrix} =
\begin{bmatrix}
cos(\psi/2)\,cos(\theta/2)\,cos(\phi/2) + sin(\psi/2)\,sin(\theta/2)\,sin(\phi/2) \\
cos(\psi/2)\,cos(\theta/2)\,sin(\phi/2) - sin(\psi/2)\,sin(\theta/2)\,cos(\phi/2) \\
cos(\psi/2)\,sin(\theta/2)\,cos(\phi/2) + sin(\psi/2)\,cos(\theta/2)\,sin(\phi/2) \\
sin(\psi/2)\,cos(\theta/2)\,cos(\phi/2) - cos(\psi/2)\,sin(\theta/2)\,sin(\phi/2)
\end{bmatrix}
$$

$$\text{(3-21)}$$

The time derivative of a unit quaternion is thus directly calculable from the corresponding body frame angular rates using Eq. 3-22a. A correction term consisting of the product of the deviation from unity λ magnitude (Eq. 3-22b) and a correction factor K is added to ensure that the unity constraint (Eq. 3-20) is always adhered to as closely as possible [24].

$$
\frac{d}{dt}\begin{bmatrix} q_0 \\ q_1 \\ q_2 \\ q_3 \end{bmatrix} =
\left(\frac{1}{2}\begin{bmatrix} 0 & -p & -q & -r \\ p & 0 & r & -q \\ q & -r & 0 & p \\ r & q & -p & 0 \end{bmatrix} + K\lambda \right)
\begin{bmatrix} q_0 \\ q_1 \\ q_2 \\ q_3 \end{bmatrix} \qquad \text{(3-22a)}
$$

$$\lambda = 1 - (q_0^2 + q_1^2 + q_2^2 + q_3^2) \qquad \text{(3-22b)}$$

The inverse conversion, which transforms a quaternion orientation representation to an Euler angle orientation triplet, is also required. In this work, a quaternion is used to store the orientation of the vehicle. This orientation quaternion must be initialized using the vehicle's initial (launch) body Euler angles with respect to the Earth-fixed axes using Eq. 3-21. During simulation, the derivative of the orientation quaternion due to the body rates is calculated using

Eq. 3-22 and the orientation quaternion is then integrated using numerical techniques in a process identical to that used for the rest of the variables in the state vector. The body's Euler angles are recovered using Eq. 3-23, Eq. 3-24 and Eq. 3.25, when required for the calculation of aerodynamic effects or for visualization purposes.

$$\psi = \tan^{-1}\left(\frac{2(q_1 q_2 + q_0 q_3)}{q_0^2 + q_1^2 - q_2^2 - q_3^2}\right) \qquad (3\text{-}23)$$

$$\phi = \tan^{-1}\left(\frac{2(q_2 q_3 + q_0 q_1)}{q_0^2 - q_1^2 - q_2^2 + q_3^2}\right) \qquad (3\text{-}24)$$

$$\theta = \sin^{-1}\left(-2(q_1 q_3 - q_0 q_2)\right) \qquad (3\text{-}25)$$

3.10 External Efforts

Flying vehicles experience and overcome a variety of internal and external forces to remain airborne. Internal forces include mechanical forces and their reactions, causing elastic structural deformations. Although these effects may be significant if they strongly affect the geometry of the vehicle, they may be disregarded for the purposes of sounding rocket flight performance prediction. Significant aero-elastic effects are only encountered during the atmospheric flight of highly deformable flying structures, such as bird's wings and the vast majority of sounding rocket airframes do not fall in that category.

There are three significant external forces that act on a rocket during flight, namely the gravitational force $m\vec{g}$, aerodynamic force $\overrightarrow{F_A}$ and propulsion force $\overrightarrow{F_m}$. At any instant in time, the state vector is sufficient for calculation of these forces (Eq. 3-26). It is useful to note that only gravitational forces are always present. Propulsion forces are only present when an on-board motor is firing whilst aerodynamic forces are encountered solely within the confines of an atmosphere.

$$\sum \overrightarrow{F_{EXT}} = \overrightarrow{F_A} + \overrightarrow{F_m} + m\vec{g} \qquad (3\text{-}26)$$

The gravitational force of the Earth accelerates the rocket towards the center of the Earth. A sounding rocket also experiences gravitational forces from other astronomical bodies such as the Sun, Moon and planets, but their relative effects are small enough to be safely disregarded for terrestrial simulations. By definition, gravitational forces act through the mass center of an

object, hence the sum moment caused by all gravitational forces is zero. An analytical model of the Earth's gravitational acceleration on a sounding rocket is presented in section 3.14.

Aerodynamic efforts act on a sounding rocket when it moves through the Earth's atmosphere. A force or moment acts along each of the vehicle's six degrees of freedom. The magnitude of aerodynamic forces and moments depend on the external geometry of the vehicle, local atmospheric properties and the magnitude and direction of the aerodynamic velocity. Aerodynamic forces and moments are thus commonly described using a set of six non-dimensional coefficients known as aerodynamic force and moment coefficients. Aerodynamic coefficients must be provided before aerodynamic efforts may be calculated. An exact evaluation of the aerodynamic coefficients for a given vehicle airframe geometry is only possible through experimentation. Approximations using wind-tunnel tests and computational fluid dynamics (CFD) simulations are commonly used to model sounding rocket aerodynamics. Approximate analytical techniques are also present. The calculations of the aerodynamic coefficients are discussed in detail in Chapter 5. For the present, it is sufficient to note that the aerodynamic force is a product of an aerodynamic reference area S, dynamic pressure $\rho(V_a)^2/2$ and the body frame aerodynamic coefficient vector transformed to the Earth-fixed frame, where the atmospheric density is denoted ρ and V_a is the aerodynamic speed (Eq. 3-27).

$$F_A = \frac{\rho S V_a^2}{2} T_{OB} \begin{pmatrix} C_A \\ C_Y \\ C_Z \end{pmatrix} \tag{3-27}$$

Rocket propulsion is based on Newton's 3rd law of motion. Thrusts experienced by a rocket are the reactions of exhaust gases expelled by the motor. These propulsion forces are evaluated by modeling the performance of the rocket motor powering the vehicle. The direction of a propulsion force is determined by the orientation of the motor nozzle in the vehicle body frame. In general, propulsion forces may also produce moments if the thrust vector does not act through the center-of-mass of the vehicle. However, the majority of sounding rockets use aligned motors and hence propulsion moments are very small, arising solely from thrust misalignments. The calculation of the propulsion force is discussed in more detail in section 3.17.

3.11 Static Atmospheric Model

The Earth's atmosphere is a layer of gases that completely envelopes the planet. Any flying vehicle travelling near the surface of the Earth must travel through the atmosphere and hence

experience aerodynamic effects. The modeling of aerodynamic effects on vehicle flight dynamics is an important part of the overall flight performance prediction process.

Mean atmospheric properties vary primarily with altitude above mean sea level. Less significant variations with the seasons and latitude are also known. For the level of accuracy generally required in sub-orbital sounding rocket flight dynamics, it is sufficient to model the altitude variation of mean atmospheric properties alone. The fluids in the atmosphere are in constant motion and hence spatial and temporal variations in atmospheric properties are also present on a local scale. It is sufficient to assume that temporal variations in local atmospheric properties are insignificant over the time-scales encountered in rocket flight dynamics. This assumption is known as the 'frozen' atmosphere or the Taylor hypothesis [23]. Further relevant assumptions may be made to simplify atmospheric modeling for flight dynamics simulations.

Air is regarded as an ideal gas (Eq. 3-28) whose ratio of specific heats R is known, allowing a variety of relatively simple empirical models to describe altitude-variation of atmospheric properties. Properties of interest for trajectory simulation are temperature T, pressure p and density ρ. The temperature derivative with altitude is known as the temperature lapse rate T_h. A piece-wise constant temperature lapse-rate is assumed, known as the Toussaint assumption (Eq. 3-29), giving a piecewise linear temperature profile (Eq. 3-30). Atmospheric properties at the lower end of any of these altitude bands of constant lapse rate are denoted as the base pressure p_o, base temperature T_0 and base density ρ_0. Laplace's pressure law (Eq. 3-31) may then be applied to the atmosphere within an altitude band, relating pressure variations to atmospheric weight. The solution of these equations for the pressure is given by Eq. 3-32 and the density in Eq. 3-33.

$$\rho = \frac{p}{RT} \tag{3-28}$$

$$T_h = \frac{dT}{dh} \tag{3-29}$$

$$T = T_0 + T_h(h - h_0) \tag{3-30}$$

$$dp = -\rho g dh \tag{3-31}$$

$$p = p_0 \left(1 + \frac{T_h}{T_0}(h - h_0) \right)^{\frac{-g}{RT_h}} \tag{3-32}$$

$$\rho = \rho_0 \left(1 + \frac{T_h}{T_0}(h - h_0) \right)^{\frac{-g}{RT_h}} \tag{3-33}$$

The above equations are simplified for atmospheric layers that display zero temperature lapse rates, giving Eq. 3-34 for the pressure and Eq. 3-35 for the density.

$$p = p_0 e^{-g(h-h_0)/RT_0} \tag{3-34}$$

$$\rho = \rho_0 e^{-g(h-h_0)/RT_0} \tag{3-35}$$

The International Standard Atmosphere model (Table 3-1) is a commonly used atmospheric model for flight simulation. It employs piece-wise exponential decay functions to model variation of pressure and density with altitude. This model applies the ideal gas, Taylor and Toussaint approximations and Laplace's law to air. It is defined for altitudes up to 84 km above mean sea level. The NRLMSISE-2000 upper atmospheric model may be used to extend the atmosphere beyond the ceiling altitude of 84 km [40].

Table 3-1: International Standard Atmosphere (1970) parameters vs. altitude band [41]

$h\ (m)$	$T_h \left(\frac{^\circ C}{m}\right)$	$T_0(K)$	$p_0(Pa)$	$\rho_0 \left(\frac{kg}{m^3}\right)$
0 – 11000	-0.0065	288.16	101325.0	1.225
11000 – 20000	0.0	216.66	22631.7	0.3639
20000 – 32000	0.0010	216.66	5474.72	0.08803
32000 – 47000	0.0028	228.66	867.98	0.01322
47000 – 51000	0.0	270.65	110.91	0.0014256
51000 – 71000	-0.0028	270.65	66.939	0.00086021
71000 – 84000	-0.002	214.65	3.9564	0.000064012

3.12 Wind Models

3.12.1 Generic Winds

In the flight dynamics literature, the local velocity of the atmospheric fluids with respect to the Earth is commonly referred to as wind. In general wind velocities may vary both spatially and temporally in a complex fashion, but the Taylor hypothesis causes temporal variations in wind velocities to be disregarded. The wind velocity vector is thus assumed to be given as a three-dimensional function of geographic latitude, longitude and altitude. Many wind models also limit the vertical component of wind velocity to zero, as climatic winds are generally horizontal.

In this work, an option is supplied to use empirical wind tables which denote the horizontal wind velocity and wind bearing as a function of altitude. An arbitrary number of altitude measurements may be supplied and linear interpolation and/or extrapolation is used to derive a continuous wind profile as a function of altitude.

3.12.2 Gradient Winds

In situations where detailed wind data are unavailable, a simple approximation may be applied to capture the general characteristics of atmospheric winds. The wind speed s is then assumed to be a linear function of altitude with gradient $\frac{ds}{dh}$ and fixed direction ψ_w, referred to as a *gradient* wind. The wind vector is limited to act below a certain ceiling altitude above which the linearity assumption fails. This approximation generates a horizontal wind vector V_w with speed s_0 at mean sea level, given by Eq. 3-36.

$$V_w = T_z(\psi_w)\left(s_0 + \frac{ds}{dh}h\right)\vec{i} \qquad\qquad (3\text{-}36)$$

3.12.3 Jet Streams

Jet streams are high altitude bands of fast moving air caused by the global-scale circulation of hot equatorial and cold polar air masses [42]. There are two such bands in each hemisphere, termed the polar and subtropical jet streams. Jet streams form bands around the Earth, loosely following a fixed latitude North or South of the Equator. The subtropical jet stream occurs at around latitude 30° and occurs at altitudes of 10 km to 16 km AMSL. The polar jet stream occurs between latitudes 45° and 60° at 7 km to 12 km altitudes. Wind velocities in jet stream may reach 360 km/h and are essentially horizontal. The effects of jet streams on aircraft and

rocket flight trajectories are significant enough to warrant specific modeling. Jet stream velocity profiles in a certain latitude band are generally invariant with longitude and may be approximated using only a parabolic velocity profile as a function of altitude. A parabolic jet stream velocity profile V_{jet} with maximum velocity $V_{jet-max}$ present between a lower altitude $h_{jet-floor}$ and upper altitude $h_{jet-ceil}$ is given as function of altitude by Eq. 3-37.

$$V_{jet} = V_{jet-max}\left(1 - \left(\frac{h - \frac{h_{jet-ceil} + h_{jet-floor}}{2}}{\frac{h_{jet-ceil} - h_{jet-floor}}{2}}\right)^2\right) \qquad h_{jet-floor} < h < h_{jet-ceil} \quad (3\text{-}37)$$

3.12.4 Turbulence

Winds often display localized random vertical gusts known as turbulence. These gusts are best described stochastically and have been well characterized using frequency spectra [43]. The dynamic response of a sounding rocket to turbulent wind gusts is important because vehicles experience sustained flights at nonzero aerodynamic incidence angles when flying through rapidly varying winds. The resulting additional drag and deviations cause a net loss in altitude performance and may even lead to instability if a marginally stable vehicle experiences severe turbulence when flying relatively slowly. In this work, the Dryden turbulence spectrum Φ_{ZZ} was used to model atmospheric turbulence as a function of spatial frequency $\bar{\omega}$ and aerodynamic speed (Eq. 3-38).

$$\Phi_{ZZ} = \frac{\sigma^2 L(1 + 3\bar{\omega}^2)}{2\pi V_a (1 + \bar{\omega}^2)^2} \qquad\qquad (3\text{-}38)$$

The turbulence correlation length L is a weak function of altitude and is approximately 150 m for all altitudes above 200 m. The turbulence speed standard deviation σ determines the severity of the turbulent gusts and is a more complex function of altitude. This parameter is related to seasonal and climatic factors. In this work, it is not modeled explicitly, but rather taken as a known input from the user.

The Dryden spectrum must be converted to the temporal domain before a turbulence gust velocity is obtained. The details of the state space conversion and the inverse Laplace transform are presented by Zipfel [24]. The equivalent transfer function in the frequency domain is given by Eq. 3-39. The state space form of this system and its time domain solution are given by Eq. 3-40 and Eq. 3-41 respectively, where τ is the turbulence gust velocity (z component) and w the spatial coordinate.

$$\frac{\tau(s)}{w(s)} = \sigma \sqrt{\frac{L}{2\pi V_a}} \frac{1+\sqrt{3}(L/V_a)s}{(L/V_a)^2 s^2 + 2(L/V_a)s + 1} \tag{3-39}$$

$$\begin{bmatrix} \dot{x}_1 \\ \dot{x}_2 \end{bmatrix} = \begin{bmatrix} 0 & 1 \\ -\left(\frac{V_a}{L}\right)^2 & -\frac{2V_a}{L} \end{bmatrix} \begin{bmatrix} x_1 \\ x_2 \end{bmatrix} + \begin{bmatrix} 0 \\ \left(\frac{L}{V_a}\right)^2 \end{bmatrix} w(t) \tag{3-40}$$

$$\tau(t) = \sigma \sqrt{\frac{L/V_a}{2\pi}} \begin{bmatrix} 1 & \sqrt{3}\frac{L}{V_a} \end{bmatrix} \begin{bmatrix} x_1 \\ x_2 \end{bmatrix} \tag{3-41}$$

3.13 Geodetic Model

The Earth is a roughly ellipsoidal planet which experiences a daily rotation about its own North-South axis. The geometry of the Earth is most accurately approximated by the Geoid, a mathematical construct based on a series of spherical-harmonic functions. It is simpler and more practical to adopt a first order spherical or second order ellipsoidal approximation for sub-orbital flight dynamics calculations. The choice of approximation affects the notions of altitude and gravitation, both of which are important in rocket flight dynamics. The Earth's main deviation from spherical geometry is a slight bulge along the equator which causes the Earth to resemble a ball slightly flattened at the poles. Other more subtle variations in the Earth's density and radius are present as a function of geographic location, but these may be ignored as their effects on sounding rocket trajectories are minute. The Earth's density distribution is also assumed to differ only along the radial dimension, so that its geometric and mass centers coincide when a spherical or ellipsoidal model is used to describe its shape. The apparent acceleration term in Earth-fixed coordinates due to the spherical geometry of the Earth A_S is given by Boiffier [23] as (Eq. 3-42). Note the dependence on latitude alone.

$$A_S = \frac{1}{(R_t+h)} \begin{bmatrix} -V_N V_Z + V_E{}^2 \tan L_t \\ -V_E V_Z - V_E V_N \tan L_t \\ V_N{}^2 + V_E{}^2 \end{bmatrix} \tag{3-42}$$

The apparent Coriolis acceleration $A_{CORIOLIS}$, expressed in Earth-fixed coordinates, is also given by Boiffier [23] (Eq. 3-43).

$$A_{CORIOLIS} = \Omega_t \begin{bmatrix} 2V_E \sin L_t + \Omega_t(R_t+h)\sin L_t \cos L_t \\ -2V_Z \cos L_t - 2V_N \sin L_t \\ 2V_E \cos L_t + \Omega_t(R_t+h)\cos{}^2 L_t \end{bmatrix} \tag{3-43}$$

3.14 Gravitational Model

The gravitational force exerted by the Earth on flying vehicles is described using Newton's law of universal gravitation. This law states that the gravitational force between two bodies is proportional to their masses and inversely proportional to the distance between their mass centers. The constant of proportionality is the universal gravitational constant G. The mass of the rocket m and its distance from the mass center of the Earth are the primary parameters needed to determine the gravitational force of the Earth. The mass of the Earth M is assumed known and constant. The mass of the vehicle varies as a function of time due to fuel consumption and stage separation events, but this variation is negated by the assumption that the mass of the vehicle is insignificant in comparison to the mass of the Earth. The respective masses being known, the evaluation of the local gravitational acceleration vector is a function of the inertial position and the Earth's geometric model. By definition, the mass center of the Earth is the origin of the inertial frame. Therefore, the magnitude of the vehicle's position vector (i.e. its mass center) in the inertial frame is the distance between the vehicle and the Earth's mass center. This is simply the sum of the Earth's radius and the vehicle altitude. The gravitational acceleration in Earth-fixed coordinates g^O is then given by Eq. 3-44.

$$g^O = \begin{bmatrix} 0 \\ 0 \\ \frac{GM}{(R_t + h)^2} \end{bmatrix} \tag{3-44}$$

The gravitational acceleration vector is always oriented directly towards the mass-center of the Earth. Due to the spherical earth assumption, the local vertical direction remains parallel to the direction of gravitational acceleration. This becomes untrue when the Earth's shape is modeled using an ellipsoid or any other non-spherical geometry and also when the Earth's density varies with latitude and/or longitude. In the case of the uniform-density ellipsoidal model, the gravitational acceleration is additionally dependent only on the latitude, offering a more accurate yet relatively simple alternative to the spherical model.

3.15 Aerodynamic Model

The aerodynamic behavior of a sounding rocket is defined by its airframe geometry, its mass distribution and the prevalent flight conditions. In a trajectory simulation, the flight conditions may be described adequately using only the vehicle orientation, aerodynamic velocity vector, the flight Mach number and the local atmospheric density. The Mach number in turn depends on local atmospheric thermodynamic properties. The airframe geometry determines the location of

the aerodynamic *Centre of Pressure* (*CP*) and the surface geometry over which aerodynamic loads act. The vehicle's internal mass distribution determines the location of the *Centre of Mass* (*CM*) which is required for aerodynamic moment calculations. This section discusses the aspects of sounding rocket aerodynamics which are relevant to trajectory simulation. A more detailed description of the techniques of sounding rocket aerodynamic analysis is provided in Chapter 5 along with the results which are used as inputs to the trajectory simulation algorithm. It is assumed that a detailed aerodynamic model is available for the vehicle and the inputs and outputs of such a model are now discussed.

Aerodynamic effects are best modeled in body axes. At any time when the body-frame aerodynamic velocity vector is not parallel to the nose (x axis) of the body frame, the vehicle experiences non-zero aerodynamic incidence angles. These angles are the angle of attack, sideslip angle, total angle of attack and the aerodynamic roll angle. The total angle of attack is the angle between the body frame x axis and the aerodynamic velocity vector. The aerodynamic roll angle is the angle between the body frame z axis and the projection of the aerodynamic velocity vector onto the body frame yz plane as shown in Figure 3-5. The aerodynamic angle of attack is denoted α, the sideslip angle β, the roll angle ϕ_a and total angle of attack α_T. The aerodynamic load factor plane is shown in cyan, representing the plane in which both the aerodynamic velocity V_a and body frame x axis lie. In this work on vehicles with tetragonal symmetry, it is assumed that the aerodynamic force and lateral accelerations are limited to the aerodynamic load factor plane, although certain complex flow effects such as vortex shedding and Magnus loads may add lateral components. The modeling of these effects is beyond the scope of this work.

The plane through which the aerodynamic force acts is known as the load factor plane. For rotationally symmetric vehicles, the aerodynamic force acts parallel to the aerodynamic velocity vector and hence the aerodynamic velocity lies on the load-factor plane. For such vehicles, this load-factor plane is defined using only the aerodynamic roll angle in body axes. Aerodynamic coefficients are thus functions of the Mach number, Reynolds's number, total angle of attack and aerodynamic roll angle. Note that all these quantities may be derived from the state vector.

In aerodynamic axes, the component of the aerodynamic velocity acting parallel to the aerodynamic velocity vector is the drag force whilst the component normal to it is the lift force. It is more convenient to transform the drag and lift forces into the body frame. The components of the aerodynamic force in body-axes are the axial force and the normal forces. The axial force acts along the body frame x axis, causing drag whilst the y and z components of the normal force act along the body frame y and z axes respectively, causing pitching and yawing. These y

and *z* normal force components are determined from the total normal and side forces by a rotational transformation through the aerodynamic roll angle.
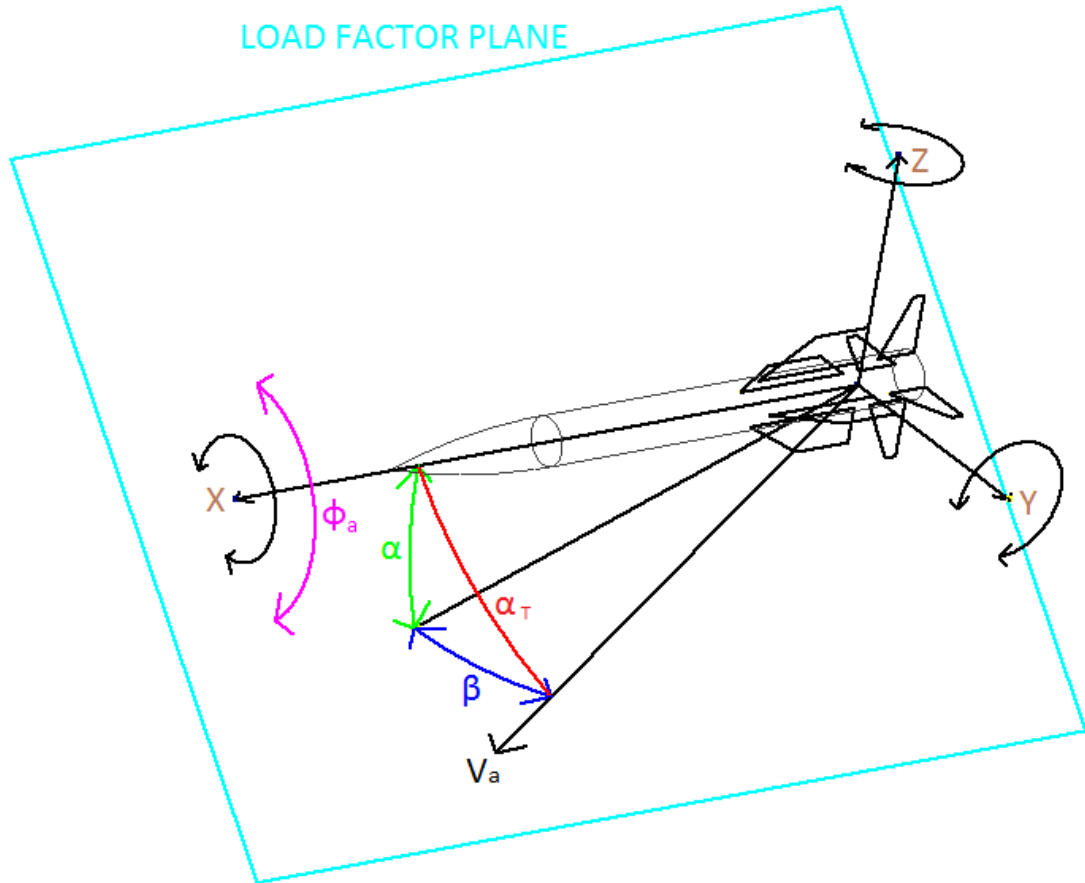
Figure 3-5: The aerodynamic incidence angles and load factor plane in the body frame.

A significant component of the total axial force experienced by a rocket is due to base pressure drag, which is discusses further in Chapter 5. Base drag is markedly lower when the rocket motor is active and the exhaust plume prevents low pressure regions from building up at the rear end of the vehicle. It is therefore more accurate to calculate the distinct axial force for a given configuration under powered and unpowered conditions and use the relevant force coefficient in simulations. The flight time and rocket motor burn time thus become feedback inputs to the aerodynamic model.

In this thesis, only sounding rockets possessing tetragonal symmetry are considered. Tetragonal symmetry implies that the vehicle has a fuselage of circular cross-section and a fin-set with four equally spaced fins of equal cant angle and identical plan-form geometry. The net effect of this fin placement pattern is a periodic variation of the aerodynamic force as a function of the aerodynamic roll angle. By convention, tetragonal symmetry places the four fins on the body

frame xy and xz planes. This makes the period of aerodynamic force fluctuation 90°. The normal force reaches a maximum every 45° of aerodynamic roll angle and a minimum at every 90°. These periodic variations in normal forces may be modeled using the square of the sine function of twice the aerodynamic roll angle. The orientation Euler angles are thus needed as inputs to the aerodynamic model.

Aerodynamic moments act to stabilize a vehicle when the *CP* is farther from the nose-tip than the *CM*. Conversely, aerodynamic moments are destabilizing when the *CM* is farther from the nose-tip than the *CP*. The distance between the *CP* and *CM* is the moment arm through which the aerodynamic force acts, causing a part of the total aerodynamic moment. Another component of the aerodynamic moment is caused by aerodynamic resistance to the angular velocity of the vehicle, thus damping or limiting angular rates. In general, damping moments act about all three rotational degrees of freedom. The roll damping moment is also known as the spin-deceleration moment whilst the effect of the roll rate in inducing side forces is termed the Magnus effect. In a vehicle with movable control surfaces, control surface deflections also contribute to the net aerodynamic forces and moments. Therefore, the angular rates are an input to the aerodynamic model as well.

For a given airframe geometry and CM profile, all aerodynamic effects are calculated using the tools discussed in Chapter 5 and supplied to the 6-DOF flight dynamics simulator in the form of aerodynamic force and moment coefficients lookup tables. These tables are supplied as functions of the aerodynamic incidence angles and the Mach number. The lookup tables of pre-calculated aerodynamic coefficients are used to retrieve the aerodynamic coefficients during simulation based on the instantaneous flight conditions. The aerodynamic incidence angles and aerodynamic force and moment coefficients are then used to calculate total body frame aerodynamic forces and moments based on Eq. 3-27 and its analogue for moments. Refer to Chapter 5 for details of the relevant equations. A total of eight aerodynamic parameters are looked up from tables as listed in Table 3-2.

Table 3-2: Aerodynamic parameter inputs to 6-DOF simulation model

Aerodynamic Parameter	Table Dependencies
Axial Force Coefficient (Powered)	Mach Number, Total AOA
Axial Force Coefficient (Unpowered)	Mach Number, Total AOA
Normal Force Coefficient	Mach Number, Total AOA, Aerodynamic Roll Angle
Centre of Pressure Location	Mach Number, Total AOA
Normal Force Gradient	Mach Number, Total AOA
Rolling Moment Coefficient	Mach Number, Total AOA, Roll Rate
Pitching Moment Coefficient	Mach Number, Total AOA, Pitch Rate
Yawing Moment Coefficient	Mach Number, Total AOA, Yaw Rate

Two-dimensional linear interpolation is used to approximate intermediate values for aerodynamic parameters that are functions of both the total angle of attack and the local Mach number. In the event that empirical lookup-tables of aerodynamic coefficients are unavailable, a second internal aerodynamic prediction model is described in detail in Chapter 5. This model is also valid only for tetragonal vehicles whose fuselages are bodies of revolution. In addition to axial force, lift force and center of pressure, this model also estimates rolling moment and pitching moment coefficients for multiple fin sets. The choice of aerodynamic model is made before simulation.

3.16 Vehicle Structural Model

A generalized physical model of a sounding rocket is needed to sufficiently describe the physical properties required for flight performance prediction. Fuel consumption leads to the time evolution of these properties and hence the vehicle physical model must also allow for temporal variations. The physical properties of a vehicle relevant to rigid body flight simulation are the density distribution, total mass, center of mass location and the moment of inertia tensor. The moment of inertia tensor I includes moments of inertia about the principal axes denoted by I_{XX}, I_{YY} and I_{ZZ} as well as the products of inertia I_{XY}, I_{XZ} and I_{YZ} for non-symmetrical configurations. It is defined in Eq. 3-46 and its components may be given special symbols as shown. The geometric complexity of the structural components of a typical sounding rocket makes it non-trivial to calculate these properties accurately. However, these properties are all lumped-parameters which are relatively insensitive to small geometric details or slight variations in density distribution. For practicality, simulations rely on a combination of simplified models of the actual vehicle structural design and measured data such the masses

of subcomponents. The accuracy of the simulations may be increased by including finer details in the structural model and vice versa.

The volumetric integrals defining the moments of inertia and products of inertia are given by Eq. 3-45. The moments of inertia can be physically interpreted as a body's resistance to rotation about a certain axis. Similarly, the products of inertia describe the asymmetry of a body's mass distribution in a certain plane described by two orthogonal axes. Bodies with a nonzero product of inertia associated with a given plane will wobble when rotated about an axis orthogonal to that plane.

$$I_{XX} = \iiint (y^2 + z^2)dm \tag{3-45a}$$

$$I_{YY} = \iiint (x^2 + z^2)dm \tag{3-45b}$$

$$I_{ZZ} = \iiint (x^2 + y^2)dm \tag{3-45c}$$

$$I_{XY} = \iiint xydm \tag{3-45d}$$

$$I_{XZ} = \iiint xzdm \tag{3-45e}$$

$$I_{YZ} = \iiint yzdm \tag{3-45f}$$

$$I = \begin{bmatrix} I_{XX} & -I_{XY} & -I_{XZ} \\ -I_{XY} & I_{YY} & -I_{YZ} \\ -I_{XZ} & -I_{YZ} & I_{ZZ} \end{bmatrix} = \begin{bmatrix} A & -F & -E \\ -F & B & -D \\ -E & -D & C \end{bmatrix} \tag{3-46}$$

When performing structural calculations, a workable approach is to assume that the sounding rocket is a rigid assembly of constant density components, each of which has a simple geometry. The use of simple geometries allows analytical evaluation of masses, center of mass locations and moments of inertia matrices for each component. This is true for geometries such as cylinders, rectangular prisms (boxes), spheres, conic sections, flat plates and the ogive. Thin shell approximations of all the aforementioned geometries may be modeled analytically as well. Point masses are used to approximate components whose geometric designs are odd, uncertain or unknown. This approach to structural modeling avoids numerical techniques and leads to computational efficiency. It is also easily scalable, facilitating relatively simple or more complex structural models and allowing progressive levels of fidelity during the various design phases.

Components with simple geometries are described using a small number of dimensional parameters. Dimensional parameters may include lengths, radii and wall thicknesses. The geometric reference point for each component is predefined using conventions. This reference origin is located at the intersection of planes of symmetry for components that possess symmetry. The small number of parameters needed for each component leads to ease of modeling and computational storage efficiency. An example of a structural component (the Phoenix-1A's oxidizer tank cylindrical shell) element is given in Table 3-3.
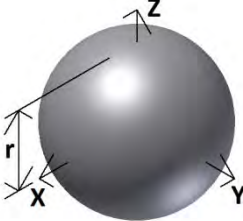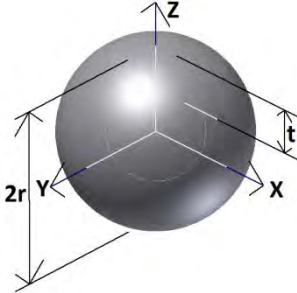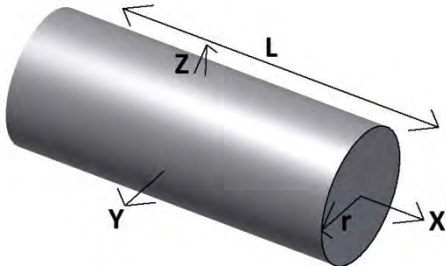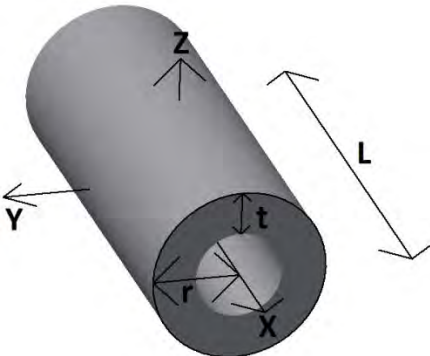
Table 3-3: Structural component parameters and example inputs and outputs

Parameter	Example Input Value	Data Type
Name	*"TankShell"*	Alphanumeric Character String
Geometry	*Annulus*	Integer Enumerator
Density	*2700 kg/m^3*	Real Number
Location	*(2 m, 0 m, 0 m)*	3-D Real Vector
Rotation	*(0°, 0°, 0°)*	3-D Real Vector
Dimensions: Length 　Outer Radius 　Wall Thickness	 *1.6 m* *0.2 m* *0.006 m*	Array of Real Numbers
Stage	*1*	Integer
Parameter	**Example Output Value**	**Data Type**
Mass	*15.797 kg*	Real Number
Local Centre of Mass	*(0 m, 0 m, 0 m)*	3-D Real Vector
Local Moment of Inertia	$\begin{bmatrix} 0.0091941 \\ 3.4445 \\ 3.4445 \end{bmatrix} kg \cdot m^2$	3-D Real Vector

Sounding rockets commonly consist of hollow, shelled components best described using wall thicknesses and outer dimensions. Examples include cylindrical airframe shell sections, fuel tank shells and motor combustion chamber walls as well as nose cones and fuel grains. Such components are modeled by the superposition of components with negative mass upon components with positive mass. This creates sum components equivalent to a solid hollow component. A summary of the simple geometries used in this work and their relevant geometric properties is presented in Table 3-4 below. Table 3-5 contains the analytical formulae used to

calculate the mass, local x position of the center-of-mass and local moment of inertia of each of the simple geometries available to the structural model.

Table 3-4: Structural model geometries

Solid Geometry	Dimensional Parameters	Symbols	Diagram
Sphere	Radius	r	
Spherical Shell	Radius Wall Thickness	r t	
Cylinder	Length Radius	L r	
Annular Prism	Length Outer Radius Wall Thickness	L r t	
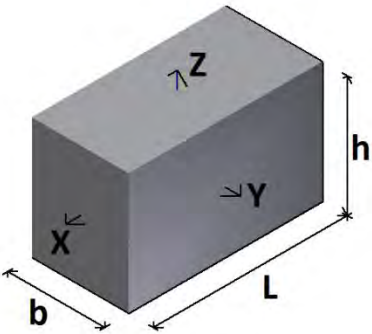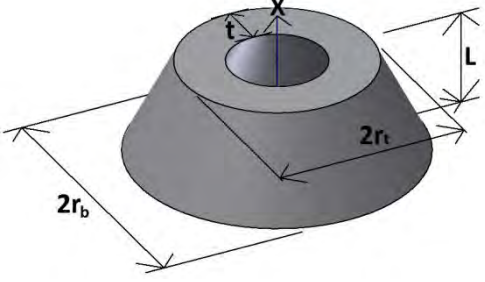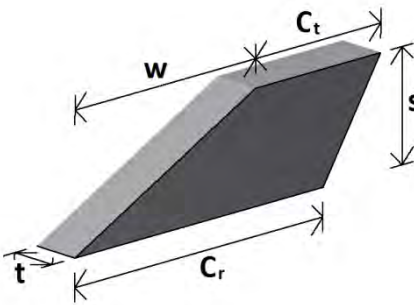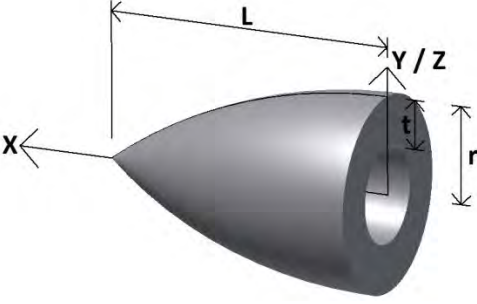
Solid Geometry	Dimensional Parameters	Symbols	Diagram
Rectangular Prism (Box)	Length Breadth Height	L b h	
Truncated Cone Shell	Height Base Radius Top Radius Wall Thickness	h r_b r_t t	
Flat Fin	Root Chord Tip Chord Wing Span Sweep Thickness Root Span	c_r c_t s w t r_t	
Ogive Shell	Length Base Radius Wall Thickness	L r t	
Point Mass	N/A	N/A	N/A

Table 3-5: Analytical geometric and inertial properties of structural model geometries

Solid Geometry	Mass (m)	Centre of Mass	Moments of Inertia
Sphere	$\frac{4}{3}\rho\pi r^3$	0	$I_{XX} = I_{YY} = I_{ZZ} = \frac{2}{5}mr^2$
Spherical Shell	$\frac{4}{3}\rho\pi(r^3 - (r-t)^3)$	0	$I_{XX} = I_{YY} = I_{ZZ} = \frac{2}{5}m(r^2 - (r-t)^2)$
Cylinder	$\rho\pi r^2 L$	0	$I_{XX} = \frac{m(r_1{}^2 + r_2{}^2)}{2}$ $I_{YY} = I_{ZZ} = \frac{m[3(r_1{}^2 + r_2{}^2) + L^2]}{12}$
Rectangular Prism(Box)	ρLbh	0	$I_{XX} = \frac{m(b^2 + h^2)}{12}$ $I_{YY} = \frac{m(L^2 + h^2)}{12}$ $I_{ZZ} = \frac{m(L^2 + b^2)}{12}$
Annular Prism	$\rho\pi(r^2 - (r-t)^2)L$	0	Eq. A-1
Truncated Cone	Eq. A-2	Eq. A-3	Eq. A-4
Flat Fin	$4\rho\frac{(c_r + c_t)}{2}st$	Eq. A-5	Eq. A-6
Ogive	Eq. A-7	Eq. A-8	Eq. A-9
Point Mass	m	0	$I_{XX} = I_{YY} = I_{ZZ} = 0$

The calculation of a vehicle's overall physical properties requires the arrangement of its constituent parts to be known. In general, a component may also possess orientation and hence a location vector and a rotation vector are provided for each component. A reference point and reference orientation vector is used for referencing the relative location and orientation of each component. In this work, the point on the body frame x axis coincident with the aft end of the vehicle is chosen as the reference origin for all structural calculations. The body frame x axis is chosen as the orientation vector's reference direction. Although initially it may seem more advantageous from a mathematical standpoint to use the body center of mass as the reference

origin of the body, it is not so. This is due to movement of the center of mass itself, with respect to the vehicle structure, as fuel consumption changes the mass distribution within a vehicle.

The total mass of the vehicle is the sum of the component masses. Due to the constant density assumption, each component mass is simply the product of its density and volume. Similarly, the total moment of inertia and product of inertia are the sum of the component moments of inertia and products of inertia respectively. However, the principal body frame axes do not generally coincide with the axes about which inertias are calculated on individual components. This is due to the unconstrained location of each component and the resulting variation in the location of the vehicle center of mass. By definition, the body frame origin is located at the overall center of mass. Prior to summation, the rotational inertias of each component about the vehicle center of mass are calculated using the parallel axis theorems for moments of inertia and products of inertia. Note that a component may possess a negative mass, with corresponding negative moments of inertia and products of inertia. Koenig's theorem (Eq. 3-47) is a generalization of the well-known parallel-axis theorem for the entire inertia matrix in three dimensions. It allows the complete inertia matrix I_G of a constituent component located at P to be calculated with reference to the overall vehicle center of mass G. Table 3.5 gives analytical formulae for the calculations of the mass, center if mass and moments of inertia for the various simple geometries used in the structural model. Note that the material density is denoted by ρ.

$$I_P = I_G + m \begin{bmatrix} b^2 + c^2 & -ab & -ac \\ -ab & a^2 + c^2 & -bc \\ -ac & -bc & a^2 + b^2 \end{bmatrix} \quad GP = \begin{pmatrix} a \\ b \\ c \end{pmatrix} \quad (3\text{-}47)$$

The product of inertia of a constant density component associated with any axis perpendicular to a plane of symmetry is zero. This property implies that any component with two perpendicular planes of symmetry possesses zero product of inertia about any of its principal axis pairs. All the simple geometries adopted in this work possess at least two orthogonal planes of symmetry except the flat plate. However, flat plates are used solely for the modeling entire tetragonal fin sets, which do feature two orthogonal symmetry planes. The general arrangement of components on a vehicle does not guarantee symmetry. A non-zero vehicle product of inertia is thus the result of component location in a non-symmetric fashion and is calculated using the parallel axis theorem for products of inertia.

The principle of substitution states that the overall vector center of mass R of an assembly of rigid components is the weighted vector average of the individual vector centers of mass R_i of each component (Eq. 3-48). The weighting factor for a component is its mass m_i. This principle

allows the calculation of the center of mass of the entire vehicle from the data defining each component and its location.

$$R = \frac{\sum_{i=1}^{n} m_i R_i}{\sum_{i=1}^{n} m_i} \qquad (3\text{-}48)$$

Temporal variations of a vehicle's physical properties are attributable to two effects: fuel consumption and internal mechanical dynamics. Such variations are simulated by varying the dimensional parameters, location parameters and density of the vehicle's constituent components in simulation time. Linear variation of dimensional parameters between extreme values allows simple modeling of fuel consumption during motor burns. Similarly, the movement of liquid fuels in fuel tanks is modeled by varying the component location vector linearly with time, between predefined start and end states. Internal mechanical dynamics are primarily caused by fluid sloshing and the movement of parachute deployment systems such as pistons. Capturing these changes requires higher fidelity subsystem models to be coupled to the overall vehicle structural model. Importantly, a more accurate model of the dynamic effects of the time evolution of fuels is achieved by coupling the dimensional parameters of fuel components to a high fidelity propulsion system model.

For programming purposes, linear temporal variations in structural parameters are defined using *Shape Variations* memory structures. A shape variation describes temporal variations in a single component on a vehicle and a vehicle may possess up to 20 shape variations. Each varying dimensional parameter of the component is provided with a design initial value, derivative and time limit. For components that move during flight, an initial location vector, a location derivative vector and a movement time limit is provided as well. The time limit in each case is referenced to the stage separation time and ignition delay for the component experiencing variations. An example of a shape variation is given in Table 3-6.

A shape variation may be used to model the regressive burn of a fuel grain in the combustion chamber of a hybrid rocket motor, as in Table 3-6. In such a case, the grain is described with an annulus and the shape variation describes the change in the annulus wall thickness. The *initial value* is the difference between the grain outer diameter and grain inner diameter. The *derivative* value is the grain regression rate and the *variation time limit* is the motor burn time.

Table 3-6: Shape variation property definitions and example

Property	Example Value	Data Type
Component	Fuel Grain	Integer (Identifier)
Changing Dimension	Wall Thickness	Integer (Identifier)
Initial Value	0.1 m	Real Number
Derivative	-0.005 m/s	Real Number
Variation Time Limit	20 s	Real number

3.17 Propulsion Model

3.17.1 Direct Thrust History Input

Rocket motors generate a net thrust force described by a three dimensional thrust vector. The thrust force magnitude is generally the product of the exhaust velocity v_e of the gases leaving the motor and the mass flow rate of these gases $\dot{m}_e$. The thrust vector is hence a temporal function of internal motor design parameters. The accurate calculation of the magnitude of the thrust force F and its direction is non-trivial as it may also be coupled to many other simulation state variables, depending on the fidelity of the propulsion modeling algorithm. In any case, the thrust vector must be a known input at any time during simulation. For simulations using an arbitrary rocket motor, a thrust curve and a nozzle exit pressure curve are required from ignition to burnout. These are supplied in table format against burn time and a suitable interpolation method is used to arrive at continuous curves for the thrust force magnitude, thrust force direction and nozzle exit pressure.

One source of coupling between the external flight dynamics and the thrust produced by a rocket motor originates from the pressure differential between the local atmospheric pressure p_a and the nozzle exit pressure p_e of motor exhaust gases. This contribution is proportional to the nozzle exit area A_e. Atmospheric pressure varies with altitude and nozzle exit pressure may also vary due to unsteady combustion dynamics. A second, potentially more significant source of coupling between the external flight dynamics and the motor's internal combustion dynamics is the changes in vehicle physical properties induced by the unsteady evolution of fuel grains and oxidizer fluid geometries. Sloshing of liquid fuels in tanks can cause the mass distribution and moments of inertia of the vehicle to oscillate rapidly, possibly destabilizing the vehicle. The simplest model of the rocket motor thrust force is given by Eq. 3-49.

$$F = v_e \dot{m}_e + (p_e - p_a)A_e \qquad\qquad (3\text{-}49)$$

3.17.2 Simple Ramped Thrust Function

The format of the thrust history provided may vary according to the purpose of the simulation. During the preliminary design phase, a simple ramp function (Eq. 3-50) may model the thrust magnitude sufficiently well. If motor parameters are better known, a piecewise cubic interpolation could be used to approximate thrust magnitudes with greater accuracy. In this work, options are provided for either approach. The ramp function is defined by the maximum thrust F_{max}, the time $t_{ramp-up}$ taken to reach the maximum thrust, the time t_{flat} to which the full thrust is sustained and the total burn time $t_{ramp-down}$.

The nature of the thrust magnitude curve varies with the type of motor used. The three primary types of chemical rocket motors are the solid, liquid and hybrid motors. Each of these motors display unique thrust characteristics and affect vehicle physical properties differently. Hybrid motors usually display a definite thrust characteristic. The thrust curve begins with a short, almost linear transient caused by the ignition charge. The stable combustion of the fuel grain is characterized by a sustained period of gradually decreasing thrust which lasts until the solid fuel is consumed. The thrust magnitude then drops sharply. Thereafter, any unspent oxidizer gas burns in the absence of solid fuels, resulting in a long, steadily diminishing 'tail' of low thrust until all the oxidizer is also consumed. Therefore, ramp functions are adequately suited to describing the thrust characteristics of hybrid motors.

$$F = \begin{cases} \dfrac{t}{t_{ramp-up}} F_{max} & 0 < t < t_{ramp-up} \\ F_{max} & t_{ramp-up} < t < t_{flat} \\ \left(1 - \dfrac{t-t_{flat}}{t_{ramp-down}-t_{flat}}\right) F_{max} & t_{flat} < t < t_{ramp-down} \end{cases} \qquad (3\text{-}50)$$

3.17.3 Thrust Misalignment

An ideal motor generates a thrust vector oriented parallel to its motor nozzle longitudinal axis. However, real motors may experience significant amount of thrust misalignment due to various non-ideal motor phenomena. These effects are modeled by rotating the ideal thrust vector about the nozzle longitudinal axis by the misalignment angle θ_m. The extent of this anomaly may be modeled analytically or measured experimentally. Often the extent of misalignment is unknown

and probabilistic calculations are necessary to account for this effect. In this work, the misalignment is assumed to be present towards a randomly selected but constant specific radial angular orientation ϕ_m. The misalignment angle is also kept constant throughout a flight. The misaligned thrust vector in body coordinates $\overrightarrow{F_m^b}$ is then given by Eq. 3-51.

$$\overrightarrow{F_m^b} = T_x(\phi_m)T_y(\theta_m)\begin{pmatrix} F \\ 0 \\ 0 \end{pmatrix} \tag{3-51}$$

3.17.4 Integrated Hybrid Rocket Performance Modeling

The UKZN hybrid rocket motor performance code by Genevieve [4] has been integrated into the flight dynamics simulation software developed in this work, forming the HYROPS framework. This integration provides full coupling between motor internal dynamics and external flight dynamics. As mentioned earlier, coupling occurs through the thrust magnitude, nozzle exit pressure and the fuel and oxidizer dimensional characteristics. The coupling thus affects the structural and propulsion subsystem models. The implementation of the HYROPS feature involves in-the-loop solution of both the flight dynamics and motor performance governing equations. Simulation inputs to the hybrid motor performance code include the simulation time, external atmospheric pressure, ambient atmospheric temperature, aerodynamic speed, Mach number and all other inputs needed for the model as defined in [4]. These may include structural properties of the vehicle such as the initial fuel grain and oxidizer tank dimensions. All these input are available through the HYROPS interface and may also be used to execute the motor performance code independently for a given motor configuration. When used as a propulsion model with a given vehicle design, the motor performance code is used to calculate instantaneous values of the following in simulation time

a) Thrust magnitude
b) Nozzle exit pressure
c) Oxidizer mass and dimensions of oxidizer column in oxidizer tank
d) Fuel grain mass and dimensions of fuel grain in combustion chamber

These outputs are used in the HYROPS structural and propulsion models to couple the two simulations and generate a combined hybrid sounding rocket simulation. For solid fuel grains whose inner surfaces regress outwards, the wall thickness parameter is forced to the output of the coupled hybrid propulsion model, overriding any shape variation outputs from the conventional structural model. Similarly, the oxidizer combustion dynamics is used to calculate

the remaining oxidizer volume and hence length of the column of oxidizer left in the oxidizer tank. This length is assigned to the respective component in the structural model representing the oxidizer fluid. The location of this component is also varied in real time to model the consumption of oxidizer such that the center of gravity and vehicle mass distribution outputs from the model reflect the effects of a real hybrid rocket motor. This coupling between the structural and propulsion models, combined with the high fidelity thrust and nozzle exit pressure histories add an additional level of realism unavailable in the other propulsion model options.

3.18 Newtonian Six Degree-of-Freedom Rocket Equations

The basic models required for describing the dynamics and kinematics of a sounding rocket have thus far been described. With these mathematical tools, it is now possible to formulate the complete 6-DOF equations of motion. The Newtonian rocket equations of motion may be formulated in any non-degenerate three-dimensional coordinate frame. Aerodynamic and propulsion efforts are easily expressed in the body frame. In contrast, the gravitational force and the apparent acceleration terms related to the Earth's curvature and rotation are best described in the Earth-fixed frame. The choice of coordinate frame is ultimately based on the number of calculations required for an evaluation of the right hand side of the equation. It is beneficial to choose the formulation that minimizes software round-off errors by limiting the number of complicated terms. However, all the various formulations are mathematically equivalent. A further consideration is that geographic locations and inertial locations must be updated in their respective coordinate frames, so a formulation in the body frame requires two transformations before the final solution is gained, leading to greater computational costs. These factors imply that the Earth-fixed frame presents the most suitable option for formulation of the linear rocket equation of motion for rotating planetary bodies. However, the body frame is a better choice for the attitude dynamics equations as well as formulations wherein the Earth is assumed fixed and flat.

Based on the assumptions made in this work, a usable form of the linear rocket equation of motion is given by Boiffier [23] as Eq. 3-52. The application of this equation in the Earth-fixed frame is now described. The aerodynamic force and propulsion force are calculated in the body frame. The sum of these two forces is then transformed into the Earth-fixed frame using T_{OB}. The gravitational acceleration vector is then added to this transformed quantity, resulting in the sum of external forces, which forms the right-hand side of the equation. The product of the mass and acceleration forms the left hand side of formulation. There are three acceleration terms in the linear equation. The first is the target variable of the equations, the kinematic acceleration. The second term accounts for the apparent acceleration towards the Earth's center-of-mass due

to the spherical geometry of the Earth. The third term is known as the Coriolis term and accounts for the apparent acceleration due to the angular velocity do the Earth's daily rotation. These terms are a function of the inertial position and kinematic velocity of the vehicle and are transferred to the right hand side. The kinematic acceleration vector is calculated by dividing this right-hand-side sum by the vehicle mass. The kinematic acceleration is integrated once to obtain the kinematic velocity in the Earth-fixed frame. The inertial velocity is obtained by transforming the kinematic velocity into the inertial frame using T_{IO}. Finally, the inertial and kinematic positions are obtained by integrating the inertial kinematic velocities respectively.

$$m \left(\frac{d}{dt} \begin{bmatrix} V_N \\ V_E \\ V_Z \end{bmatrix} + \frac{1}{(R_t + h)} \begin{bmatrix} -V_N V_Z + V_E{}^2 \tan L_t \\ -V_E V_Z - V_E V_N \tan L_t \\ V_N{}^2 + V_E{}^2 \end{bmatrix} + \right.$$

$$\left. \Omega_t \begin{bmatrix} 2V_E \sin L_t + \Omega_t (R_t + h) \sin L_t \cos L_t \\ -2V_Z \cos L_t - 2V_N \sin L_t \\ 2V_E \cos L_t + \Omega_t (R_t + h) \cos {}^2 L_t \end{bmatrix} \right) = m \begin{bmatrix} 0 \\ 0 \\ Gm_t / (R_t + h)^2 \end{bmatrix} +$$

$$\frac{\rho S V_a{}^2}{2} T_{OB} \begin{bmatrix} C_A \\ C_Y \\ C_Z \end{bmatrix} + T_{OB} \begin{bmatrix} F_z^m \\ F_y^m \\ F_x^m \end{bmatrix} \tag{3-52}$$

It is more useful to formulate the attitude dynamics equations, as done by Boiffier [23] in Eq. 3-53, in the body frame. Moments due to thrust force and aerodynamic loads are calculated about the origin of the body frame (i.e. vehicle center of mass).

$$\begin{bmatrix} A\dot{p} - E\dot{r} - F\dot{q} + rq(C - B) - Epq + Frp + D(r^2 - q^2) \\ B\dot{q} - F\dot{p} - D\dot{r} + rp(A - C) - Frq + Dpq + E(p^2 - r^2) \\ C\dot{r} - D\dot{q} - E\dot{p} + pq(B - A) - Dpr + Erq + F(q^2 - p^2) \end{bmatrix}$$

$$+ \begin{bmatrix} A(rq_t - qr_t) + (C - B)(qr_t + rq_t) + 2p_t(Fr - Eq) + 2D(rr_t - qq_t) \\ B(pr_t - rp_t) + (A - C)(pr_t + rp_t) + 2q_t(Dp - Fr) + 2E(pp_t - rr_t) \\ C(qp_t - pq_t) + (B - A)(qp_t + pq_t) + 2r_t(Eq - Dp) + 2F(qq_t - pp_t) \end{bmatrix}$$

$$+ \begin{bmatrix} r_t q_t(C - B) + D(r_t{}^2 - q_t{}^2) + Fr_t p_t - Ep_t q_t \\ r_t p_t(A - C) + E(p_t{}^2 - r_t{}^2) + Dp_t q_t - Fr_t q_t \\ p_t q_t(B - A) + F(q_t{}^2 - p_t{}^2) + Er_t q_t - Dp_t r_t \end{bmatrix} = \frac{\rho S l V_a{}^2}{2} \begin{bmatrix} C_l \\ C_m \\ C_n \end{bmatrix} + \begin{bmatrix} M_{F_x}^b \\ M_{F_y}^b \\ M_{F_z}^b \end{bmatrix}$$

$$\tag{3-53}$$

A fundamental reason for the use of the body frame for angular dynamics is that the inertia matrix remains a constant in the body frame despite the changing orientation of the vehicle. The gravitational force does not cause a moment as it always acts at the center of mass of the vehicle

and hence there is no need to transform the gravitational force from the Earth-fixed frame to the body frame. The attitude effects of the Earth's spherical geometry and daily rotation are formulated and most efficiently evaluated in the Earth-fixed frame, before transformation into the body frame using T_{BO}. These terms are subtracted from the moment sum. This leaves a system of three linear equations due to the coupling between the inertia matrix and the derivative of the kinematic angular velocity. The components of this derivative are obtained by inverting the system of equations using Cramer's rule. The kinematic angular velocity is then obtained by integration. The derivative of the orientation quaternion in the body frame is then calculated from the kinematic angular velocity using Eq. 3-22. The orientation quaternion is finally obtained by integration and converted back to an Euler angle triplet using Eq. 3-23, Eq. 3-24 and Eq. 3-25 thereafter.

The latitude and longitude of the vehicle are needed for the geodetic representation of the trajectory as well as the evaluation of the Coriolis and geodetic spherical geometry terms in the equations. The navigation equations are used to evaluate the derivative of the latitude and longitude in the Earth-fixed frame as a function of the kinematic velocity and the latitude itself. The integration required to obtain the latitude and longitude are also carried out in the Earth-fixed frame. The effect of the Coriolis term is transferred through the functional dependence of the navigation equations on the kinematic velocity.

3.19 Launch Rail Modeling

Sounding rockets are commonly stabilized early in their flight by launching them from linear launch rails or launch tubes. The launch rail is oriented to the required launch altitude and azimuth angles. While the rocket is on a rail, it is constrained to slide along the vector parallel to the rail. Useful parameters from launch rail simulation include the rail exit velocity and rail exit aerodynamic angles. These parameters provide information about the aerodynamically stability of the vehicle at the moment it leaves the rail and commences free flight. Most sounding rockets require a minimum aerodynamic velocity before fins are capable of reliably stabilizing the vehicle against low altitude wind gusts.

The launch rail is simulated by projecting the instantaneous kinematic acceleration vector $\overrightarrow{\dot{V}_k}$ onto the rail's normalized direction vector in Earth-fixed coordinates until the vehicle moves far enough to clear the rail and hence regain all six degrees of freedom. The rail is considered cleared when the center-of-mass of the vehicle leaves the top end of the rail. The length of the rail is assumed to be known. Friction forces are neglected based on the assumption that the rail

is well lubricated. It is also assumed that the rail is perfectly rigid and completely damps any lateral forces exerted on it by the rocket without any significant mechanical response.

The rail direction vector $\overrightarrow{d_R}$ is defined using the launch azimuth angle ψ_0 and launch elevation angle θ_0 as in Eq. 3-55. The launch rail acceleration vector $\overrightarrow{\dot{V}_{k_R}}$ is then calculated from the kinematic velocity time derivative (Eq. 3-54) by performing a vector projection onto the rail direction vector as in Eq. 3-56.

$$\overrightarrow{\dot{V}_k} = \frac{d}{dt}\begin{pmatrix} V_N \\ V_E \\ V_Z \end{pmatrix} \tag{3-54}$$

$$\overrightarrow{d_R} = T_z(\psi_0)T_y(\theta_0)\vec{i} \tag{3-55}$$

$$\overrightarrow{\dot{V}_{k_R}} = \left(\overrightarrow{\dot{V}_k} \cdot \overrightarrow{d_R}\right)\overrightarrow{d_R} \tag{3-56}$$

3.20 Parachute Recovery System Model

The Newtonian six-degree-of-freedom equation of motion is directly applicable to the parachute assisted descent and recovery phase of sounding rocket missions. However, it is assumed that perfectly rotationally symmetric parachute canopies do not experience significant rotational aerodynamic moments, leaving five degrees of freedom. The landing impact point and terminal descent velocity are the primary parameters desired from a parachute recovery simulation. Parachutes experience wind induced angles of attack and sideslip angles, resulting in drift. The total drift distance is an important parameter in the flight planning process. The approach taken in this work for modeling the parachute flight dynamics aims to estimate the wind drift distance with accuracy whilst keeping the model complexity low.

The kinematic frameworks remain the same as for general flight dynamics simulations, with the parachute canopy polar axis being aligned with the body frame z axis. It is assumed that the rocket payload also aligns itself along the body frame z axis.

Although the actual mass of the parachute canopy is small in relation to the payload, the effective mass of the canopy-payload combination is greater due to the added mass effect. The added mass effect accounts for the mass of fluid trapped within the canopy due to its open geometry. This added mass increases the effective linear and translational inertia of the canopy-

payload combination, significantly altering it flight dynamics. The added mass is defined as the product of the fluid density, a representative canopy volume and a dimensionless coefficient known as the added mass coefficient. The added mass is thus a time varying quantity, depending on local atmospheric conditions.

The preferred method of modeling the structural geometry during the recovery phase is to treat the parachute-payload combination as a single rigid body. This approach ignores any aero-elastic effects and treats the shroud lines as taut infinitely rigid members. The canopy is assumed to be fully open during the descent. The resulting system possesses radial symmetry about the body frame x axis.

The initial conditions set for the recovery phase simulations are the final conditions assumed for the parachute deployment phase. The deployment is a complex transient process affected by the deployment altitude and velocity, amongst many other factors. It may be assumed that a successful deployment leaves the system in a vertical position with the body frame x axis oriented downwards a short duration after the deployment. Alternative sets of post-deployment conditions may specify zero aerodynamic angles and zero angular rates, ensuring that any dynamic effects from the earlier flight phases are not carried over to the recovery phase simulation. In this work, the former alternative is taken. The deployment duration is specified from empirical parachute testing in the absence of a more detailed model.

Actual parachute aerodynamic behavior is complicated by various aero-elastic effects which are beyond the scope of this work. The aerodynamic modeling of a parachute is limited to the canopy and assumes the canopy maintains its fully deployed shape during descent. It is also assumed that the canopy is a body of revolution about the body frame x axis and hence its aerodynamic characteristics are independent of its roll angle. These simplifications reduce the canopy aerodynamic model to two dimensions and hence the lift, drag and pitching moment coefficients completely describe the aerodynamic characteristics. Dynamic derivatives are neglected due to the complexity involved in their calculation and the relative insignificance of dynamic effects in determining the descent trajectory. Typical sounding rocket parachute recoveries are characterized by low subsonic speeds and hence any compressibility effects are also ignored. The aerodynamic characteristics are then functions of the altitude and the total incidence angle. In this work, the drag coefficient is thus assumed constant as is the derivative of the normal force with total angle of attack. Refer to Chapter 5 for more detail on the implications of these assumptions.

3.21 Multi-Staging and Darting

Darting and staging are common techniques used to maximize rocket altitude performance. From the modeling and simulation perspective, multi-stage vehicles portray two key differences from single-stage vehicles. Firstly, the separations of spent stages cause abrupt changes in vehicle geometries, with corresponding changes in structural and aerodynamic properties. Secondly, multi-stage vehicles do not follow the traditional flight phases of single stage sounding rocket. Each stage experiences a launch or separation phase, powered boost phase followed by an unpowered coast phase before the following separation event occurs and the spent motor falls back to earth in a descent phase. These differences require a generalization of the single-stage sounding rocket flight pattern. Apart from the overall performance, the dynamic response of a multi-stage vehicle to the swift changes in inertial and aerodynamic properties during stage separation is also of interest to the vehicle designer.

A structural model of a multistage vehicle may be formalized by assigning each component of a complete multistage vehicle an integer stage number (Figure 3-6). A separation event for the vehicle stage n creates two vehicles, one powered and one unpowered. The powered vehicle is termed the stage $n + 1$ and consists of the logical continuation of the vehicle stage n whilst the unpowered vehicle is termed step n and typically consists of dead mass from stage n such as spent motor boosters and fuel tanks. The final stage N of a N stage vehicle does not experience separation. The separation time for each stage $t_s(n)$ is predefined as part of the vehicle design, except for the final stage. A component is included in structural computations only if the simulation time corresponds to a stage where that component is present. Thus a component with stage number n is considered as part of all the stages $m \leq n$ of the powered vehicle for simulation times $t < t_s(n)$ and is uniquely considered part of the unpowered vehicle step n for $t \geq t_s(n)$.
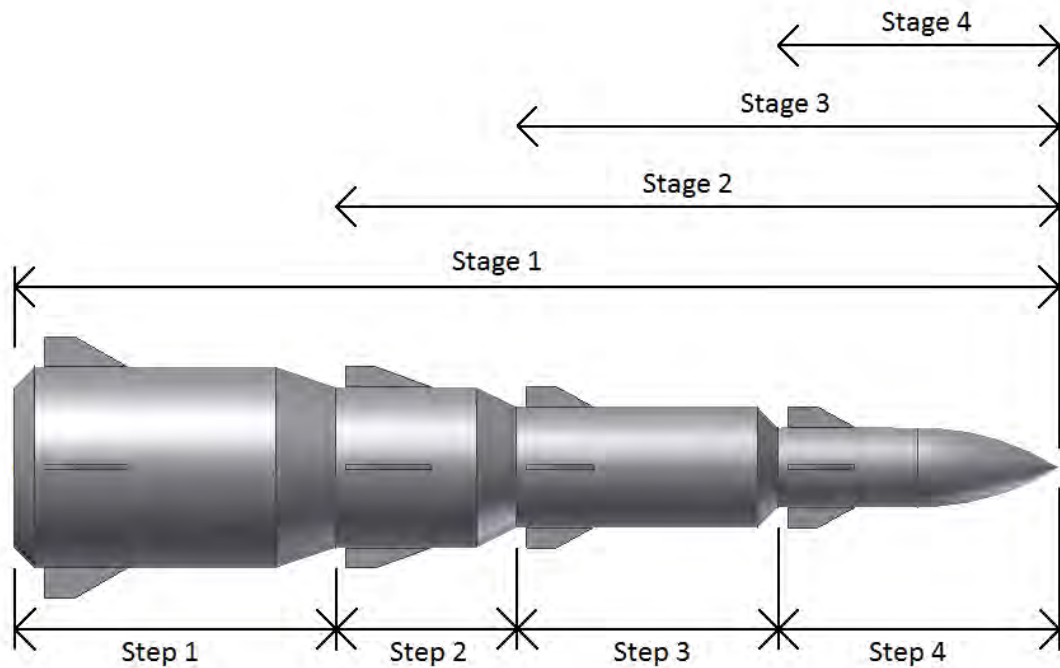
Figure 3-6: Definitions of stages and steps on a four stage rocket. In this work, a maximum of four stages are simulated but the methods are applicable to any number of stages.

In general, each powered stage of a multi-stage vehicle possesses a unique propulsion system. The time input to the propulsion system model during a given stage is adjusted relative to the previous stage's separation time and the delay from that separation event and the ignition of the motor on the current stage. This allows the definition of the propulsion system design irrespective of the stage on which it is used. During simulation, only the corresponding stage's propulsion model is employed to determine the thrust vector and fuel geometries.

Upon a stage separation event the new stage and step vehicles inherit the state vector of the pre-separation stage. The forward stepping nature of the numerical solver allows subsequent trajectories of the separated vehicles to be computed afterwards, as the initial state vector contains the requisite data for all subsequent vehicle dynamics. During the overall simulation process, a main powered vehicle of N stages is simulated until termination. The state vector at each of the $N - 1$ stage separation events is subsequently loaded from the main vehicle simulation output data to facilitate the simulation of the $N - 1$ step vehicles. In addition to the final stage of the main vehicle, any of the step vehicles may feature recovery systems which are modeled in the usual manner for the respective trajectory.

Both tandem-staged (clustered) and series-staged vehicles are within the scope of the above method. However, it is always assumed that a stage separation event causes a single rigid body

to detach off the main vehicle. This is a reasonable assumption as the aerodynamic and inertial characteristics of several identical boosters discarded under identical flight conditions are similar and hence their subsequent trajectories may be regarded as identical. Any dispersion in the individual trajectories is readily treated statistically.

Stage separation events also lead to changes in basic airframe dimensions, leading to significantly different aerodynamic characteristics from stage to stage and step. Corresponding tables of aerodynamic coefficients must be provided for multi-stage simulation. For a N stage vehicle, $2N - 1$ distinct vehicle airframe configurations are encountered, N configurations for the N stages of the main powered vehicle and $N - 1$ configurations for $N - 1$ steps produced.

3.22 Numerical Solution of the Newtonian 6-DOF Rocket Equations

The Newtonian and Eulerian rocket flight dynamics equations are second order nonlinear ordinary vector differential equations. The nature of the solution process is dependent on the number of degrees of freedom desired and the mathematical complexity of the input models that determine the external forces and moments and hence the linear and angular acceleration vectors respectively. The level of generality and fidelity required in simulation geared towards the design of high altitude sounding rockets leads to compound non-trivial expressions for the acceleration vectors. The integration of these complex expressions using analytical techniques is mathematically unfeasible.

In practice, the solution of this equation requires numerical time-integration methods. Numerical techniques approximate solutions to mathematical problems using numerical computation rather than symbolic algebra. Numerical integration methods divide the domain of integration into a large number of short but finite intervals of size Δt defined in Eq. 3-57 as the difference between an initial time t_i and final time t_{i+1}. Derivatives are assumed to remain approximately constant during each interval. The integration of the differential quantities then takes on an algebraic nature as the problem is reduced to approximating the area under the curve in a short section of the derivative function. Two integrations are needed at each time step, the first integrating accelerations to obtain velocities and the second integrating these velocities to obtain positions and orientations.

$$\Delta t = t_{i+1} - t_i \qquad (3\text{-}57)$$

The approximate solutions generated using numerical methods contain finite errors. For a given problem, the selection of an appropriate numerical method should take into account the

computational cost as well as the magnitude of errors incurred in the solution. The bounds on numerically induced errors must be known for a solution to be meaningful. The selection of the time-step size is essential in bounding discretization errors. There are several approaches to the selection of an optimal time-step size. The use of a fixed time-step size leads to a more predictable computational cost per simulation, but this approach is generally inefficient as it does not exploit temporal variations in the magnitude of the derivatives being estimated. Numerical integration errors are proportional to the absolute values of derivatives at a given time-step. The implication is that if time derivatives are small and the solution changes slowly, using a larger time-step size will still produce an acceptably accurate solution and vice versa. This observation motivates the use of adaptive time-stepping techniques. In this work fixed time stepping was used despite its inefficiency and future research will aim to improve on time step selection.

The computational cost of a simulation is proportional to the total number of calculations performed and the total number of memory reads/writes made during the solution process. In general, the total computational cost is directly proportional to the number of time-steps during the simulation period. The time required to complete a simulation on a given machine is further complicated due to memory caching and latency effects. A general rule is that the computational cost of memory access operations is inversely proportional to the random access memory size and cache size of the machine in question.

A great variety of numerical time integration methods have been developed. A broad categorization may be achieved by considering implicit and explicit methods. The two classes differ in that implicit methods estimate time derivatives using unknown quantities (from the future) whilst explicit methods estimate derivatives using quantities already known. Implicit methods have the advantage that they may provide unconditionally stable solutions, but this generally comes at a greater computational cost as implicit methods require the solution of a system of equations at each time-step. Explicit methods generate unstable solutions if the time-step size is not chosen correctly, but their computational cost is relatively lower.

Numerical integration techniques may be thought of as piecewise integrations of the derivative function over large numbers of small subintervals of the solution domain. In the case of the equation of motion, these are time step intervals of duration Δt. The solution function is approximated over each time-step using a finite order Taylor series expansion. The order of a numerical integration method refers to the order of the first term ignored during the truncation of this Taylor series approximation of the solution. Higher order methods therefore require larger numbers of Taylor series terms to be evaluated. The order defines the relationship

between solution errors and time-step size. Methods of higher order offer greater reductions in error for a given reduction in time-step size but incur larger computational costs. Given the derivative of the state vector $\dot{X}_\iota$ as a function f of time t_i and the state vector itself X_i at beginning of time step interval i, integration methods may be formulated (Eq. 3-58). An integration method is thus an algebraic relation using the derivative function and time step duration to generate the state vector X_{i+1} at the beginning of the next time step interval $i + 1$.

$$\dot{X}_\iota = f(X_i, t_i) \qquad (3\text{-}58)$$

Two common numerical integration methods were employed in this work. The first is the Explicit Euler (EE) method (Eq. 3-59) which is a first order explicit scheme.

$$X_{i+1(EE)} = X_i + (\Delta t)\dot{X}_i \qquad (3\text{-}59)$$

The highly popular Runge-Kutta 4 (RK4) method (Eq. 3-60), presented by Karbon [32], employs a 4th order explicit scheme. Both methods are single-step and applicable to vector differential equations. The choice of time-step size is based on the concept of time-step independence. This involves reducing time-step size until the solution remains effectively unchanged with further reduction, indicating that discretization is not the dominant source of error. The EE and the RK4 methods differ in the manner in which derivatives are approximated, with the RK4 needing four derivative evaluations per step, in contrast to the EE which requires only one. Consequently, the use of the RK4 scheme incurs a linear fourfold increase in computational cost.

$$X_{i+1(RK4)} = X_i + \frac{\Delta t}{6}(K_1 + 2K_2 + 2K_3 + K_4) \qquad (3\text{-}60)$$

$$K_1 = f(t_i, X_i) \qquad (3\text{-}61a)$$

$$K_2 = f\left(t_i + \frac{\Delta t}{2} +, X_i + \frac{\Delta t}{2}K_1\right) \qquad (3\text{-}61b)$$

$$K_3 = f\left(t_i + \frac{\Delta t}{2} +, X_i + \frac{\Delta t}{2}K_2\right) \qquad (3\text{-}61c)$$

$$K_4 = f(t_i + \Delta t, X_i + \Delta t K_3) \qquad (3\text{-}61d)$$

When a high order method such as RK4 is applied to a 2nd order differential equation such as the Newtonian rocket equations, the method must be applied in succession to obtain the first

derivative and the solution. It is important to note that only state vector components from the current time step may be used to calculate the new state vector at the next time step and that values of updated states cannot be used (as intermediate inputs) until the entire integration process for the current step is completed.

3.23 Uncertainty Modeling

The scope of a flight performance simulation is limited by the uncertainty of its input variables. Poorly known input parameters affect the applicability of the solution in the vehicle design process. There are several uncertainties in input parameters in the flight performance simulation processes described in this work. From a simulation perspective, any input that is not accurately known in reality must be regarded with uncertainty. Examples of such inputs include wind, thrust misalignment and manufacturing tolerances in the mechanical structure of the vehicle. Another class of uncertainties arises from the idealized modeling of several inherently non-ideal systems. Examples of such systems include the launch rail, the atmosphere and the aerodynamic interactions. The net effect of these uncertainties is an expected distribution in flight performance parameters about their nominal values. It is desirable to predict the extent to which flight performance parameters may deviate from their nominal values. This information may be used to calculate statistical confidence intervals for flight performance predictions, which are often required by launch service providers.

Two basic approaches are available to quantify the effects of simulation input uncertainties, both involving stochastic modeling. The first is to vary each input discretely within its range of uncertainty and conduct a number of simulations. The number of simulation instances needed using this approach climbs exponentially when the number of uncertain input variables is increased. In addition, there is a linear increase in computational cost with an increase in uncertainty magnitude for a given sampling interval. These factors make the direct simulation approach unattractive. A second, more practical technique is to introduce statistically defined random variations simultaneously in every uncertain input parameter. A fixed number of simulation instances are then conducted. This technique is known as the Monte Carlo method. The probability distribution function of these artificial input perturbations is determined by the nature of the uncertainties being modeled. When the statistical nature of an uncertainty is unknown, it is reasonable to use a Gaussian distribution of a certain amplitude and standard deviation as the uncertainty probability distribution function. If a known distribution is available for a particular input, it is applied for better effect.

In this work, the *brute force* Monte Carlo method was adopted as a simple but generic means of quantifying uncertainties. Uncertainties are present in the propulsion model, initial launch angles, wind model and aerodynamic coefficients. Potentially unreliable systems and/or process provide another source of uncertainties. In the case of sounding rockets, these systems include the recovery parachute deployment processes and the ignition and stage separation mechanisms on multi-stage vehicles. It is assumed that these mechanical systems have a binary state of functionality and a known probability of failure. Table 3-7 gives a list of inputs which may be perturbed in Monte Carlo simulations, along with the manner in which uncertainty magnitude is input.

Table 3-7: Monte Carlo uncertainty inputs

Input Variable	Nature of Uncertainty	Units
Thrust Direction	Angular Misalignment about Mean	rad
Thrust Magnitude	Proportional Uncertainty about Mean	N
Motor Burn Time	Proportional Uncertainty about Mean	s
Wind Direction	Angular Uncertainty about Mean	rad
Wind Magnitude	Proportional Uncertainty about Mean	m/s
Launch Altitude	Angular Misalignment about Mean	rad
Launch Azimuth	Angular Misalignment about Mean	rad
Force Coefficient	Proportional Uncertainty about Mean	Non-dimensional
Moment Coefficient	Proportional Uncertainty about Mean	Non-dimensional
Centre of Pressure	Proportional Uncertainty about Mean	Non-dimensional (Calibers)
Recovery System	Boolean Failure Probability in [0 1]	Non-dimensional
Stage Ignition	Boolean Failure Probability in [0 1]	Non-dimensional
Stage Separation	Boolean Failure Probability in [0 1]	Non-dimensional
Fin Cant Angle	Angular Misalignment about Mean	rad

The application of the input uncertainty standard deviation σ on an input P with mean μ is given by the perturbed input P_{MC} as described in terms of the normal distribution N in Eq. 3-62. This is applicable to inputs with zero mean such as thrust misalignment. Boolean probabilities are translated into binary inputs by calculating a random number in the interval [0 1] and using a

successful system only if the random number is greater than the probability of system failure specified in the Monte Carlo model.

$$P_{MC} = P\big(1 + N(\mu, \sigma)\big) \tag{3-62}$$

The output distributions obtained from a batch Monte Carlo simulation is contextualized by comparison against the nominal solution. The nominal solution is generated by running the solver with all uncertainties reset to zero. A comparison of the nominal flight parameters against the mean Monte Carlo flight parameters reveals the net bias and/or deviation due to the input uncertainties. The Monte Carlo parameter variances and standard deviations are then used to place confidence intervals on the nominal flight parameters based on the multivariate Normal distribution.

3.24 Flight Performance Analysis

The time history of the state vector generated by the numerical rocket equation solver constitutes a large volume of data which is neither necessarily intuitive nor even directly useful to the sounding rocket system designer. A basic analysis of the data must be performed with the aim of deriving a few salient flight performance parameters which may be used to improve the vehicle design in the next iteration of the design process. Table 3-8 lists these parameters and their significance to system design. These are primarily extreme values and boundary values of the state vector data and are calculated using relatively little computational resources. Several average aerodynamic coefficients are also included for a measure of the aerodynamic efficiency of the vehicle.

Monte Carlo runs are characterized by a large number of simulation runs, each of which must undergo the basic analysis described earlier. This also produces a potentially large dataset comprising flight performance parameter arrays. The sounding rocket engineer is interested in the statistical properties of this dataset. The automated calculation of basic statistics, such as the mean and standard deviation of each flight parameter, is essential for facilitating swift design. These calculations were automated as part of the post-processing analysis which was also applied to the automated vehicle optimization algorithm described in section 3.26.

Table 3-8: Basic flight performance analysis outputs

Parameter	Units	Applications
Apogee Altitude	m	Payload Delivery Recovery System Flight Safety
Maximum Range	m	Telemetry Limits
Maximum Velocity	m/s	Thermal Loads Structural Loads Aero-elasticity
Maximum Acceleration	m/s^2	Payload Safety Structural Loads
Apogee Time	s	Payload Timing
Flight Time	s	Recovery Flight Planning Flight Safety
Splashdown Velocity	m/s	
Impact Range	m	
Splashdown Coordinates	{Latitude °, Longitude °, Altitude m}	
Average Stability Margin	Calibers (Non-dimensional)	Vehicle Stability
Median Lift Coefficient	Non-dimensional	Aerodynamic Performance
Median Drag Coefficient	Non-dimensional	
Net Aerodynamic Impulse	Ns	Flight Performance Energy Efficiency
Net Propulsion Impulse		
Net Gravitational Impulse		

3.25 High-Level Simulation Process

The overall trajectory simulation process for a single multi-stage vehicle begins with a simulation of the powered main vehicle for all stages, with booster steps being discarded as the simulation progresses. This main trajectory is then used to subsequently extract initial conditions for each booster stage based on the time when booster was discarded. Figure 3-7 shows a flowchart of this process. Note that the booster trajectories may be simulated in any order. The simulation of each stage involves the solution of the differential equations of rocket motion using the numerical methods discussed earlier. Termination criteria are used to end a simulation. A primary termination criterion is the return of the vehicle to the ground and penetrating it, indicated by the vehicle altitude reaching above a positive threshold value (recall that the Earth-fixed frame *z* axis is positive downwards). A maximum number of time steps are

also used as a termination criterion to prevent software memory overflows. Indications of numerical instability may also be used as a termination criterion by imposing limits on the acceleration and velocity states of the vehicle. The selection of a suitable termination criterion is a key element in ensuring robustness when multiple runs are executed for the purposes of Monte Carlo simulation or vehicle optimization. In such cases, the algorithm should be able to terminate anomalous simulations and prevent them from wasting computational resources.
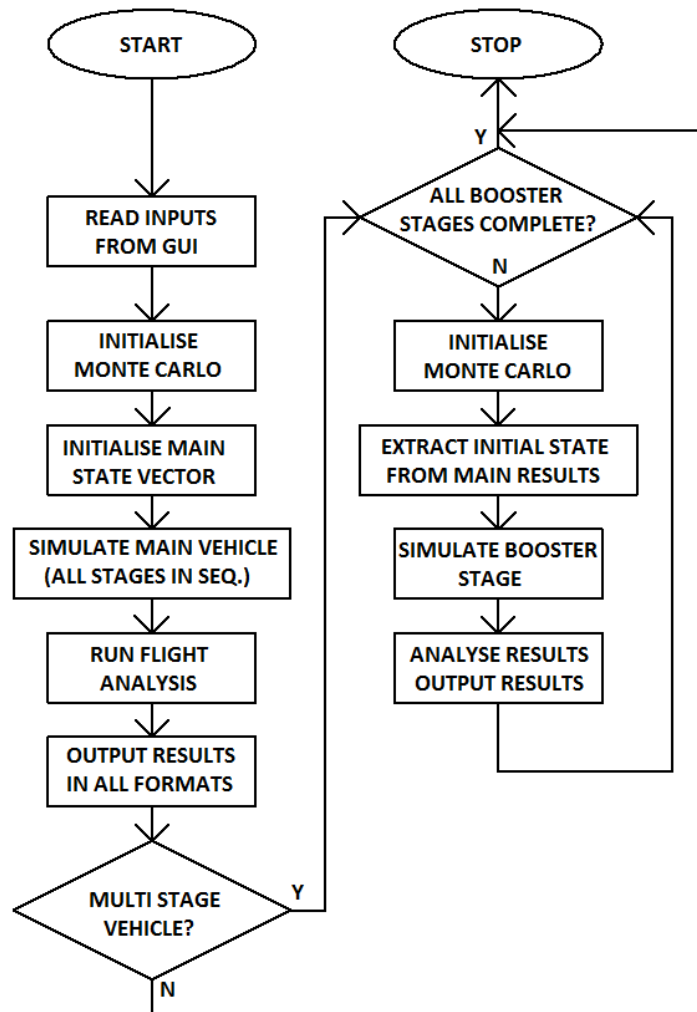
Figure 3-7: Flowchart of high-level simulation process for multi-stage simulations

3.26 Vehicle Automated Optimization

A vehicle configuration composed of structural and aerodynamic geometries, motor performance parameters and flight sequencing information represents a highly multidimensional parameter space. For a given configuration, the sounding rocket designer wishes to find the optimal set of design values that define a vehicle with the best possible performance. Relevant criteria for performance may include total cost, apogee altitude, energy efficiency, and many

others. A trajectory prediction tool is useful for predicting the flight performance of a vehicle, represented by a point in the design parameter space. The trajectory simulator thus acts as a 'fitness' evaluator for a particular design. Once the fitness is calculable, a variety of optimization techniques may be used to search for the optimal parameter set. However, there may be several measures of fitness that may be desired for a sounding rocket, such as the maximization of apogee altitude alongside the minimization of the average impact dispersion. This is a multi-objective optimization problem and is complicated by the tradeoff between objectives. This work is limited to single objective optimization and it is assumed that the objective with the greatest priority is known by the designer.

Before a strategy for vehicle optimization is adopted, a general reduction in the dimensionality of the parameter space is desirable. This is due to the fact that many minor details in a typical vehicle design do not directly affect the flight performance. However, such details are often themselves a result of major configuration parameters which are relevant in determining performance. Examples of such major parameters in a typical hybrid rocket include the oxidizer tank and motor chamber aspect ratios, nose fineness ratio, fuel grain aspect ratio and motor thrust distribution. A more practical approach is to adopt a relatively small set of real-valued *key design variables* P_i each of which represents an independent determinant of flight performance. It is then possible to find relations that define every other design variable in the entire vehicle as a function of these key design variables. If a particular vehicle design parameter is unaffected by the key design variables, it remains constant. In the optimization framework adopted in this work, relations that define details of vehicle design such as dimensions, motor performance information, flight sequencing data are termed *effects*. An effect is essentially an algebraic formula combined with parameters which define what aspect of the vehicle design it defines. The use of effects allows the algorithm to optimize any aspect of a vehicle design by driving parameters which feed into any of the underlying mathematical models that are used to predict the vehicle performance. As a result, it becomes possible to optimize all the aspects of a vehicle design in a single optimization run. Effects are implemented using an equation evaluator. Each key design variable is assigned a unique symbol and the effect formula is defined in terms of these symbols. The formula may also contain the common algebraic operators as well as trigonometric and transcendental functions. The value of the effect is then calculated using the key design variable inputs. Table 3-9 lists various effect types available for implementing key design variables. Refer to Chapter 5 for formal definitions of the aerodynamic parameters.

Table 3-9: Optimization effect types and associated parameters

Effect Type	Parameter 1	Parameter 2
Structural – Dimension	Part Name	Dimension
Structural – Location	Part Name	Axis (X/Y/Z)
Aerodynamics – Nose Length	Stage No.	N/A
Aerodynamics – Nose Base Radius	Stage No.	N/A
Aerodynamics – Fuselage Segment Length	Stage No.	Segment No.
Aerodynamics – Fuselage Segment Base Radius	Stage No.	Segment No.
Aerodynamics – Reference Area	Stage No.	N/A
Shape Variation – Initial Parameter Value	Part Name	Dimension
Shape Variation – Parameter Time Derivative	Part Name	Dimension
Shape Variation – Parameter Variation Time Limit	Part Name	Dimension
Shape Variation – Initial Location Coordinate	Part Name	Axis (X/Y/Z)
Shape Variation – Location Coordinate Time Derivative	Part Name	Axis (X/Y/Z)
Shape Variation – Location Coordinate Variation Time Limit	Part Name	N/A
Motor Thrust Function – Ramp-Up Time	Stage No.	N/A
Motor Thrust Function – Ramp Plateau End Time	Stage No.	N/A
Motor Thrust Function – Ramp-Down Zero Time	Stage No.	N/A
Motor Thrust Function – Maximum Thrust Magnitude	Stage No.	N/A
Staging – Stage Separation Time	Stage No.	N/A
Staging – Total Length	Stage No.	N/A

A stricter definition of the parameter space is necessary if a practical vehicle is to be optimized. Constraints are required on all the key design variables to define a finite search space. Every key design variable is limited to a finite interval so that an optimization study using n key design variables represents at worst a search within a box in $n$dimensional hyperspace. More complex limitations on the values that a set of key design variables may be needed to keep the results realistic. In this work, constraints are formally defined using an inequality operator and a pair of algebraic formulae for defining the left-hand-side and right-hand side of the inequality. Any solution that does not satisfy all constraints is rejected during the optimization process.

Genetic algorithms mimic evolutionary biological process to find an optimal solution within a given search space. It has been shown that organisms use evolution to adapt to changing environmental conditions [44]. Evolution leads to adaptation by giving individuals in a population with a greater fitness for survival a larger chance of propagating their genetic

information to future generations. Over numerous generations, the net effect is that individuals whose genes favor survival are preserved in a population's gene pool whilst those that do not are discarded.

A genetic algorithm applies an analogous process to an optimization problem. A potential solution is represented as a sequence of genes (i.e. a single individual) and a large number of such individuals are created to represent the population. Initially, genes in the entire population are randomly selected. The algorithm then iterates through a number of generations. The performance of each individual is calculated at every generation and only individuals with superior performance are selected to breed into the next generation. The selection process may be deterministic or stochastic. Deterministic selection may involve a selection criterion such as a minimum performance level whereas a stochastic selection technique gives a superior performer a proportionally greater chance of being a parent for the next generation. Once a suitably fit subset of the current generation is selected as parents for the next generation, a new generation is produced via breeding. The breeding process involves swapping or mixing the genes of two suitably fit parent individuals in a process known as crossover. It is also necessary to randomly perturb a fraction of the gene pool in the new generation in order to maintain genetic diversity and prevent the solution space from becoming unsuitably concentrated around a limited number of superior individuals. This process is termed mutation and is defined by a *mutation probability* which determines the chances of a particular gene being randomly perturbed during crossover. The mutation process prevents the algorithm from converging around local maxima or minima and increases the chances of finding global optima. A genetic algorithm is entirely empirical and no knowledge of the mechanism by which a gene favors better performance is necessary. Figure 3-8 presents a high-level flowchart of the genetic algorithm used for sounding rocket optimization. Note that two populations (a parent generation and a child generation) need to be stored in memory and that the number of individuals in each generation is not constrained.
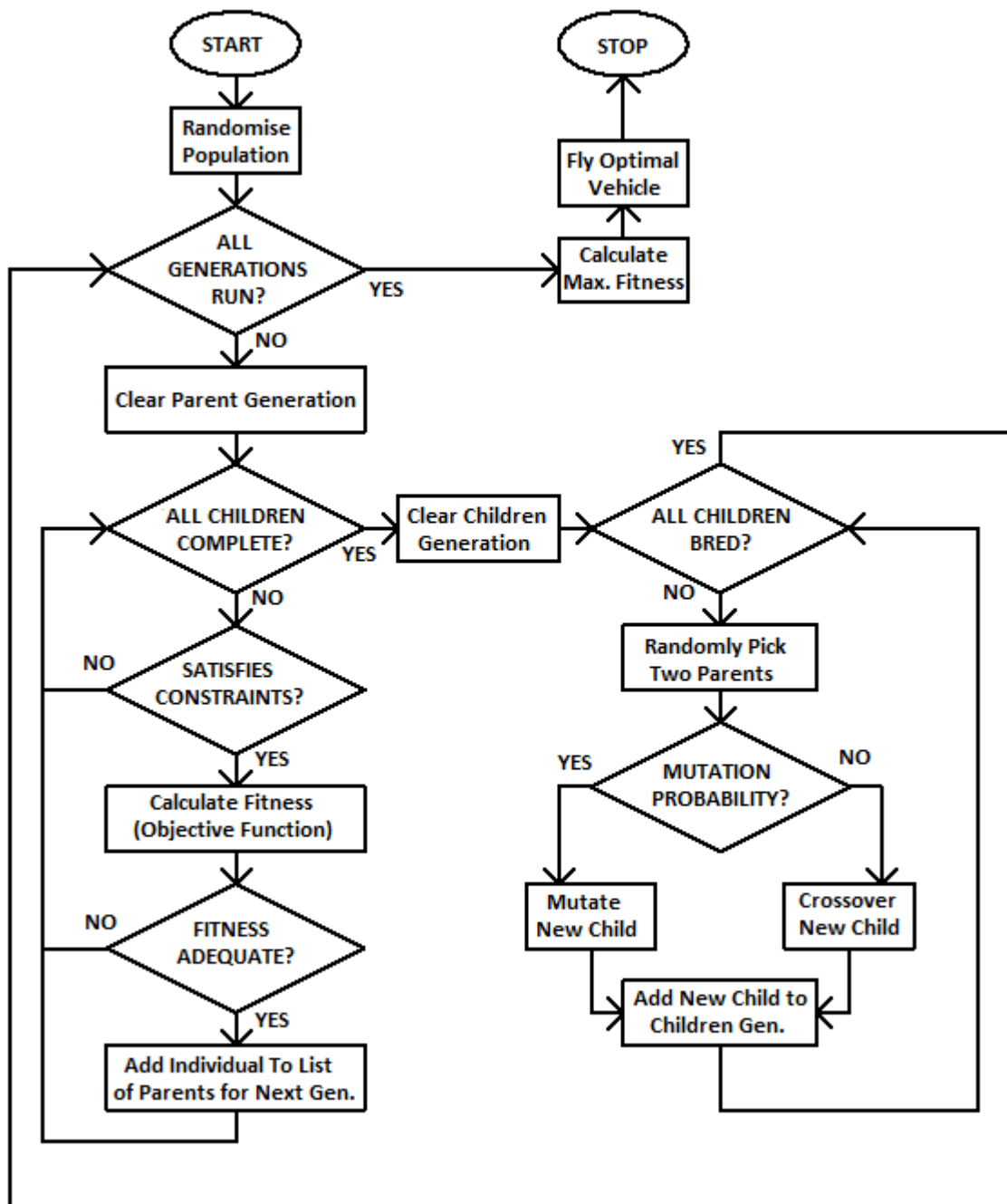
Figure 3-8: High-level flowchart of the genetic algorithm used to optimize sounding rocket design.

Traditionally, genetic algorithms have used binary strings as genetic representations of individuals in the simulated population. This is unsuitable for vehicle designs as the vast majority of design variables are real valued and only a few are integers. It is thus necessary to adopt a real valued genetic representation. Minor modifications to the traditional algorithm are required to accommodate this change. Firstly, the crossover process consists of randomized pseudo-averaging of the gene values from the parent individuals and does not involve direct

substitution or swapping of genes. There are several randomized pseudo-averaging techniques that have been developed for use with real-valued genetic algorithms. In the generation of a crossover gene g_c, the simplest alternative is the selection of a uniformly distributed random number in the interval bounded by the parents' gene values. In this work, the *BLX-α* technique [45] is adopted for its simplicity and performance. Given two parent gene values g_{p1} and g_{p2} this technique chooses a random number $\mathcal{R}$ in the interval which extends beyond the parent values by a factor α greater than difference between the two parent values. The *BLX-α* technique is formulated in Eq. 3-63.

$$g_c = g_{p1} - \alpha|g_{p1} - g_{p2}| + \mathcal{R}|g_{p1} - g_{p2}|(1 + 2\alpha) \quad where \quad g_{p2} > g_{p1} \quad (3\text{-}63)$$

The implementation of a genetic algorithm in sounding rocket vehicle optimization requires a genetic representation of a particular rocket design as well as an objective function to gauge the fitness of a given gene set. The reduced parameter set key design parameters are put into vector form to give a workable real-valued genetic representation. A generic objective function (fitness function) is adopted to allow optimization against the various performance parameters that are of interest to the sounding rocket designer. An algebraic relation is used to describe this custom objective function using a set of pre-calculated metrics. This reduces the original multi-objective optimization problem to a simpler single-objective problem. A list of typical objectives of interest to sounding rocket performance optimization is given in Table 3-10.

Table 3-10: Objective (fitness) functions available for sounding rocket optimization

Objective Metric	Units	Typical Objective
Apogee Altitude	m	Bound Within Interval
Aerodynamic Impulse	Ns	Minimise
Range	m	Bound Within Interval
Fuel Mass	kg	Minimise
Dead Mass	kg	Minimise
Fuel to Mass Ratio	N/A	Maximise
Maximum Stagnation Temperature	K	Minimise
Maximum Velocity	m/s	Minimise
Maximum Acceleration	m/s^2	Minimise
Propulsion Impulse	Ns	Bound Within Interval
Specific Impulse	s	Maximise
Average Total Angle of Attack	rad	Minimise

Objective Metric	Units	Typical Objective
Average Drag Coefficient	N/A	Minimise
Average Lift Coefficient	N/A	Minimise
Minimum Stability Margin	m	Maximise

CHAPTER 4

HYROPS Software Implementation and Results

4.1 Review of Existing Rocket Trajectory Simulation Software

Historically, software tools for the simulation of rockets and rocket-like vehicle trajectories have been developed independently for both defense and scientific applications. The Newtonian 6-DOF equations of motion have been used to predict trajectories since the advent of the first programmable computers. An early example of a military 6-DOF missile simulation code is presented by Minor [46]. Such codes were often implemented in low-level programming languages such as FORTRAN, limiting their scope. However, the current state-of-the-art in missile simulation remains vague due to the industry-wide censorship of such software in most countries. The advent of DOS and GUI in the 1980's allowed the integration of more sophisticated simulation routines into single applications. CADAC [47] is one such software tool, capable of 3-DOF, 5-DOF and 6-DOF dynamic simulations with generalized input and output capabilities as well as stochastic modeling features. Whilst codes like CADAC are capable of efficiently solving the core 6-DOF equations of motion and associated control dynamics, the integration of the entire vehicle's simulation and design phases of the development cycle is not possible.

The rocket trajectory prediction problem may be viewed as a subset of the broader flight dynamics prediction problem for aircraft. Flight simulators have been used to perform 6-DOF trajectory simulation on aircraft for decades. However, the key difference is that rockets experience a much larger range of accelerations and velocities than conventional aircraft. Aircraft are also more aerodynamically diverse as opposed to rockets, which often feature rotationally symmetric airframes. Further to these obvious distinctions, there are different manners in which rockets are used and controlled when compared with aircraft. These factors combine to render conventional aircraft flight simulation codes of little use in the simulation of rocket propelled crafts. Therefore, rocket trajectory simulators have been historically distinct from generic flight simulators although certain advanced codes do integrate aspects of both for applications in space-planes, multi-phase space missions, launch vehicle trajectory optimizations and other integrated simulations.

Established industrial aerospace simulation platforms such as the trajectory optimizer ASTOS by ASTOS Solutions and the generic aerospace management system Satellite Toolkit (STK)

developed by Analytical Graphics (AGI) are widely capable. These packages offer scope for vehicle trajectory simulation ranging from small model rockets to extra-terrestrial missions. However, modeling parameters are often limited and detail must be added using scripting or add-on modules. These tools are focused on the overall mission performance of a space-going vehicle rather than the accurate prediction of its entire trajectory.

Another class of rocket trajectory simulators has been developed to target the model rocketry hobbyists. Model rocketry enthusiasts often wish to predict the performance of a design before investing in building a model. The majority of model rocket simulation codes have been developed recently and feature relatively advanced GUI and visualization functions for users with minimal technical knowledge. Popular software in this category include RockSim (and its successor RockSim Pro), OpenRocket, RasAero, WRASP, Launch and Ascent. RockSim and RockSim Pro are 3-DOF and 6-DOF commercial codes respectively. OpenRocket is an open-source 6-DOF model rocket simulator developed by Niskanen [48]. Unfortunately, none of the abovementioned model rocket simulators offer the modeling scope, GUI and visualization options, model integration and uncertainty modeling capabilities needed for the complete design and multi-disciplinary optimization of a high altitude general purpose sounding rocket. A summary of some important similarities and differences in functionality between HYROPS and other existing high-altitude sub-orbital rocket simulation software is presented in Table 4-1.

Table 4-1: Comparison of HYROPS and existing high-power model rocket simulation tools

Functionality	Open Rocket	RockSim	RockSim Pro	HYROPS
Degrees of Freedom	6	3	6	6
Geodetic Model	Spherical, Rotating Earth	Flat Earth	Ellipsoidal, Rotating Earth	Spherical, Rotating Earth
Maximum Altitude	100 km	100 km	620 km	Unrestricted
Roll Modeling / Initial Roll Rate	Yes / No	No / No	Yes / Yes	Yes / Yes
Maximum Mach No.	10	2	10	10
Recovery System (Stages)	Multiple (Multi-Stage)	Dual (Multi-Stage)	Dual (Multi-Stage)	Dual (Multi-Stage)
Structural Model	Model Rocket	Model Rocket	Model Rocket	Fully Generic

Functionality	Open Rocket	RockSim	RockSim Pro	HYROPS
Staging (Maximum Stages)	Yes (unrestricted)	Yes (3)	Yes (3)	Yes (4)
Propulsion Model	Solid / Model Rocket Motors	Solid / Model Rocket Motors	Solid / Model Rocket Motors	Detailed Hybrid / Generic Motor Inputs
Launch Rail	Yes	Yes	Yes	Yes
Launch Altitude / Launch Velocity	> 0 m, 0 m/s	0 m / 0 m/s	> 0 m / > 0 m/s	> 0 m / > 0 m/s
Numerical Solver	Adaptive RK4	Adaptive RK4	Adaptive RK4	Fixed Step RK4
Wind Model	Turbulence Only	1D Winds	1D Winds	3D Winds, Turbulence, Jet Streams
Motor Clustering	Yes	Yes	No	Yes
Monte Carlo	No	Yes	Yes	Yes
Mass Asymmetry	No	No	Yes	Yes
Automated Optimization	Trajectory Optimization Only	No	No	Multidisciplinary Design Optimization
Fins (Max. No.)	Generic (Unrestricted)	Generic (Unrestricted)	Generic (Unrestricted)	Trapezoidal (4 Fins Only)
Trajectory Visualization	2D	2D	2D	3D
Structural Visualization	2D	3D	3D	3D
Google Earth Compatibility	No	No	Yes	Yes

4.2 Selection of Development Platform

There are several programming platforms capable of implementing the sounding rocket trajectory prediction algorithms described in the previous chapter, including the well established MATLAB platform with the integrated Simulink simulation environment. The selection of the

most suitable platform for the HYROPS sounding rocket simulation tool was based on computational performance, algorithmic flexibility and scope of use.It was decided that an independent implementation from first principles was desirable. The Microsoft Visual C++ programming language was chosen as it is an established industry standard with wide ranging computing capabilities and it generates applications compatible with or adaptable to virtually all operating systems.

4.3 HYROPS Objectives, Philosophy and Motivation

The UKZN HYROPS software package is a standalone application for the Microsoft Windows operating system that implements the flight dynamics simulation techniques presented in this thesis. The HYROPS tool was developed in the Microsoft Visual C++ 2008 Standard Edition software development environment. This chapter outlines the implementation details of the software and the results generated to validate this implementation. The methodology behind its development is discussed with regards to applications in sounding rocket design and simulation. The UKZN HYROPS software was developed with a key set of objectives:

1) Sufficient core functionality
2) User friendliness
3) User interfacing
4) Interactive visualization of results
5) Basic flight performance analysis
6) Data loading and logging
7) Adaptability, flexibility and generality in software architecture
8) Design and optimization capabilities

The above objectives were selected to address a number of issues which motivated the development of the new software tool itself. It was noted that existing solutions with sufficiently advanced functionality were often very costly. Furthermore, commercial solutions with the desired scope were not found. It was found that packages offered some of the desired functionality often with much greater depth but could not offer all of the desired capacity in the proportions required for the swift development of sounding rocket technologies. The challenges present in the suite of existing software which HYROPS was meant to overcome included the following

a) Lack of integration (all desirable functionality not offered)
b) Lack of independence (not standalone software)

c) High costs

d) Export restrictions, e.g. U.S. International Trade in Arms Regulations (ITAR)

e) Lack of expandability (not open source)

f) Lack of visualization capacity (hinders results interpretation)

Given these challenges, HYROPS was developed from the outset to ensure that the UKZN Phoenix program would have a software tool capable of matching the program needs in terms of technical as well as logistical functionality and also allowing for future expansion at a minimum cost.

4.4 HYROPS Graphical User Interface (GUI)

4.4.1 Installation and User Manual

A copy of the HYROPS tool is included on the DVD disc accompanying this dissertation. This DVD contains the HYROPS executable application, named *FlightDynamics.exe*, which may be executed from any directory location after installation. Installation is manually performed by the user and simply involves copying of the folder named *DATA* from the DVD to the workstation's *C* drive (root directory). A detailed description of the installation process is provided in the *readme.txt* file on the DVD. A user manual for the HYROPS tool is also provided in the *HYROPSUserManual.pdf* file. The HYROPS software has been installed and tested on workstations operating on the Windows XP, Windows Vista and Windows 7 operating systems only. The software requires at least 400 Mb of free hard drive space and approximately 2 GB of RAM for smooth operation. It does not use multi-core processor capabilities and a minimum processor speed of 1.5 GHz is recommended. An installation of the latest version of the Microsoft Dot.Net framework is a pre-requisite for the use of the software.

4.4.2 User Interface Layout

The software interface was designed to allow separate user input on the various simulation subsystem models. Once sufficient inputs exist, a command is used to run a single simulation or batch simulations for uncertainty quantification. SI units are used throughout the software tool as a matter of convention. Interactive vehicle design is possible through a continuously updated three dimensional rendition depicting the vehicle's constituent components. A screenshot of the application front-end is shown in Figure 4-1.
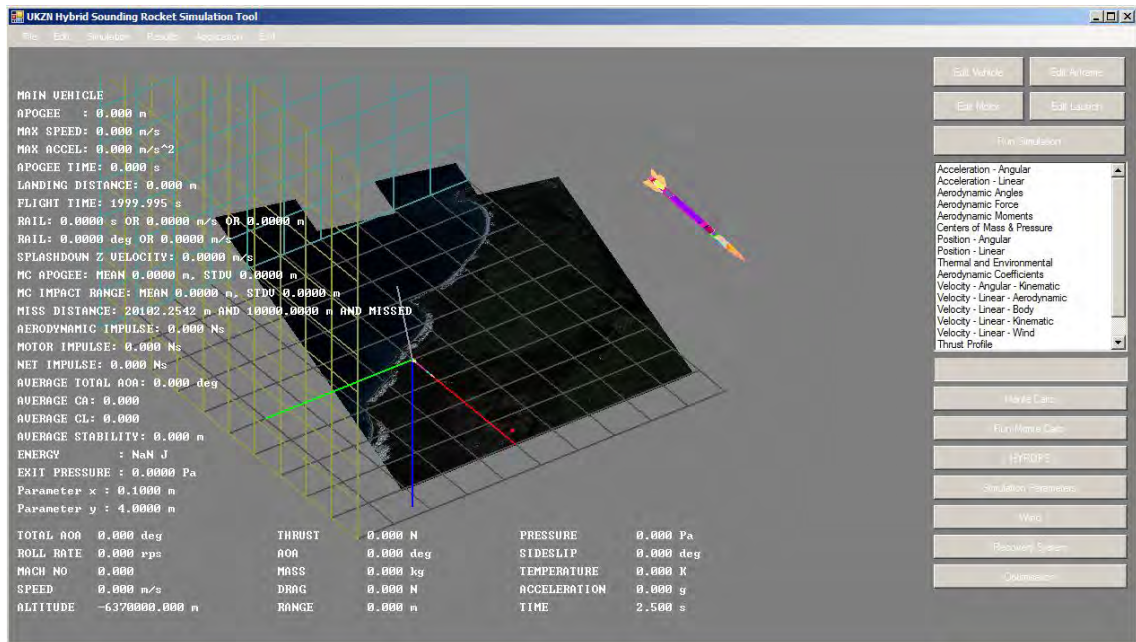
Figure 4-1: A screenshot of the HYROPS software Windows front end application.

4.4.3 Result Plots

The HYROPS tool offers the user multiple selectable plots for graphing trajectory prediction results. Plotted variables are grouped so as to convey maximum intuitive information about the trajectory. The components of the state vector are all plotted against time. Other relevant environmental and mechanical variables such as the Mach number, local ambient and stagnation temperatures, aerodynamic coefficients, aerodynamic forces, aerodynamic moments, thrust curve, ambient pressure and motor exit pressure, center of mass and center of pressure are also plotted against time. In addition, a Mach number histogram is provided to convey information on the most significant Mach regimes encountered during a simulation. All plots are scaled automatically and may be zoomed and panned on the horizontal axis for detailed inspection of results. Figure 4-2 shows a screenshot of the plotting functionality.
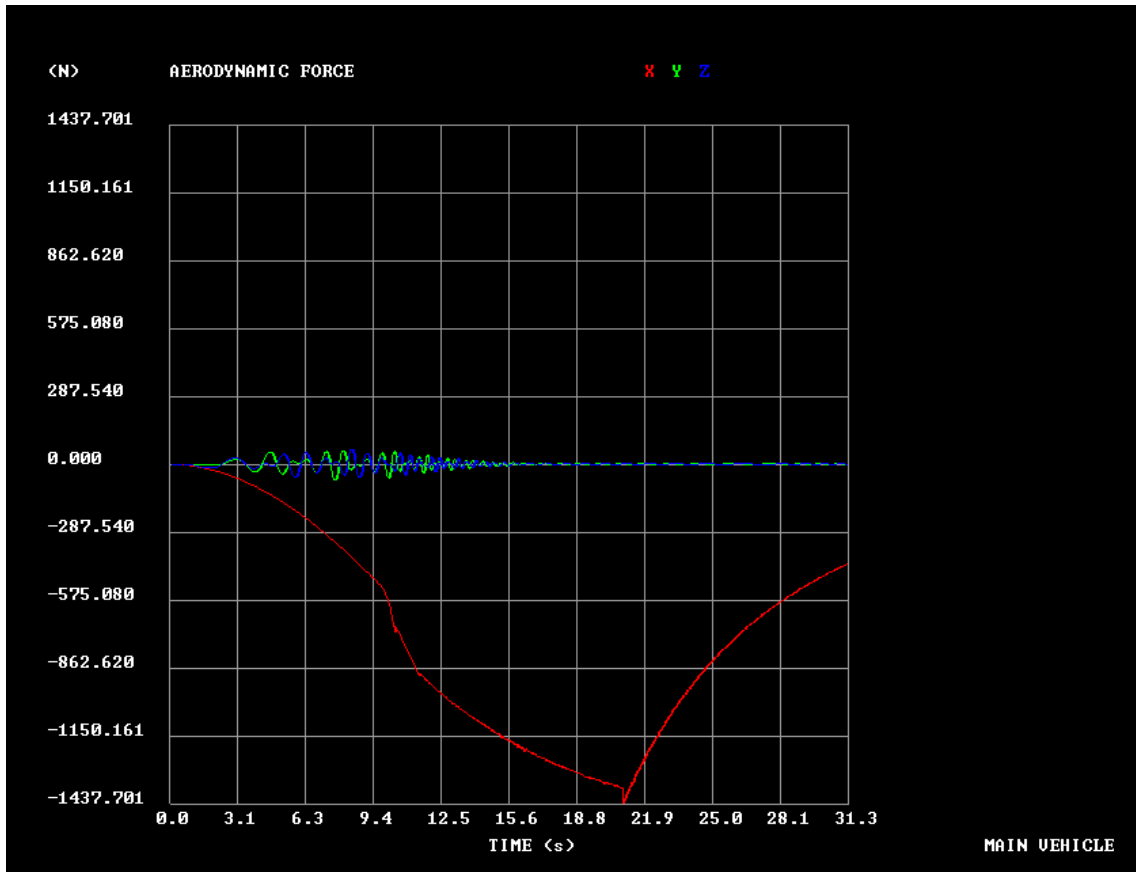
Figure 4-2: HYROPS plot showing a portion of the Pheonix-1A's aerodynamic force history.

4.4.4 Trajectory Visualizations

The HYROPS software offers four trajectory visualization options. The first is a three dimensional Cartesian space referenced to the Earth-fixed frame wherein the body frame and vehicle are animated along the flight trajectory (Figure 4-3). The projected ground track is also simultaneously rendered as an indication of the vehicles relation to land features. The vehicle geometry is rendered to convey the body frame orientation. Cartesian grids are also rendered to convey scale. Multiple stage and booster combinations are rendered for synchronous representation of multi-stage trajectories. Parachute canopies are also rendered for vehicles featuring recovery systems. Vectors such as the aerodynamic, kinematic and wind velocity are also optionally rendered in this graphic. Monte Carlo splashdown points for the main vehicle and any boosters are distinctly plotted in this view using different colors. The graphic is entirely scalable, pan-able and rotatable around all three Cartesian axes using the keyboard and mouse. The animation speed is also variable and the user may pause and step the animation forward or in reverse if necessary.
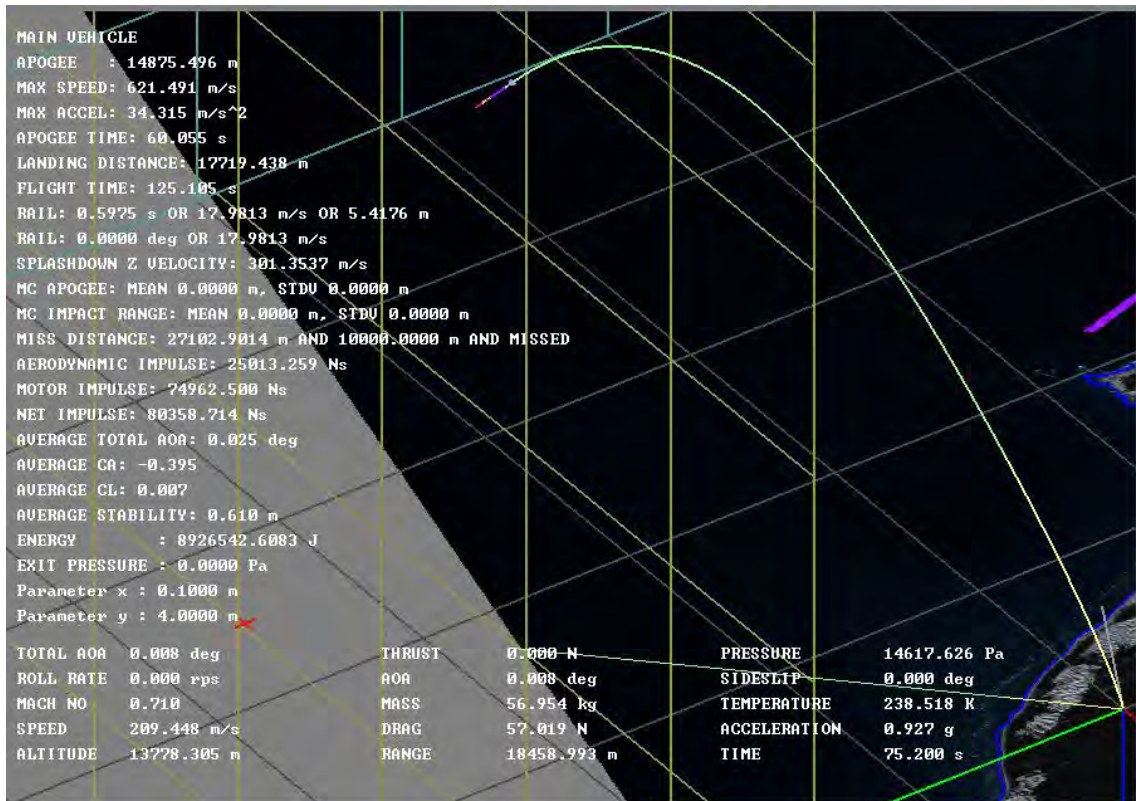
Figure 4-3: Screenshot of the HYROPS 3D trajectory animation window. Overall trajectory parameters are printed along with instantaneous flight conditions during animations.

The structural design, aerodynamic model and attitude dynamics of the vehicle are visualized in detail using a second dedicated graphic (Figure 4-4). This graphic displays the body frame in three dimensions with the origin at the vehicle mass-center. All the structural components or airframe geometries of the vehicle are rendered to scale and the vehicle orientation reflects the orientation of the body frame. This allows the user to quickly and efficiently visualize the attitude dynamics of the vehicle. The rendition is animated and reflects all shape variations effects, stage separation events and optionally displays salient body-frame velocity vectors as arrows. This graphic is also scalable, pan-able and rotatable and the animation speed, direction and stepping may also be controlled by the user as necessary. In addition, options are available to render the vehicle or airframe in cutaway and/or wireframe mode with the vehicle reduced in half longitudinally. Individual components are always colored distinctly for clarity.
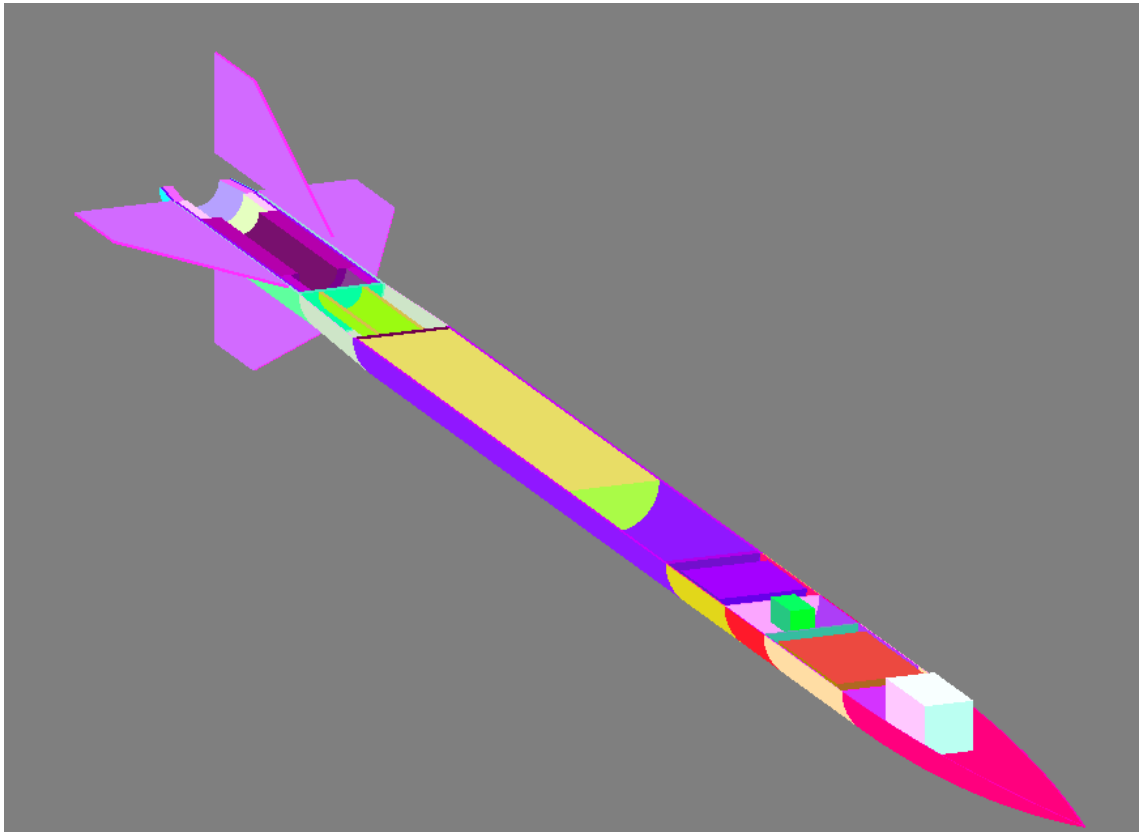
Figure 4-4: Screenshot from HYROPS animation of the structural design view of the simulated vehicle.

A Cartesian two-dimensional geographic vector map is provided in a separate animated graphic for the visualization of vehicle ground tracks and Monte Carlo footprints. Context is provided using detailed vector data for sub-national and international boundaries, coastlines and infrastructure such as urban concentrations and road networks, as shown in Figure 4-5. Vector international boundaries are displayed in white, along with Western Cape (South Africa) regional and district borders in red. The green path is the ground track of the vehicle (in this case a satellite in elliptical orbit) and the blue area encloses the visibility footprint of the vehicle. Specific vector data layers may be hidden or displayed optionally. The map is scalable and pan-able and offers animation controls like the other graphics modes.
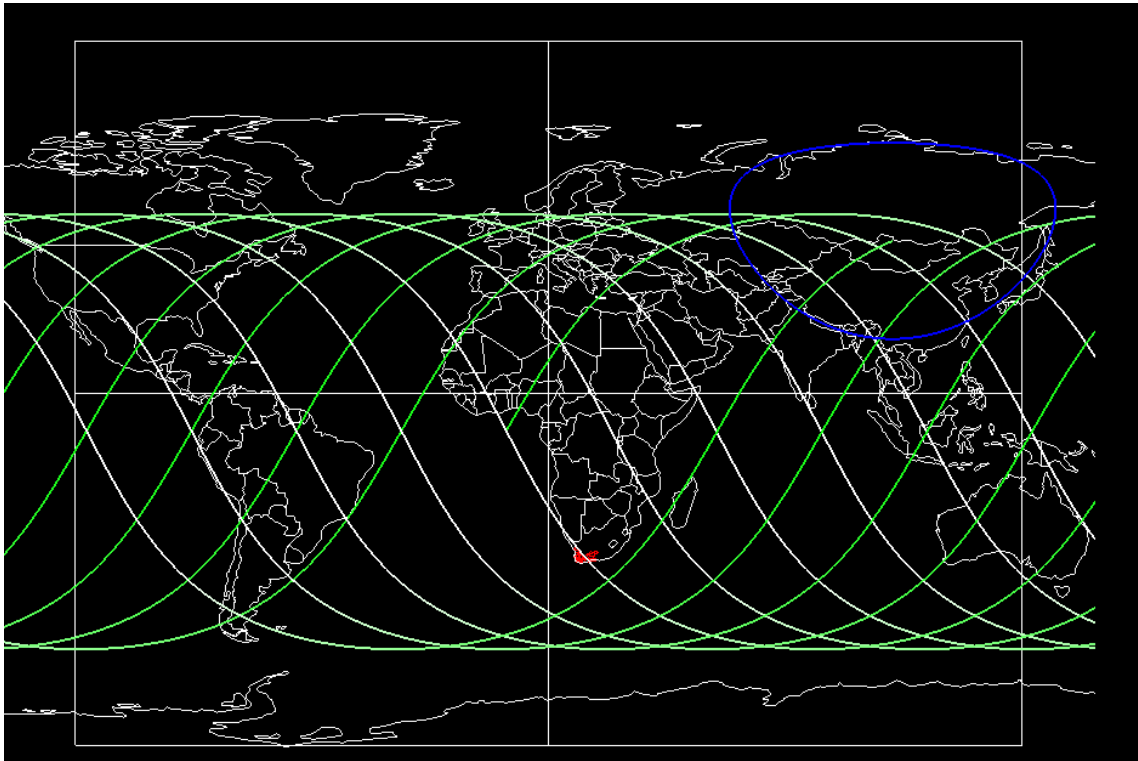
Figure 4-5: Screenshot of HYROPS Geodetic animation.

Although the HYROPS tool's primary purpose is the modeling of sub-orbital sounding rocket trajectories, its kinematic and geodetic models are general enough to allow the simulation of orbital trajectories. Trajectories on the global scale are animated on a three dimensional globe (Figure 4-6). This view displays the trajectory of the vehicle and its ground track as seen from the Earth-fixed frame. The effects of the spherical geometry of the Earth and the Coriolis acceleration are thus easily observable. This feature also provides ground tracks and visibility footprints for Earth based observations of orbiting spacecraft. The view is scalable, pan-able and rotatable like the other 3D renditions in the software and it features similar animation controls. The globe is rendered with several vector data layers showing international political boundaries, local district and provincial boundaries as well as latitude and longitude graticules.
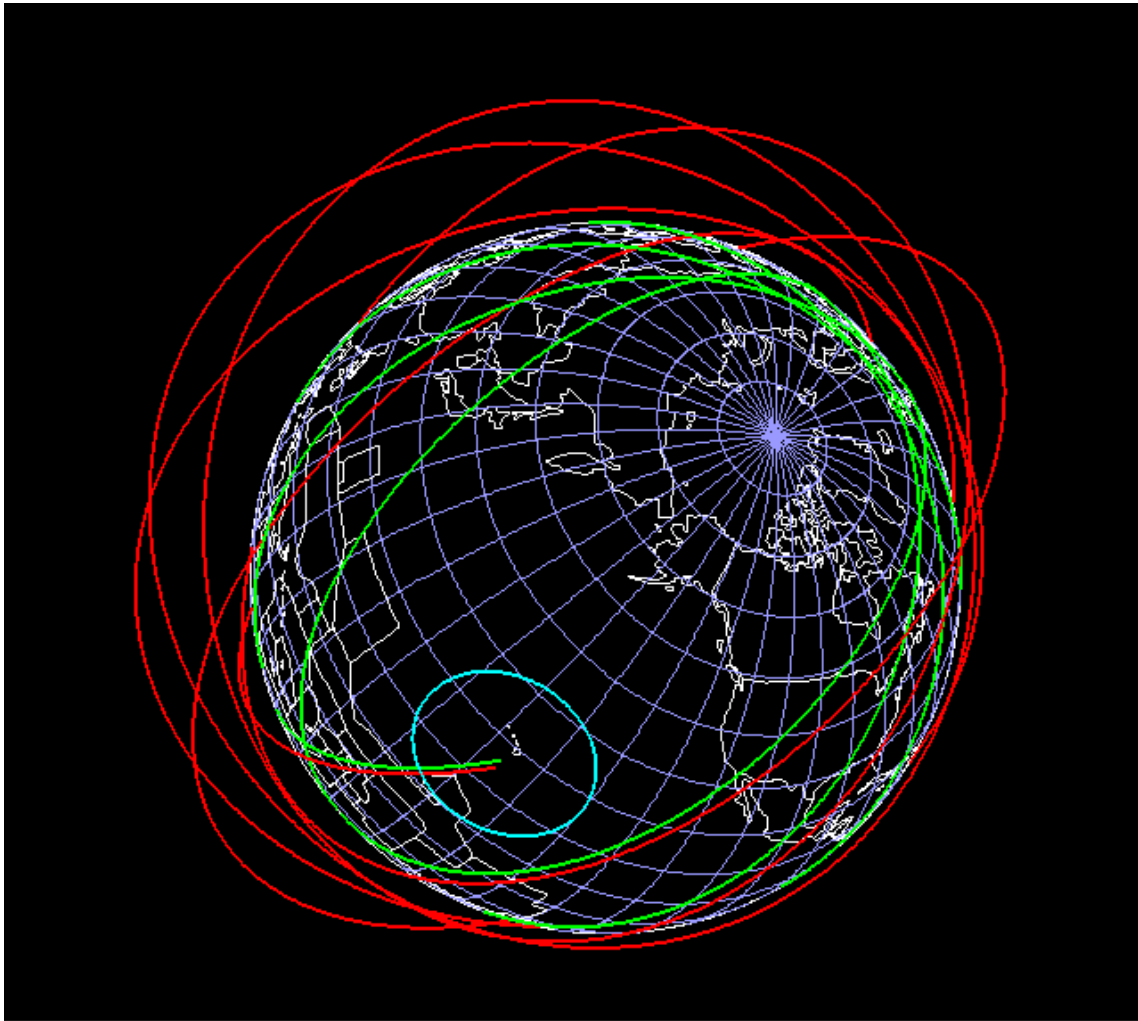
Figure 4-6: Screenshot from the HYROPS global trajectory animation, displaying several orbits of a satellite in elliptical orbit around the Earth. The orbital trajectory is in red, the corresponding ground tracks in green and the footprint of visibility of the satellite in cyan.

4.5 HYROPS Data Input / Output Interface

4.5.1 Storage File Formats

Several file formats were defined to allow for the non-volatile storage and retrieval of launch scenarios, vehicle designs, trajectory outputs, optimization inputs and aerodynamic or thrust curve input on disk. Vehicle, trajectory, optimization and launch scenario data is stored in binary format for disk-space conservation and to facilitate data conservation. Aerodynamic and thrust input curves are stored in textual format for easy editing using common spread sheet software such as Microsoft Excel. The .csv and .kml file formats are also compatible with the

MATLAB mathematical computing environment and the Google Earth geographic visualization software. A list of file types compatible with HYROPS is given in Table 4-2 below.

Table 4-2: File types used in the HYROPS software

File Type	File Extension	Read/Write
Vehicle Design Input	.veh	R/W
Trajectory Output	.trj	R/W
Launch Scenario Input	.rsc	R/W
Google Earth Output	.kml	W
Aerodynamics Table Input	.aer	R
Thrust Curve Input	.csv	R
Trajectory Output	.csv	W
Optimization Input	.opt	R/W

4.5.2 Result Output Formatting

Internally, HYROPS uses running variables to conserve memory. Nevertheless, the state vector and all other relevant time varying variables, including both simulation outputs and intermediate variables are stored in memory in time-stamped arrays and written to output files at the end of each simulation run. Outputs to the GUI in the form of plots and animations are read from these internal time series arrays. Table 4-3 summarizes the various HYROPS outputs.

Table 4-3: HYROPS outputs summary

Output Variable	Data Format	Units	Temporal Format	Graphic
Apogee Altitude	Real Number	m	Per Flight	Text
Maximum Speed	Real Number	m/s	Per Flight	Text
Maximum Acceleration	Real Number	m/s^2	Per Flight	Text
Splashdown Range	Real Number	m	Per Flight	Text
Time to Apogee	Real Number	s	Per Flight	Text
Time to Splashdown	Real Number	s	Per Flight	Text
Splashdown Vertical Speed	Real Number	m/s	Per Flight	Text
Acceleration – Linear	3D Vector	m/s^2	Time Series	Time Plot
Acceleration – Angular	3D Vector	rad/s^2	Time Series	Time Plot
Aerodynamic Force	3D Vector	N	Time Series	Time Plot

Output Variable	Data Format	Units	Temporal Format	Graphic
Aerodynamic Moment	3D Vector	Nm	Time Series	Time Plot
Position – Linear – Geographic	3D Vector	m	Time Series	Time Plot, Animation
Position – Angular	3D Vector	m	Time Series	Time Plot, Animation
Velocity – Angular – Kinematic	3D Vector	rad/s	Time Series	Time Plot
Velocity – Linear – Aerodynamic	3D Vector	m/s	Time Series	Time Plot
Velocity – Linear – Body	3D Vector	m/s	Time Series	Time Plot
Velocity – Linear – Kinematic	3D Vector	m/s	Time Series	Time Plot
Velocity – Linear – Wind	3D Vector	m/s	Time Series	Time Plot
Aerodynamic Coefficients – Linear	3D Vector	N/A	Time Series	Time Plot
Angle of Attack	Real Number	rad	Time Series	Time Plot
Sideslip Angle	Real Number	rad	Time Series	Time Plot
Total Angle of Attack	Real Number	rad	Time Series	Time Plot, Text
Vehicle Mass	Real Number	kg	Time Series	Time Plot, Text
Centre of Mass – Body Frame x	Real Number	m	Time Series	Time Plot
Centre of Pressure – Body Frame x	Real Number	m	Time Series	Time Plot
Local Mach Number	Real Number	N/A	Time Series	Time Plot, Text
Local Absolute Temperature	Real Number	K	Time Series	Time Plot
Local Total Absolute Temperature	Real Number	K	Time Series	Time Plot, Text
Thrust Force Magnitude	Real Number	N	Time Series	Time Plot, Text

4.5.3 Graphical User Interface Inputs

The HYROPS GUI offers the user launch inputs as described in Table 4-4 and high-level vehicle design inputs as described in Table 4-5. These inputs are used to as a basis for further user input on structural components, shape variations, aerodynamic and thrust curve input files and the use of the integrated hybrid rocket motor performance simulator developed by Genevieve [4].

Table 4-4: Simulation launch inputs (initial conditions)

Input	Type	Units	Range
Launch Azimuth Angle	Real Number	°	0° to 360°
Launch Elevation Angle	Real Number	°	0° to 90°
Launch Altitude	Real Number	m (AMSL)	> 0 m
Launch Latitude	Real Number	°	-90° to 90°
Launch Longitude	Real Number	°	0° to 360°
Initial Velocity	Real 3D Vector	m/s	Real Numbers
Launch Rail Present	Boolean	N/A	Yes or No

Table 4-5: High-level vehicle design inputs

Parameter	Range	Units	Application to Model
No. of Stages	≤ 4	N/A	Structural, Aero, Propulsion
No. of Parts	> 0	N/A	Structural
No. of Shape Variations	≥ 0 and ≤ 20	N/A	Structural
Stage Ignition Delays	≥ 0	s	Propulsion
Stage Separation Times	≥ 0	s	Structural, Aero, Propulsion
Thrust Model Type	Curve Input, Ramp Function or HYROPS	N/A	Propulsion
Aerodynamic Model Type	Internal or Table	N/A	Aero
Main Parachute CD	≥ 0	N/A	Aero
Main Parachute Diameter	≥ 0	m	Aero
Main Parachute Deployment Altitude	≥ 0	m	Aero
Drogue Parachute CD	≥ 0	N/A	Aero

Parameter	Range	Units	Application to Model
Drogue Parachute Diameter	≥ 0	m	Aero
Drogue Parachute Deployment Delay	≥ 0	s	Structural, Aero
Nozzle Exit Area	≥ 0	m^2	Propulsion

4.6 Integration of Geographic Information Systems (GIS) Data

The geographic context of a sounding rocket flight is important for several reasons. Most nations impose aviation restrictions based on geographic location and altitude. In some cases, international treaties relating to aviation are also applicable. Permissions to operate sounding rockets in a particular airspace must be obtained before operations commence. Planned trajectories are thus always matched to geopolitical and administrative boundaries during the mission planning phase. An important function of the flight performance prediction tool is to facilitate this process. In a global context, the position of a flying vehicle is best defined using geographic coordinates and an altitude. A user-friendly manner of visualizing the results of a flight simulation is to display the geographic location and altitude of the vehicle on a map along with relevant geopolitical data. Statistical distributions of splash-down/impact points are also needed to portray the possible extent of security zone needed for the launch and recovery of sounding rockets.

The sounding rocket simulation tool incorporates raster satellite imagery of the launch vicinity as well as vector data representing the coastlines, district and provincial borders and also the local road network. Vector data is imported in the common *ESRI Shapefile* format. The trajectory of the sounding rocket can then be easily contextualized within the surrounding countryside. Natural features of significance such as mountain ranges, lakes and rivers are represented in the satellite imagery. Manmade features of interest include nature reserves, airports, populated places and testing ranges. Some of these features are shown in Figure 4-7. A 10 m resolution geo-referenced satellite image of the region from the NASA EO1-ALI satellite [49] is draped onto the ground. Western Cape district municipality [50] borders (in blue) are also displayed in vector format. Further contextualization of flight trajectory data is made possible through the export of trajectory paths in the Google KML file format. KML files may be visualized in the Google Earth virtual Earth software, allowing trajectory data at any locale to be viewed together with a large variety of associated GIS datasets. KML files are also generated for Monte Carlo runs, recording splashdown impact points and other relevant flight performance

analysis outputs. Figure 4-8 shows a screenshot from Google Earth with HYROPS generated trajectory and Monte Carlo footprint .kml file loaded.


```
MAIN VEHICLE
APOGEE    : 2304682.486 m
MAX SPEED: 8062.258 m/s
MAX ACCEL: 11.353 m/s^2
APOGEE TIME: 728.420 s
LANDING DISTANCE: 342867803.585 m
FLIGHT TIME: 1999.995 s
RAIL: 0.0000 s OR 0.0000 m/s OR 0.0000 m
RAIL: 0.0000 deg OR 0.0000 m/s
SPLASHDOWN Z VELOCITY: 0.0000 m/s
MC APOGEE: MEAN 0.0000 m, STDV 0.0000 m
MC IMPACT RANGE: MEAN 0.0000 m, STDV 0.0000 m
MISS DISTANCE: 22360.6798 m AND 10000.0000 m AND MISSED
AERODYNAMIC IMPULSE: 0.000 Ns
MOTOR IMPULSE: 0.000 Ns
NET IMPULSE: 196881.599 Ns
AVERAGE TOTAL AOA: 45.650 deg
AVERAGE CA: 0.000
AVERAGE CL: 0.000
AVERAGE STABILITY: 0.200 m
ENERGY        : NaN J
EXIT PRESSURE : 0.0000 Pa
Parameter x : 0.1000 m
Parameter y : 4.0000 m

TOTAL AOA   0.000 deg      THRUST      0.000 N      PRESSURE      0.000 Pa
ROLL RATE   0.000 rps      AOA         0.000 deg    SIDESLIP      0.000 deg
MACH NO     0.000          MASS        0.000 kg     TEMPERATURE   0.000 K
SPEED       0.000 m/s      DRAG        0.000 N      ACCELERATION  0.000 g
ALTITUDE    -6370000.000 m RANGE       0.000 m      TIME          800.000 s
```

Figure 4-7: Screenshot of the HYROPS launch scenario of the Phoenix-1A in the Denel Overberg Test Range, Western Cape, South Africa.
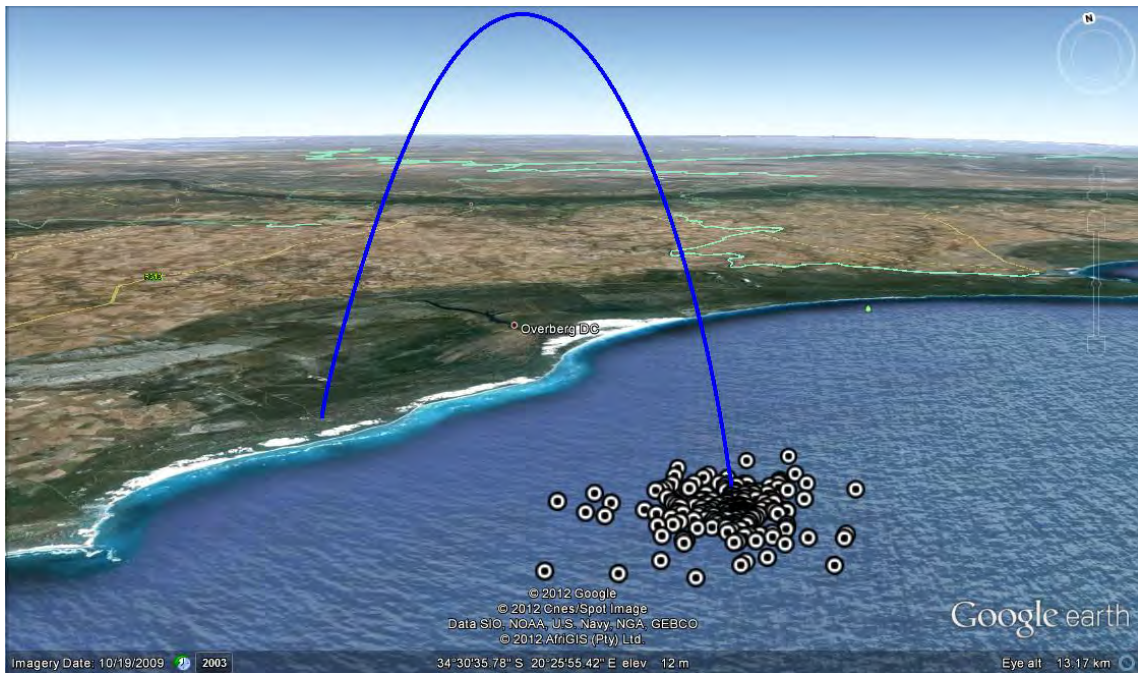
Figure 4-8: Google Earth visualization of trajectory and Monte Carlo output .kml files from HYROPS. The nominal Phoenix-1A trajectory is displayed in blue whilst a set of 200 Monte Carlo impact points are rendered in black and white bulls-eyes.

4.7 HYROPS Results and Validation

4.7.1 Basic Dynamics - Nike Apache Sounding Rocket

The validity of the HYROPS flight dynamics model was established by comparison with flight data available in the literature. The fidelity of the core solver and basic mathematical models was measured by comparing overall flight performance parameters such as the apogee altitude and impact range for industrial sounding rockets whose performance characteristics are published. The NASA Nike Apache sounding rocket was chosen as its performance fell within the upper bounds of the HYROPS software simulation scope and its two stage configuration allowed multi-stage functionality to be validated concurrently. The Nike Apache was a two-stage solid fuelled sounding rocket with a payload range of 50 lb. to 80 lb. and a nominal apogee range of 115 miles to 160 miles depending on launch and payload conditions. As its name suggests, the Nike Apache used a Nike M5-E1 first stage booster and a Thiokol Chemical Corporation Apache TE-307 second stage motor. The vehicle also used a set of four stabilizing fins on each step. Table 4-6 gives some salient data on the vehicle and Figure 4-10 displays its basic dimensions. The Nike Apache was extensively used by NASA between 1961 and 1978, primarily for atmospheric soundings. The HYROPS model of the vehicle is shown in Figure 4-9.
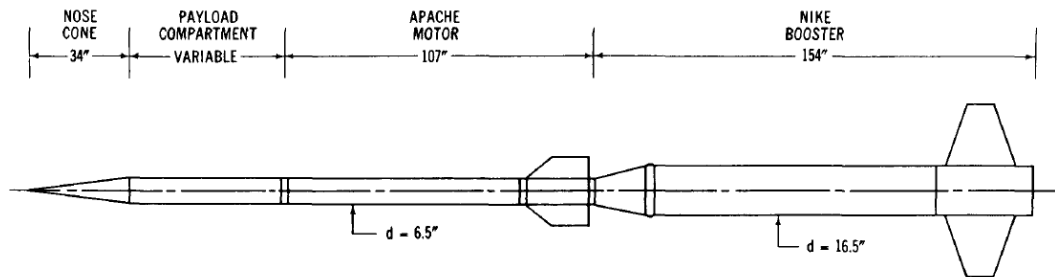
Figure 4-9: Layout and basic dimensions of the Nike Apache 'clean' configuration, as used by Jenkins [51]
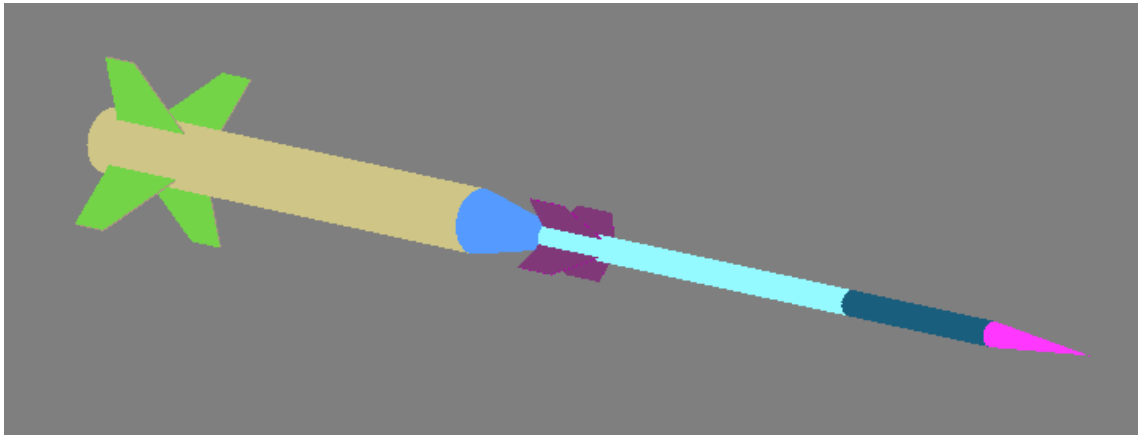
Figure 4-10: The Nike Apache 'clean' configuration, as modeled in HYROPS. The dimensions and component masses were reproduced as closely as possible from the data of Jenkins [51]

Table 4-6: The NASA Nike-Apache sounding rocket [51]

Characteristic	Value
Step 1 Vehicle	*Nike M5-E1 Booster*
Step 1 – Empty Mass	250 kg
Step 1 – Fuel Mass	347 kg
Step 1 – Average Thrust	195.6 kN
Step 1 – Burn Time	3.4 s
Step 2 – Vehicle	*Apache Thiokol TE 307 Sustainer*
Step 2 – Empty Mass	39 kg
Step 2 – Fuel Mass	60 kg
Step 2 – Average Thrust	21 kN
Step 2 – Burn Time	6 s

HYROPS simulation of the Nike Apache used the internal aerodynamics predictor and turned off the Earth rotation feature for greater similarity with the simulation conditions employed by Jenkins [51]. Jenkins presents some basic vehicle data and a theoretical performance summary for the Nike Apache 'clean' configuration whilst Dembrow and Jamieson [52] present some measured flight data. The results presented by Jenkins used a two-dimensional, zero-lift, spherical non-rotating Earth *N* stage simulation and hence were expected to differ slightly from the HYROPS predictions and the actual flight data. The unavailability of temporal thrust curves led to the use of ramp functions based on the average thrust values and burn times presented in

Table 4-6 for each of the stages. Figure 4-11 shows 'carpet' plots of flight predictions from HYROPS and Jenkins. HYROPS apogee predictions differed by an absolute average of 1.66 % with small overestimates for lower launch elevation angles and slight underestimates of near-vertical launch angles. Impact range predictions differed more significantly, with the HYROPS predictions consistently falling between 9 % and 13 % short of those by Jenkins. This difference is primarily a result of gravity turn effects which are excluded in the Jenkins results. The nominal Nike Apache flight involves a 50 lb. payload with a launch elevation angle of 80°. Time plots for this flight are presented by Jenkins [51] and were compared with HYROPS predictions. Figure 4-12 and Figure 4-13 show the velocity and position comparisons respectively.
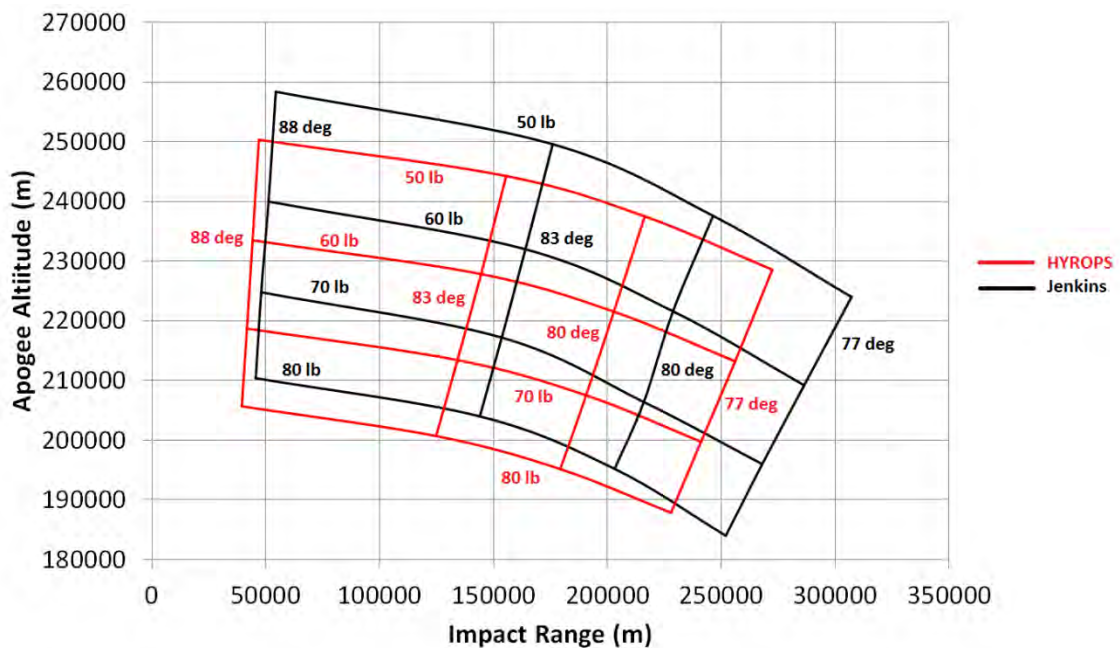
Figure 4-11: Carpet plots of apogee altitude and impact range for the Nike Apache clean configuration, using HYROPS and the results from Jenkins [51]. Launch elevation angles are 77°, 80°, 83° and 88° whilst payload masses used are 50 lb., 60 lb., 70 lb. and 80 lb.
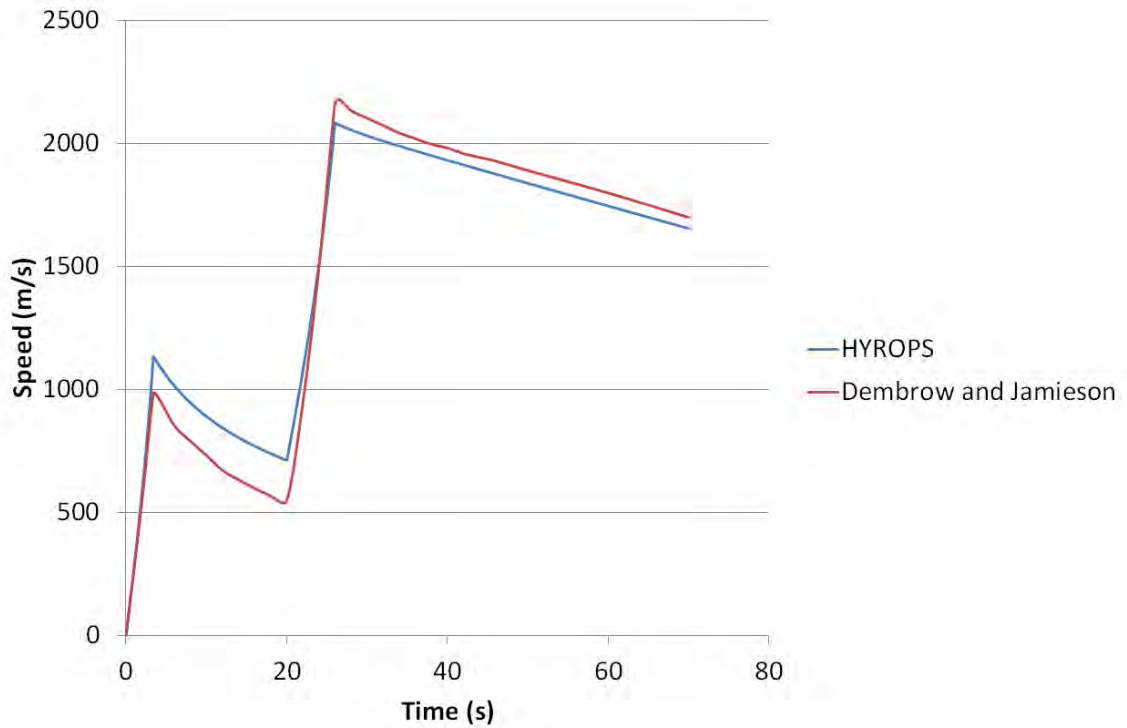
Figure 4-12: Comparison of kinematic speed histories of the nominal clean Nike Apache using HYRPOS and the results of Dembrow and Jamieson [52]. Launch elevation angle is 80° and payload mass 50 lb.
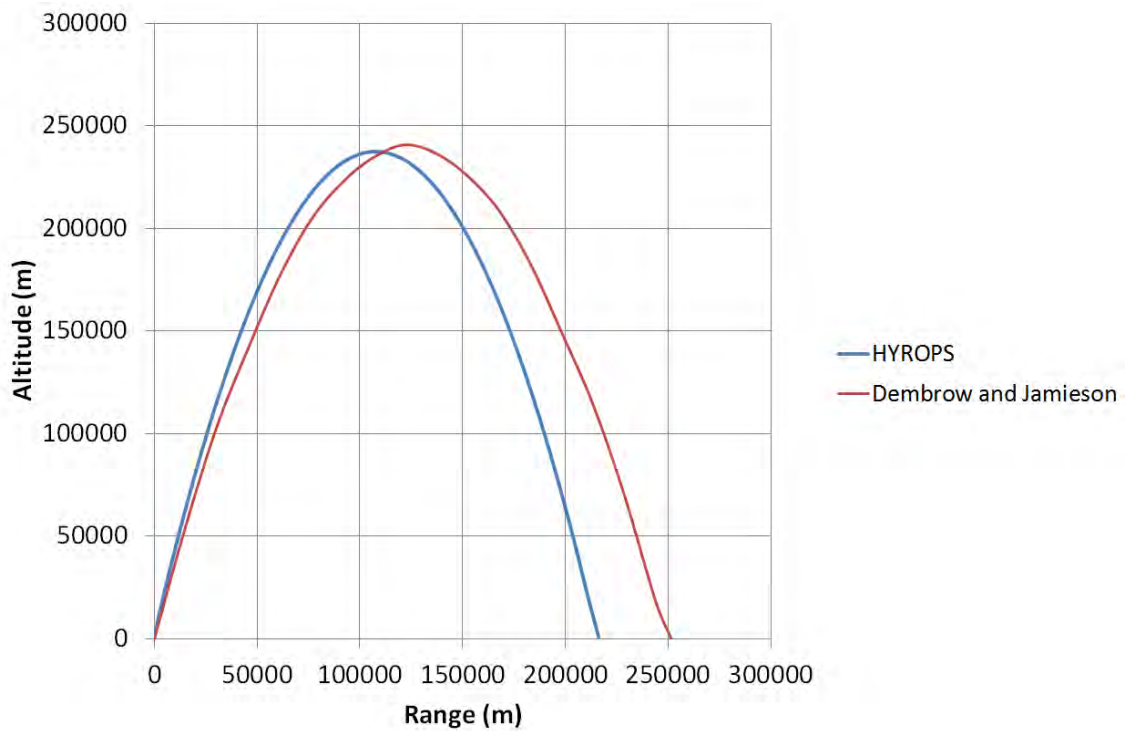
Figure 4-13: Comparison of altitude vs. range for the nominal clean Nike Apache using HYRPOS and the results of Dembrow and Jamieson [52]. Launch elevation angle is 80° and payload mass 50 lb.

4.7.2 Phoenix-1A Nominal Trajectory

The Phoenix-1A vehicle was introduced to HYROPS by simplifying each of the major subsystems of the structural design such that they could be represented using one of the simple geometries available to the HYROPS vehicle structural model. As the design progressed, the number and accuracy of the input components and their dimensional and inertial attributes was increased. The configuration of the model was also tailored to suit optimization studies on the main performance driving structural members such as the oxidizer tank, motor casing, nose and fins. Table 4-7 summarizes the structural model inputs.

Table 4-7: Structural component inputs for Phoenix-1A model in HYROPS

Component Name	Geometry	Density (kg/m^3)	x-Location (m)	Dimensions (m)	Mass (kg)
TankShell	Annulus	2700.0	1.85	*L = 1.6* *r = 0.1* *t = 0.006*	15.797
TankEnds1	Cylinder	2700.0	1.059	*L = 0.018* *r = 0.094*	1.349
TankEnds2	Cylinder	2700.0	2.641	*L = 0.018* *r = 0.094*	1.349
Nitrous	Cylinder	755	1.81	*L = 1.484* *r = 0.094*	31.102
FCBulkhead	Cylinder	2700.0	3.1465	*L = 0.007* *r = 0.096*	0.547
Skirting	Annulus	1600.0	2.7965	*L = 0.293* *r = 0.098* *t = 0.002*	0.571
MainBay	Annulus	1600.0	3.35	*L = 0.4* *r = 0.1* *t = 0.002*	0.796
DrogueBay	Annulus	1600.0	2.8	*L = 0.3* *r = 0.1* *t = 0.002*	0.597
MainBulkhead	Cylinder	2700.0	3.5465	*L = 0.007* *r = 0.098*	0.570

Component Name	Geometry	Density (kg/m³)	x-Location (m)	Dimensions (m)	Mass (kg)
DrogueBulkhead	Cylinder	2700.0	2.9465	*L = 0.007* *r = 0.098*	0.570
MainParachute	Cylinder	300.0	3.35	*L = 0.3* *r = 0.09*	2.290
DrogueParachute	Cylinder	300.0	2.8	*L = 0.2* *r = 0.09*	1.527
Nose	Ogive Shell	1600.0	3.55	*L = 1.0* *r = 0.1* *t = 0.002*	1.581
Electronics	Box	1600.0	3.05	*l = 0.1* *b = 0.05* *h = 0.05*	0.4
Payload	Box	500.0	3.75	*l = 0.2* *b = 0.1* *h = 0.1*	1.0
FCBay	Annulus	1600.0		*L = 0.2* *r = 0.1* *t = 0.002*	0.398
Taper	Truncated Cone Shell	1600.0	1.05	*L = 0.3* *r$_1$ = 0.1* *r$_2$ = 0.09* *t = 0.002*	0.567
Conduit	Annulus	7800.0	0.9	*L = 0.3* *r = 0.05* *t = 0.009*	6.021
InjectorBulkhead	Cylinder	7800.0	0.7425	*L = 0.015* *r = 0.084*	2.594
MotorCasing	Annulus	2700.0	0.425	*L = 0.65* *r = 0.09* *t = 0.006*	5.756
ThermalLiner	Annulus	350.0	0.4175	*L = 0.635* *r = 0.084* *t = 0.006*	0.679

Component Name	Geometry	Density (kg/m³)	x-Location (m)	Dimensions (m)	Mass (kg)
FuelGrain	Annulus	924.0	0.435	$L = 0.4$ $r = 0.078$ $t = 0.053$	6.339
BoatTail	Truncated Cone Shell	1600.0	0.1	$L = 0.1$ $r_1 = 0.09$ $r_2 = 0.075$ $t = 0.002$	0.164
Fins	Fin Set	2700	0.1	$c_r = 0.6$ $c_t = 0.2$ $w = 0.4$ $s = 0.2$ $t = 0.006$ $r_t = 0.09$	5.184
Nozzle	Truncated Cone Shell	2700.0	0.1	$L = 0.1$ $r_1 = 0.083$ $r_2 = 0.068$ $t = 0.02$	1.852
Sleeve	Annulus	1600.0	3.2	$L = 0.5$ $r = 0.098$ $t = 0.006$	0.975
NozzleCap	Truncated Cone Shell	7800.0	0.1	$L = 0.1$ $r_1 = 0.088$ $r_2 = 0.073$ $t = 0.005$	1.911
PreSpacer	Annulus	950.0	0.68	$L = 0.11$ $r = 0.078$ $t = 0.02$	0.893
PostSpacer	Annulus	950.0	0.1625	$L = 0.125$ $r = 0.078$ $t = 0.02$	1.015

The fuel grain was represented using an annulus with shape variation on the wall thickness to model the fuel consumption. Similarly, the nitrous oxide in the oxidizer tank was represented using a cylinder with a shape variation diminishing its length and moving its location x

coordinate rearwards as the motor burn progressed. Table 4-8 summarizes these shape variation inputs.

Table4-8: *Shape variations* on fuel components of the Phoenix-1A

Component	Variation Property	Value
Nitrous	Length – Initial Value	1.484 m
Nitrous	Length – Time Limit	20 s
Nitrous	Length – Derivative	-0.0742 m/s
Nitrous	Location – Initial Value	$(1.81 \quad 0 \quad 0)\,m$
Nitrous	Location – Time Limit	20 s
Nitrous	Location – Derivative	$(-0.0371 \quad 0 \quad 0)\,m/s$
FuelGrain	Wall Thickness – Initial Value	0.053 m
FuelGrain	Wall Thickness – Time Limit	20 s
FuelGrain	Wall thickness – Derivative	-0.00265 m/s

The nominal trajectory inputs are summarized in Table 4-9 below. It should be noted that for simplicity, the nominal trajectory did not use wind inputs or a recovery system. The trajectory was thus ballistic. The fins were left un-canted to disable spin dynamics so that the basic pitching angular dynamics from the simulation could be observed. Table 4-10 presents salient flight performance parameters from the nominal trajectory using the thrust curve provided by Genevieve [4] which is shown in Figure 4-17. The nominal altitude history is shown in Figure 4-14 and the nominal speed history in Figure 4-15. Figure 4-16 shows the nominal pitch rate history. The trajectory did not have a significant yaw rate at any stage of flight in the absence of winds and the spin rate was nearly zero throughout the flight as the vehicle had un-canted fins.

Table 4-9: Nominal scenario inputs for Phoenix-1A ballistic trajectory

Input Parameter	Value
Launch Rail Angles	$(0° \quad 80° \quad -135°)$
Launch Coordinates	$(34.6°\,S \quad 20.3°\,E \quad 0\,m)$
Initial Velocity	$(0 \quad 0 \quad 0)\,m/s$
Thrust Input	Nominal Phoenix-1A PV-1 (Refer to Figure 4-17)
Launch Rail Length	7 m
Winds	None
Recovery System	Not used

Table 4-10: Nominal Phoenix-1A flight performance

Parameter	Value	Units
Apogee Altitude	15013.0	m
Maximum Speed	571.1	m/s
Maximum Acceleration	32.8	m/s^2
Flight Time (Ballistic)	125.9	s
Apogee Time	60.7	s
Splashdown Speed (Ballistic)	302.13	m/s
Rail Exit Speed	20.1	m/s
Rail Exit Time	1.22	s
Average Stability Margin(Ballistic)	0.60	m
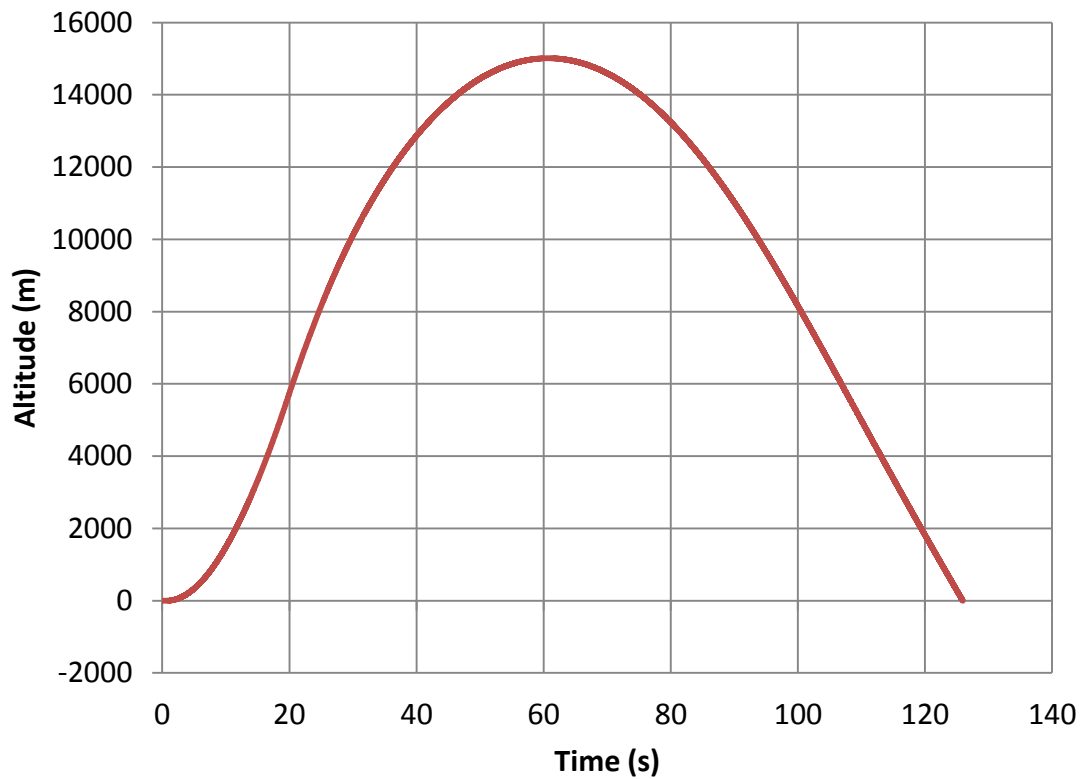
Figure 4-14: Nominal Phoenix-1A altitude history. The trajectory shape is classical for single stage sounding rockets.
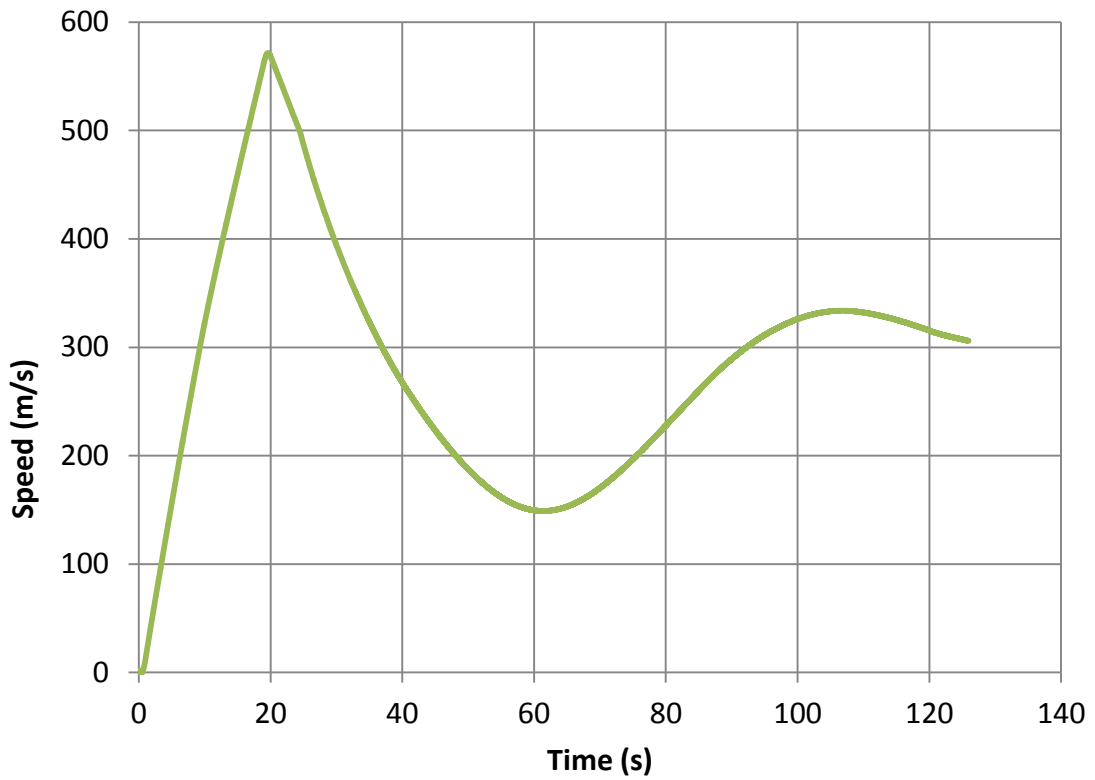
Figure 4-15: Nominal Pheonix-1A speed history. Note the burn out (approx. 20 s) velocity is medium supersonic and that the vehicle still maintains a horizontal 150 m/s speed at apogee.
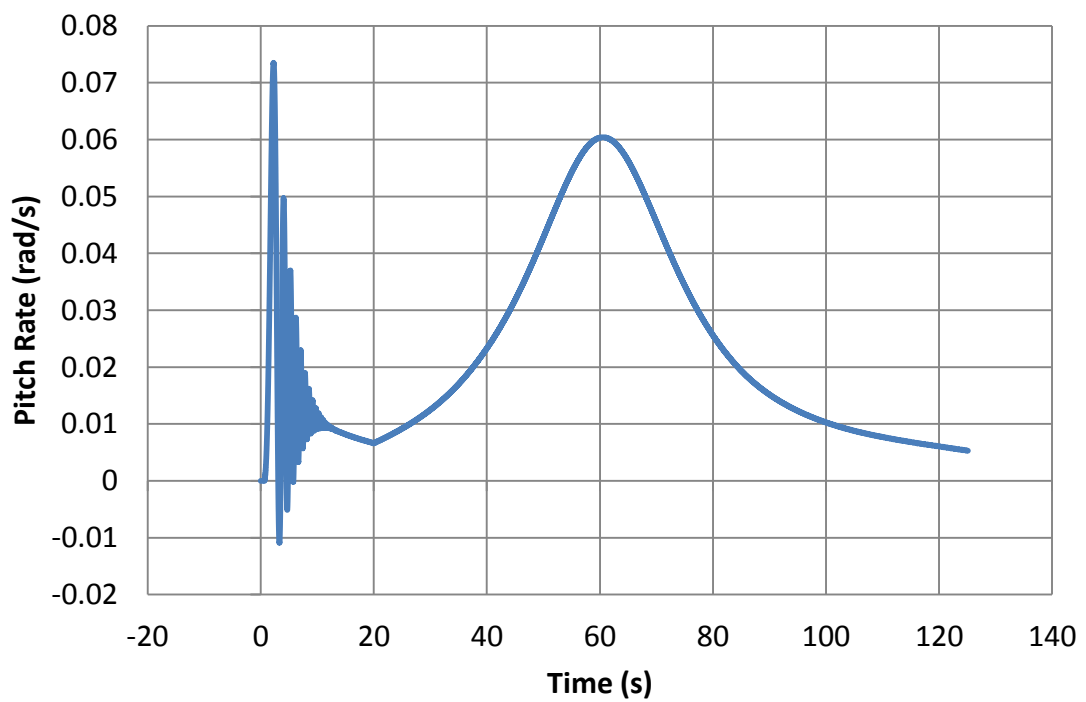
Figure 4-16: Nominal (un-spun) Phoenix-1A pitch rate history. Note the initial pitch oscillation before the vehicle becomes stable and follows a classic gravitational tip-over at apogee.
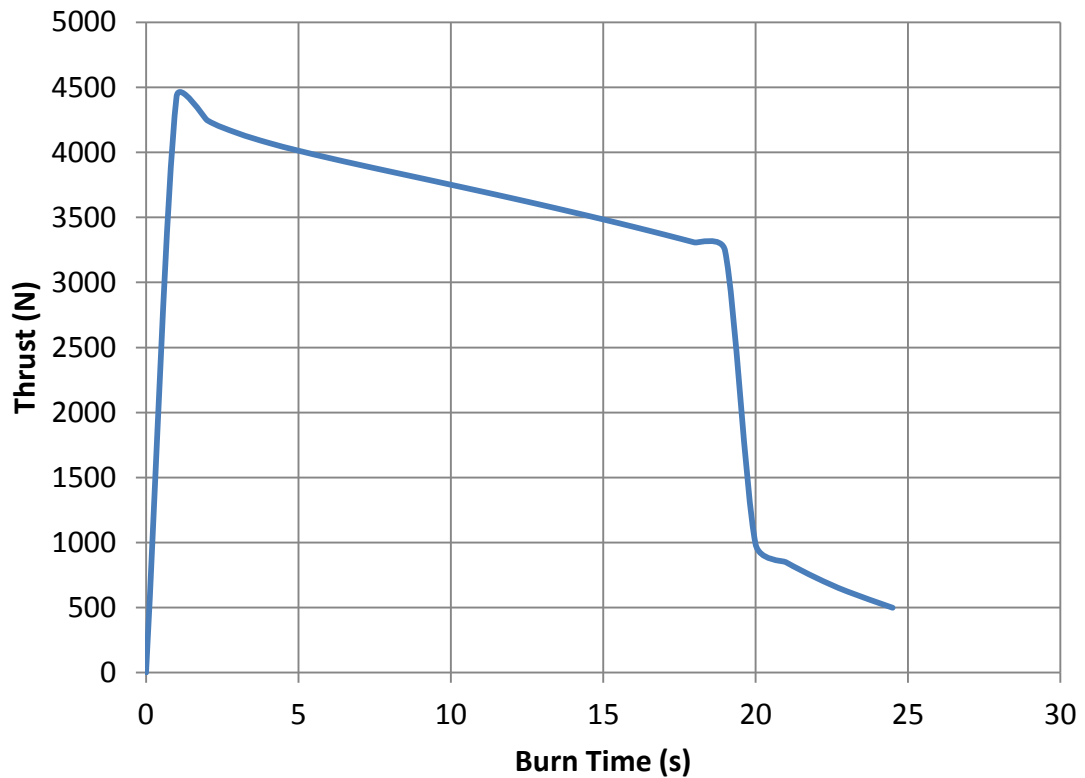
Figure 4-17: Phoenix-1A PV-1 nominal thrust curve used for Phoenix-1A nominal trajectory. Supplied by Genevieve [4]

4.7.3 Spherical, Rotating Earth Geodetic and Gravitational Models

There are several categories of orbits commonly used by artificial satellites of the Earth, including circular orbits (such as equatorial orbits and geostationary orbits) and elliptical orbits (such as polar orbits and sun-synchronous orbits). It was noted that under the spherical Earth assumption, the HYROPS software would be capable of modeling all these orbits with reasonable accuracy The HYROPS geodetic and gravitational models were validated by initializing the code with vehicles placed in low-earth orbit (LEO), with correctly pre-calculated position and velocity inputs to maintain orbital motion indefinitely. Simulations were then executed and it was determined whether the vehicles followed trajectories as predicted by the equations of orbital mechanics. The fundamental equations of elliptical orbital mechanics (Eq. 4-1 and Eq. 4-3) provide the orbital velocity v as a function of orbital radius r given the orbit semi-major axis a, orbital eccentricity e and orbital true anomaly angle θ. The orbital period P is given by Eq. 4-2 [53].

$$v = \sqrt{GM\left(\frac{2}{r} - \frac{1}{a}\right)}$$ (4-1)

$$P = 2\pi\sqrt{\frac{a^3}{GM}}$$ (4-2)

$$r = \frac{a(1-e^2)}{1+e\cos\theta}$$ (4-3)

The relevant input parameters for the orbital trajectories consisted only of the initial position coordinates and initial velocity vector. The launch altitudes of over 84 km did not necessitate the use of any specific launch angles as the absence of the atmosphere would not incur any aerodynamic effects. The Phoenix-1A vehicle was used with motor thrust magnitude set to zero so as to allow gravitational and apparent acceleration terms to solely govern the trajectory, although any vehicle with nonzero mass would have sufficed. The launch rail model was also disabled to ensure this. A large time step of 0.25 s was used to ensure flight times great enough to complete multiple orbits without expending the software memory. Table 4-11 summarizes the inputs for the orbital scenarios. It was found that in all cases the trajectories resulted in multiple orbits with the correctly predicted orbital period, apogee and perigee altitudes and ground track drifts resulting from the Earth's daily rotation. Figure 4-18, 4-19 and 4-20 show HYROPS screenshots of the output equatorial circular, polar circular and elliptical trajectories respectively. The geostationary trajectory could not be visualized as it does not produce a ground track or trajectory. The elliptical orbit perigee altitude and orbital period was verified using Eq. 4-3 and Eq. 4-2 respectively.

Equation 4-1 was used to calculate the Northward (Earth-fixed frame x direction) speed needed to set the vehicle into a circular polar orbit. In the circular case, the semi major axis equals the orbital radius which is simply the sum of the Earth radius and launch altitude. The resulting linear speed was found to be 7790 m/s. For the equatorial orbit, the Eastward speed had to be compensated for the angular velocity of the Earth, $7.292 \times 10^{-5}\ rad/s$, which at 200 km altitude would impart an extra 479 m/s of linear speed in the Easterly direction to the vehicle. Therefore, the launch speed in this case was reduced to 7310.918 m/s. The elliptical orbit was chosen with an arbitrary initial velocity in the Northeasterly direction to validate if the Coriolis cross-coupling terms were implemented correctly. The geostationary orbit was simulated in a similar fashion to the circular orbit, except that a zero velocity was applied at the orbital radius at which the Eastward velocity due to the Earth's rotation would be canceled out. This radius was thus calculated by equating the circular orbital velocity to the linear velocity due to the

Earth's rotation (Eq. 4-4).The requisite radius was found to be 42167.942 km and the corresponding altitude was 35797.942 km. As expected, the vehicle was found to remain stationary with respect to the Earth fixed frame under these conditions, thus correctly simulating a geostationary satellite on the Equator. Note that the zero initial velocity input is required as the initial velocity input in HYROPS is referred to the Earth fixed frame and not the inertial frame.

$$\sqrt{\frac{GM}{r}} = \Omega_t r \qquad (4\text{-}4)$$

Table 4-11: Orbital validation test scenario input summary

Scenario	Launch Coordinates(L_g L_t)	Launch Altitude (km)	Launch Velocity (m/s)
Polar Circular	($0° E$ $90° N$)	200.0	(7790.003 0 0)
Equatorial Circular	($0° E$ $0° N$)	200.0	(0 7310.918 0)
Elliptical	($0° E$ $0° N$)	200.0	(7000 4000 0)
Geostationary	($0° E$ $0° N$)	35797.942	(0 0 0)
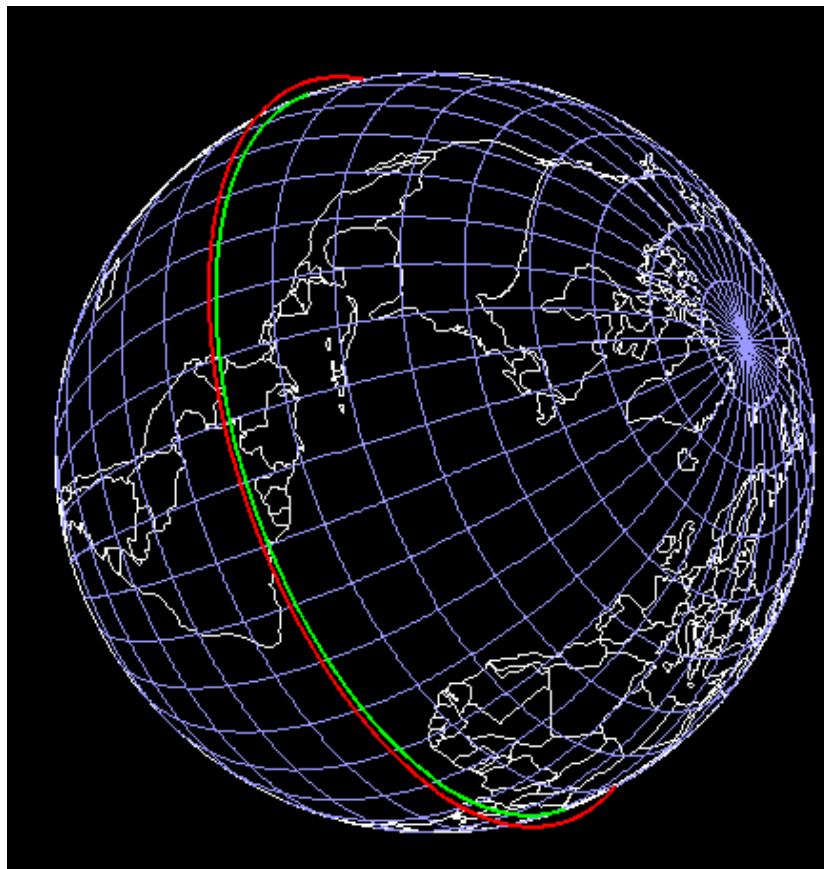
Figure 4-18: Equatorial orbit at 200 km altitude. Flight Path in red and ground track in green.
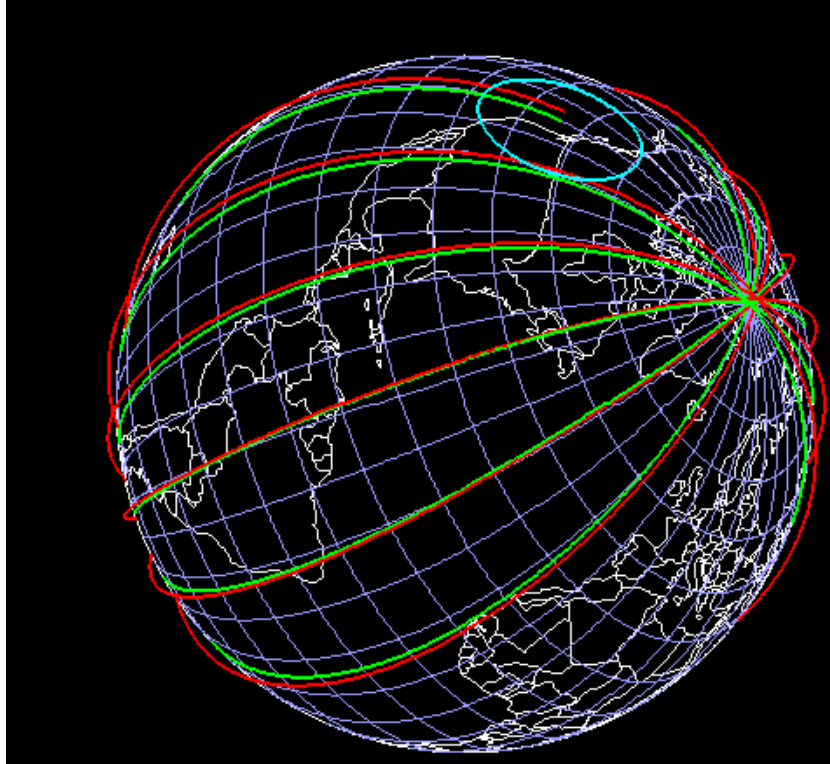
Figure 4-19: Polar orbit at 200 km altitude. Flight Path in red and ground track in green.
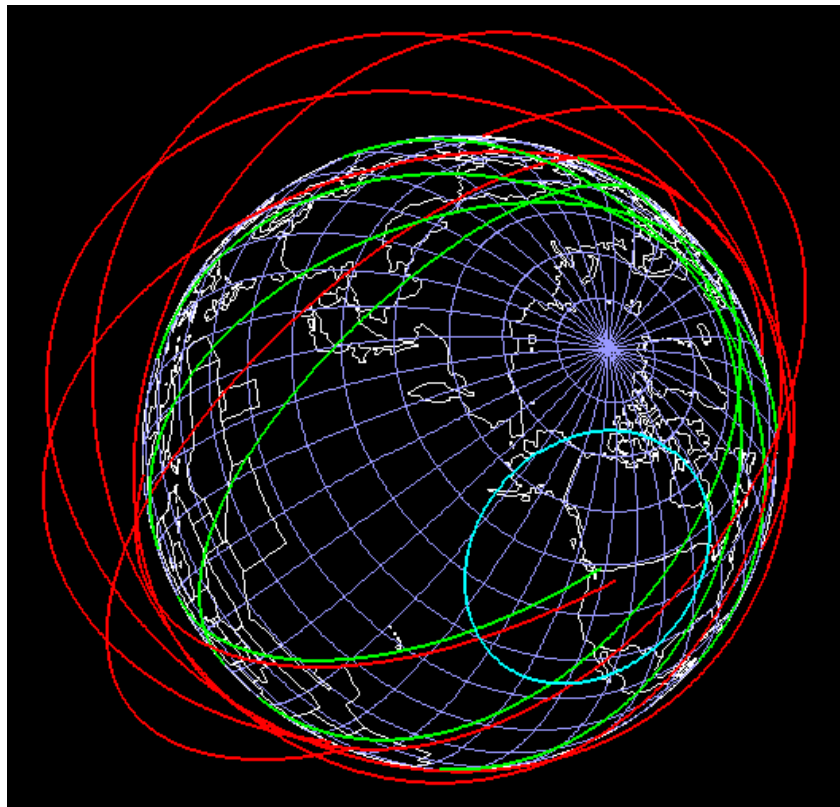
Figure 4-20: Elliptical orbit with 200 km perigee in a Northeasterly flight path. Flight Path in red and ground track in green.

4.7.4 Wind Effects

The effect of winds on the dynamic aerodynamic response is crucial in the understanding of the dynamic stability of a sounding rocket. The prediction of the wind induced deviation in the trajectory shape and splashdown point is also beneficial for the vehicle recovery process. Both the gradient wind profile and monthly wind table data were tested on the spinning Phoenix-1A nominal vehicle with an 80° launch elevation angle and 3750 N, 20 s burn thrust profile. The effect of a jet stream was also included with the gradient model. The gradient wind input used a Northerly 1 m/s ground level wind with a wind magnitude increase of 1 m/s per kilometer of altitude up to 20 km. An Easterly 50 m/s jet stream was used between 10 km and 15 km altitude. The Denel OTR supplied January and July wind profiles for the OTR area were used from the monthly wind tables. All runs used a southeasterly (-135°) launch azimuth from the OTR at sea level.

Figure 4-21 shows the resulting altitude histories whilst Figures 4-22 and 4-23 show the ground track histories and vehicle elevation angle histories respectively. Note the unique deflections in the vehicle elevation angle as it passes through the jet stream (flight times 30 s to 50 s ascending and 73 s to 93 s descending) in the Gradient + Jet Stream scenario (green curve). This is a manifestation of the jet stream induced angle of attack. It was very apparent from the results that small wind gradients do not cause significant deviations in the trajectory as they do not produce large angles of attack. This remains true even for a jet stream of maximum speed 50 m/s (180 km/h) as this speed differential is reached over an altitude range of 2500 m. However, sharp changes in winds at certain altitudes present in the January OTR wind data would cause significant deviations despite the wind speed remaining relatively low. This effect is more prominent at low altitudes during the ascent phase as the smaller aerodynamic velocities in the initial phases of flight tend to produce larger angles of attack for a given wind speed.
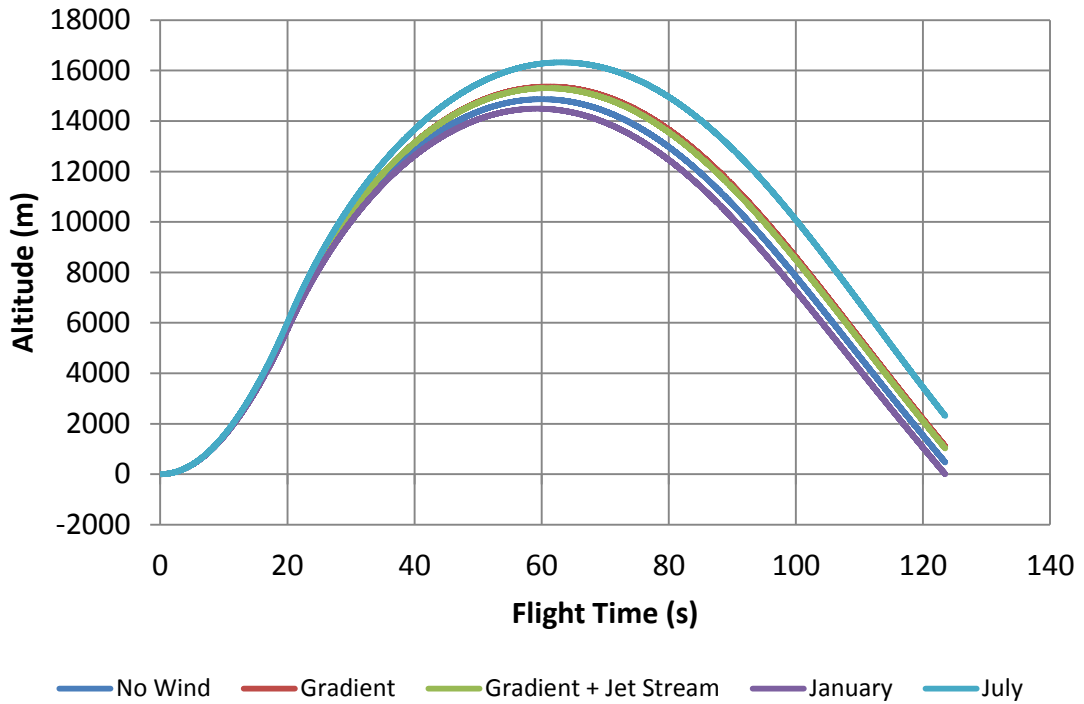
Figure 4-21: Altitude histories of the Phoenix-1A subjected to the various wind scenarios. Note that the two monthly wind profiles six months apart cause an apogee altitude difference of approximately 10 %, highlighting the need for wind modeling.
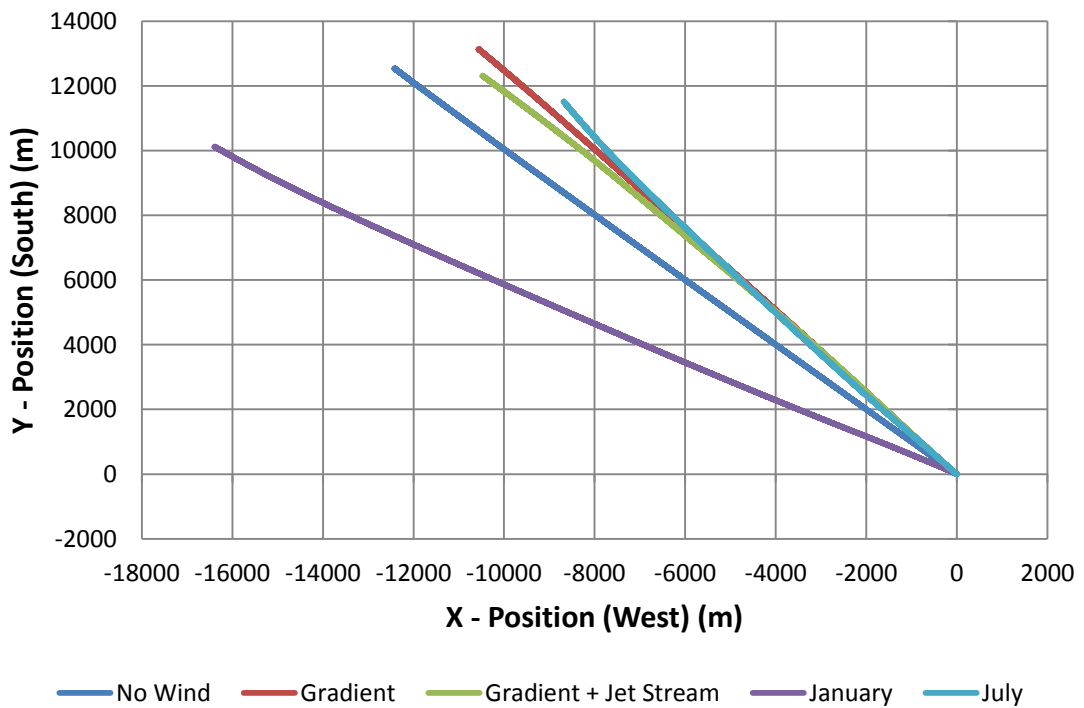
Figure 4-22: Ground tracks of the Phoenix-1A subjected to the various wind scenarios. The launch point is the inertial origin at (0   0).
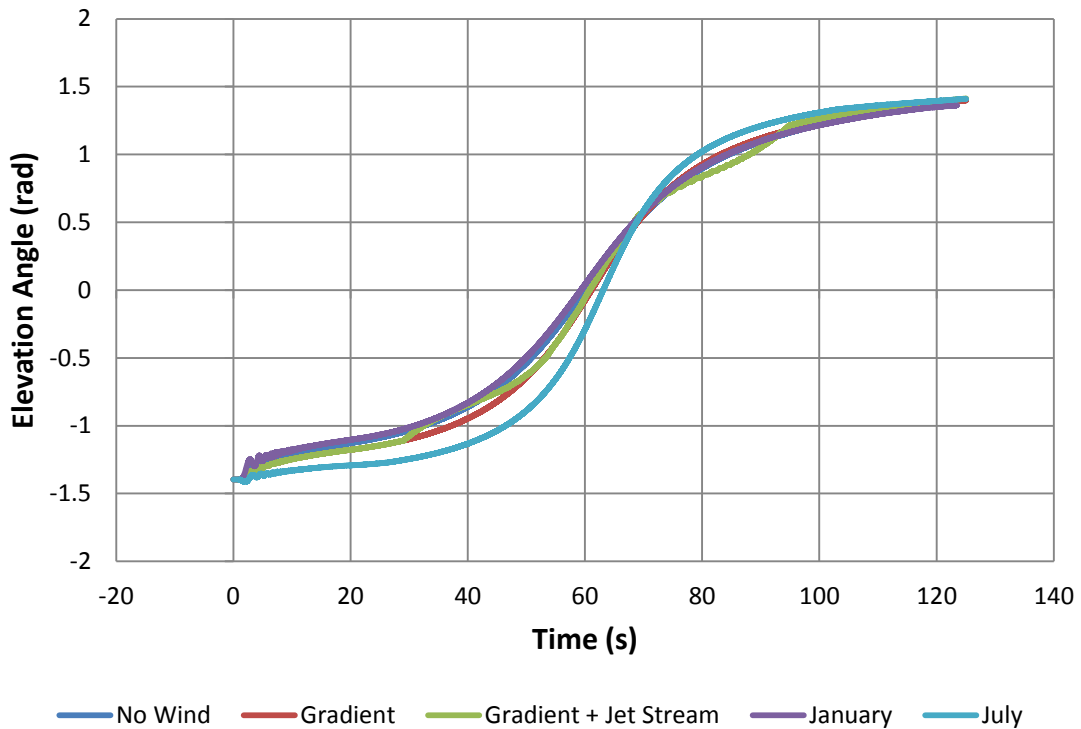
Figure 4-23: Elevation angle histories of the Phoenix-1A subjected to the various wind scenarios.

4.7.5 Parachute Recovery Dynamics

The dual-parachute recovery feature of the HYROPS tool was tested for terminal velocity prediction on the Phoenix-1A design. The effect of various winds on the parachute kinematic behavior was also investigated. The Phoenix-1A nominal trajectory was run with dual recovery under a combination of a gradient wind and a jet stream. The gradient wind was Northerly with a gradient of 1 m/s per kilometer of altitude up to an altitude of 20 km. The jet stream was of maximum speed 30 m/s, applied between 10 km and 15 km altitude at a southeasterly bearing of 160°. The parachute drag coefficients were varied about their nominal design values and the effects observed. Table 4-12 summarizes these inputs and presents the output splashdown speeds and drift ranges. Figure 4-24 displays the visualization of the resulting trajectories in Google Earth and Figure 4-25 displays a similar screenshot from HYROPS. The results exhibit trends as expected, with larger drag coefficients causing slower splashdown speeds but incurring more drift. The results also indicated that the nominal parachutes would give the Phoenix-1A a rather hard splashdown at 9 m/s which would be unsuitable for a splashdown on land.

107
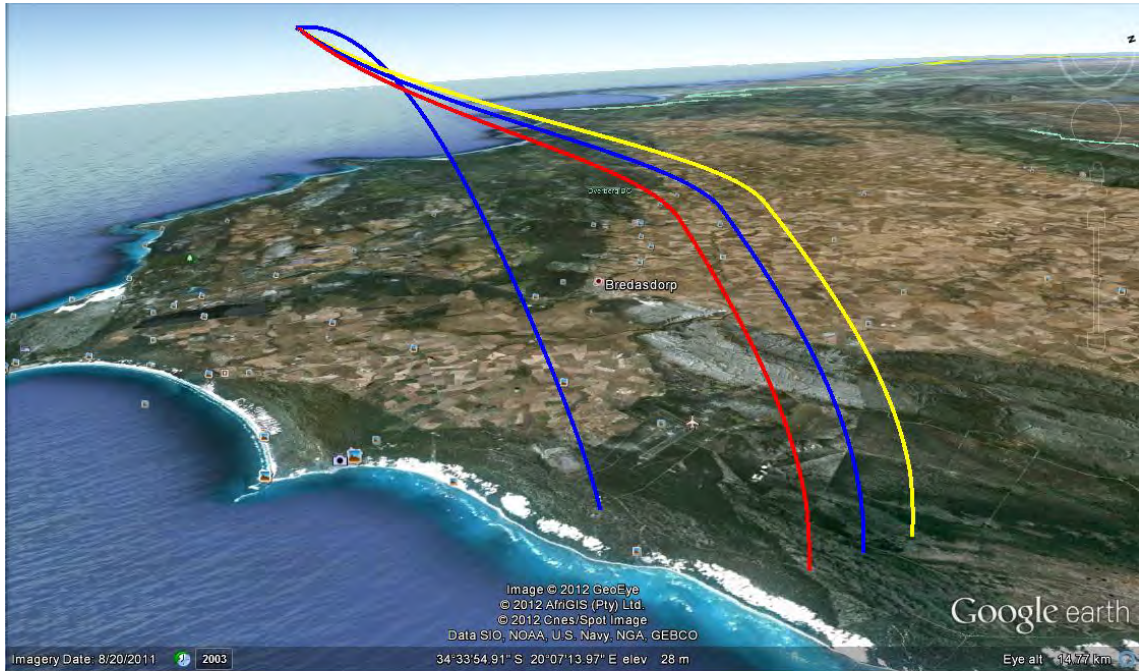
Figure 4-24: Google Earth visualization of three parachute recovery simulation scenarios using a combination of gradient wind and jet stream.

Table 4-12: Recovery system dynamics study results summary

Scenario	Drogue	Main	Splashdown (m/s)	Drift (km)	Flight Time (s)
1	1.29	2.92	10.2	9.1	1338
2	0.75	1.50	14.2	6.7	1027
3	1.00	4.00	8.7	7.8	1240

It was found that the parachute simulation failed to remain stable when subjected to monthly winds profiles provided by Denel OTR. The large wind gradients found in these profiles was found to be the primary reason for these instabilities. The simplistic parachute aerodynamic model was incapable of generating the correct moments for returning the system to a stable angle of attack region after the sharp wind gradients had induced large angles of attack.
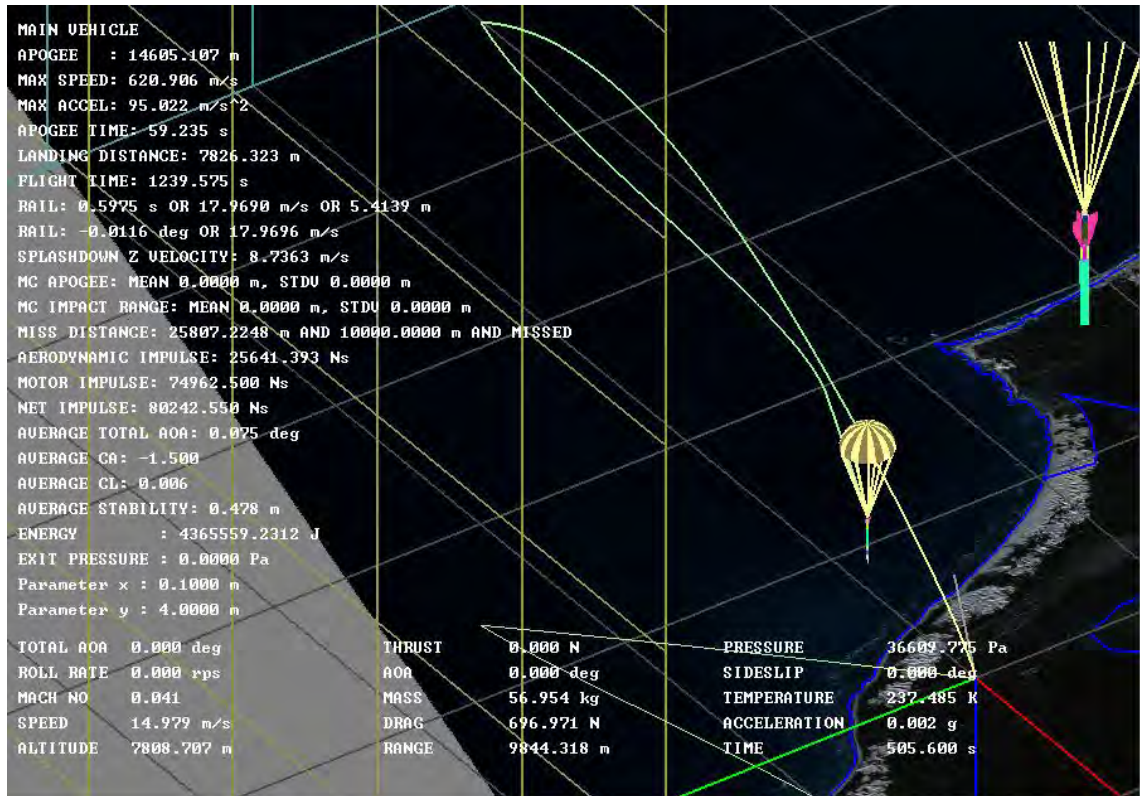
Figure 4-25: HYROPS screenshot of parachute descent simulation scenario 3 as described in Table 4-11. Note that the descending trajectory changes direction sharply at 10 km altitude, as the vehicle leaves the jet stream.

4.7.6 Monte Carlo Statistical Treatment

The Monte Carlo uncertainty modeling feature was used to generate splashdown probability footprints for the nominal Phoenix-1A.The Monte Carlo feature was used to estimate the effectiveness of spin stabilization in reducing ballistic splashdown dispersion in the vehicle. Thrust misalignments and aerodynamic asymmetries are the primary causes of dispersion in unguided rocket flight. A study using 200 Monte Carlo runs was conducted and the results demonstrated a marked reduction in statistical dispersion of the spinning Phoenix-1A in comparison with the un-spun Phoenix-1A subjected to equal thrust misalignment uncertainties. Small misalignment angles of 0.05° and 0.1° were chosen to test the system sensitivity. Figure 4-26 and Figure 4-27 show the splashdown footprints wherein it is apparent that spin reduces the dispersion of the impact point significantly. Histograms of the impact point distributions are given for each combination of spin and thrust misalignment in Figure 4-28, Figure 4-29, and Figure 4-30 and Figure 4-31. The results demonstrated a clear tendency of the spinning vehicle to reduce the standard deviation in impact range across the batch, although a small bias on the mean value is also introduced. Table 4-13 summarizes the resulting statistics.
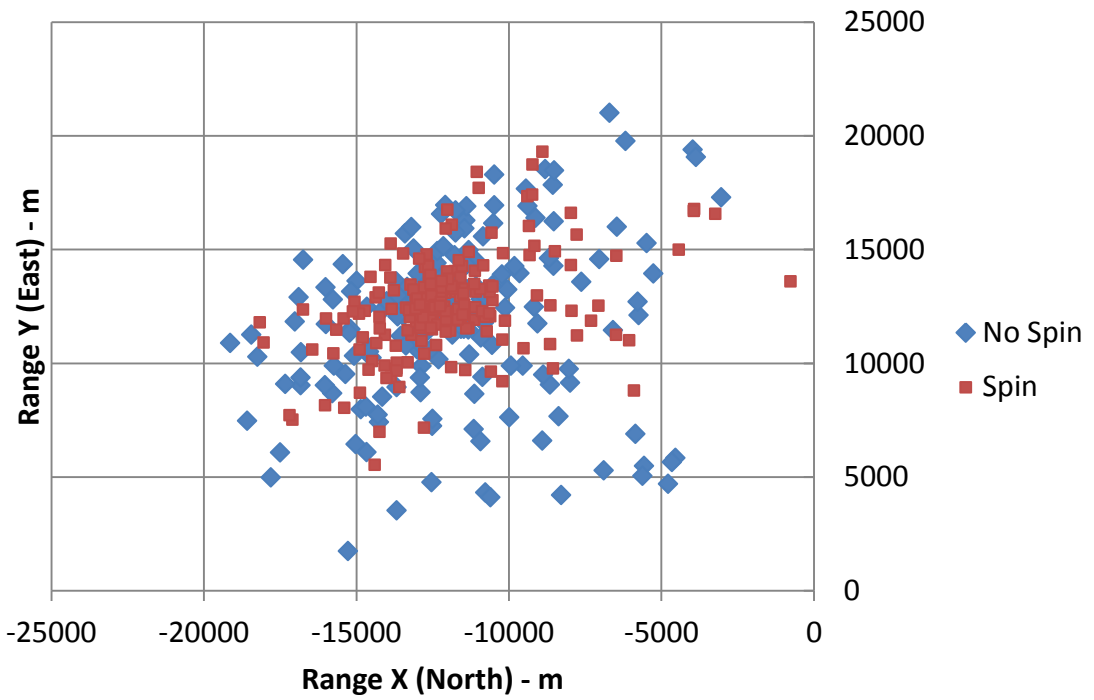
Figure 4-26: 200 run Monte Carlo impact point distribution for 0.1° thrust misalignment
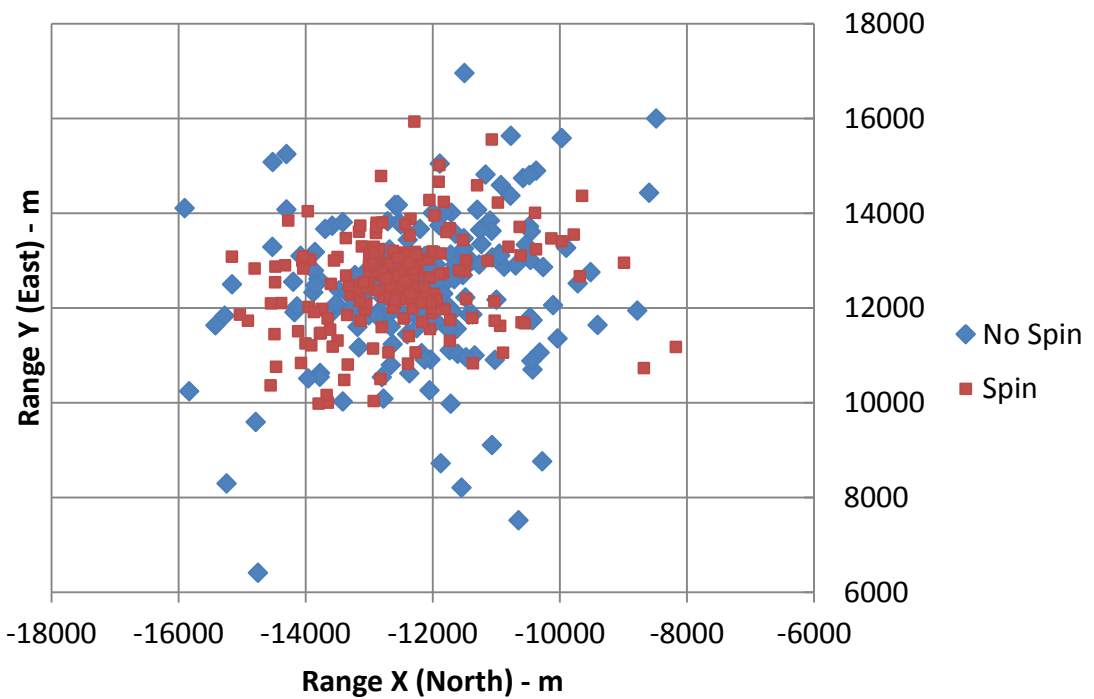
Figure 4-27: 200 run Monte Carlo impact point distribution for 0.05° thrust misalignment
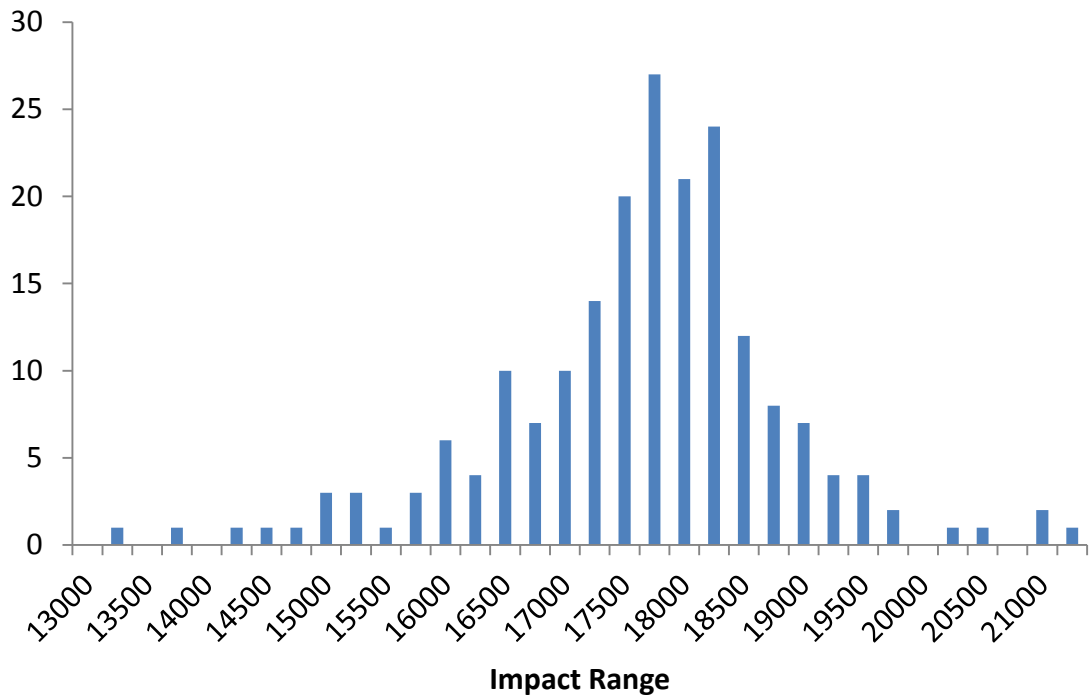
Figure 4-28: Impact range histogram for no spin scenario, 0.05° thrust misalignment
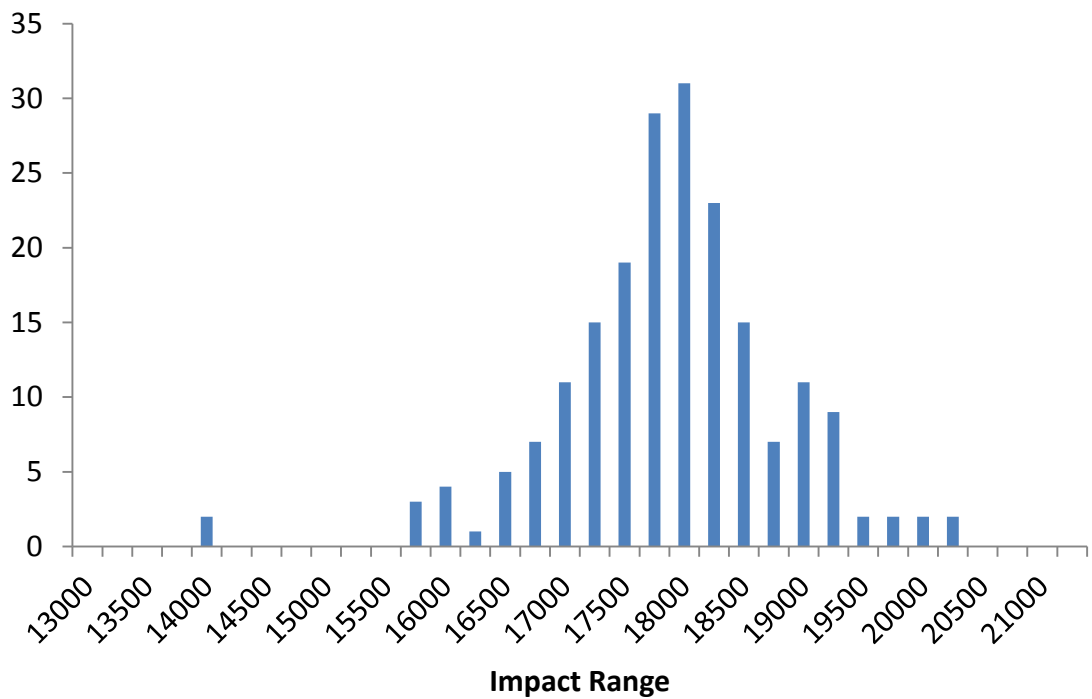
Figure 4-29: Impact range histogram for spinning vehicle scenario, 0.05° thrust misalignment
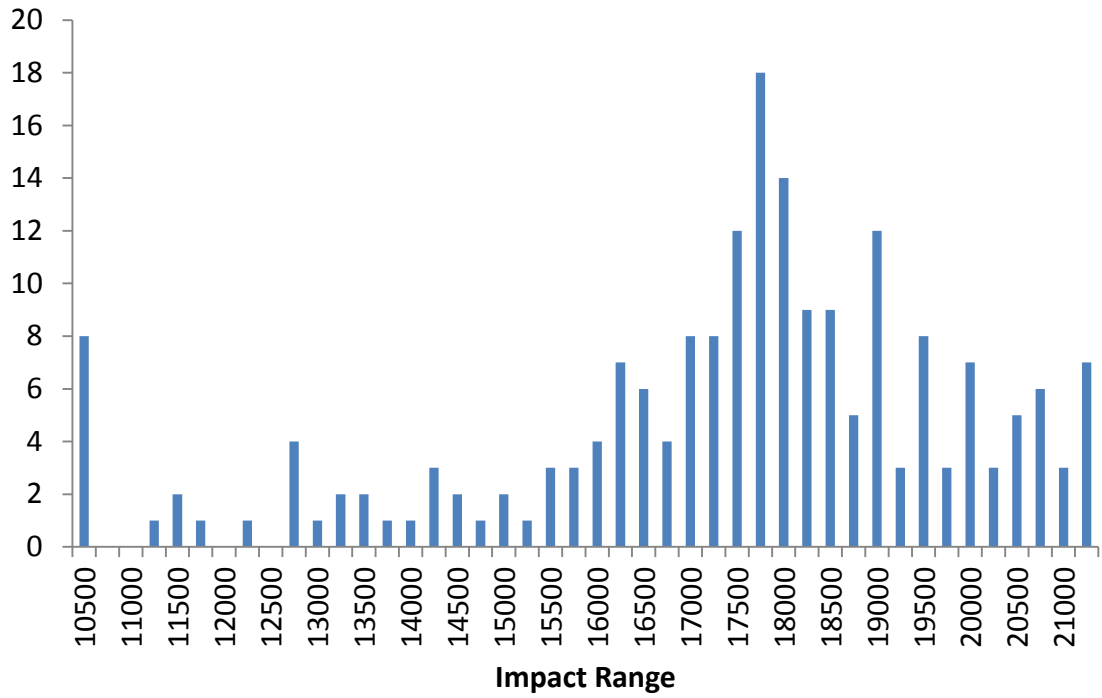
Figure 4-30: Impact range histogram for no spin scenario, 0.1° thrust misalignment
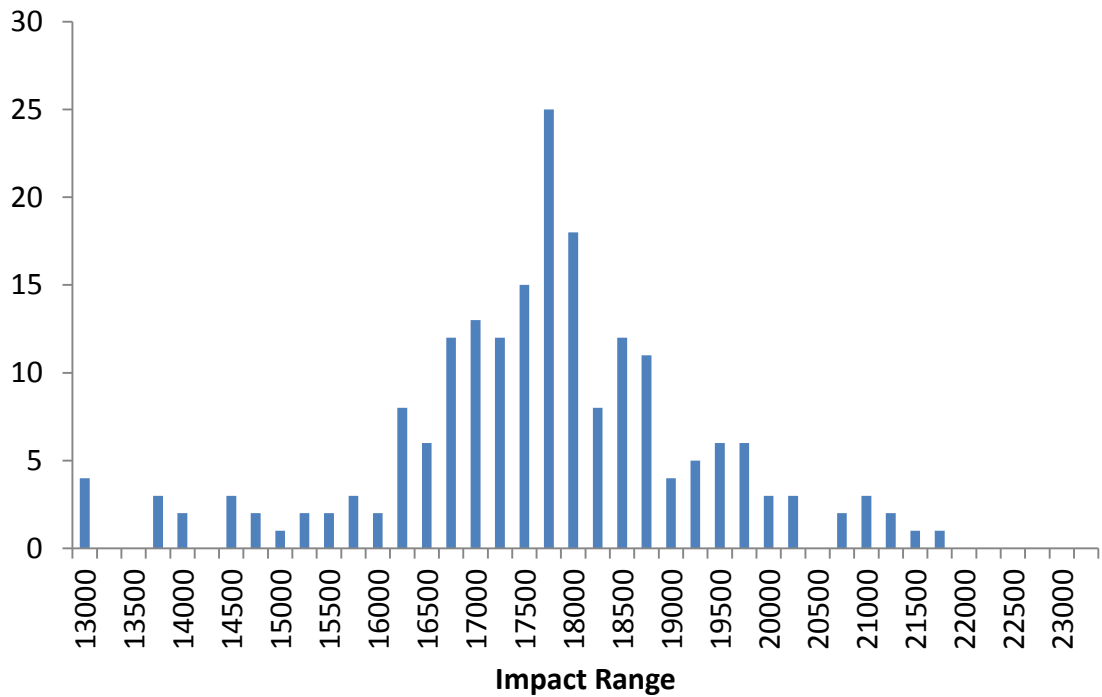
Figure 4-31: Impact range histogram for spinning vehicle scenario, 0.1° thrust misalignment

Table 4-13: Monte Carlo thrust misalignment induced dispersion mitigation using spin

	Standard Deviation (m)			
	Apogee		Impact Range	
Thrust Misalignment (Standard Deviation)	0.05°	0.1°	0.05°	0.1°
No Spin	534.3	1089.1	1220.6	2873.7
Spin	401.7	748.5	929.9	1675.1
% Reduction	**24.8**	**31.3**	**23.8**	**41.7**

It was noted that spin reduced dispersion further for the larger thrust misalignment angles. The results demonstrated that the greater engineering effort incurred in the development and modeling of all the six degrees of freedom are justifiable when high-fidelity dynamic effects such as non-ideal vehicle dynamics must be predicted.

The results from the study also indicated that even very small misalignment angles could cause significant dispersion in the trajectory if the misalignment is maintained at a single radial direction over the entire flight. This causes deviations to build up over the motor burn. The results are somewhat pessimistic as real rocket motors often experience much larger misalignment angles but these are almost never constant at a single radial direction but are rather known to vary in radial direction randomly. This does not eliminate dispersion entirely as a bias component may exist such that deviations build up over time and cause a significant deflection in overall flight path.

4.7.7 Vehicle Optimization

The effectiveness of the HYROPS optimization functionality was evaluated on the Phoenix-1A design by the introduction of several key design variables. Given that the vehicle diameter was designed around the flight-weight oxidizer tank, it was necessary to vary the oxidizer tank diameter to determine the optimal length-to-diameter ratio for the vehicle given a requisite fixed oxidizer tank volume. Another unknown in the design was the nose length to base-diameter ratio (i.e. fineness ratio). Whilst it is known that larger fineness ratios produce lower pressure drag, it was not known whether this benefit would outweigh the added surface friction drag from the larger surface area noses with larger fineness ratios would produce. In addition, larger fineness ratios would produce longer noses for a given nose base diameter and hence add extra mass. Therefore, the nose fineness ratio was also optimized. A third unknown was the fin span. The effect of larger fin area on overall dynamic stability and incidence angle minimization

would counteract the added mass of larger spanning fins. This nature of this tradeoff on apogee performance was also unknown and hence it was added to the list of key design variables given in Table 4-14. The resulting design *effects* needed to implement the optimization are presented in Table 4-15.

Table 4-14: Phoenix-1A optimization study - Key design variables

Key Design Variable	Symbol	Range	Initial Value	Optimal Value	Units
Oxidizer Tank Diameter	D	$0.15 \leq D \leq 0.25$	0.2	0.179	m
Nose Fineness Ratio	F	$3 \leq F \leq 7$	5	3.9	N/A
Fin Span	S	$0.15 \leq S \leq 0.25$	0.2	0.198	m

The nominal Phoenix-1A vehicle was optimized for maximum apogee altitude using these key variables, yielding a maximum apogee altitude 16726 m, 11.65 % greater than the original nominal apogee altitude of 14 980 m. Population size per generation was limited to 100 to test the algorithm robustness. The study used a mutation rate of 0.02 (2%) and a *BLX-α* parameter of 0.25. These were chosen based on recommendations from the literature [45]. Only five generations were run to investigate whether the algorithm can generate a solution swiftly.

Table 4-15: Effects used for Phoenix-1A optimization study

Effect Type	Formula	Parameter 1	Parameter 2
Structural - Dimension	D/2	TankShell	Outer Radius
Structural - Dimension	0.064/(D*D)	TankShell	Length
Structural - Location	1.05+(0.032/(D*D))	TankShell	X
Structural - Dimension	0.03*D	TankShell	Wall Thickness
Structural - Dimension	D/2	Taper	Base Radius
Structural - Dimension	(D/2)-(0.03*D)	TankEnds1	Radius
Structural - Dimension	(D/2)-(0.03*D)	TankEnds2	Radius
Structural - Location	1.05+(0.032/(D*D))-0.009	TankEnds2	X
Structural - Dimension	D/2	MainBay	Outer Radius
Structural - Dimension	D/2	DrogueBay	Outer Radius
Structural - Dimension	D/2	FCBay	Outer Radius
Structural - Dimension	(D/2)-0.002	Skirting	Outer Radius
Structural - Dimension	(D/2)-0.002	Sleeve	Outer Radius

Effect Type	Formula	Parameter 1	Parameter 2
Structural - Dimension	D/2	Nose	Base Radius
Structural - Dimension	(D/2)-0.004	MainBulkhead	Radius
Structural - Dimension	(D/2)-0.004	DrogueBulkhead	Radius
Structural - Dimension	(D/2)-0.004	FCBulkhead	Radius
Structural - Dimension	0.45*D	MainParachute	Radius
Structural - Dimension	0.45*D	DrogueParachute	Radius
Structural - Location	1.2+(0.064/(D*D))	DrogueBay	X
Structural - Location	1.45+(0.064/(D*D))	FCBay	X
Structural - Location	1.75+(0.064/(D*D))	MainBay	X
Structural - Location	1.95+(0.064/(D*D))	Nose	X
Structural - Location	1.3535+(0.064/(D*D))	DrogueBulkhead	X
Structural - Location	1.2535+(0.064/(D*D))	FCBulkhead	X
Structural - Location	1.9535+(0.064/(D*D))	MainBulkhead	X
Structural - Location	1.2+(0.064/(D*D))	DrogueParachute	X
Structural - Location	1.75+(0.064/(D*D))	MainParachute	X
Structural - Location	1.2035+(0.064/(D*D))	Skirting	X
Structural - Location	1.6+(0.064/(D*D))	Sleeve	X
Structural - Location	2.15+(0.064/(D*D))	Payload	X
Structural - Location	1.45+(0.064/(D*D))	Electronics	X
Structural - Dimension	(D/2)-(0.03*D)	Nitrous	Radius
Structural - Dimension	(0.95*(0.064/(D*D)))-0.009	Nitrous	Length
Shape Variation - Initial Parameter Value	(0.95*(0.064/(D*D)))-0.009	Nitrous	Length
Shape Variation - Parameter Derivative	(0.009-(0.95*(0.064/(D*D))))/20	Nitrous	Length
Shape Variation - Initial Location	1.068+(((0.95*(0.064/(D*D)))-0.009)*0.5)	Nitrous	X
Shape Variation - Location Derivative	(((0.95*(0.064/(D*D)))-0.009)*0.5)/20	Nitrous	X
Structural - Dimension	0.5*D	Payload	Breadth
Structural - Dimension	0.5*D	Payload	Height
Structural - Dimension	0.25*D	Electronics	Breadth
Structural - Dimension	0.25*D	Electronics	Height

Effect Type	Formula	Parameter 1	Parameter 2
Aerodynamic - Nose Radius	D/2	Stage 1	N/A
Aerodynamic - Fuselage Segment Length	(0.064/(D*D))+0.9	Stage 1	Segment 1
Aerodynamic - Fuselage Segment Radius	D/2	Stage 1	Segment 1
Aerodynamic - Reference Area	3.14159*D*D*0.25	Stage 1	N/A
Structural - Dimension	D*N	Nose	Length
Aerodynamic - Nose Length	D*N	Stage 1	N/A
Staging - Total Length	1.95+(0.064/(D*D)) +(D*N)	Stage 1	N/A
Structural - Dimension	0.12/S	Fins	Root Chord
Structural - Dimension	0.04/S	Fins	Tip Chord
Structural - Dimension	S	Fins	Wing Span

The result of the optimization study indicated that the initial Phoenix-1A design had been designed around a larger than optimal diameter of 200 mm whereas the optimal diameter was around 180 mm. The nominal nose fineness ratio of 5 was found too high. The algorithm output a nose fineness of 3.9, such that the nose drag reduction over a fineness 3.9 nose by the nominal nose was insufficient to offset the added mass of the longer nominal nose. The nominal fin span of 200 mm was found to suit the vehicle design well. The nominal and optimized airframes are visually compared in Figure 4-32. It is interesting to note that the transonic area rule effect is eliminated in the optimized airframe as the main fuselage diameter converges to the motor combustion chamber diameter of 180 mm. This is just one example of how the fidelity of the subsystems modeling ultimately determines the validity of the optimization results. In this study, either the aerodynamic modeling was not of high enough fidelity to capture the area rule effect or the effect itself had a weaker influence on the apogee altitude than other more significant factors such as overall mass and skin friction drag.
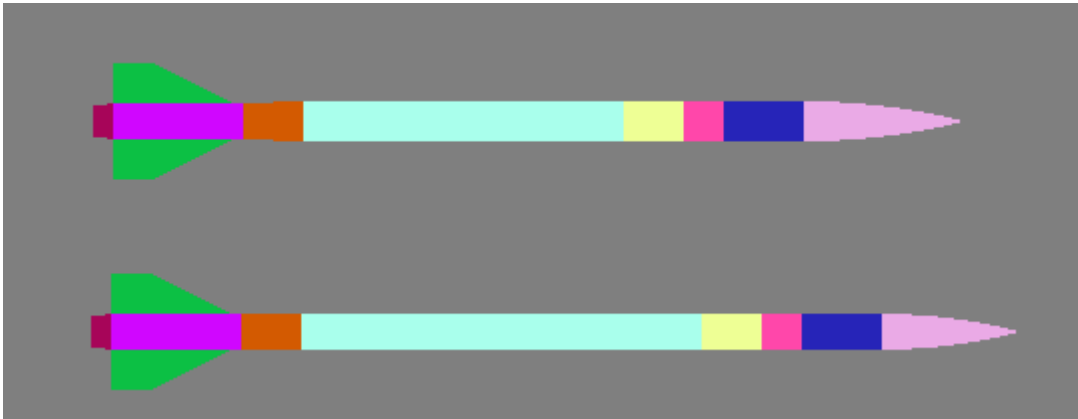
Figure 4-32: Comparison of the nominal Phoenix-1A (top) and the optimized Phoenix-1A (bottom) rendered in side view in HYROPS.

It is insightful to observe the evolution of population fitness statistics as the genetic algorithm progresses through generations. It was noted that the average of the fitness function, in this case the apogee altitude, increased in an approximately linear fashion throughout the five-generation run, suggesting that five generations was perhaps too few and that running more generations of the algorithm could improve the vehicle further. However, a similar look at the maximum apogee altitude as a function of generation number revealed a plateau after five generations. Further generations would thus increase the average fitness of the population but would leave the optimal solution relatively unchanged. Figure 4-33 plots the average and maximum apogee altitude against the generation number.
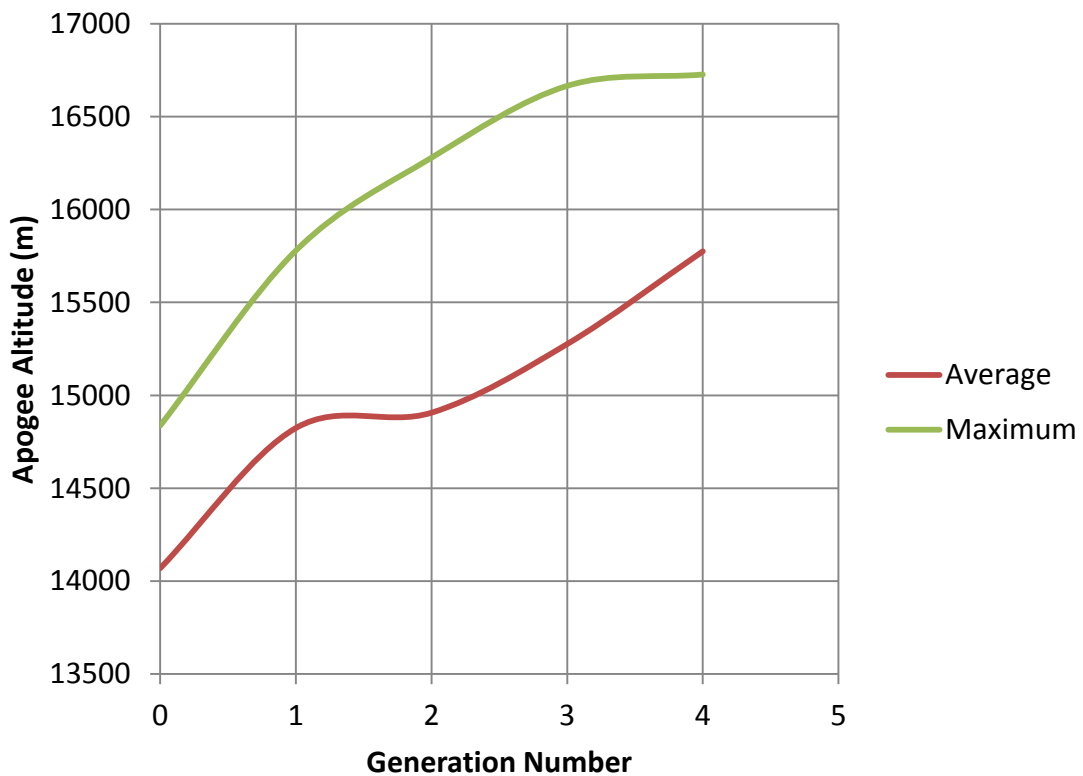
Figure 4-33: Average and maximum apogee altitude evolution as progressive generations are run in the genetic algorithm.

4.7.8 Launch-Rail Length Sensitivity

The minimum length of launch rail required to safely launch the Phoenix-1A was an unknown, being coupled to the vehicle's aerodynamic performance. A longer launch rail would allow the vehicle to leave the rail with a higher aerodynamic velocity. It was not known at what speed the aerodynamic effectiveness of the fins would make the vehicle reliably statically stable. A launch-rail length sensitivity study was conducted to investigate the issue. The study used the nominal Phoenix-1A configuration with a sea-level based, south-easterly, 80° elevation launch direction. The nominal 20 s burn time, 3750 N ramped thrust function was also used. Wind disturbances were suppressed to make the effect of the launch rail length apparent, although wind effects could be significant sources of destabilization in early flight. The rail length was varied from 0 m (no launch rail) to 15 m in 1 m increments. This resulted in a corresponding apogee altitude variation from 14175 m to 15102 m, indicating that the use of launch rail may lead to an increase in apogee altitude of up to 6 %. Significantly, it was also noted that the absence of a launch rail did not cause the vehicle to experience instabilities early during flight. Figure 4-34 shows the apogee altitude and landing distance sensitivity. It was decided that a 7 m

launch rail would be adequate for the Phoenix-1A whilst remaining within the cost and weight constraints of the vehicle's mobile launch platform.
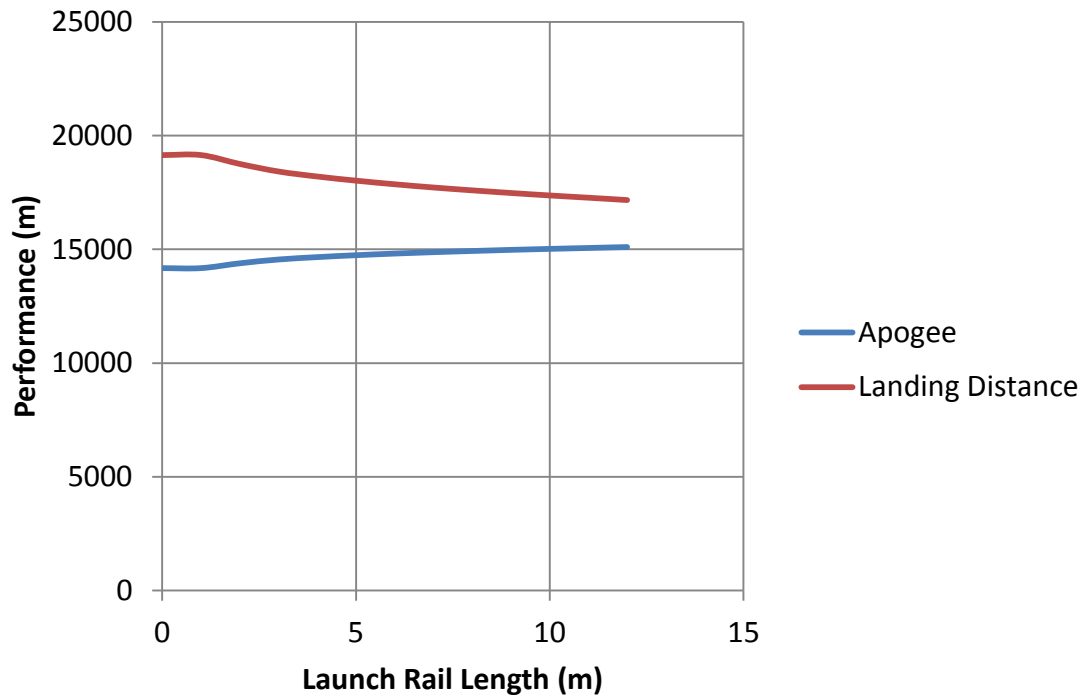
Figure 4-34: Apogee and landing distance sensitivity due to launch rail length variation.

CHAPTER 5

Sounding Rocket Aerodynamics

5.1 Introduction

Aerodynamic forces are a reaction from a body's motion through the Earth's atmosphere. Almost all sounding rockets are launched from the Earth's surface and must fly through layers of the atmosphere during ascent to the required altitude. Sounding rocket aerodynamic design aims to tailor the vehicle's airframe characteristics to achieve the specified flight performance whilst keeping the airframe design within the technical and logistic constraints imposed by overall vehicle design problem. Aerodynamic behavior is invariably coupled to other aspects of the vehicle design such as the aero-structure and propulsion system. This chapter describes a sampling of methods selected for the aerodynamic analysis of sounding rockets, along with some high-level results. These methods were selected from the vast pool of methods that have been developed over the decades and there remains significant scope for improvement and refinement through the exploration of the various alternative techniques. An overview of the application of the chosen methods, in conjunction with the HYROPS tool, in the trajectory simulation of sounding rockets is also provided. A review of the design know-how, gathered from the literature, regarding the qualitative design of a sounding rocket airframe's major components is given. Their application to the design of the Phoenix-1A airframe is also discussed briefly.

5.2 A Brief Review of Methods of Aerodynamic Analysis

5.2.1 Analytical Solution

The airflow over the external geometry of a sounding rocket is governed by the Navier-Stokes equations for Newtonian fluids (Eq. 5-1), which describe the dynamics of a continuum of fluid due to the conservation of mass, momentum and energy. They are highly coupled, non-linear partial differential equations which do not possess a general closed-form solution. Analytical solutions are known only for a very limited set of simple geometries for dimensionally reduced steady state flows such as the two dimensional cross-flow around a cylinder. Additional simplifications such as the neglect of viscous effects may also allow solution using advanced mathematical techniques over more complex domains, as in the panel method. However, for all

practical purposes, the analytical solution of the complete equations over the domain of a
sounding rocket airframe remains impossible.

$$\rho \left(\frac{\partial \boldsymbol{v}}{\partial t} + \boldsymbol{v} \cdot \nabla \boldsymbol{v} \right) = -\nabla p + \mu \nabla^2 \boldsymbol{v} + (\mu + \mu^v) \nabla (\nabla \cdot v) + \boldsymbol{f} \qquad \text{(5-1)}$$

5.2.2 Wind Tunnel Tests

The inherent complexity of the fluid flow around a sounding rocket airframe favors empirical
rather than analytical investigation. Sounding rocket aerodynamic behavior was originally
investigated solely using scale model wind tunnel tests, as was the case for most aircraft design.
An example is shown in Figure 5-1.

Figure 5-1: Wind tunnel model of an F-16 fighter showing upper-body vortex shedding during
testing [54]

Dimensional analysis may be used to derive non-dimensional quantities that describe
characteristic ratios of fluid flow parameters. The conservation of these characteristic quantities
from the vehicle to a scaled down model airframe allows the designer to simulate flight
conditions in a wind tunnel. Measurements of forces and moments on a scaled model of a
vehicle in such a wind tunnel wherein the flow velocity and incidence angles are varied are
often the most accurate means of characterizing aerodynamic behavior. Measurements have
been historically taken using spring balances but recent advances in micro-electro-mechanical-
systems (MEMS) have seen the widespread use of electronic strain gauges to measure forces
and moments. However, the effective use of wind tunnel testing is costly and time consuming,
requiring the production of suitable geometrically accurate scaled models, high-power wind
generating devices and appropriate tunnels. Force and moment measurement equipment must
also be calibrated for each model. Furthermore, the range of flight conditions reproducible in a

tunnel is limited by the size of the tunnel, the maximum wind speed and maximum incidence angles at which a model may be suspended in the tunnel. The time and effort involved in replicating all the design iterations for wind tunnel testing also makes the airframe optimization process inefficient. As greater supersonic speeds are achieved, it also becomes increasing difficult to generate sufficiently high Mach number conditions in wind tunnels. Additional complexity is also introduced if measurements of velocity and pressure are required at awkward locations on the model, especially if the model is small. In this work, wind tunnel facilities of adequate fidelity were unavailable and this approach to aerodynamic research was never explored.

5.2.3 Empirical Correlations

Empirical correlations for aerodynamic coefficients are created by fitting mathematical models to wind tunnel measurements and flight test data. Measurements made for simpler configurations or specific aerodynamic components are particularly suited to this approach. Sounding rockets airframes considered in this work may be separated into the fuselage and the fins. The fuselage is a body of revolution of varying radius whilst the fins are effectively short wings arranged orthogonally around the fuselage circumference. Great research effort has been placed in the past on the development of empirical correlations to approximate the salient aerodynamic characteristics of such common rocket airframe configurations. A software compendium of such correlations may be used for simulation purposes and for the first iteration of the aerodynamic design of a new rocket configuration. A compendium of aerodynamic data for aircraft has been compiled by the USAF in the USAF Digital DATCOM [55]. The Digital DATCOM presents aerodynamic coefficient prediction methods for subsonic, transonic, supersonic and hypersonic flight.

The need for basic software generated empirical aerodynamic coefficient tables led to the use of the Rogers Aero-science RasAero program [56]. This software tool performs basic empirical aerodynamic coefficient predictions on rocket airframes with a cylindrical body with a rear boat-tail, a cone or ogive nose and a single set of trapezoidal fins. Both three-fin and four-fin fin-sets are supported. The tool is capable of modeling friction drag effects and uses a modified form of Barrowman's methods for calculating the center of pressure. Plume effects on base drag are also modeled and the user is given the option of selecting rounded, square, wedge, diamond, hexagonal or biconvex fin sections. Launch lugs, rail guides and launch shoes are supported and the program also includes the effects of a fin-can. Figure 5-2 shows a screenshot from the software.

The basic outputs of the software include estimates of the powered on and powered off drag coefficient, lift coefficient, center of pressure location and normal force coefficient slope for angles of attack up to 15° for Mach numbers up to Mach 5. The software also estimates these coefficients for Mach number up to Mach 25 for angles of attack up to 4°. These outputs were used in the HYROPS software in interpolated lookup table format for the preliminary generation of trajectories for the Phoenix-1A vehicle.
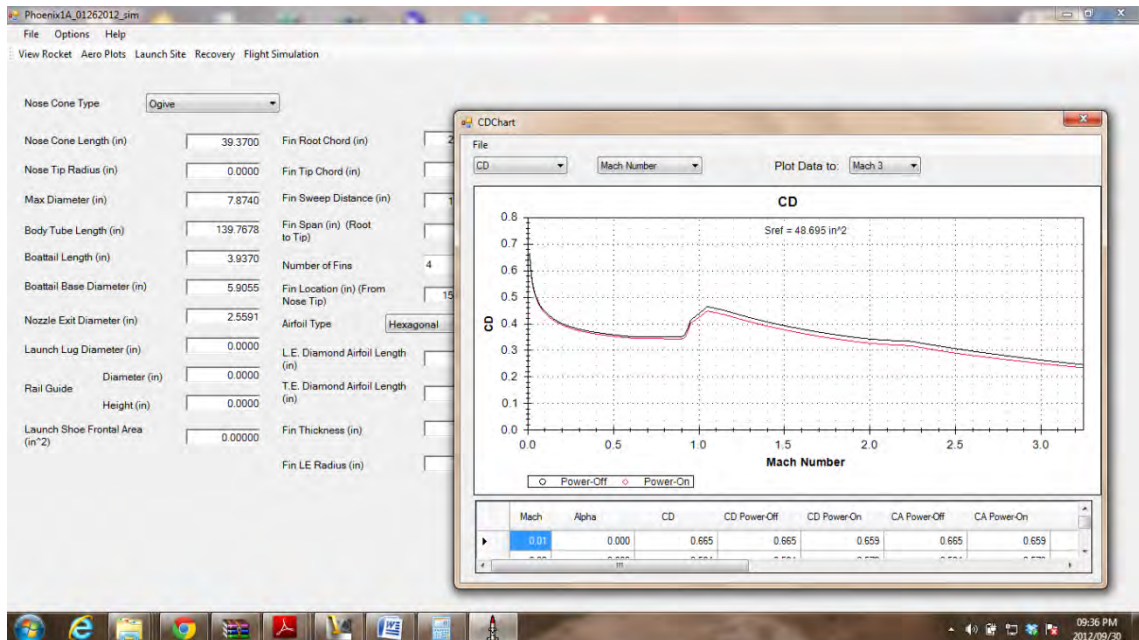
Figure 5-2: Screenshot of the RasAero software showing aerodynamic coefficient plots based on airframe geometric inputs for the Phoenix-1A sounding rocket.

5.2.4 Computational Fluid Dynamics (CFD)

As indicated earlier, analytical and empirical aerodynamic solutions are available only for a very limited set of geometries and are often highly approximate by nature. Such solutions often simplify the governing laws of fluid motion and are thus unable to capture subtle flow effects, which limit their accuracy. However, direct solution of the governing partial differential equations (PDE) for complex geometries is possible using numerical methods developed for continuum mechanics such as the finite element method (FEM), finite volume method (FVM) and the finite difference method (FDM). These techniques divide the complex solution domain into a mesh of numerous small elements, each of which has a known simple geometry. The governing PDE is then applied over each of these small sub-domains using algebraic methods, resulting in a large, sparse linear system. Iterative numerical solution of this linear system gives the flow properties as a function of space and time over the domain. The results summed

spatially and temporally to derive the overall aerodynamic parameters. When applied to atmospheric aerodynamics the Navier-Stokes equations and energy equation are solved most commonly using the finite volume method. This process is known as computational fluid dynamics and has been popularized over the last few decades by the exponential growth in affordable computing capacity available to aerodynamicists.

The relatively recent advent of CFD techniques for numerical flow analysis offers advantages over both wind tunnel testing and empirical prediction codes. However, CFD aerodynamic analyses require significant computational resources and knowledge of the underlying mathematical techniques for successful application. In this work, empirical codes were used for the airframe design iterations whilst the final design was qualitatively validated using CFD software for the validation of thermal loading conditions. These studies are discussed in more detail Chapter 6. Figure 5-3 shows a sample result, simulated using the StarCCM+ CFD package. Note the multiple shock waves and region of low pressure behind the vehicle.
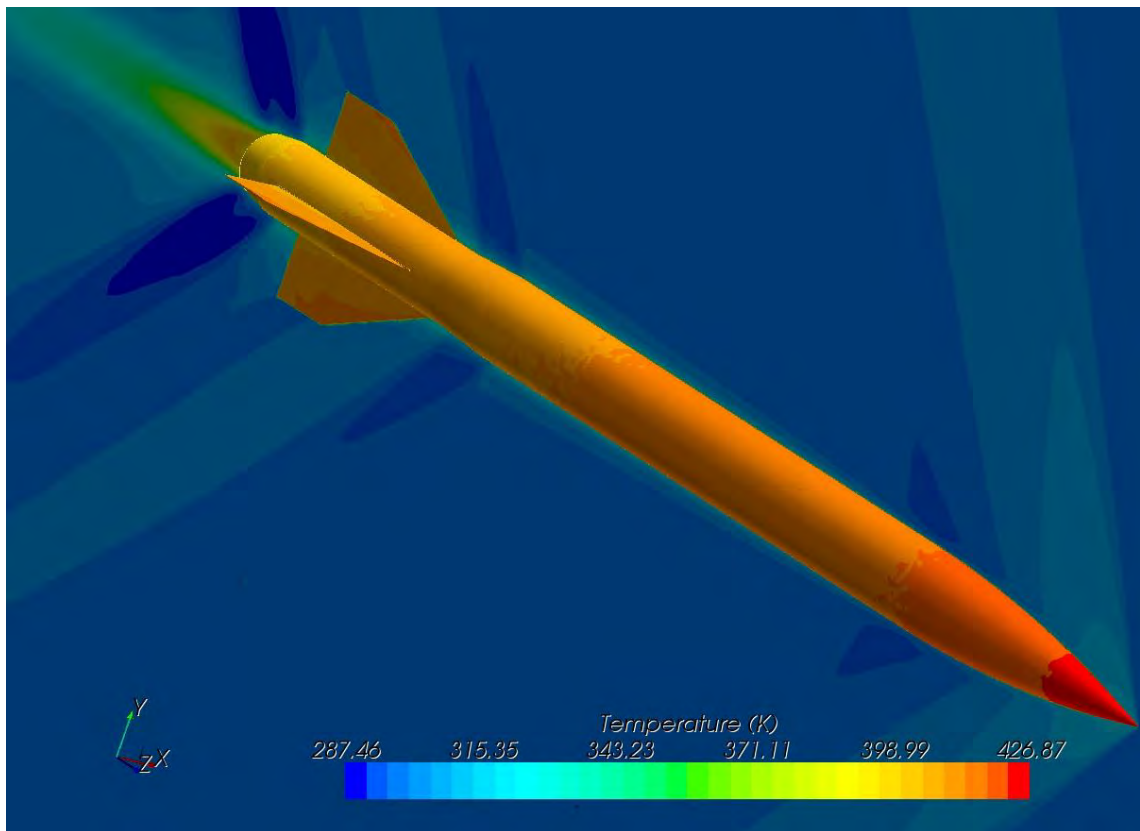
Figure 5-3: 3D visualization of air temperature in the flow-field around an early prototype airframe model of the Phoenix-1A sounding rocket flying at zero incidence angles at Mach 1.5.

5.3 Airframe Definition

The airframe is defined as those external surfaces of a vehicle which are exposed to and interact with the atmosphere. Sounding rocket airframes are conventionally divided into several functional parts, each of whose influence on the overall aerodynamic characteristics may be studied relatively independently. A basic airframe configuration consists of a nose, a fuselage and one or more sets of stabilizing surfaces. Depending on the vehicle launch technique, launch lugs, launch buttons or launch rails may also form part of the airframe. Sundry components such as telemetry antennae and camera probes may also interact with the airflow. Accounting for interdependencies between specific airframe components is necessary for accurate aerodynamic modeling. Aerodynamic design involves the development of a suitable airframe geometry given required aerodynamic, structural and aesthetic specifications of a vehicle. For the purposes of this work, a sounding rocket airframe is assumed to comprise only of the following components, as shown in Figure 5-4.

1) A nose, which is a body of revolution with a pointed tip, of either ogival or conic profile
2) A fuselage, a body of revolution with linearly varying radius (i.e. piecewise conical) profile
3) Any number of fin sets, with each set comprising of four thin planar trapezoidal fins
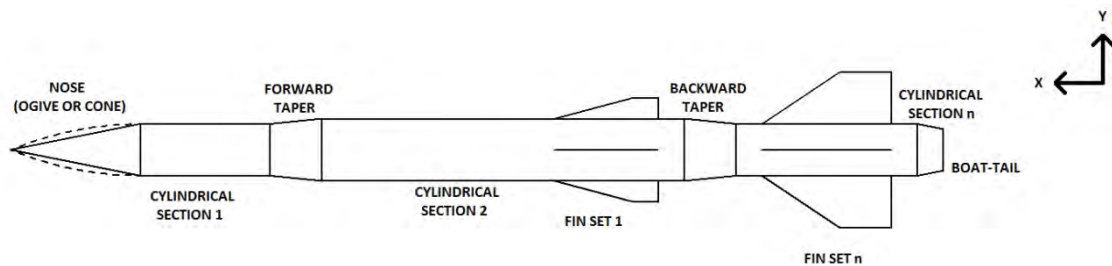
Figure 5-4: Longitudinal view of an example of the airframe model adopted in this work, showing a nose, two sets of four trapezoidal fins, one forward and one rearward facing shoulder (taper) and a boat-tail at the rear of the airframe.

It should be noted that these definitions limit the aerodynamic model to conventional sounding rockets without accommodating for tandem boosters and other lateral attachments, non-conical fuselage shoulders or unconventional nose profiles as well as any fuselages of non-circular cross section. All fin sets are also required to sit completely within sections of the fuselage where the radius does not vary. For practical purposes, the number of fin sets is limited to four whilst the number of discrete fuselage segments of linearly varying radius is limited to thirty. The airframe thus described has notable symmetry characteristics

a) Orthogonal mirror symmetry (tetragonal symmetry) about the body frame y and z axes

b) Rotational symmetry about the airframe x axis with a period of 90°

By the convention mentioned in Chapter 3, in this work all longitudinal dimensions are referred from the rear end of vehicle with the x coordinate increasing in the forwards direction towards the nose tip. However, the definition of the airframe segments starts with the nose, from the front of the vehicle and progresses with each segment aft-wards, with the first segment being assigned the number 0. Each segment is assigned a length L, a fore radius r_1 and aft radius r_2. The base radius of the nose r_n is thus equal to the fore radius of segment 0. The nose also has a length L_n. Figure 5-5 shows this dimensioning convention. A definition of the plan-form dimensions of the trapezoidal fins is also presented in Figure 5-6, as required for various calculations. The relevant dimensions are the root chord C_r, tip chord C_t, sweep w, span s, root span r_t and thickness t.
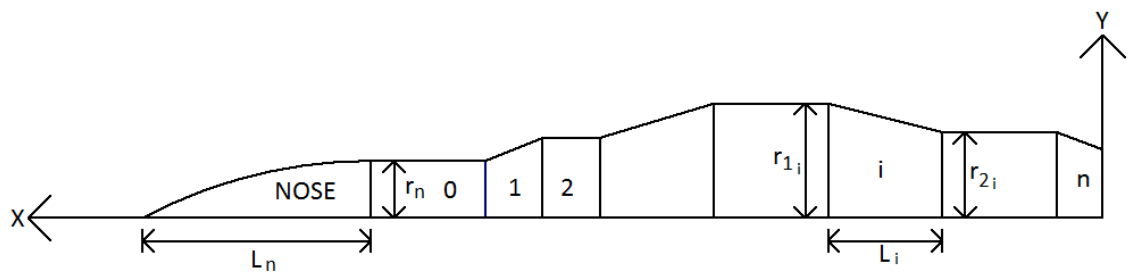
Figure 5-5: The fuselage segments and nose dimensioning convention, shown in body axes.
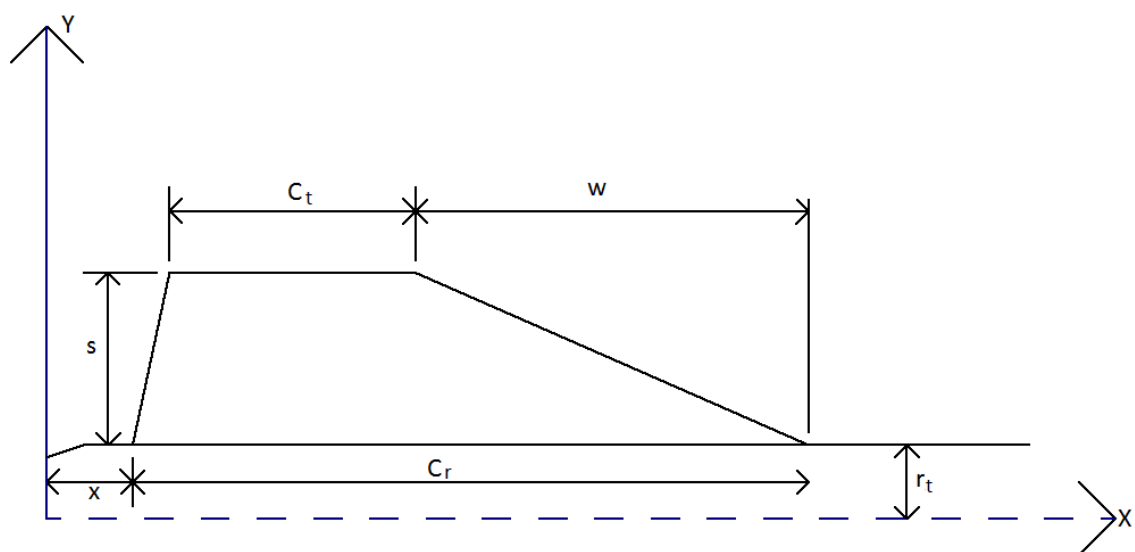
Figure 5-6: Dimension definitions of the trapezoidal fin. Note that the x location of the fin set is measured from the rear end of the vehicle to the rear end of the root chord.

5.4 Aerodynamic Incidence Angles

The standard sounding rocket airframe described earlier will travel through a steady fluid under equilibrium conditions with its aerodynamic velocity vector oriented parallel to the airframe x axis. This is a result of the rotational and tetragonal symmetries present on such airframes. Under equilibrium conditions such a vehicle will not experience any forces along its body frame y and z axes and is said to travel at zero angle of incidence. A single parameter, the total angle of attack α_T, may be used to describe the incidence orientation of an airframe with tetragonal symmetry (Eq. 5-6). For vehicles with only a single transverse plane of symmetry, such as airplanes and cruise missiles, two incidence angles are used to describe the orientation between the aerodynamic velocity vectors and the airframe x axis. These are the angle of attack α and the sideslip angle β and describe the incidence of the airframe z axis and y axis respectively (Eq. 5-3 and Eq. 5-4 respectively). These angles may be calculated by projecting the aerodynamic velocity vector (Eq. 5-2) to the body frame V_a^b. The incidence angles become nonzero when the body-frame aerodynamic velocity displays nonzero y and z components. The aerodynamic roll angle ϕ_a is the angle between the body frame local vertical (xz) plane and the load factor plane in which the total angle of attack lies (Eq. 5-5). Refer to Figure 3-5 for a diagram of the various aerodynamic incidence angles in the body frame.

$$V_a^b = \begin{bmatrix} u_a^b \\ v_a^b \\ w_a^b \end{bmatrix} \tag{5-2}$$

$$\alpha = \tan^{-1}\left(\frac{w_a^b}{u_a^b}\right) \tag{5-3}$$

$$\beta = \sin^{-1}\left(\frac{v_a^b}{V_a}\right) \tag{5-4}$$

$$\phi_a = \tan^{-1}\left(\frac{v_a^b}{w_a^b}\right) \tag{5-5}$$

$$\alpha_T = \cos^{-1}\left(\frac{u_a^b}{V_a}\right) \tag{5-6}$$

5.5 Aerodynamic Coefficients

Assuming that the airframe is a rigid body, aerodynamic effects may be formalized by considering the aerodynamic effort on each of the vehicle's six degrees of freedom. These constitute three aerodynamic forces, one for each of the three linear degrees of freedom and three aerodynamic moments, one for each of the three attitude degrees of freedom. These lumped parameters are representative of the aerodynamic loading on the entire vehicle. If aerodynamic loads are great enough to significantly deflect the vehicle airframe and alter aerodynamic characteristics, the rigid body assumption fails. In such situations, the coupling between structural and aerodynamic loading results in aero-elasticity. Aero-elastic effects are insignificant enough to be ignored on conventional suborbital sounding rocket vehicles except for certain thin geometries such as stabilizing fins and parachute canopies.

The aerodynamic force may be expressed in either the body frame or the aerodynamic frame. In either case, it is useful to resolve the aerodynamic force into a component parallel to the body frame x axis and a component perpendicular to the body frame x axis. Non-dimensional coefficients of the parallel component are known as the drag coefficient C_D in the aerodynamic frame and the axial force coefficient C_A in the body frame. Similarly, the perpendicular component is known as the lift coefficient C_L in the aerodynamic frame and the normal force coefficient C_N in the body frame. Airframes with tetragonal symmetry display a load factor plane as discussed in Chapter 3, and this breakdown takes on a particular significance as the normal aerodynamic force component is known to lie in the load factor plane. In this case, the total angle of attack is used to relate the quantities between the frames using a two-dimensional transformation lying in the load factor plane (Eq. 5-7).

$$\begin{bmatrix} C_A \\ C_N \end{bmatrix} = \begin{bmatrix} \cos \alpha_T & -\sin \alpha_T \\ \sin \alpha_T & \cos \alpha_T \end{bmatrix} \begin{bmatrix} C_D \\ C_L \end{bmatrix} \tag{5-7}$$

As mentioned in Chapter 3, aerodynamic coefficients are formalized by resolving the aerodynamic force in the body frame, as this presents advantages in the formulation of the equations of motion. The normal force coefficient (Eq. 5-10) can then be resolved into its respective y and z components, C_Y and C_Z, using the aerodynamic roll angle (Refer to Figure 3-5). The components of the aerodynamic force vector $\overrightarrow{F_A}$ can be written in terms of the atmospheric density ρ, reference area A and aerodynamic speed V_a (Eq. 5-8). The axial force coefficient remains independent (Eq. 5-9).

$$\vec{F_A} = \begin{pmatrix} F_X^B \\ F_N^B \sin(\phi_A) \\ F_N^B \cos(\phi_A) \end{pmatrix} = \begin{pmatrix} C_A \\ C_Y \\ C_Z \end{pmatrix} \frac{1}{2}\rho A V_a^2 \tag{5-8}$$

$$C_A = \frac{F_X^B}{\frac{1}{2}\rho A V_a^2} \tag{5-9}$$

$$C_N = \frac{F_N^B}{\frac{1}{2}\rho A V_a^2} \tag{5-10}$$

In analogy to the aerodynamic forces, aerodynamic moments can be expressed in body axes by introducing non-dimensional coefficients on the moments acting about of the body frame axes (Eq. 5-11). The rolling moment M_X^B, pitching moment M_Y^B and yawing moment M_Z^B are thus associated with the rolling moment coefficient C_l, pitching moment coefficient C_m and yawing moment coefficient C_n respectively. In the case of moments, an aerodynamic reference length l is also needed to normalize the moment arm.

$$C_l = \frac{M_X^B}{\frac{1}{2}\rho A l V_a^2} \tag{5-11a}$$

$$C_m = \frac{M_Y^B}{\frac{1}{2}\rho A l V_a^2} \tag{5-11b}$$

$$C_n = \frac{M_Z^B}{\frac{1}{2}\rho A l V_a^2} \tag{5-11c}$$

A distinction must be made between aerodynamic effects in equilibrium flight and additional aerodynamic effects due to dynamic flight behavior. The *static* aerodynamic coefficients C_j already described quantify aerodynamic loads at equilibrium (Eq. 5-12), with flight parameters constant. In contrast, *dynamic* effects are encountered during non-equilibrium flight conditions. *Dynamic derivatives* $C_{j_{x_i}}$ are dimensionless coefficients that account for variations in the static aerodynamic coefficients caused by the time variance of flight conditions (Eq. 5-14). These derivatives are themselves functions of the flight conditions x_i (Eq. 5-13) and hence coupled to other static and dynamic aerodynamic loads. A general expansion of the definition of the aerodynamic coefficients is needed to define the dynamic derivatives. An aerodynamic

coefficient may be expanded about it static value $C_j^S(x_i)$ using a Taylor series in terms of the flight conditions (Eq. 5-15). For the purposes of trajectory simulation, it is generally assumed that the dynamic variations are linear and that higher order terms in the Taylor series are negligible. Certain second order partial derivatives of the aerodynamic coefficients may also be nonzero for a given airframe configuration. Arbitrarily higher order dynamic derivatives are commonly zero or have insignificant effect on the high level flight performance (Eq. 5-16).

$$C_j = \{C_A \quad C_Y \quad C_Z \quad C_l \quad C_m \quad C_n\} \tag{5-12}$$

$$x_i = \{\alpha_T \quad \phi_A \quad u \quad v \quad w \quad p \quad q \quad r \quad \dot{p} \quad \dot{q} \quad \dot{r}\} \tag{5-13}$$

$$C_{j_{x_i}} = \frac{\partial C_j}{\partial x_i} \tag{5-14}$$

$$C_j(x_i) = C_j^S(x_i) + \sum_{i=1}^{11} \frac{\partial C_j}{\partial x_i} x_i \tag{5-15}$$

$$C_{j_{x_1 x_2 \ldots x_k}} = \frac{1}{k!}\left(\frac{\partial C_j}{\partial x_1 \partial x_2 \ldots \partial x_k}\right) \tag{5-16}$$

It is obvious that if dynamic derivatives of all orders were to be considered, an infinite number of dimensionless derivative coefficients would exist. For practical reasons, the design and modeling of rocket aerodynamics is limited solely to those dynamic derivatives which have a significant impact on rocket flight performance parameters. In this work a sufficiently detailed aerodynamic model is adopted to capture all significant aerodynamic characteristics whilst keeping model complexity to a minimum.

The aerodynamic coefficients are functions of the airframe design and prevailing flight conditions. These functional dependencies are summarized in Table 5-1. It should be noted that these dependencies vary according to the configuration of the vehicle. Rockets which display one plane of symmetry display significantly more degrees of aerodynamic coupling than do rockets with two planes of symmetry such as those considered in this work.

Table 5-1: Summary of aerodynamic coefficient dependencies

Parameter	Symbol	Determines
Total Angle of Attack	α_T	$(C_X \quad C_Y \quad C_Z \quad C_l \quad C_m \quad C_n)$
Aerodynamic Roll Angle	ϕ_a	$(C_Y \quad C_Z \quad C_m \quad C_n)$
Free-stream Mach Number	M	$(C_X \quad C_Y \quad C_Z \quad C_l \quad C_m \quad C_n)$
Body Frame Roll Rate	p	$(C_l \quad C_m \quad C_n)$
Body Frame Roll Orientation	ϕ	$(C_Y \quad C_Z \quad C_m \quad C_n)$
Free-stream Reynolds Number	R_e	$(C_X \quad C_Y \quad C_Z \quad C_l \quad C_m \quad C_n)$
Body Frame Pitch rate and Yaw rate	q, r	$(C_Y \quad C_Z \quad C_m \quad C_n)$

5.6 Fluid Flow Regimes and Dimensionless Parameters

5.6.1 Reynolds Number

The Reynolds' number R_e is a dimensionless parameter used to characterize the magnitude of viscous effects in comparison to inertial effects. It is useful in rocket aerodynamics as a predictor for the onset of flow separation and turbulent flow. Viscous, laminar boundary layer characteristics dominate at low Reynolds' numbers and turbulence inducing inertial effects dominate at higher Reynolds' numbers. The characteristic length L is used to normalize the dimensions of the flow geometry. The number is calculated according to Eq. 5-17.

$$R_e = \frac{\rho V L}{\mu} = \frac{V L}{\nu} \tag{5-17}$$

Drag characteristics are a function of flow regime. Flow separation also causes vortex shedding from certain geometries. These include the aerodynamic shoulders, boat tails and fins. At large angles of attack, the fuselage and nose may also experience vortex shedding due to flow separation in the cross-flow direction. Under typical conditions, the transition from laminar to turbulent flow occurs very rapidly on a sounding rocket airframe and only a small portion of the airframe is under laminar flow. Therefore, in this work it is assumed that turbulent flow is prevalent throughout the vehicle airframe. This is a conservative assumption as drag characteristics are more severe in the turbulent regime and lifting surfaces display lower efficiencies.

5.6.2 Sonic Speed

The sonic speed is the speed at which a pressure wave can be propagated through a fluid. It is relevant to aerodynamics of rockets as compressibility effects begin to dominate the flow around a sounding rocket airframe for vehicle speeds greater than the sonic speed whilst pressure driven effects dominate aerodynamic characteristics for vehicle speeds much lower than the sonic speed. The sonic speed a of an ideal gas is a function of temperature and hence altitude, given by Eq. 5-18. The constants in the equation are the ratio of specific heats k and the universal gas constant R.

$$a = \sqrt{kRT} \qquad\qquad (5\text{-}18)$$

5.6.3 Mach number

The Mach number is defined as the ratio of the vehicle aerodynamic speed to the local atmospheric sonic speed (Eq. 5-19).

$$M = \frac{V_a}{a} \qquad\qquad (5\text{-}19)$$

Sounding rocket airframes are designed with a focus on expected flight conditions. Since aerodynamic characteristics are strongly correlated to the flight velocity or Mach number, it is useful to optimize an airframe design for the Mach number range the vehicle will nominally encounter. Flight simulation is essential for this purpose. Several velocity (or Mach) regions may be defined for effectively characterizing aerodynamic behavior. The subsonic Mach region refers to speeds well below the sonic speed. The unique effects in the vicinity of the sonic speed (known as transonic effects) are insignificant in the subsonic region. The transonic velocity region encompasses the sound barrier and is used to characterize speeds that incur the unique effects of transcending the sonic speed. Mach numbers significantly greater than the sonic speed but less than Mach 5 constitute the supersonic velocity region. Finally, the hypersonic region represents speeds greater than Mach 5 and mainly characterizes very high speed aerodynamic complexities.

5.6.4 Compressibility Factor

The compressibility factor β is a dimensionless quantity used to compensate for compressibility effects which become significant as Mach numbers rise above the low subsonic regime. It is calculated from Eq. 5-20 and often used in empirical aerodynamic correlations to relate subsonic and supersonic quantities.

$$\beta = \begin{cases} \sqrt{M^2 - 1} & for\ M \geq 1 \\ \sqrt{1 - M^2} & for\ M \leq 1 \end{cases} \qquad (5\text{-}20)$$

5.7 Symmetry

Sounding rocket airframes often possess geometric symmetry. Rotational symmetry and reflection symmetry are both possible on sounding rocket airframes about the longitudinal axis. Symmetry has the effect of duplicating aerodynamic characteristics about different axes. Maple and Synge [57] have extensively investigated the vanishing of dynamic derivatives in configurationally symmetric airframes. For the special case of a vehicle possessing tetragonal symmetry (rotational symmetry with a period of 90°) or reflection symmetry, Maple and Synge have derived two rules for vanishing derivatives. Aerodynamic symmetry presents advantages such as ease of manufacture, lower complexity in vehicle dynamic response and increased stability. Additionally, symmetrical airframes display less flight dispersion when unguided and hence exhibit more predictable flight dynamics [21].

5.8 Empirical Aerodynamic Prediction Techniques

5.8.1 Drag and Axial Force

Drag is defined as the component of the aerodynamic force that acts in the opposite direction to the vehicle aerodynamic velocity vector. The drag coefficient is the most important aerodynamic parameter as it effectively limits the fly-out range of a sounding rocket. There are several distinct sources of drag on a generalized sounding rocket airframe. These include pressure drag, friction drag, induced drag, base drag, wave drag and parasitic drag. The sum of these various effects and their interdependence makes the drag optimization process nontrivial. It is useful to investigate each source of drag and its relative severity under the expected flight conditions so that an optimal configuration may be chosen.

Pressure drag (also known as *form drag*) is the resultant drag force arising from the static pressure distribution on the airframe during flight. It arises from the energy spent in diverting the flow of air around the airframe during flight. It is present under all flight conditions and is dependent solely on the geometry of airframe components. In particular, pressure drag is strongly influenced by the nose geometry and fin cross sectional profile. Components that cause the flow to speed up cause a drop in airframe surface pressures and vice versa. The flow is forced to slow down and stagnate forward of the nose and fins, creating local high pressure

133

regions. Conversely, the flow speeds up to fill the voids left aft of the moving vehicle, creating low pressure regions. This difference in pressure distribution causes the pressure drag force.

For noses that are bodies of revolution, the zero-lift nose pressure drag coefficient $C_{D_{(NOSE)}}$ is a function of the nose radius profile. For the supersonic case, Niskanen [48] provides an approximation (Eq. 5-21) which is used for both conic and tangent ogive profiles. The nose tip half angle is denoted ε_n.

$$C_{D_{(NOSE)}} = (2.1(\sin \varepsilon_n)^2) + \frac{\sin \varepsilon_n}{2\beta} + C_{N\,\alpha(NOSE)}\alpha_T^2 \qquad (5\text{-}21)$$

In the subsonic region a reasonable approximation (Eq. 5-22) is obtained for cones and tangent ogives using an exponential extrapolation as a function of the Mach number scaled with the nose drag coefficient at Mach 1. Note the ratio of specific heats denoted k.

$$C_{D_{(NOSE)}} = C_{D_{(NOSE)\,M=1}} M^{\frac{\left(\frac{4}{1+k}\right)\left(1-\frac{\sin \varepsilon_n}{2}\right)}{\sin \varepsilon_n}} \qquad (5\text{-}22)$$

The subsonic zero-lift body pressure drag is known to be zero for cylindrical fuselage sections. For forward facing tapered shoulders, the pressure drag is estimated from the pressure drag of a conical nose in subsonic flow whilst backward facing transitions use the base drag as an estimator for pressure drag. In each case, the coefficient is scaled using the projected transition area which is the difference between the transition root and base cross sectional areas.

The subsonic body drag coefficient at angle of attack $C_{D_{BODY}}(\alpha_T)$ is estimated using the method of Hopkins [58] as presented in the USAF Digital DATCOM (Eq. 5-23). In this method, the total body volume is denoted V_B and the body radius is denoted r. The body length is denoted l_{BODY} and the parameter η is the ratio of drag on a finite cylinder to the drag on an infinite cylinder. The parameter c_{D_c} is the steady-state cross-flow drag on an infinite cylinder. The factor $(k_2 - k_1)$ is the Munk apparent mass factor which is a function of the body fineness ratio. The longitudinal location x_0 is the body station where the flow ceases to be potential and S_0 is the body cross sectional area at x_0.

$$C_{D_{BODY}}(\alpha_T) = 2\frac{(k_2-k_1)}{(V_B)^{2/3}}\alpha_T^2 S_0 + \frac{2\alpha_T^3}{(V_B)^{2/3}}\int_{x_0}^{l_{BODY}} \eta r c_{D_c} dx \qquad (5\text{-}23)$$

Fins also generate significant amounts of pressure drag. It is useful to categorize fins based on their leading and trailing edge profiles. Three broad categories of edge profiles may be identified: squared off, sharply tapered and rounded. The fin leading edge drag coefficient $C_{D(FIN\ LE)}$ is then estimated by treating the fin as a profile in two-dimensional flow. For squared off leading edge profiles, the subsonic pressure drag coefficient is then approximately equal to the stagnation frontal drag coefficient $C_{D(STAG\ CYL)}$ of a squared-off cylinder in frontal flow, given by the correlation in Eq. 5-24 as squared off leading edges effectively experience stagnated flow across the face. Rounded leading edges behave like a cylinder in cross flow, whose approximate drag coefficient characteristic is given by Niksanen [48] as Eq. 5-25. Squared off trailing edges generate pressure differences similar to the base of the vehicle fuselage. For trailing edges, the base drag coefficient $C_{D_{BASE}}$ under identical Mach conditions is used for squared off trailing edges and half this value is used for round trailing edges (Eq. 5-26). The total fin set pressure drag coefficient $C_{D(FIN)}$ is thus the sum of the fin leading edge drag coefficient and the fin trailing edge drag coefficient $C_{D(FIN\ TE)}$ referred to the fin frontal area (which is the product of the fin thickness and exposed fin span), multiplied by the number of fins in the set. This can then be referred to the vehicle aerodynamic reference area by scaling with the ratio of the reference area over fin frontal area (Eq. 5-27). Note the dependence on the fin cant angle δ in case the fins are canted.

$$C_{D(STAG\ CYL)} = \begin{cases} 0.85\left(1 + \frac{M^2}{4} + \frac{M^4}{40}\right) & M < 1 \\ 0.85\left(1.84 - \frac{0.76}{M^2} + \frac{0.166}{M^4} + \frac{0.035}{M^6}\right) & M \geq 1 \end{cases} \tag{5-24}$$

$$C_{D(FIN\ LE)} = \begin{cases} C_{D(STAG\ CYL)} & for\ Squared\ off\ LE \\ \begin{cases} (1-M^2)^{-0.417} - 1 & for\ M < 0.9 \\ 1 - 1.785(M - 0.9) & for\ 0.9 \leq M \leq 1 \\ 1.214 - \frac{0.502}{M^2} + \frac{0.1095}{M^4} & for\ M > 1 \end{cases} & for\ Rounded\ LE \end{cases} \tag{5-25}$$

$$C_{D(FIN\ TE)} = \begin{cases} \frac{C_{D_{BASE}}}{2} & for\ Rounded\ TE \\ C_{D_{BASE}} & for\ Squared\ off\ TE \end{cases} \tag{5-26}$$

$$C_{D(FIN)} = N\left(C_{D(FIN\ TE)} + C_{D(FIN\ LE)}\right)\frac{A}{st\cos\delta} \tag{5-27}$$

Supersonic *wave drag* is a specific form of pressure drag produced by shock waves on any aerodynamic surface that produces a normal force. It is also induced on the fuselage due to protuberances. Wave drag only becomes a significant contributor to the overall drag force during the transonic, supersonic and hypersonic regimes. The main shock wave generating features are the nose, shoulders and boat-tail as they change the fuselage cross sectional area significantly. Fins are also responsible for a small part of the total wave drag effect. The relative location of aerodynamic components determines the interactions between their respective shock waves and the generation of additional interference drag. Analogous to shock waves, *expansion fans* result from components that cause a drop in the supersonic pressure coefficient, such as boat tails and the trailing edges of fins. These are also contributors to the overall wave drag.

Base drag is also a specific case of pressure drag formed at the rocket base surface. At subsonic speeds, this area of low pressure has a great pressure differential with respect to the rest of the flow [21]. The presence of a plume from the rocket motor may significantly reduce effective base area and hence base drag. Therefore, it is useful to analyze rocket pressure drag forces separately for the powered and unpowered flight phases, particularly in the subsonic velocity regime. A boat-tail is often used to limit base drag by reducing the effective base area.

The method (Eq. 5-28) used by Niskanen [48] for approximating the subsonic base drag coefficient $C_{D_{BASE}}$ is adapted to account for jet plume effects (Eq. 5-29). The base drag is diminished during powered flight by subtracting the nozzle exit area A_{NOZZLE} from the base area A_{BASE}. The base drag coefficient is thus proportionally reduced to give the powered base drag $C_{D_{BASE(POWERED)}}$. Angle of attack effects are ignored for all Mach ranges.

$$C_{D_{BASE}} = \begin{cases} 0.12 + 0.13M^2 & for\ M < 1 \\ \frac{0.12}{M} & for\ M > 1 \end{cases} \qquad (5\text{-}28)$$

$$C_{D_{BASE(POWERED)}} = C_{D_{BASE}} \frac{A_{BASE} - A_{NOZZLE}}{A_{BASE}} \qquad (5\text{-}29)$$

Skin-friction drag is the resistance to fluid motion brought about by the interaction of the airflow with non-smooth airframe components. Small irregularities on airframe surfaces hinder the localized flow of air very close to these surfaces and energy is lost in diverting air molecules around these irregularities. The airframe surface roughness determines the severity of friction drag, particularly on surfaces with high proximal tangential velocities, such as the fuselage and fins. The development of boundary layers due to viscous effects plays a large role in skin

friction effects. The friction drag force is proportional to the airframe surface area exposed to external flow (wetted area) and hence the skin friction drag coefficient is referenced to the wetted area instead of a geometric characteristic. Skin friction drag is heavily dependent on the surface Reynolds' number and temperature and also the free-stream Mach number. In the supersonic regimes, compressibility effects also affect the severity of friction drag notably.

In this work, the generic empirical methods presented by Niskanen [48] and USAF Digital DATCOM [55] are adapted to the flow regimes encountered in sounding rockets. Niskanen [48] uses a correlation (Eq. 5-30) for skin friction drag coefficient C_f in the turbulent regime and Eq. 5-31 for the compressibility corrected skin friction drag coefficient C_{f_c}

$$C_f = \begin{cases} 0.0148 & for\ R < 10^4 \\ \frac{1}{(1.5\ln R_e - 5.6)^2} & for\ 10^4 < R < 51\left(\frac{R_S}{L}\right)^{-1.039} \\ 0.032\left(\frac{R_S}{L}\right)^{\frac{1}{5}} & for\ R \geq 51\left(\frac{R_S}{L}\right)^{-1.039} \end{cases} \tag{5-30}$$

$$C_{f_c} = \begin{cases} C_f\left(1 - \frac{M^2}{10}\right) & for\ M < 1 \\ \frac{C_f}{(1+0.15M^2)^{0.58}} & for\ M \geq 1 \\ \frac{C_f}{1+0.18M^2} & for\ R > 51\left(\frac{R_S}{L}\right)^{-1.039} \end{cases} \tag{5-31}$$

In the relations, note that R_s is the surface roughness height which drives the skin friction drag force as well the onset of turbulence. The drag coefficient due to skin friction C_{D_F} can then be referenced from the vehicle aerodynamic reference area using the total wetted surface area of the rocket A_{WET} (Eq. 5-32).

$$C_{D_F} = C_{f_c}\left(\frac{A}{A_{WET}}\right) \tag{5-32}$$

Induced drag is the additional drag due to flow complexities when flying at nonzero aerodynamic incidence angles. The presence of lift forces under these conditions causes additional fluid flow structures to develop, such as vortices and flow separation regions. These lead to an overall increase in the aerodynamic resistance to motion. Induced drag is typically regarded as being parabolic in nature as it increases with the square of the lift coefficient.

Parasitic drag is a combination of the abovementioned drag effects generated by unusual protuberances or irregularities on the airframe. Parasitic drag is often analyzed empirically due to the vast range of geometries and configurations such irregularities may possess. A detailed analysis of parasitic drag possibly generated by non-idealities in the generic airframe model adopted is beyond the scope of this work.

5.8.2 Lift, Normal Force and Pitching Moment

Normal forces are generated on a rocket when there is pressure variation on the airframe at different transverse locations. For rotationally symmetric vehicles this is solely possible when flying at an angle of attack. Significant normal forces are only generated by stabilizing surfaces such as fins as well as fuselage components that exhibit varying cross sectional area, such as the nose, shoulders and boat-tail. Sounding rocket airframes utilize normal forces to maintain a stable trajectory and the design process aims to produce net normal forces at favorable locations on the airframe to aid stability.

For bodies of revolution in subsonic flight at relatively small total angles of attack (0° to 5°), the normal force is a linear function of the angle of attack. Viscous effects are small and the normal force coefficient derivative is sufficient to predict the normal force under these conditions. For moderate angles of attack (5° to 15°) viscous effects gain significance and the normal force becomes a quadratic function of the angle of attack.

In this work, linear slender body theory [59] is adopted for subsonic flow normal force predictions at small angles of attack whilst empirical methods form the USAF Digital DATCOM [55] are used for predicting the viscous contribution to normal force at larger angles of attack. Transonic normal forces are approximated by linearly interpolating subsonic and supersonic values using appropriate boundary conditions. The relations are also applicable to the nose, which is also a body a revolution with a forward radius of zero. Normal forces on a body of revolution are proportional functions of the total angle of attack and the normal force coefficient slope C_{N_α} is supplied by the majority of empirical methods. The subsonic segment normal force coefficient slope for a segment with length L, forward radius r_1 and aft radius r_2 is given by slender body theory in Eq. 5-33 and the corresponding pitching moment coefficient slope C_{m_α} in Eq. 5-34, where V_{bs} is the volume of the body.

$$C_{N_\alpha} = \frac{2\pi}{A}(r_2^2 - r_1^2)\frac{\sin(\alpha_T)}{\alpha_T} \tag{5-33}$$

$$C_{m_\alpha} = \frac{2\pi}{A}(\pi L r_2^2 - V_{bs})\frac{\sin(\alpha_T)}{\alpha_T} V_{bs} = \frac{\pi L}{3}(r_1^2 + r_1 r_2 + r_2^2) \tag{5-34}$$

Normal forces are also generated on cylindrical bodies flying at angles of attack, but this effect is not captured by linear slender body theory. Niskanen [48] presents a correlation to approximate the cylinder normal force coefficient slope $C_{N_\alpha(CYL)}$ in Eq. 5-35 where A_P is the projected area of the cylinder.

$$C_{N_{\alpha(CYL)}} = 1.1\frac{A_P}{A}(\sin\alpha_T)^2 \tag{5-35}$$

The supersonic body of revolution normal force coefficient $C_{L_{BOR}}$ and pitching moment coefficient slope $C_{m_\alpha(BOR)}$ are estimated using the method of Allen and Perkins [60] as presented in the USAF Digital DATCOM (Eq. 5-36 and Eq. 5-37 respectively). This method is also applicable to noses which are bodies of revolution. The projected area of the body of revolution is denoted by A_P, the volume of the body by V_B and the center of pressure location relative to the moment reference center is denoted by X_C.

$$C_{L_{BOR}} = 2\alpha_T + c_{D_c}\alpha_T^2\frac{A_P}{A} \tag{5-36}$$

$$C_{m_{\alpha(BOR)}} = \left(\frac{2V_B}{Al} - 1\right) - c_{D_c}\frac{A_P}{A}\alpha_T X_c \tag{5-37}$$

Niskanen [48] approximates the subsonic trapezoidal four-fin set normal force coefficient slope using the result form linear thin wing theory and the method of Diedrich [61] in Eq. 5-38. The fin total area is denoted by A_{FIN}.

$$C_{N_\alpha} = \frac{\frac{4\pi s^2}{A}}{1 + \sqrt{1 + \left(\frac{\beta s^2}{A_{FIN}\cos\vartheta}\right)^2}} \tag{5-38}$$

where ϑ is the mid-chord sweep angle defined by Eq. 5-39.

$$\vartheta = \tan^{-1}\left(\frac{w + \frac{C_t - C_r}{2}}{s}\right) \tag{5-39}$$

In supersonic flow, the method used by Niskanen [48] is an adaptation of Busemann theory (Eq. 5-40).

$$C_{N_\alpha} = \frac{NA_{FIN}}{2A}(K_1 + K_2\alpha_T + K_3\alpha_T^2) \tag{5-40}$$

where the coefficients K_1, K_2 and K_3 are given in Eq. 5-41.

$$K_1 = \frac{2}{\beta} \tag{5-41a}$$

$$K_2 = \frac{(\gamma+1)M^4 - 4\beta^2}{4\beta^4} \tag{5-41b}$$

$$K_3 = \frac{(\gamma+1)M^8 + (2\gamma^2 - 7\gamma - 5)M^6 + 10(\gamma+1)M^4 + 8}{6\beta^7} \tag{5-41c}$$

The center of pressure X_P is defined as the location on the airframe about which no aerodynamic moments are produced. It represents the location where the net aerodynamic force may be thought to act, if it were concentrated at a single point. The location of the center of pressure is a function of the aerodynamic load distribution. The determination of the center of pressure location is central to the aerodynamic stability characterization of a rocket. Aerodynamic load distributions vary significantly with flight conditions and hence the center of pressure moves during flight. The lever arm through which aerodynamic moments are produced is the distance between the center of pressure and the center of mass. The symmetry assumption imposed in this work limits the center of pressure to lie on the body frame x axis and hence the prediction method presented is solely for determining the x coordinate of the center of pressure. The pressure distribution $p(x)$ is thus only a function of the x coordinate and the center of pressure is given by Eq. 5-42.

$$X_P = \frac{\int_0^L xp(x)dx}{\int_0^L p(x)dx} \tag{5-42}$$

The center of pressure location of each airframe component is sensitive to both the aerodynamic incidence angles and the Mach number. The overall center of pressure of an airframe may be

calculated by weighting the center of pressure location of each of its constituent surfaces by its respective aerodynamic normal force. This weighting may also be based on the normal force coefficients of the constituent surfaces (Eq. 5-43), provided that they are scaled to the same reference area.

$$X_P = \frac{\sum_{j=1}^{m} X_{P(j)} C_{N(j)}}{\sum_{j=1}^{m} C_{N(j)}}$$

(5-43)

For an individual component whose normal force coefficient and pitching moment coefficient are known, the center of pressure relative to the pitching moment center is given by Eq. 5-44.

$$X_P = \frac{C_m}{C_N l}$$

(5-44)

where l is the reference moment-arm used for moment calculations. If the aerodynamic incidence angles are very small or zero, l'Hospital's theorem states that the continuous limiting values of the derivatives of the respective coefficients may be used instead, as in Eq. 5-45.

$$X_P = \frac{C_{m\alpha}}{C_{N\alpha} l}$$

(5-45)

The analytical subsonic center of pressure location for planar trapezoidal fins $X_{P_{FIN}}$ based on Barrowman's derivation from linear theory is presented by Niskanen [48] in Eq. 5-46.

$$X_{P_{FIN}} = \frac{w(c_r + 2c_t)}{3(c_r + c_t)} + \frac{c_r^2 + c_t^2 + c_r c_t}{6(c_r + c_t)}$$

(5-46)

For supersonic flows, the correlation in Eq. 5-47 is used by Niskanen [48] but is only applicable for Mach numbers greater than two. Note the fin aspect ratio κ defined by Eq. 5-48. In this work, the center of pressure travel due to angle of attack was not modeled as trapezoidal fin centers of pressure do not travel greatly over the small angle of attack range modeled.

$$X_{P_{FIN}} = \bar{c} \frac{\kappa\beta - 0.67}{2\kappa\beta - 1}$$

(5-47)

$$\kappa = \frac{2s^2}{A_{FIN}}$$

(5-48)

5.8.3 Dynamic Derivatives

5.8.3.1 Moment Damping Coefficients

Moment damping derivatives are the most important dynamic derivatives from a vehicle stability standpoint. These derivatives represent the reduction to the pitching, yawing and rolling moments due to aerodynamic resistance to the vehicle's angular motion. In the absence of damping, the orientation degrees of freedom of a vehicle will oscillate about the equilibrium value when subjected to disturbances. For vehicles possessing tetragonal symmetry, the characteristics in pitch and yaw are identical and hence only two unique damping moment characteristics need to be estimated, namely the pitch and roll damping moments. Damping moments only exist during angular motion as they are dynamic effects.

5.8.3.2 Pitch Damping

The pitch damping moment may be characterized by the rotational motion of a cylinder about its lateral axes. Pitching causes the fuselage to move perpendicular to the nose axis, in opposite directions around the moment center, creating cross-flow. The resulting drag has two components, one induced by the fuselage and another by the fins. A useful estimate for the cylindrical component is obtained by treating the flow as purely cross flow around a cylinder. The distance from the moment center is proportional to the velocity of this apparent lateral motion. Longitudinal variations in fuselage and/or nose diameter also cause the total drag force experienced at a longitudinal location to vary. The integral of the pitching drag over the length of the airframe and the location of the equivalent point force determine the instantaneous pitch damping moment. Calculation based on this method of reasoning must use the projected area of the fins and the fuselage segments under consideration. The variation in fuselage and nose radius is accounted for by deriving an equivalent diameter. For a body of m segments and nose the equivalent diameter D_{eq} is given by Eq. 5-49, where the nose has length L_{nose} and projected area $A_{nose(projected)}$ and a segment has fore radius r_{1_i}, aft radius r_{2_i} and length L_i.

$$D_{eq} = \frac{A_{nose(projected)} + \sum_{i=1}^{m} \left(r_{1_i} + r_{2_i} \right) L_i}{L_{nose} + \sum_{i=1}^{m} L_i} \qquad (5\text{-}49)$$

It is known from theory that the drag coefficient of a cylinder in cross flow is approximately 1.1 with reference area being the projected plan-form area of the cylinder. Niskanen [48] uses this

to derive the pitching motion drag force contribution dF from a short segment of cylindrical fuselage of length dL in Eq. 5-50.

$$dF = 1.1 \left(\frac{\rho(q dL)^2}{2} \right) \left(2 \frac{D_{eq}}{2} dL \right)$$
(5-50)

The above differential must be integrated over the length of the fuselage, separately for segments fore and aft of the center of mass L_{cg} of longitudinal position to ensure that the pitching q and hence velocity at a given longitudinal location is calculated correctly. Thus, for a fuselage with m segments and a nose, the total averaged pitch damping moment coefficient contribution $C_{m_q(FUSELAGE)}$ is given by Eq. 5-51.

$$C_{m_q(FUSELAGE)} = \left(\frac{1.1 D_{eq} \left(L_{cg}^4 + \left((L_{nose} + \sum_{i=1}^{m} L_i) - L_{cg} \right)^4 \right)}{4 l A} \right) \left(\frac{q}{V_a} \right)^2$$
(5-51)

The contribution of a fin set of N fins (located at $L_{fin-set}$ relative to the moment center) to the pitch damping moment coefficient $C_{m_q(FIN\ SET)}$ is similarly derived via chord-wise integration over the fin by Niskanen [48] in Eq. 5-52.

$$C_{m_q(FIN\ SET)} = \left(\frac{0.6 N \left(\frac{s(r_c + r_t)}{2} \right) \left(L_{fin-set} + \frac{w}{2} + \frac{r_t + r_c}{4} \right)^2}{l A} \right) \left(\frac{q}{V_a} \right)^2$$
(5-52)

In the above relation, it is assumed that the effective projected area of the fins is half the total area at any given moment. The total pitch damping is then simply the sum of the nose-body contribution and the contribution from each fin set.

5.8.3.3 High Order Dynamic Derivatives

Rocket airframes may encounter aerodynamic effects characterized by second order dynamic derivatives, but the vast majority of these are eliminated by the use of mirror and rotational symmetry [57]. Notable effects include the Magnus force, vortex shedding and vortex impingement. These phenomena induce unsteady rolling moments and an estimation of this unwanted induced roll rate is often useful but difficult to obtain. The Magnus force is caused by the cross-flow of air when a rocket flies at an angle of attack whilst spinning about its longitudinal axis. The interaction between the circulation due to the spin and the cross-flow

creates asymmetric pressure distributions on either side of the airframe, inducing a side force. The contribution of the Magnus effect to the total normal force is generally minor.

5.8.4 Spin-Forcing and Spin (Roll) Damping Coefficients

Rolling or spinning refers to the angular velocity about the body frame x axis. Spin is often induced on unguided sounding rockets primarily to reduce trajectory dispersion caused by thrust misalignments, dynamic imbalances and unpredictable (turbulent) wind disturbances. A spinning rocket prevents rotational asymmetries in the vehicle loading and inertial characteristics from building up a directional bias in the trajectory by distributing these asymmetries equally about the vehicle spin axis. A secondary effect of spin is the introduction of an angular momentum about the spin axis. The gyroscopic tendency of the vehicle to preserve angular momentum and the orientation of the spin axis introduces an extra stabilizing effect against side loads. This effect is only significant in vehicles with small length to diameter ratios and high roll moments of inertia. Sounding rockets almost always experience unintentional spin induced from design and manufacturing non-idealities such as an off-axis center of gravity or misaligned fins. These effects are often used to inherently spin stabilize a rocket. Spin stabilization also carries a drag penalty which becomes significant at high spin rates.

There are several techniques to induce a sounding rocket to spin. The first category of techniques involves fin modification and includes fin-canting and the use of fin-tabs. Spin may also be induced actively using small spin thruster motors that fire tangentially about the vehicle spin axis. Furthermore, helical launcher rails may be used to impart an initial spin rate on rail-launched sounding rockets.

The spin (roll) damping moment is produced primarily by fin drag during spinning (rolling) motion. This effect is analogous to the rotation of a flat plate through a fluid. The radial distance from the roll axis of a point on the fin proportionally determines the velocity of that point for a give roll angular velocity. The total drag force is the integral of the differential drag force due to roll experienced at each point on the fin surface. Since the radial distance of a chord-wise strip of fin surface is constant, this integration is one dimensional in the span-wise (radial) dimension.

Canted fins will now be examined in more detail as they were used on the Phoenix-1A vehicle for spin stabilization. For vehicles with canted fins, the rolling moment coefficient may be separated into a roll forcing term and a roll damping term (Eq. 5-53). Canting forces a fin to fly

at an angle of attack equal to the cant angle, generating an added lift force which results in the roll forcing term $C_{l(f)}$. However, any small segment of fin surface on a rolling vehicle also encounters a tangential lift force proportional to the product of its radial distance from the roll axis and the roll angular velocity. The net effect is a resistance to roll which results in the roll damping term $C_{l(d)}$.

$$C_l = C_{l(f)} + C_{l(d)} \tag{5-53}$$

The method presented Niskanen [48] for trapezoidal canted fins was used for the prediction of the spin forcing moment and the spin damping moment. This method divides each fin into span-wise into a series of thin strips over which the pressure coefficient is assumed constant. The fin-cant angle δ acts as an angle of attack and the fin normal force derivative coefficient is used to calculate the normal force developed on each strip. A summation over all the strips is then used to calculate the total rotational force. The result is given in Eq. 5-54. The span-wise location of the mean aerodynamic chord y_{MAC} for trapezoidal fins is given by Eq. 5-55.

$$C_{l(f)} = \frac{(y_{MAC} + r_t) C_{N_\alpha} \delta}{l} \tag{5-54}$$

$$y_{MAC} = \frac{s(C_r + 2C_t)}{3(C_r + C_t)} \tag{5-55}$$

The subsonic and supersonic spin damping moment coefficient for a set of trapezoidal fins is also given by Niskanen [48]. The subsonic result is given by Eq. 5-56. Note the dependence on the roll rate. The supersonic result is given by Eq. 5-57.

$$C_{l(d)} = \frac{2N\pi p}{\beta A l V_a} \left(\frac{C_r + C_t}{2} r_t^2 s + \frac{C_r + 2C_t}{3} r_t s^2 + \frac{C_r + 3C_t}{12} s^3 \right) \tag{5-56}$$

$$C_{l(d)} = \frac{N}{Al} \left(\frac{C_r + C_t}{2} r_t^2 s + \frac{C_r + 2C_t}{3} r_t s^2 + \frac{C_r + 3C_t}{12} s^3 \right) \tag{5-57}$$

5.8.5 Prediction Results

Although an accurate and reliable range of empirical formulae for rocket aerodynamics does not exist over all flight conditions and flow regimes, an attempt has been made in this work to

145

compile the most basic set of empirical techniques into an internal aerodynamics prediction capability. This capacity is similar to that offered by the RasAero software and dedicated aerodynamic prediction codes such as Missile DATCOM. Table 5-2 summarizes the method used for each parameter by velocity region. Drag coefficient outputs for the Phoenix-1A airframe are presented in Figure 5-8 whilst lift coefficient outputs are shown in Figure 5-9 and center of pressure location outputs are shown in Figure 5-7. The validity of the HYROPS internal aerodynamics code was investigated by comparison against nominal Phoenix-1A trajectories run with RasAero aerodynamic table inputs. Figure 5-11 compares the axial force coefficient histories whilst Figure 5-10 compares the axial force magnitude histories. Figure 5-12 compares the Mach number histories. It is apparent form the results that although the internal model agrees fairly closely with the RasAero model, differences do exist in certain regions of the flight envelope, particularly in the transonic Mach number regime where both models rely heavily on interpolations to fair subsonic and supersonic techniques. The HYROPS internal model also shows distinct anomalies in its prediction of the zero angle of attack center of pressure location estimate. This has little effect on the trajectory as normal forces are by definition entirely absent or very small at or near zero angle of attack. The exclusive use of the aerodynamic lift and pitching moment coefficient slopes in the calculation of the zero angle of attach center of pressure location (Eq. 5-45) led to the loss of continuity from predictions for nonzero angles of attack, wherein the calculations are based primarily on the component-wise pitching moment coefficient and normal force or lift force coefficient.
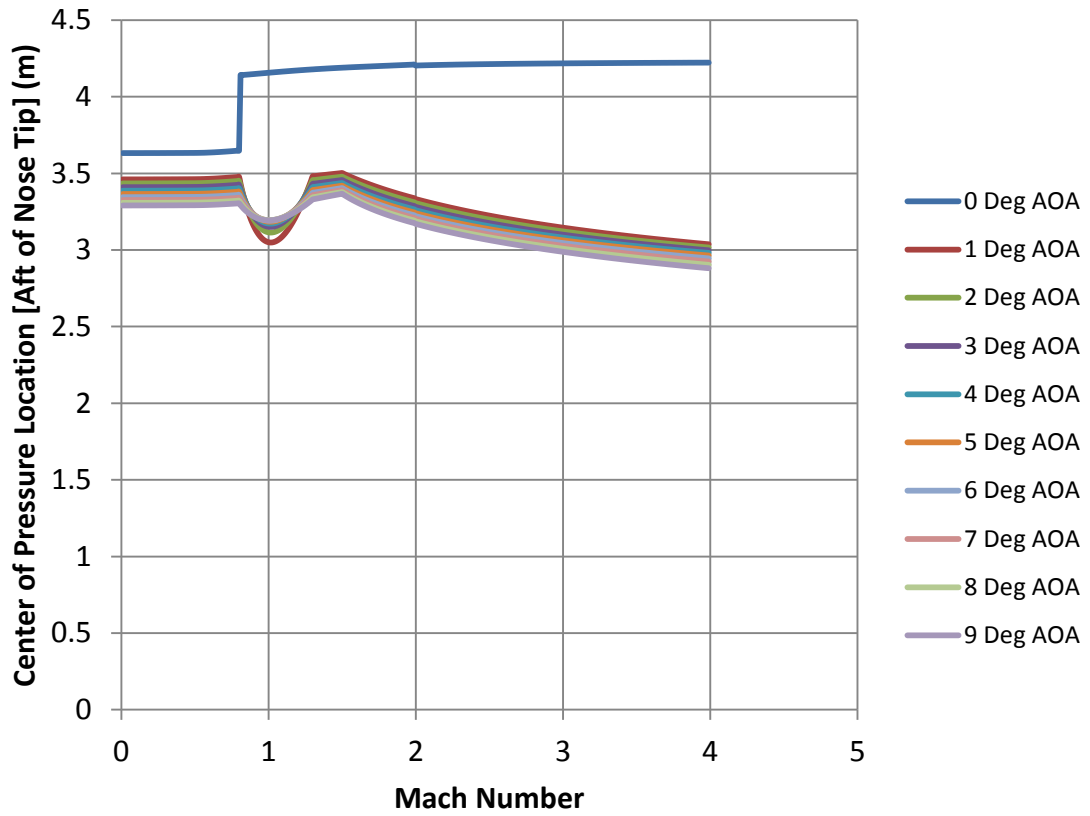
Figure 5-7: HYROPS predictions of the Phoenix-1A center of pressure location vs. Mach number for total angles of attack from 0° to 9°. Note the anomalous nature of the prediction for the 0° angle of attack case.
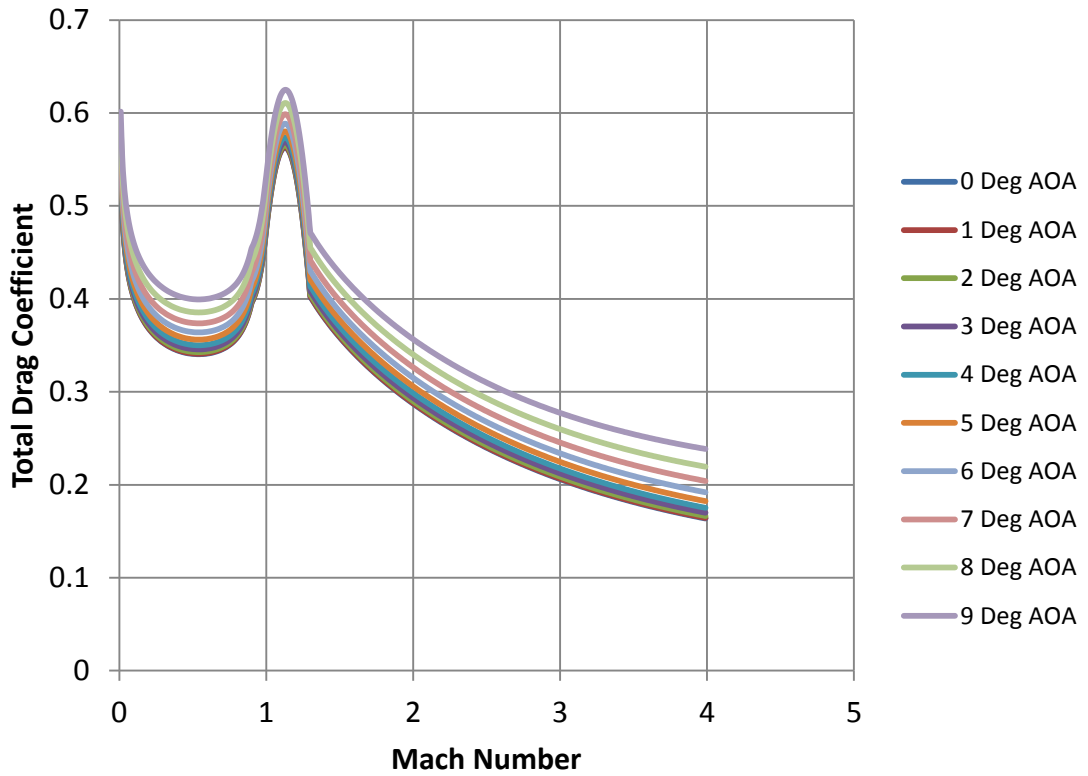
Figure 5-8: HYROPS Phoenix-1A predictions of total drag coefficient vs. Mach number for total angles of attack from 0° to 9°. The transonic drag rise is overestimated by the interpolation techniques.
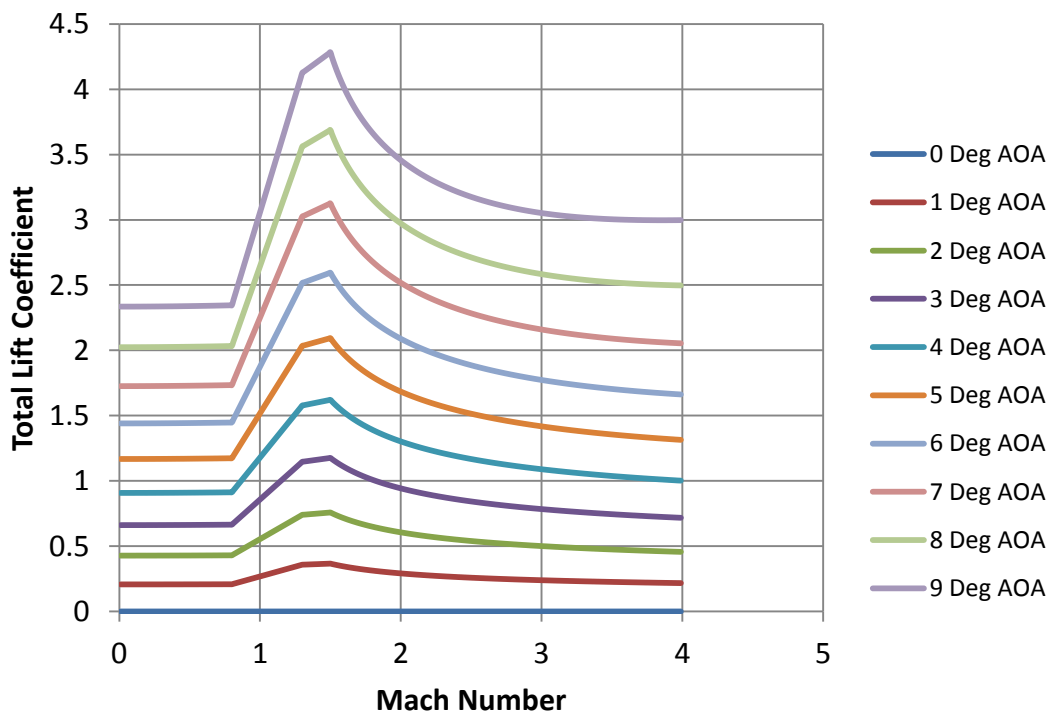
Figure 5-9: HYROPS Phoenix-1A predictions of lift coefficient vs. Mach number for total angles of attack from 0° to 9°

148
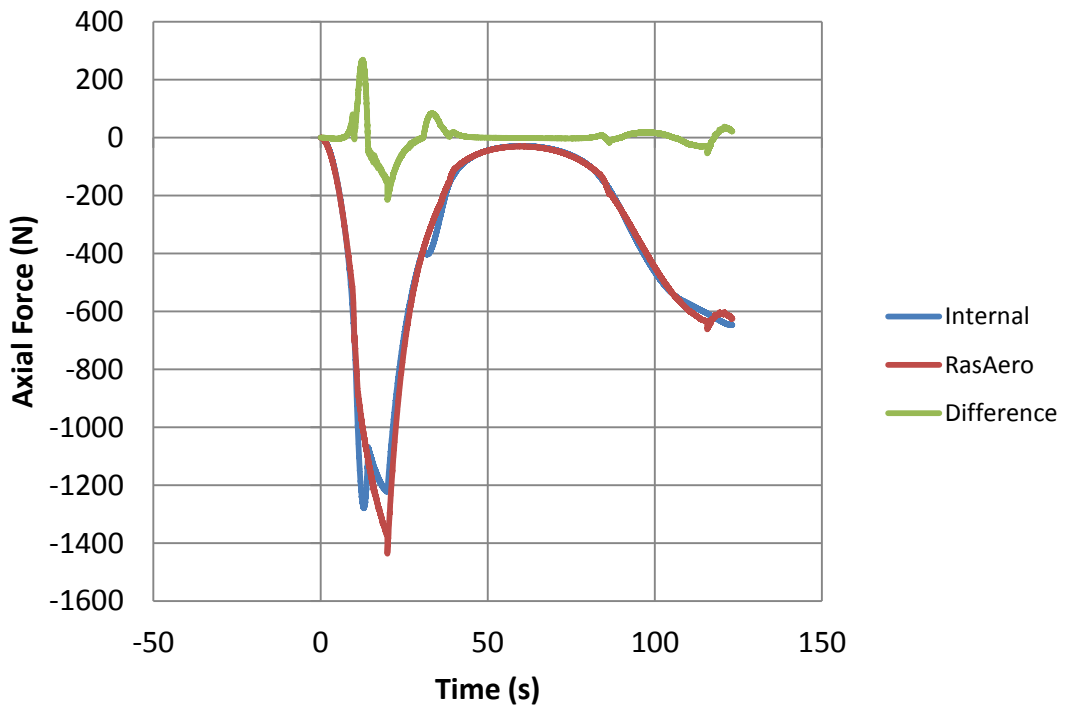
Figure 5-10: Comparison of Phoenix-1A nominal trajectory axial force history using aerodynamic coefficient tables from RasAero and the HYROPS internal aerodynamic prediction model, showing average deviations in the region of only 7 %.
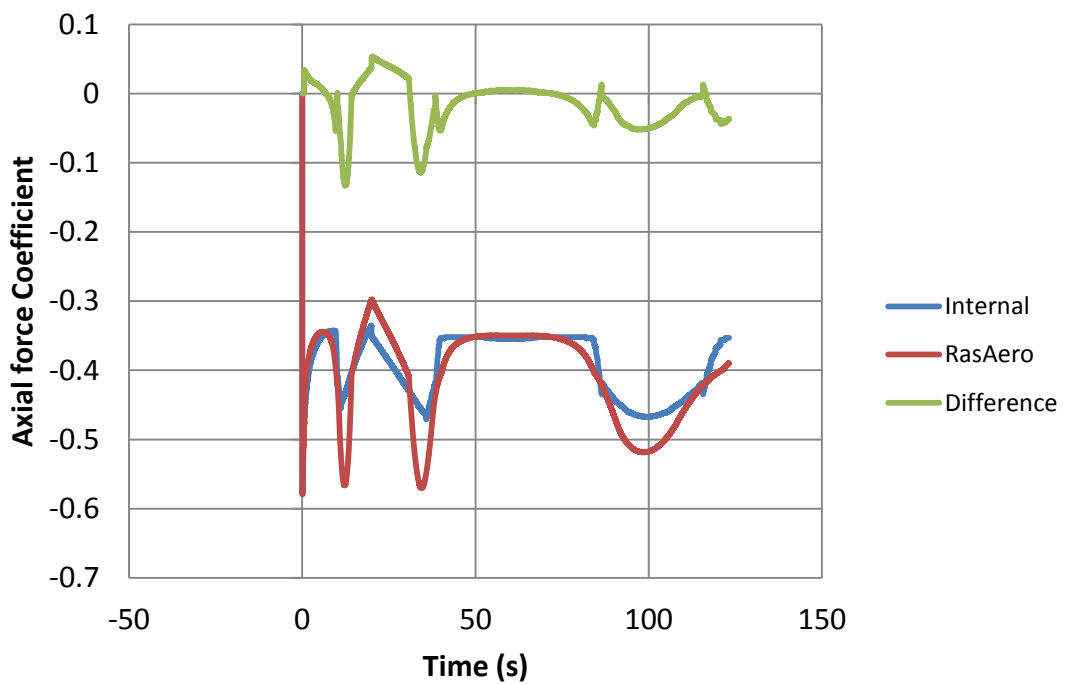
Figure 5-11: Comparison of Phoenix-1A nominal trajectory axial force coefficient history using aerodynamic coefficient tables from RasAero and the HYROPS internal aerodynamic prediction model, showing an average deviation in the region of 10 %.
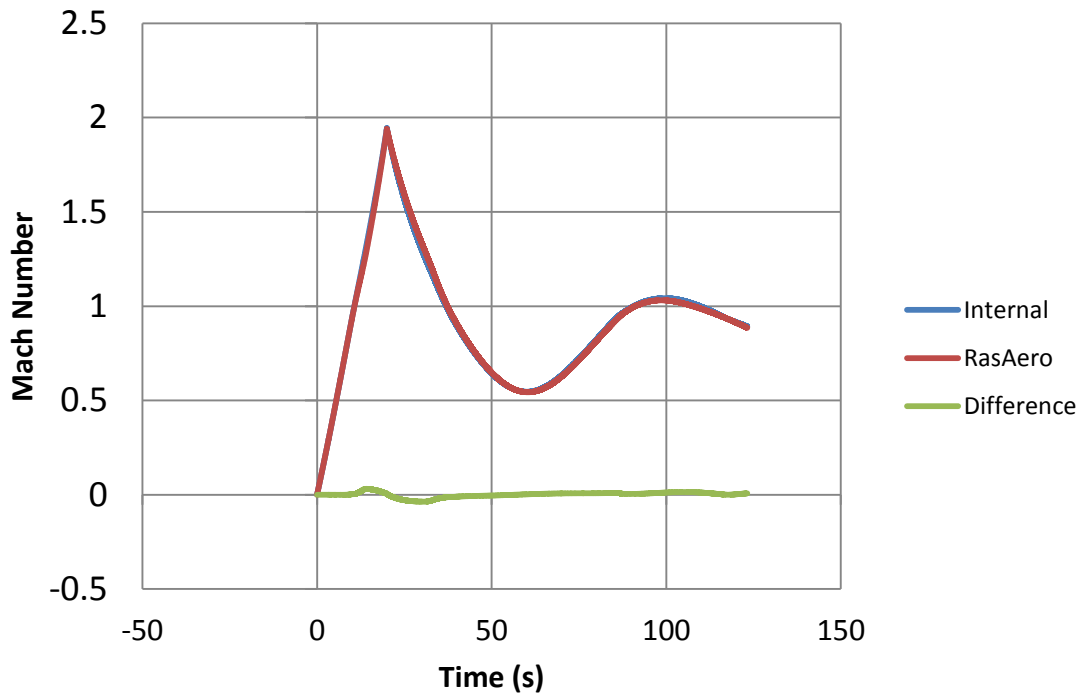
Figure 5-12: Comparison of Phoenix-1A nominal trajectory Mach number history using aerodynamic coefficient tables from RasAero and the HYROPS internal aerodynamic prediction model, showing very good agreement throughout the flight.

Table 5-2: Summary of prediction techniques by flight regime

Aerodynamic Characteristic	Subsonic	Transonic	Supersonic
Nose Pressure Drag (Ogive and Cone)	Eq. 5-22	Interpolation	Eq. 5-21
Cylindrical Fuselage Segment Pressure Drag	Eq. 5-23	Not Modeled	Not Modeled
Forward Transition Pressure Drag	Eq. 5-22	Interpolation	Eq. 5-21
Backward Transition Drag (incl. Boat-tail)	Eq. 5-28	Eq. 5-28	Eq. 5-28
Base Pressure Drag	Eq. 5-28 or Eq. 5-29	Eq. 5-28 or Eq. 5-29	Eq. 5-28 or Eq. 5-29
Skin Friction Drag	Eq. 5-31	Eq. 5-31	Eq. 5-31
Fin Pressure Drag	Eq. 5-27	Eq. 5-27	Eq. 5-27
Fuselage (Body of Revolution) Lift	Eq. 5-33 or Eq. 5-35	Interpolation	Eq. 5-36
Fin Lift	Eq. 5-38	Interpolation	Eq. 5-40
Fin Roll Forcing Moment	Eq. 5-54	Eq. 5-54	Eq. 5-54
Fin Roll Damping Moment	Eq. 5-56	Interpolation	Eq. 5-57
Fuselage Pitching Moment (and C.P.)	Eq. 5-34	Interpolation	Eq. 5-37

Aerodynamic Characteristic	Subsonic	Transonic	Supersonic
Fin Pitching Moment (and C.P.)	Eq. 5-46	Interpolation	Eq. 5-47
Fuselage Pitch Damping Moment	Eq. 5-51	Eq. 5-51	Eq. 5-51
Fin Pitch Damping Moment	Eq. 5-52	Eq. 5-52	Eq. 5-52

5.9 Aerodynamic Design of the Phoenix-1A Hybrid Sounding Rocket

5.9.1 High-Level Design Goals

Unguided sounding rockets are primarily designed in two crucial aerodynamic performance areas. The first is drag, representing the atmospheric resistance to the motion of the rocket. Drag forces hinder the motion of a vehicle, depleting kinetic energy. The design goal is to reduce drag as far as possible so as to provide maximal flight performance with minimal energy input. The second key aerodynamic design goal is stabilization. Stability implies the tendency to resist unwanted changes in vehicle orientation, so as to maintain the desired flight trajectory. Aerodynamic loads may be used to stabilize a vehicle inherently. The use of a stable airframe throughout flight is crucial to the performance of an unguided sounding rocket.

5.9.2 Design for Stability

A stable flight is characterized by a smooth, predictable trajectory with only transient deviations from equilibrium. Stability can be formalized as the passive tendency of aerodynamic forces to reduce any deviation from equilibrium. During flight a variety of unpredictable disturbances tend to deflect a rocket away from its preferred orientation and trajectory. Disturbances may include wind gusts, motor thrust fluctuations or misalignments and internal disturbances of a mechanical nature such as the sloshing of liquid fuels. In order to follow the nominal trajectory, a sounding rocket must reject these unpredictable disturbances. Vehicles with onboard control and actuation systems may actively reject disturbances. In contrast, disturbance rejection must be passive in unguided vehicles, leading to the notion of static stability.

A sounding rocket is statically stable in the longitudinal plane (pitch) if it tends to return to equilibrium when a pitching disturbance rotates the vehicle away from the orientation of zero pitch. This is only possible if the aerodynamic pitching moment created by the normal forces tends to reduce the angle of deviation. The center of pressure of a statically stable vehicle is thus more aft longitudinally than the moment center (center of mass) in a right handed coordinate system. All unguided sounding rockets are designed to be nominally longitudinally stable. The

degree of stability is measured by the difference in longitudinal position between the centers of mass and pressure, known as the stability margin. A common rule of thumb is the location of the center of pressure under all flight conditions between one and two calibers aft of the center of mass.The longitudinal location of the center of pressure is governed by the distribution of normal force generating airframe components along the longitudinal axis. In this regard, the airframe of a typical sounding rocket may be divided into two categories: surfaces of revolution and fins. Surfaces of revolution with increasing radius in the aft-ward direction produce positive normal force and cause the center of pressure to move forward towards the nose. Such surfaces include nose cones. Conversely, surfaces with decreasing radius in the aft-ward direction, such as boat-tails, produce negative normal force and tend to move the center of pressure aft-ward.

The rotational inertia of a vehicle tends to oppose changes in orientation and may be used to stabilise a vehicle. This effect is known as gyroscopic stability and is only effective in vehicles that possess a large roll moment of inertia. Nevertheless, most rockets are long and slender and their roll moment of inertia is small compared to their longitudinal moments of inertia. Therefore, significant gyroscopic stability is only possible with relatively high spin rates which are only attained at high speeds. However, stability is of greatest concern when vehicle speeds are low and disturbances strong. Therefore, rocket stability design is focused on ensuring stability in the initial period of flight just after launch, as well as during the coasting phase and ballistic descent. Vehicles with a low thrust to weight ratio experience slower acceleration and are thus more susceptible to wind destabilization. These factors lead to the use of launch rails to provide a rocket with a sufficiently high initial velocity. The sizing and longitudinal positioning of significant lift generating components such as fins and after-bodies are the key parameters in the design of inherently stable airframes. The design constraint is that the center of pressure must lie sufficiently aft of the center of gravity for the entire flight condition envelope of the vehicle.

The Phoenix-1A airframe was designed around the fuselage structure which had too many constraints from the other subsystems it housed such as the propulsion system and recovery system. Therefore, adequately large fins were the only means available to ensure static stability. The fins were positioned as far aft on the fuselage as possible, to ensure that the center of pressure could be kept further aft. During the structural design the mass distribution was also kept as far forward as possible to move the center of mass further forward. The boat-tail length was minimized and the taper angle restricted to ensure that it produced a minimum of negative normal force. Similarly, the nose fineness ratio was increased to produce positive normal force at the fore end of the airframe.

5.9.3 Nose

The nose cone is the foremost section of the airframe. They are usually bodies of revolution with aft-ward increasing radius. Several revolution profiles are commonly used on sounding rockets, including hemispheres, tangent and secant ogives, cones, power curves, the Haack series curve and piecewise combinations thereof. The subsonic nose pressure drag is generally insignificant. However, pressure wave drag and shock effects contribute significantly to total drag in the transonic and supersonic flight regimes. The choice of nose profile is based on the flight regime and the thermos-structural performance of the airframe material. The choice of optimal nose profile for various flight applications has been the focus of much research from the aerospace industry and amateur rocketry enthusiasts alike. The Haack series has been mathematically demonstrated to produce minimum drag at zero angle of attack [62]. Figure 5-13 shows examples of common nose profiles and ranks them in order of drag performance in transonic flight.
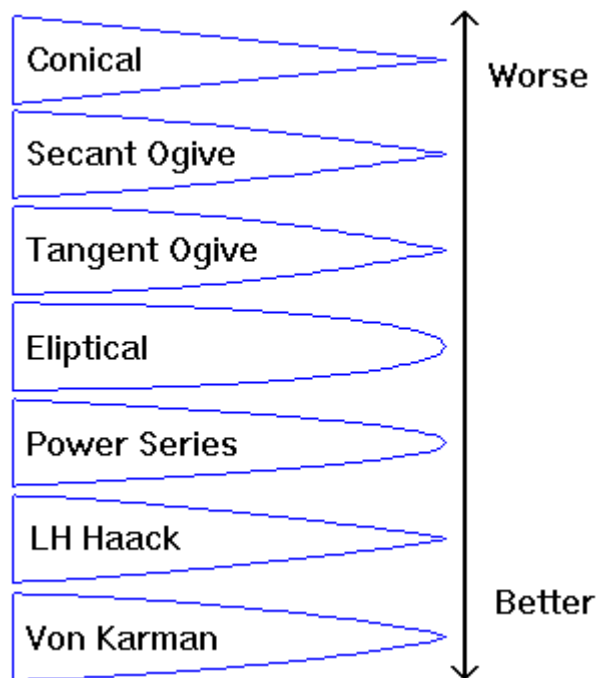
Figure 5-13: Various nose cone profiles used on all forms of rockets, arranged in order of suitability to transonic flight [62]

Nose tips experience high thermal loads due to fluid stagnation and proximity to Mach cones. The choice of pointed or blunted nose tips is based on the predominant flight regime and the thermo-structural load carrying capacity of the nose tip material. Often, the nose tip must be reinforced using materials capable of adequate thermal performance. High supersonic and hypersonic vehicles often use blunted nose shapes as they avoid direct contact between the

Mach cone (shock wave front) and the nose tip. Low subsonic vehicles also benefit from a small radius at the nose tip. Blunted noses are characterized using the bluffness ratio, which is the ratio of the nose radius to the blunted tip radius.

A tangent ogive nose was selected for the Phoenix-1A. It was noted that the vehicle would encounter transonic and low supersonic speeds during the major part of its ascent, especially in the flight phases where it would build up altitude. Certain profiles are more effective in the transonic and low supersonic velocity regimes, as seen in Figure 5-14. The cone was not selected as it limits nose volume and would negatively impact payload volume whilst offering little to no drag reduction advantage. Of the options available, the tangent ogive was also the best compromise between simplicity and performance. The accurate manufacture of the other profiles would be challenging due to the presence of mathematically defined curves not easily machined using conventional linear or circular contour machining operations. Larger fineness ratio noses offer less drag and the Pheonix-1A was designed with nose fineness ratio of five to ensure favorable drag characteristics and ample payload volume. As discussed in the next section (5.9.4) the diameter of the nose base was fixed to 200 mm resulting in a total nose length of 1 m.

Comparison of drag characteristics of various nose shapes in the transonic-to-low Mach regions. Rankings are: superior (1), good (2), fair (3), inferior (4).

Figure 5-14: Transonic and low-supersonic nose performance comparison against Mach number for various nose profiles. Adapted from [63]

5.9.4 Fuselage Sections

Sounding rockets mid-body structures most often use a circular cross section, as this minimizes surface area, which in turn ensures minimal friction drag. A cir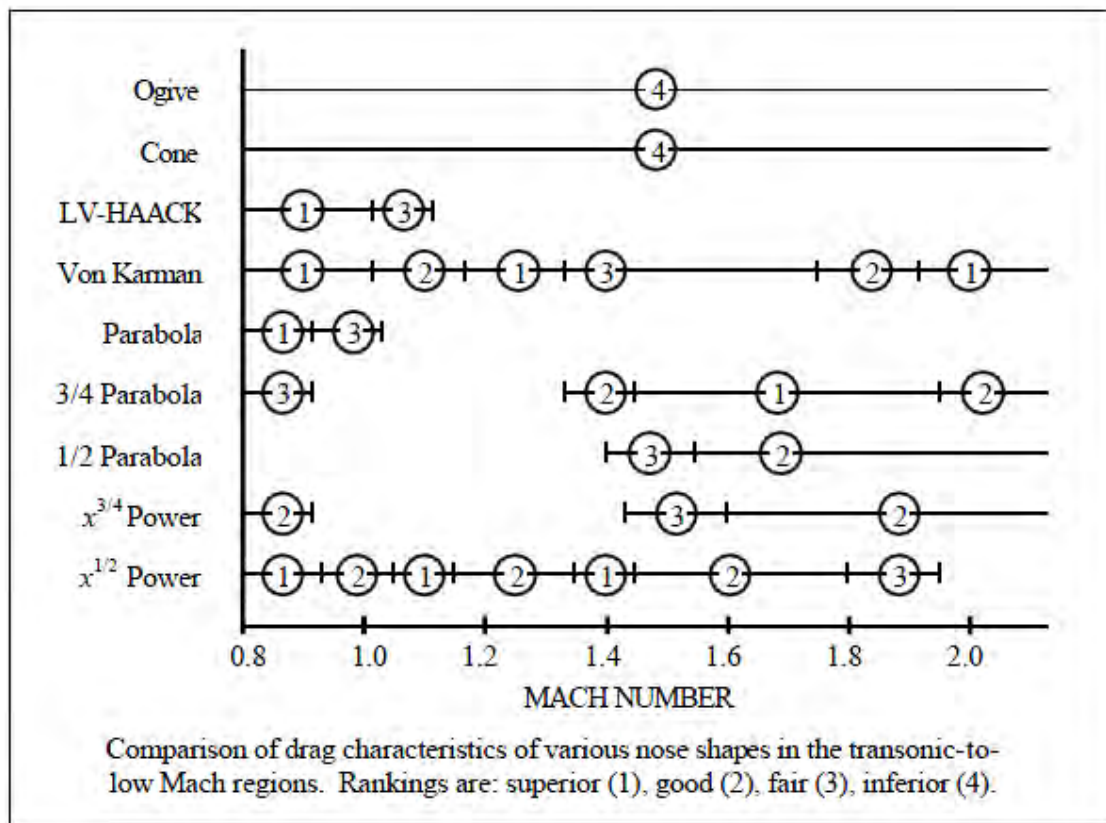cular cross section also facilitates ease of manufacture and offers optimal load carrying capacity. The main fuselage design parameter is then the fineness ratio, defined as the ratio of the length of the fuselage to its largest diameter. The fineness ratio determines the overall surface area and the volume of the fuselage. Cylindrical fuselage sections do not produce normal forces at zero angle of attack and hence do not generate pressure drag or shock waves. The primary source of fuselage drag is consequently friction drag and hence it is desirable to minimize the total surface area by judicious selection of the fineness ratio.

The transonic area rule states that transonic wave drag is minimized if the total vehicle cross sectional area remains constant over the length of the vehicle [64]. This may be exploited by reducing the fuselage diameter at longitudinal locations where other airframe components such as fins and protrusions increase overall cross sectional area. The area is applicable to vehicles that experience significant periods of transonic flight. The rule is often applied by reducing the tail fuselage diameter in compensation for the fins.

Secondary design considerations for conventional cylindrical mid-bodies include protrusions. Protrusions may include fastener heads, launch shoes, launch lugs, launch buttons, telemetry antennae, camera probes, pressure sensors and similar irregularities. These tend to disrupt the flow and may induce significant drag penalties, especially if flow stagnation occursdue to their presence. Furthermore, large protrusions may induce asymmetric aerodynamic tendencies which are extremely difficult to characterize, creating uncertainty and lowering performance reliability. It is essential during the structural design of an airframe to minimize the number and size of protrusion on the fuselage. If unavoidable, they should be placed in a radially symmetrical fashion around the body x axis to preserve the overall airframe symmetry.

The Phoenix-1A fuselage primary diameter of 200 mm was fixed by the oxidizer tank diameter which in turn was governed by materials availability, manufacturability and cost constraints. The secondary diameter was the PV-1 motor casing outer diameter, specified by the motor design to be 180 mm. The area rule was exploited on the vehicle by placing the fins on the casing. The backward facing transition from the tank diameter to the casing diameter, structurally representing the oxidizer feed system, was assigned a length of 300 mm with a linear diameter reduction, resulting in a taper angle of less than 2°. Such a shallow taper angle would not generate a significant amount of negative lift nor lead to flow separation [21].

5.9.5 Fins

Fins are the commonest passive stabilization device used on sounding rockets. Their design is focused on producing the correct amount of lift at a minimum drag penalty. A large variety of fin designs have been proposed for a multitude of applications (Figure 5-15). The types most suited to sounding rockets include common coplanar fins and the more exotic wrap-around fins (WAF), tangent fins, ringtails and grid-fins. The latter display more complex aerodynamic characteristics and tend to be used only where space is very limited. A conventional coplanar fin set consists of several identical thin planar surfaces projecting from the fuselage of a sounding rocket ata specific longitudinal location. A selection of the appropriate fin variety should be based on several design criteria. These include the operational Mach number regime and characteristics in roll. The optimal fin configuration should provide sufficient lift for stability whilst minimizing drag.

TETRAGONAL   TRIGONAL   TANGENTIAL

WRAP-AROUND   GRID   MULTI-GRID
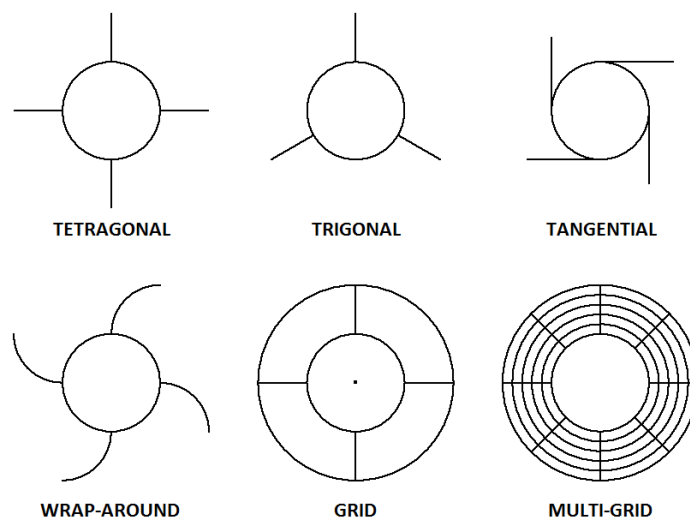
Figure 5-15: Various fin configurations viewed from the fuselage rear. Note the range of geometries which may be used to generate lift, despite their similar functionality.

Planar fin aerodynamic effectiveness is strongly affected by the fin cross section profile and the plan-form geometry (Figure 5-16). It is desirable to design fins for maximal lift generation efficiency. Regions of turbulent flow near the fin roots, leading edges and trailing edges must be minimized for this reason. Thermo-structural considerations often limit maximal allowable lift loads subjected to a fin aero-structure. Stagnation thermal loads exist at the fin tips and fin flutter considerations limit the maximum normal loads.

The plan-form geometry is most relevant in the positioning of fin center of pressure and center or pressure travel due to incidence whilst the plan-form area determines the absolute lift force

produced. The commonest plan-form shape used is the trapezoid as it is simple yet effective for most applications. The position of the fin center of pressure is important in overall vehicle stability as a large fraction of overall lift is generated by the fins. This motivates the use of swept back trapezoidal fins over rectangular plan-form shapes. Larger plan-form areas produce greater lift, drag and induced drag forces.
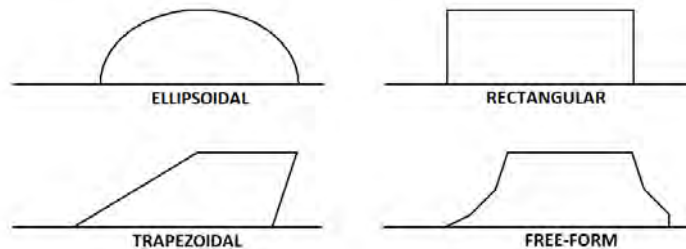
Figure 5-16: Fin plan-form designs used on sounding rockets.

Cross section profiles commonly used on sounding rocket fins include standard NACA airfoils, biconvex profiles, square profiles, hexagonal profiles and diamonds (double-wedges). Figure 5-17 shows several popular profiles. Once a plan-form and cross-section combination is chosen, the maximum thickness is the primary design parameter. Despite their variety, all the profiles may be roughly characterized using a combination of pointed, squared or rounded trailing edges and leading edges. The fin cross section profile correlates strongly with fin pressure drag and lift characteristics, in a similar manner to aircraft wing airfoils. Trapezoidal fin drag is mainly determined by the fin thickness to chord ratio, taper ratio and aspect ratio. Induced drag due to tip vortices is also a significant contributor. At supersonic speeds sharp leading edges provide better wave drag performance. In contrast, blunt edged airfoil sections produce less drag at subsonic speeds. The choice of profile is governed by drag requirements, the need for spin (which may be induced using cambered fins) and the most importantly manufacturing constraints. The manufacture of accurate asymmetric or complex fin profiles using specialized materials is often too costly or involved and may force the designer to use a less optimal profile.
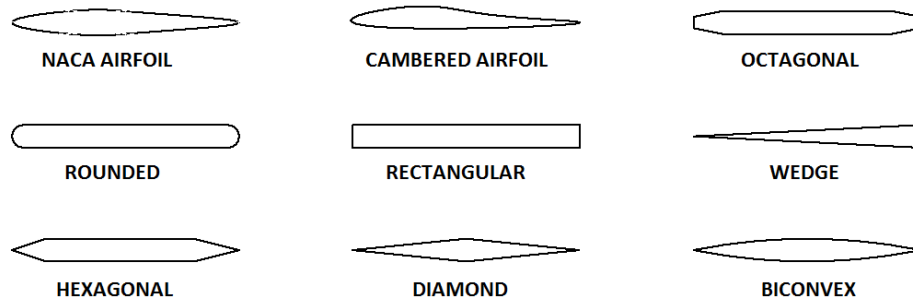
Figure 5-17: A variety of fin cross-section has been developed to tailor the lift and drag characteristic of planar fins.

The fin set overall aerodynamic loads are not simply a multiple of the individual fin characteristicsdue to fin-fin interference and fin-body interference, especially in the transonic and supersonic velocity regions. The primary consideration is the number of fins. A greater number of fins in a set allows smaller plan-form area but may increase overall drag due to interference effects and wave drag. Severe fin interference occurs at supersonic speeds when Mach cones from adjacent fins impinge. Similarly, fin-body interference occurs due to fin Mach cone impingement on the body. The vast majority of sounding rocket designs employ three or four relatively large fins in a set, aiming to minimize interference effects. A very basic approximation of the interference normal force coefficient slope induced on the fins due to the body $C_{N_\alpha}^{F(B)}$ is given by Eq. 5-58.

$$C_{N_\alpha}^{F(B)} = 1 + \frac{r_t}{r_t + s} \tag{5-58}$$

Fins are more prone to aero-elastic effects due to their high surface area to volume ratio. Any fin manufactured from an elastic material will flutter in response to unevenly distributed aerodynamic loads across its surfaces. If the fins lack adequate rigidity, flutter induced cyclical stresses may cause the fins to shear or break apart. Several researchers have investigated fin flutter due to the effect being a significant cause of failure in early sounding rocket flights. The method adopted in this work is a simplification presented and detailed in Chapter 6. This particular approach relates the maximum safe free-stream velocity and pressure to the fin geometry and effective shear modulus of the fin material. A safe maximum ratio of fin geometric parameters and shear modulus is known to exist, based on empirical observations of fin flutter failures. Refer to Chapter 6, section 6.7 for the application of fin flutter analysis to the Phoenix-1A fin design.

The Phoenix-1A was specified with a single set of four fins to limit individual fin size, facilitate ease of performance analysis, manufacture and launch and also to maintain airframe tetragonal symmetry as it reduces vehicle performance uncertainties. The trapezoidal plan-form was selected as it is commonly used and its characteristics are accurately predicted using the analytical techniques already discussed in this work. Trapezoidal fins possess simpler geometries and are cheaper to manufacture accurately when compared to other geometries such as elliptical fins. There was no overriding need to limit center of pressure travel hence the fin sweep was limited to give a straight trailing edge, resulting in what is known as a 'clipped-delta' configuration. The total area needed per fin was determined to be 0.08 m^2 using a combination of the HYROPS tool and RasAero software in the iterative vehicle design process, constraining the center of pressure to lie at least one caliber aft of the center of mass throughout nominal flight. A final design with root chord of 600 mm, tip chord of 200 mm, sweep of 400 mm and a span of 200 mm was specified. The fin location was specified to be 50 mm fore of the boat-tail root, situating the fin set on the Phoenix-1A PV-1 motor casing. This also constrained the fin root chord to 600 mm. The hexagonal cross section was selected primarily due to manufacturing constraints as machinery available to the program would not be able to machine compound curves on the thin fin plates. The leading and trailing edge tapers were also specified to 25 mm based on machining limits. This design was a compromise between the better performing biconvex profile and simpler rounded and rectangular profiles. The fin maximum thickness was calculated to be 6 mm based on the fin flutter analysis mentioned earlier. More detailed discussions of the structural design calculations and the manufacture of the fins are given in Chapter 6.

5.9.6 After-bodies (Boat-tails)

Boat-tails are tapered fuselage sections at the base of a rocket. They are used to reduce the effective base drag area and hence the base drag coefficient. The aim of rocket boat-tail design is to minimize base area without causing flow separation or destabilization. Flow separation is usually avoided for subsonic atmospheric flows when the taper angle is less than 8°. The length of the boat tail section is also highly influential on the overall drag reduction, as too long a boat-tail produces excessive wave drag. The negative lift produced by a boat tail moves the overall center of pressure towards the nose, decreasing the vehicle static stability margin. Therefore, boat-tails designs tend to minimize length whilst maintaining an acceptable area reduction ratio. The magnitude of the boat tail normal force may be approximated using slender body theory, which predicts that the center of pressure of a conical boat-tail is located 0.6 boat-tail lengths aft of its base [21]. Given these numerical indicators, the Phoenix-1A was specified with a boat-tail

with an 8° taper angle and a length of 90 mm, approximately half the diameter of the original base (i.e. the Phoenix-1A PV-1 motor casing diameter of 180 mm).

5.9.7 Phoenix-1A Aerodynamic Design Specification

An overall geometric specification for the Phoenix-1A airframe was derived using the techniques described in this chapter through the iterative design process outlined in Chapter 6. It should be noted that various minor deviations from this specification were to be expected on the actual hardware arising from manufacturability, assembly and integration constraints. Therefore, this specification was treated as a guideline rather than a strict definition. Figure 5-18 shows the major dimensions on this airframe specification. The major dimensions of the vehicle were the length of 4.55 m, the maximum body diameter of 200 mm and the maximum fin span of 580 mm. These dimensions were significant in the design of the vehicle's GSE and its integration thereon. Care was taken during the aerodynamic design specification process to ensure that the airframe would be compatible to the GSE and the separately design PV-1 flight motor. Protuberances such as launch lugs and fastener heads were also tolerated on the airframe when crucial to the integration of the vehicle and its supporting systems.
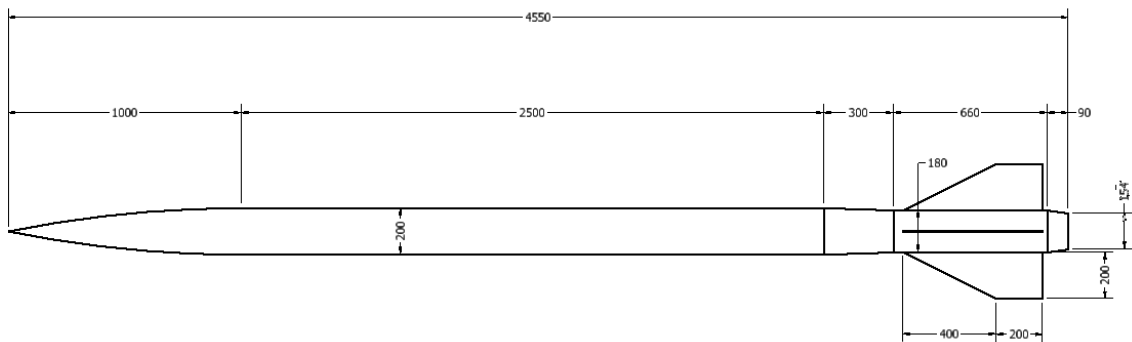
Figure 5-18: The Phoenix-1A airframe specification used for structural design.

160

CHAPTER 6

Phoenix-1A Structural Design and Manufacture

6.1 Introduction

This chapter describes the methodology and process used for the structural design of the UKZN Phoenix-1A sounding rocket aero-structure, excluding the vehicle's PV-1 motor combustion chamber and its internals. The PV-1 flight weight hybrid rocket motor mechanical design by Genevieve [4] was an integrated part of this design process from its inception. Design guidelines from the aerospace and defence literatures were followed where relevant. A guiding philosophy of the design was to minimise complexity, aiming to limit costs, increase robustness and mitigate performance uncertainty. The design was constrained to the airframe geometry specifications and the vehicle flight dynamics characteristics through multiple dependencies hence the designs described in this chapter cannot be viewed independently. The design process was related to the methods of Chapter 3 and Chapter 6 as well as the design of the vehicle's electromechanical systems as described in Chapter 7. Figure 6-1 shows a cutaway view of the Phoenix-1A's major structural subsystems. Note the PV-1 hybrid motor integrated at the rear of the vehicle.
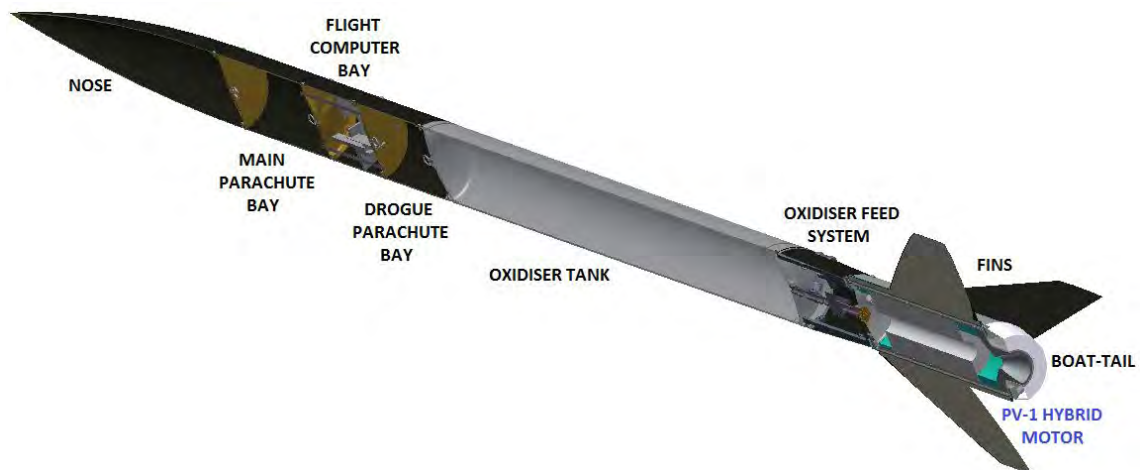
Figure 6-1: CAD cutaway of the Phoenix-1A design, showing only the major structural components.

6.2 Iterative Design Loop

The Phoenix-1A structural design was an iterative process based on data obtained through simulation, involving the UKZN HYROPS tool as well as the materials selection and costing process and the FEA and CFD analyses phases. The iterative process was necessitated by the high degree of coupling between the vehicle's flight performance dynamics, its aerodynamic characteristics and the physical resources available to the design in terms of funding and access to manufacturing and materials technologies. The process started with the vehicle subsystems being modelled in the HYROPS tool using the current best estimates of component materials (hence densities) and dimensions. The resulting structural geometry was then assigned a best fit external aerodynamic geometry. The combination of the structural configuration model and aerodynamic geometry model was then simulated through the HYROPS tool and the vehicle flight performance predicted. In the case of the flight performance specification not being met, the process reverted to the design of the structural and aerodynamic configurations and imposed alternative configuration choices and/or material choices. If the flight performance specifications were met, the design progressed to the next phase wherein the materials availability and manufacturability of the structural components was surveyed. If the survey outcomes were negative, the design again was reverted to the initial structural and aerodynamic configuration design. If the survey outcomes were positive, the process progressed to the next phase wherein the detailed structural geometry design and FEA analyses were performed at the component level along with CFD analysis of overall vehicle thermal loading if necessary. This phase also involved the analysis of internal subsystem loads such as the parachute deployment shock loading. The design was again reverted to the initial phase if the structural and thermal reserve factor specifications were not met. If the design was deemed successful, a refined structural configuration model and aerodynamic model was implemented in the HYROPS tool and the final flight performance prediction was generated. The iterative design process output could then be optimised using the constrained optimisation function of the HYROPS tool if deemed necessary. The constraints for such a process would be derived from the results of the materials and manufacturability surveys, FEA and CFD analyses and the vehicle thermal, structural and flight performance specifications. A schematic flow diagram of the iterative design loop is shown in Figure 6-2. The process is defined using bi-directional arrows to emphasize the possibly non-linear path which may be taken in each iteration.
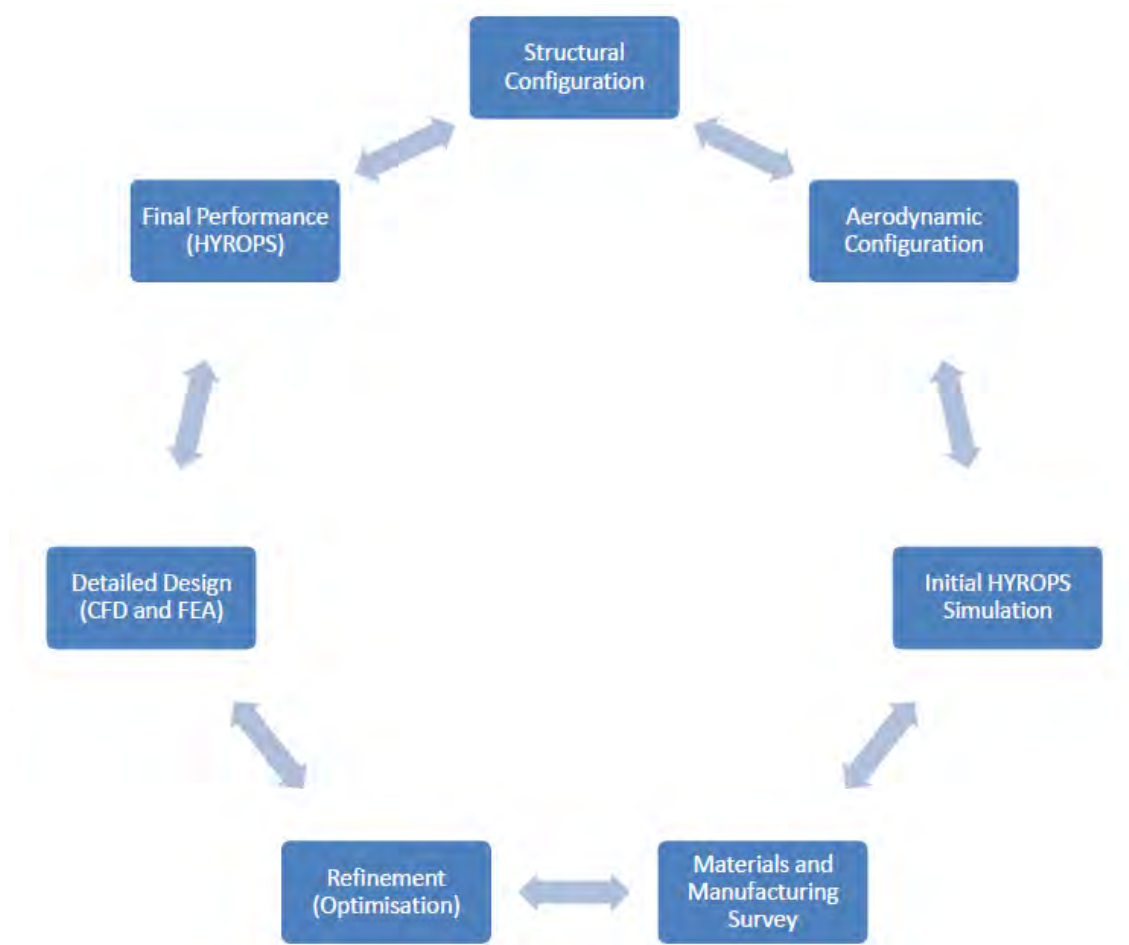
Figure 6-2: Stages of the iterative design loop reflected the couplings between performance and design.

6.3 Materials Availability Survey and Selection Criteria

Emphasis must be placed on materials selection during the design of a sounding rocket. Material choices often determine the trade-offs between overall performance, cost and reliability. The vehicle thrust-to-weight ratio and fuel-to-mass ratio parameters are strongly related to material specific strength, which is defined as the ratio of an isotropic material's tensile yield strength to its bulk density. The selection of structural materials for sounding rockets is also dependent on several other material properties such as

1) Yield strength under compressive and shear loading
2) Thermal performance in the operational temperature range
3) Rigidity (resistance to shear deflections)
4) Stiffness (resistance to tensile and compressive deflections)
5) Tolerance to vibration, shock, fatigue and impact loads

6) Electrochemical compatibility with operating environment

The design required the selection of materials capable of providing the specified component performance within the cost, availability and manufacturability constraints imposed by the programme resources. The selections were part of the high-level iterative vehicle design process. The convergence of such a process is not guaranteed hence a fair amount of engineering judgement was also needed to ensure that the materials selection process was comprehensive enough in its scope to meet the vehicle's design specifications whilst keeping within the design time frame and programme budget. It was noted from the very early phases of the work that these constraints could be ranked in decreasing priority as follows

1) Cost
2) Local availability (in desired geometry, amount and state)
3) Local manufacturability
4) Impact on vehicle performance
5) Suitability for re-use
6) Aesthetic appeal
7) Innovation

A summary of data for various materials considered for the structural design of the Phoenix-1A airframe and internal structures is presented in Table 6-1.

Table 6-1: Materials considered for the Pheonix-1A structural design

Material	Yield Strength (MPa)	Young's Modulus (GPa)	Density (kg/m^3)	Typical Applications	Relative Cost
Stainless Steel (316)	220	200	8000	Oxidiser Tank Structural	Low
Stainless Steel (431)	690	215	7700	Oxidiser Tank Structural	High
Duplex Stainless Steel (SAF 2205)	460	200	7800	Oxidiser Tank Structural	High
Duplex Stainless Steel (SAF 2507)	530	200	7800	Oxidiser Tank Structural	High

Material	Yield Strength (MPa)	Young's Modulus (GPa)	Density (kg/m³)	Typical Applications	Relative Cost
Aluminium Alloy (6082-T6)	240	70	2685	Oxidiser Tank Structural Fins	Moderate
Aluminium Alloy (7075 T6)	503	71.7	2810	Oxidiser Tank Structural Fins	Very High
Aluminium Alloy (2219 T851)	352	73.8	2840	Oxidiser Tank Structural Fins	Very High
Titanium Alloy (Grade 5)	1100	114	4430	Oxidiser Tank Structural Fuselage Fins	Extremely High
CFRP (epoxy matrix)	250 to 450	70	1600 to 1800	Oxidiser Tank Fuselage Fins	High
Kevlar FRP	100 to 1000	20 to70	1400	Fuselage Fins	High
GFRP	85 to 340	6.5 to 12	1000 to 2000	Fuselage Fins	Moderate

6.4 Overall Mass Budgeting

The Phoenix-1A was designed without a baseline from which overall vehicle dimensions and masses could be extrapolated for a first iteration aero-structure. This necessitated that the HYROPS tool be used to explore the solution space. A first iteration design was derived by placing the key structural subsystems around the PV-1 flight motor and the PV-1oxidiser tank in particular. An approximate mass budget was allocated to each subsystem based on the vehicle payload specification and the predicted flight performance trends against varying fuel masses and varying vehicle launch masses. Fuel to mass ratios and subsystem weight fractions (of total vehicle mass) from existing sounding rocket designs were also used as guidelines when such data was available in the literature. In general, it was noted that single stage low and medium

altitude hybrid sounding rocket designs rarely achieved fuel-to-mass ratios greater than 0.5, with typical launch masses (for vehicles with motor specific impulse of about 200 s) lying in the 80 kg to 100 kg range. The single subsystem with the greatest mass budget was almost always the oxidiser tank. The payload typically comprised of less than 10 % of the vehicle launch mass and often less than 5 %. Approximately 60 % of the total vehicle empty mass was devoted to the propulsion system in most designs. This was primarily due to the high fuel internal pressures, requiring large wall thicknesses on fuel storage tanks and motor combustion chambers. Table 6-2 lists the major subsystems and their mass allocation.

Table 6-2: Phoenix-1A subsystems mass budget

Subsystem	Mass (kg)	% of Total Mass	% of Empty Mass	Flight Phase
Oxidiser Tank	18.5	19.47	32.17	All
PV-1 Motor	14.5	15.26	25.22	All
Forward Airframe	5.0	5.26	8.70	All
Oxidiser Feed System	3.0	3.16	5.22	All
Rear Airframe	6.0	6.32	10.43	All
Flight Computers	0.5	0.53	0.87	All
Recovery Hardware	4.0	4.21	6.96	Descent
Payload	1.0	1.05	1.74	All
Fuel	37.5	39.47	65.22	Boost
Internal Supporting Structures	5.0	5.26	8.70	All
Phoenix-1A	**95.0**	**100.00**	**165.22**	**N/A**

6.5 Finite Element Analysis (FEA)

Knowledge of stress distributions and deflection distributions are essential in the mechanical design of most of the structural components of a sounding rocket. The complex nature of the geometry and combined loading conditions on the Phoenix-1A structural components made analytical prediction of overall structural performance impossible. This was also often true at the component level. Critical components were analysed using Finite Element Analysis (FEA) software to validate their design. The finite element (FE) method is a numerical technique used to solve continuum mechanics problems governed by partial differential equations (PDE's) over complex domains. The method relies on the process of discretisation, which entails dividing the complex domain into numerous small finite 'elements' over which an algebraic approximation of the governing differential equation is easily integrated using numerical methods. In FEA

software, this process is known as meshing. In the structural mechanics problem, the FE method is used to calculate the components of the global matrix equation (Eq. 6-1) that proportionally relates loads acting on each element to nodal displacements across all the finite elements. The interrelation of the unknown internal loads and nodal deflections over adjacent element results in the large linear system which is solved using iterative matrix inversion techniques such as the Gauss-Siedel method, method of successive over-relaxation, conjugate gradient (CG) method or algebraic multi-grid (AMG) method. The stress, defined as the force acting along a certain direction in the material per unit area, is then derived by spatial differentiation of the internal force distribution solution. Linearity is expressed through the Young's modulus, the constant of proportionality between stress and displacement. The Phoenix-1A structural components were all specified to operate in the linear (elastic) region and all except the forward airframe shell were built from either steel or aluminium alloys, both of which are isotropic materials. The linearity property, combined with the absence of any significant transient loading with the exception of the fins, allowed the FEA process to focus solely on the linear static response to the loading conditions.

$$F_I = K\delta + F_E \qquad\qquad (6\text{-}1)$$

The MSc SimXpert FEA package was used for linear static stress analysis of the Phoenix-1A structural components. This package is a Windows front-end user interface for the MSc NASTRAN FE solver. The SimXpert interface was used for the input of the component geometry in the IGES format, converted from component models designed in the Autodesk Inventor CAD modelling package. The geometric models were then linked to a NASTRAN material model defined using the material stiffness properties and Poisson's ratio. Isotropic materials required a single stiffness applicable in all directions whereas non-isotropic materials were defined using their stiffness characteristics along the different vector orientations.

MSc NASTRAN meshes geometries using a variety of element types. Linear, planar and volumetric elements are used for meshing one, two or three dimensional structures respectively. Element types may also be classified according to whether they allow linear or quadratic variation of properties. Linear elements possess nodes only at their boundary interfaces with adjacent elements whilst quadratic elements possess additional nodes at the geometric centres of their edges, areas or volumes. Quadratic elements allow a higher order approximation of variables in the continuum at the expense of greater computational and memory requirements. Table 6-3 lists various relevant element types available in NASTRAN.

Table 6-3: NATSRAN finite element types

Element	Dimensions	Nodes	Order	Total Degrees of Freedom
ROD	1	2	1st	2
BAR	1	2	1st	6
BEAM	1	2	1st	12
SHELL	2	4	1st	24
TRI3	2	3	1st	18
TRI6	2	6	2nd	36
TET4	3	4	1st	24
TET8	3	8	2nd	48

Loads and boundary conditions (LBC) inputs are used in SimXpert to model external forces and displacement constraints respectively. Boundary conditions may be used to fix all of the six degrees of nodal freedom at a node (point), along an edge (curve), on a surface or within a sub-volume of the mesh. This is termed a *fully-fixed* constraint. Alternatively, a *general constraint* may be used to fix one or more of the three rotational and three translational degrees of nodal freedom at a point (node), along an edge, on a surface or within a sub-volume of the mesh. Similarly vector forces may also be applied directly at a point, along an edge or on a surface. Pressure loads are applied to a surface as a special case where a vector of magnitude equal to the product of the pressure and element face area is applied to each element of a surface in the direction of the element's local normal vector.

The solutions for the stress and deflection distributions may be plotted using surface fringe plots in the SimXpert interface and analysed for yielding. For isotropic materials, a useful equivalent yield stress criterion is the von-Mises stress σ_v, defined by Eq. 6-2, where the stress tensor components are defined by Eq. 6-3.

$$\sigma_v = \sqrt{\frac{1}{2}[(\sigma_{11} - \sigma_{22})^2 + (\sigma_{22} - \sigma_{33})^2 + (\sigma_{33} - \sigma_{11})^2 + 6(\sigma_{12}^2 + \sigma_{23}^2 + \sigma_{31}^2)]} \quad (6\text{-}2)$$

$$\boldsymbol{\sigma} = \begin{pmatrix} \sigma_{11} & \sigma_{12} & \sigma_{13} \\ \sigma_{21} & \sigma_{22} & \sigma_{23} \\ \sigma_{31} & \sigma_{32} & \sigma_{33} \end{pmatrix} \quad (6\text{-}3)$$

The outputs from a linear static FEA comprise the two-dimensional or three-dimensional stress, strain and deflection (displacement) distributions in the components geometric continuum. The design requirements are satisfied if the extremes of the stress and deflection distributions are

within the allowable range for the material in question and the specified reserve factor in strength for the component.

6.6 CFD Thermal Analysis

The maximum airframe temperature under worst case flight conditions was required as an input to the materials selection process. The transient nature of the dynamic pressure and temperature distributions on the airframe made an analytical approach to the problem nontrivial, especially given the supersonic speed of the flow. However, it was obvious from inspection that maximum pressure and temperature conditions would occur at or near regions of stagnated flow on the airframe, namely the nose-tip and the fin leading edges. Another area of concern was the nitrous oxide oxidiser tank, whose internal pressure would have to be passively regulated to ensure that thermal dissociation of the nitrous oxide was prevented.

A basic CFD study on the airframe was carried out at several Mach numbers to determine the range of steady state maximal temperatures which may be expected on the Phoenix-1A during a nominal flight. The commercial CD-Adapco StarCCM+ CFD package was used as it was available to the project and was found capable of such a study. Speed, temperature and ambient pressure outputs from the HYROPS tool were used to harmonise the CFD inputs with the expected ambient flight conditions for a chosen flight time, altitude or Mach number condition. The StarCCM+ solver was configured to run a three-dimensional steady state compressible flow simulation using full coupling between the pressure and velocity solution steps. The fluid physical model employed a viscous ideal gas atmospheric model. Turbulence was imposed using the software's K-Epsilon turbulence modelling option. The domain consisted of a body frame x axis aligned cylindrical air volume of radius 5 m, extending from 5 m in front of the airframe nose tip to 10 m behind the airframe boat-tail. The airframe itself was defined by performing a Boolean subtraction of the airframe geometry from the cylindrical air volume in the Autodesk Inventor CAD software, leading to internal domain boundaries corresponding to the airframe surface. The geometry was then imported into StarCCM+ in the *IGES* file format. This domain was meshed using approximately five million polyhedral cells with refinement closer to the airframe surface. Figure 6-3 shows a rendition of parts of this mesh. Note the much finer mesh size on the airframe walls (nominally 1 cm) compared to the domain outer boundaries (nominally 50 cm). Polyhedral cells were chosen as they offered better convergence properties [65]. Five layers of thin, boundary aligned prism cells were also used exclusively on the airframe geometry to capture viscous boundary layer effects. Free-flow velocity boundary conditions were imposed on the cylindrical domain's outer surfaces, with the desired free-stream Mach number, flow direction unit vector and ambient temperature being defined on

these boundaries. The flow direction unit vector was used to impose the overall aerodynamic incidence angle. In all cases zero incidence angles were used hence the flow direction vector was always in the direction of the negative body-frame x axis and hence parallel to the cylindrical sides and normal to the circular front and back end surfaces of the cylindrical domain. The airframe itself was defined with no-slip wall boundary conditions. The simulation was run on machines with 8 core parallel processing capabilities, with each run taking approximately 12 hours to complete.
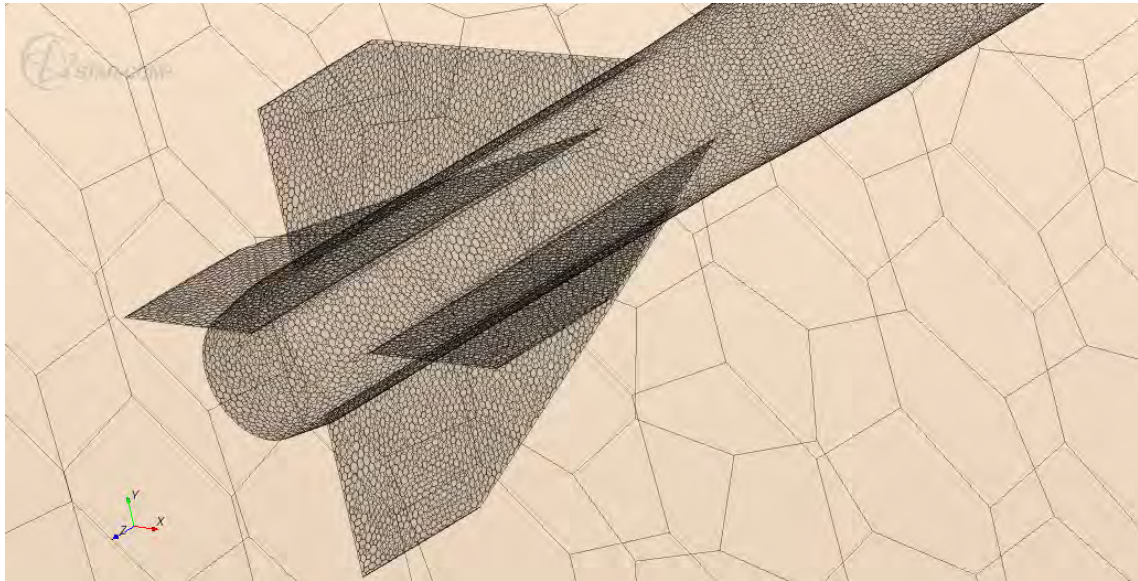

Figure 6-3: Part of the Phoenix-1A airframe mesh generated in StarCCM+. Only surfaces are shown.

The analysis was conducted with free-stream Mach numbers of 0.5, 1.5 and 2.25. These values were chosen based on HYROPS outputs with the aim of exploring airframe thermal and structural loads under maximum dynamic pressure and maximum Mach number conditions. The vehicle was predicted to reach a maximum speed of Mach 2.25 with optimistic motor performance in ideal wind and thrust misalignment conditions at motor burnout. However, the maximum dynamic pressure prediction was complicated by the varying ambient pressure and density during ascent. A transonic case was omitted as the simplistic prism layer boundary mesh and the ideal gas air model would invalidate the results, given the complex interactions between localised subsonic and supersonic flows that are encountered under transonic flight conditions.

Outputs from the study included airframe surface and air volume Mach number, pressure, temperature, velocity and density distributions as well as overall airframe dimensionless force and moment coefficients due to both pressure and shear effects on the airframe surfaces. Figure

6-4 shows the worst case temperature distribution output on the airframe. The nose tip temperature was 545 K, well above the thermal deformation temperature of most epoxy resins. The calculation of the force and moment coefficients required the definition of reference axes, speeds and densities as well as reference areas and moment arms. The drag coefficient was calculated for comparison against predictions using the RasAero software and found to compare favourably with disagreements of less than 10 %.
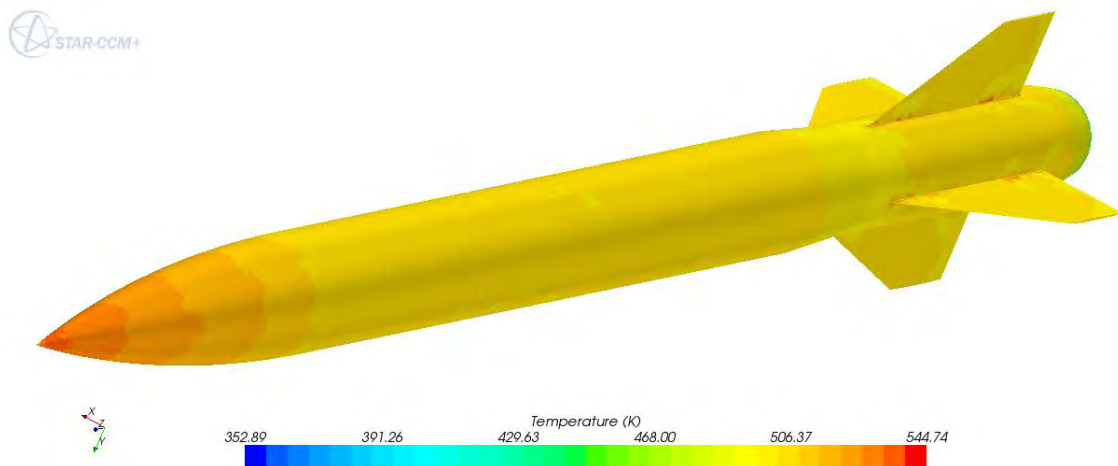

Figure 6-4: Worst case zero-incidence steady state thermal distribution on the Phoenix-1A airframe for sea level conditions at Mach 2.25.

The resulting temperature distributions on the airframe indicated a steady state maximum temperature of 545 K at Mach 2.25 under sea level conditions. At a conservatively low burnout altitude of 6000 m, this dropped to 454 K due to the lower ambient temperature, lower atmospheric density and lower ambient pressure. The lower Mach number scenarios did not yield a higher maximum temperature under any combination of ambient conditions, leading to the expected conclusion that the maximum thermal loading occurs at motor burnout. Given the very transient nature of these loads and the maximum thermal transfer time of approximately 20 s (i.e. the motor burn-out duration), these steady results were themselves deemed very conservative as the airframe would be subject to a rather limited heat transfer duration in reality. Therefore, the design condition was fixed at 454 K and materials capable of enduring this temperature for at least 30 s were solely chosen for use on the airframe exterior surfaces.

6.7 Forward Airframe Design and Manufacture

The airframe geometries could be classed into two categories: surfaces of revolution and fins. The former includes the nose ogive, the parachute and flight computer bays, the motor fairing shoulder covers and the boat-tail. These are all effectively shell structures and their primary design parameter is the wall thickness. The need for access to the oxidiser feed system during assembly and launch necessitated the separation of the aerodynamic shoulder into two halves, one of which would be removable. Each of these halves would be fastened to the struts connecting the oxidiser tank to the PV-1 motor combustion chamber (Refer to sections 6.9.2 and 6.9.3 for further details). Figure 6-5 is schematic of the same showing the manner in which the four cylindrical sections of the airframe and the nose ogive are joined together using bulkheads and the oxidiser tank to form the separable parachute bays, flight computer bay and payload bay. The parachute bays are sliding fits between the inner and outer cylindrical sections. Note the two inner cylindrical sections forming the drogue parachute bay and the flight computer bay (pink and green respectively). Note also the two outer cylindrical sections in red and orange. The sections are joined to each other and the nose (brown) and oxidiser tank (blue) using radial bolts at four locations. Three bulkheads (purple) are used to separate the resulting chambers. The bidirectional arrows indicate freedom of sliding motion during parachute deployments. Figure 6-6 is a CAD rendition of the forward section of the Phoenix-1A airframe, detailing the integration of the black (Carbon fibre epoxy composite) airframe sections with the internal supporting structures and oxidiser tank.
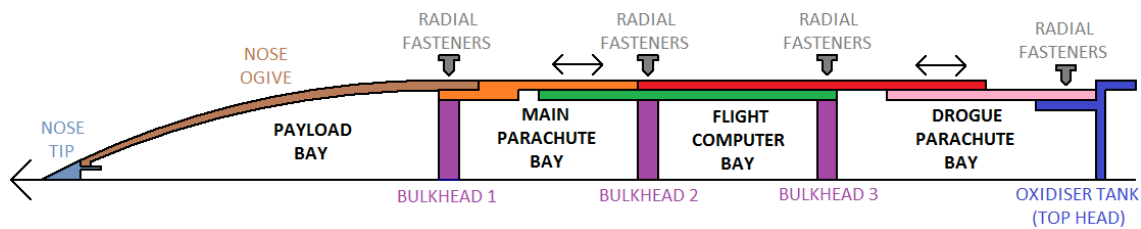

Figure 6-5: Sectional schematic of the Phoenix-1A forward airframe.
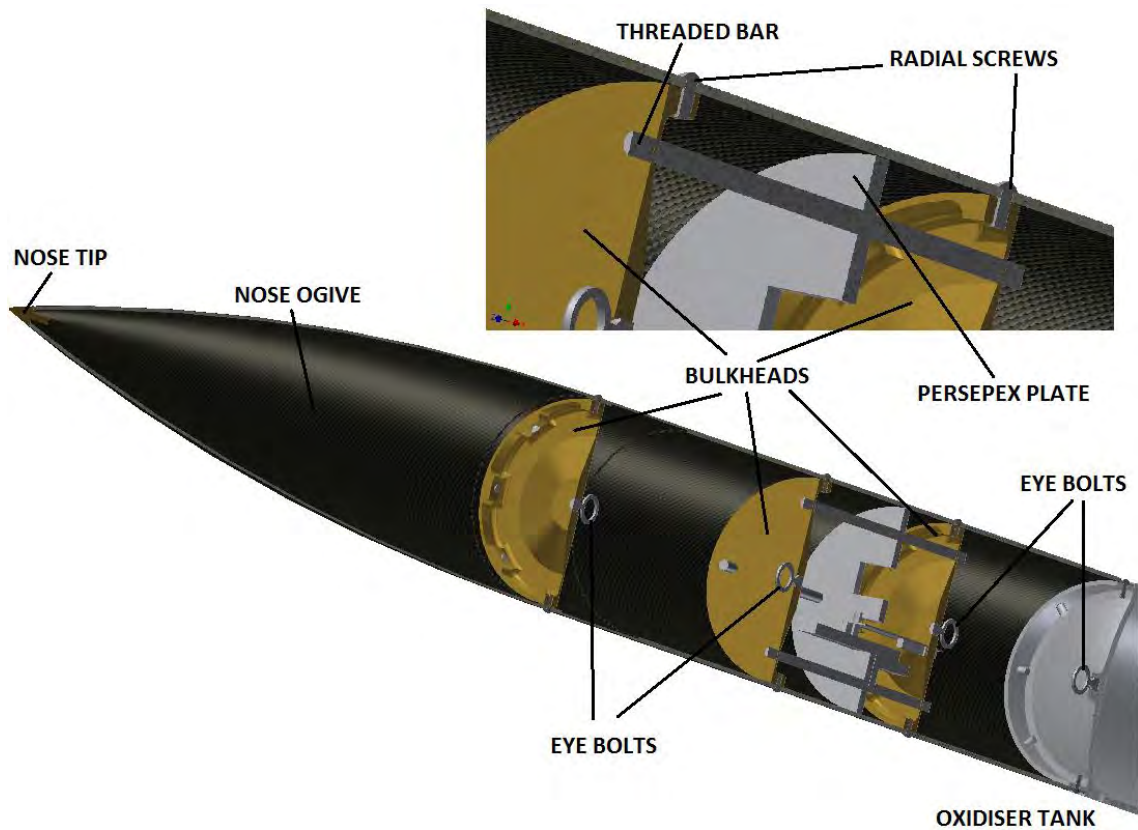
Figure 6-6: CAD cutaway view of the Phoenix-1A forward airframe (only showing major structural components).

The forward fuselage structures of the Phoenix-1A sounding rocket were dimensioned according to the airframe geometry specification presented in Chapter 5. The design of the structural elements used to realize these geometries is presented in this section. The following criteria were used to select the material for the airframe components, in order of relevance:

1) Availability
2) Cost
3) Manufacturability
4) Specific strength
5) Thermal performance
6) Reusability

Materials considered for the airframe fell into two categories: metal alloys and composites. The requirement for high specific strength and the highly anisotropic loading conditions on the airframe made composite materials potentially attractive. Polymer matrix reinforced composites were deemed feasible alternatives within the constraints of the project budget. Matrix materials were limited by the high thermal resistance requirements. Epoxy was chosen for its thermal

performance, suitable cost and widespread availability. Reinforcing fibres were limited to carbon fibre, fibreglass and Kevlar. Metal alloy alternatives were also constrained by expense and availability in the appropriate grade, geometric form and temper. Accessible materials with performance in the feasible range were duplex stainless steels, solution heat-treated aluminium alloys and titanium. Titanium would have suited the forward airframe very well, but it was discounted based on its extreme cost and specialised machining requirements.

The unavailability of either steel or aluminium tubing in the desired diameter and thickness range was a primary factor in the selection of carbon fibre reinforced polymer (CFRP) composite as the aero-structure material. Carbon fibre reinforcement was also selected over alternatives such as glass fibre or Kevlar as it offered appreciably greater structural performance at an acceptable cost.

Results from the FEA and CFD analyses were used to predict the aerodynamic thermal and structural loading on the forward airframe. In addition to these, the airframe would also be exposed to internal propulsion loads during the boost phase and deployment shock loads during parachute deployment. However, the axial nature of the combined drag, propulsion and deployment shock loads allowed a simple evaluation of the longitudinal stress in the airframe cylindrical sections. This stress was found to be far lower than the material yield limit along any of the materials principal axes. The anisotropic nature of the material would only be manifested in the aerodynamic lateral loading due to body lift and aerodynamic flow impingements at non zero angles of attack.

The in-plane orientation in which reinforcement fibres are laid in a layered composite component is a significant factor in determining tensile strength in different in-plane directions. The degree of anisotropy can be controlled and strength optimised by layering the composite with fibres aligned parallel to the in-plane directions of maximal loading. Anisotropy can also be minimised by averaging out the fibre orientation over several layers. However, out-of-plane anisotropy is retained and must be accounted for during component design. The scope of this optimisation was limited in the Phoenix-1A airframe as only twill-weave carbon fibre fabric was available to the project at an acceptable cost. Twill weaves have the effect of averaging in-plane strength in the orthogonal directions of the weave, leaving diagonal orientations of poorer tensile strength midway between the directions of weave. Therefore, layer to layer 45° increments in fibre orientation offered better in plane isotropy. Nevertheless, the dominance of the axial loading on the airframe required maximal strength in one orthogonal direction and hence all the layers were designed with the fabric in the same orientation, with one of fibre directions always axial and the other consequently always in the hoop direction. This

arrangement was maintained as far as possible in the section of varying radius such as the nose ogive and boat-tail.

The airframe wall thickness design relied on a FEA for validation. A laminate based FEA on the cylindrical airframe components was carried out with the aim of predicting structural performance. The NASTRAN orthotropic 2D (Ortho2D) laminate material model was used to emulate the behaviour of the carbon fibre reinforcement and the geometry was meshed using quadrilateral quadratic shell elements. A local cylindrical coordinate system was set up with its z axis along the cylindrical axis. Laminate anisotropic material properties and loads were specified in this coordinate frame. The twill weave was approximated by placing layers of laminate in the model with fibres in perpendicular orientations. The alternation between orientations was expected to average out strengths to model the effect of the twill weave globally. A representative 0.5 m section of the airframe cylindrical fuselage was analysed as the loading conditions on the rest of the cylindrical sections would be similar. Fully-fixed constrains were used on the edges at either end of the cylinder to emulate the fasteners whilst the 400 N nominal lateral loading was applied as an inward facing distributed force unidirectional across one half of the cylinder's outer surface. The initial wall thickness estimates of 3 mm for the nose ogive and 2 mm for the remainder of the airframe composite sections were found to be adequate. Although the FEA results may have indicated that the thickness were somewhat conservative, they were not reduced as a number of uncertainties accompanied the process. These included inherent uncertainties in the strength distributions of hand-made composite parts as well as design complexities unaccounted for, such as fibre seams, edge effects and small-scale anisotropy. It was deemed acceptable to moderately overdesign as the forward airframe represented a relatively small part of the total vehicle mass budget. Another reason was the anticipated difficulty of accurately manufacturing components with wall thicknesses lower than 2 mm. The FEA results gave equivalent stresses in all the layers below 10 MPa. The large reserve factor assured that the structures would operate safely under nominal loading. Figure 6-7 through to Figure 6-10 display the stress distributions in the model x and y axes in the innermost and outermost layers of the laminate model. Note the overall low stress levels and the edge effects.
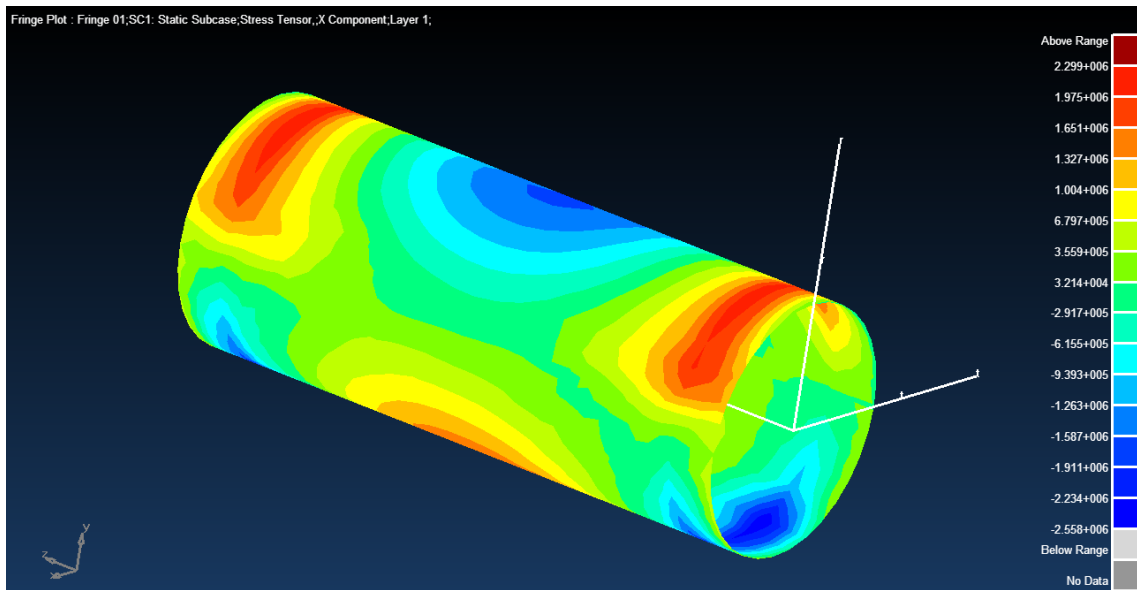
Figure 6-7: MSc SimXpert X direction stress distribution in airframe section (innermost layer) due to 400 N distributed lateral loading (in the x direction).
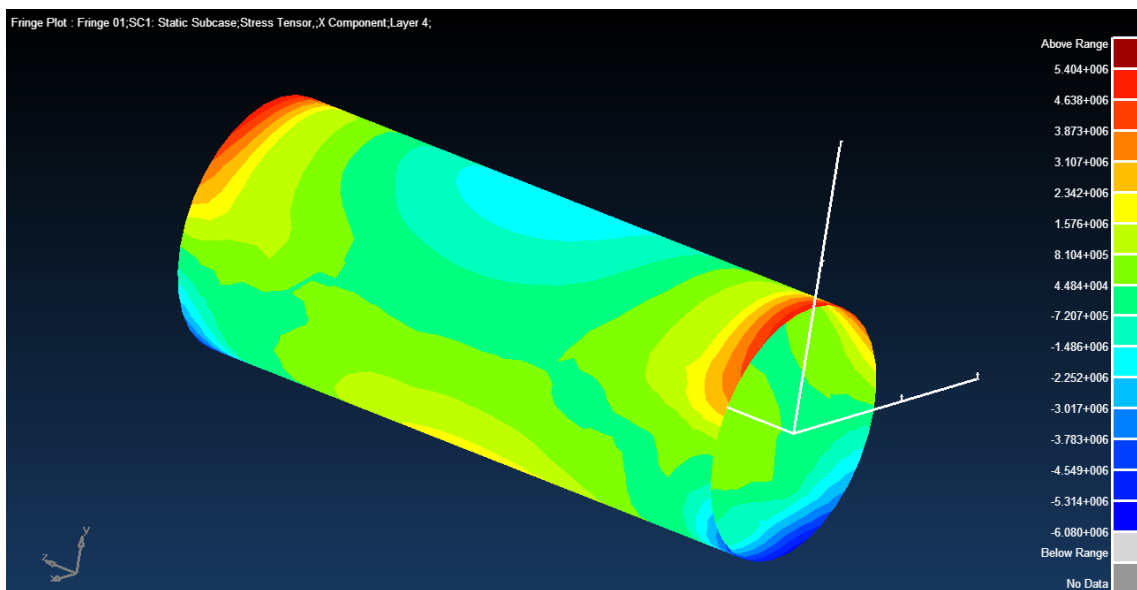
Figure 6-8: MSc SimXpert X direction stress distribution in airframe section (outermost layer) due to 400 N distributed lateral loading.
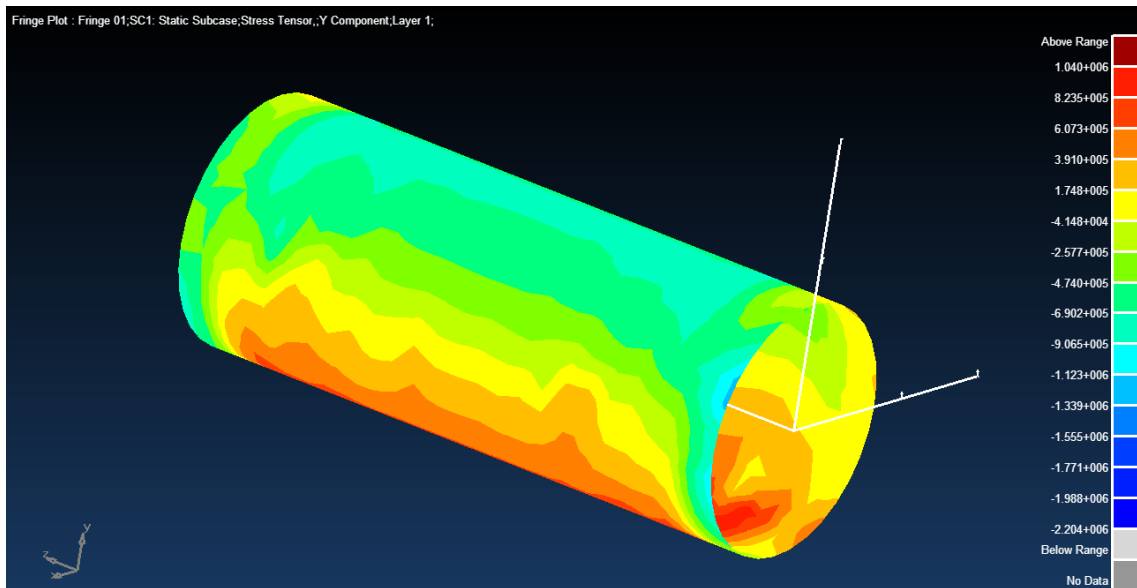
Figure 6-9: MSc SimXpert Y direction stress distribution in airframe section (innermost layer) due to 400 N distributed lateral loading.
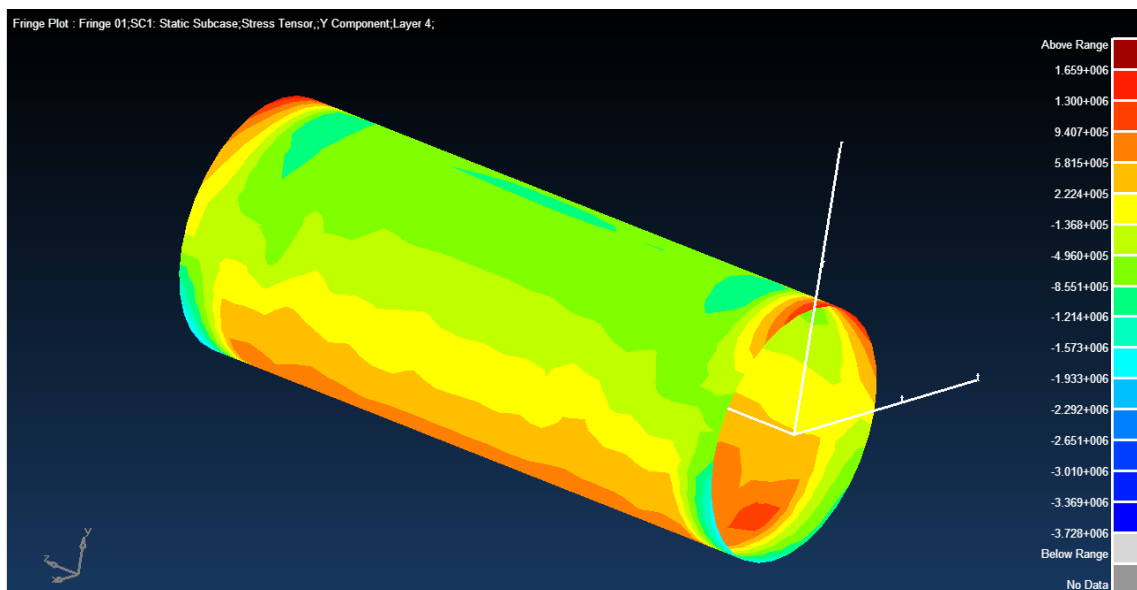
Figure 6-10: MSc SimXpert Y direction stress distribution in airframe section (outermost layer) due to 400 N distributed lateral loading.

The integration of the airframe to the internal components required methods of joining. Mechanical and adhesive methods were considered. Factors affecting the selection of fastening technique included manufacture and assembly considerations, thermal effects and the transfer of worst case structural loads. Inspection of the loading conditions indicated that the magnitude of

the radial side forces were much lower than the axial aerodynamic force. However, the small airframe wall thickness did not allow the use of conventional radial-axial bolted connections. Radial screws were incorporated into the upper airframe design despite drag contribution from the protruding screw-heads. It was reasoned that the simplicity and reliability of this design and its ease of manufacture and assembly would outweigh the added drag as well the mass of the screws themselves.

Twill-weave carbon fibre cloth with a weight of 196 g/m^2 was used for all the carbon fibre-epoxy composite components. The anticipated thermal loading at a maximum flight temperature of 454 K prohibited the use of room-temperature curing epoxy resin systems, which typically display a heat deflection temperature of 375 K. Therefore, the Technoresin LR 296 high temperature resin matrix system was used with the Technoresin EH-4 catalyst. This system was tested using sample lay-ups and displayed structural stability when subjected to a temperature of 455 K for sustained periods. Table 6-4 lists the properties of this resin system.

Table 6-4: The Technoresin LR-296 Laminating Epoxy Resin

Property	Value
Viscosity	9000 Pa.s
Heat Deflection Temperature (HDT)	453 K
Post Curing Schedule	25°C – 24 hours 80°C – 2 hours 170°C – 3 hours
Cure Temperature Ramp Up/Down Rate	20°C/hr
Catalyst Weight %	30
Colour	Clear Amber
Catalyst	Technoresin EH-4

Pine internal moulds were used to impart the required geometry to the components during the wet lay-up process. These moulds were turned and sanded to a fine surface finish for dimensional accuracy. Several layers of 50 micron polyethylene sheeting were carefully taped onto the surface of the moulds to ensure that the components could be freed from the moulds when the resin matrix had cured. Care was taken to ensure that creases and wrinkles were avoided on the polyethylene sheeting, resulting in a high quality inner surface finish. Figure 6-11 and Figure 6-12 show the welded lay-up jig for the cylindrical sections and the free standing nose mould respectively. Note the wear on the pine mould from the removal of finished sections. The white mandrel was used to neatly stow the roll of carbon fibre cloth in tension.

Figure 6-11: The jig used for the hand lay-up of the Phoenix-1A's forward airframe cylindrical sections.

Figure 6-12: The pine mould used to manufacture the nose ogive.

The manufacture of the CFRP forward airframe sections utilised the wet hand lay-up technique. This involved the application of alternating layers of matrix and reinforcement onto the mould surface with the desired geometry of the composite component. It was also necessary to initially apply a release agent on the mould surface to prevent the cured matrix from bonding with the mould material. This was essential for the removal of the component subsequent to the matrix drying period. If difficult to remove by hand, dry components were removed from the moulds after expansion by the slight application of heat on the outer surfaces. The dry components were cured in ovens according to the curing schedule of the resin matrix. The outer surfaces of the cylindrical airframe components were given a better finish by turning them on a lathe with a sand paper covered tool. The outer (aerodynamic) components were also given a final external coating of resin and left to cure at room temperature. This layer of resin ensured that fibre reinforcement was not exposed to the atmosphere. A final manual finishing operation was applied to the outer airframe components using successive smoothing going up to 1000 grit (fine) sand paper. This imparted a surface finish of an aerodynamically acceptable quality.

The CFD simulation revealed that foremost section of the airframe nose were a region of high thermal loading due to the flow stagnation at the tip of the nose. Similar stagnation thermal loads were observed at the fin leading edges. A separate pointed nose tip structure was designed for the nose ogive as carbon fibre epoxy composite materials with sufficiently high heat deflection temperatures were either too expensive, locally unavailable, or involved impractical complexities in design and manufacture. Aluminium 6082-T6 alloy was used on the nose tip for minimal weight. The tip was turned from a 100 mm diameter billet of the materials and attached to the nose ogive CFRP structure using high performance epoxy adhesives. The tip wall thickness was designed conservatively to ensure structural integrity under axial aerodynamic and thermal loading. However, the component was designed hollowed out as far as possible for further mass reduction. Despite the nose being a tangent ogive, the tip was designed to be a tangential cone to the nose. This made the geometry simpler and easier to manufacture accurately. The deviation from the true ogive over the short arc length of the tip was deemed aerodynamically negligible. Figure 6-13 shows the assembly of the nose tip on the nose ogive and Figure 6-14 shows a technical drawing of the nose tip, showing the weight reduction obtained by boring the insides of the tip structure out to a depth of 120 mm. Note the conical profile and the 17.6 mm cylindrical rear profile where the adhesive would be applied to attach the tip to the nose ogive..

Figure 6-13: Sectional CAD assembly rendition of the nose ogive and the aluminium nose tip.

Figure 6-14: Technical drawing of the nose tip with hidden detail.

6.8 Fin and Fin Attachment-Rail Design and Manufacture

The airframe aerodynamic design specified four clipped-delta plan-form trapezoidal fins with hexagonal cross sectional aerofoil profiles. The material selection for the fins was dictated by specific strength considerations, fin flutter limitations on flexural rigidity and manufacturing constraints.

The fin geometric design employed a taper ratio of three, with a root chord of 600 mm and a tip chord of 300 mm. A 200 mm span was used to obtain the 0.04 m² target area per fin. The basic fin thickness was determined to be 6 mm based on fin flutter considerations and the flexural properties of aluminium alloy 6082 T6. Torsion and flexure effects were analysed in detail by Theodersen [66]. However, the simple but popular empirical fin flutter failure prediction method resulting from the work of Martin [67] is given by Eq. 6-4. In this relation, the fin aspect ratio is denoted A and the fin thickness and fin mean chord are denoted by t and c respectively. Note that the relation assumes the use of Imperial units.

$$X = \frac{39.3A^3}{\left(\frac{t}{c}\right)^2 (A+2)}$$ (6-4)

In Eq. 6-4, the quantity X is read from Figure 3 in the work of Martin [67] through the linear functional relation in Eq. 6-5, where the fin taper ratio is denoted λ and the atmospheric pressure is p and the seal level atmospheric pressure p_0. The shear modulus of the fin material is denoted G_E.

$$\left(\frac{p}{p_0}\right)\left(\frac{\lambda+1}{2}\right) X \propto G_E$$ (6-5)

The critical flutter velocity V_f for a given fin design can then be determined from the following relation given my Martin [67] in Eq. 6-6. The speed of sound is denoted by a.

$$\left(\frac{V_f}{a}\right)^2 = \frac{G_E}{\left(\frac{p}{p_0}\right)\left(\frac{\lambda+1}{2}\right)X}$$ (6-6)

Using this technique, a minimum fin thickness of 6 mm was found necessary for the Phoenix-1A at sea level given the expected maximum speed of 700 m/s and the mean fin chord length of 400 mm. The fin taper ratio was 1/3 as it is the ratio of the fin tip chord (200 mm) to the fin root chord (600 mm) and the fin aspect ratio was calculated using Eq. 5-48. The low shear modulus of aluminium (26 GPa) led to the relatively large fin thickness being required. However, the even lower shear modulus of carbon fibre epoxy composites prevented its use in the fins despite the better specific strength of that material.

Each fin plan-form was laser-cut from stock 6 mm thick aluminium alloy 6082-T6 plate. Milling machines were then used to machine the tapers on the leading and trailing edges required for obtaining the hexagonal aerofoil profile. The milling operation relied on an angled

vice to impart the required taper. A 0.3 mm radius was imparted to the leading and trailing edge tips for structural strength considerations and better subsonic flow properties. The fins were given a fine polished finish by the manual application of wet emery 1000-grit water-paper. The roots of the leading and trailing edge tapers were also smoothened to weaken shock waves and expansion fans at transonic or supersonic speeds. The final fin geometry is shown in Figure 6-15. Note the 11 mm flat faced lower extension for slotting into fin attachment rails that in turn connect onto the fuselage at the motor combustion chamber.
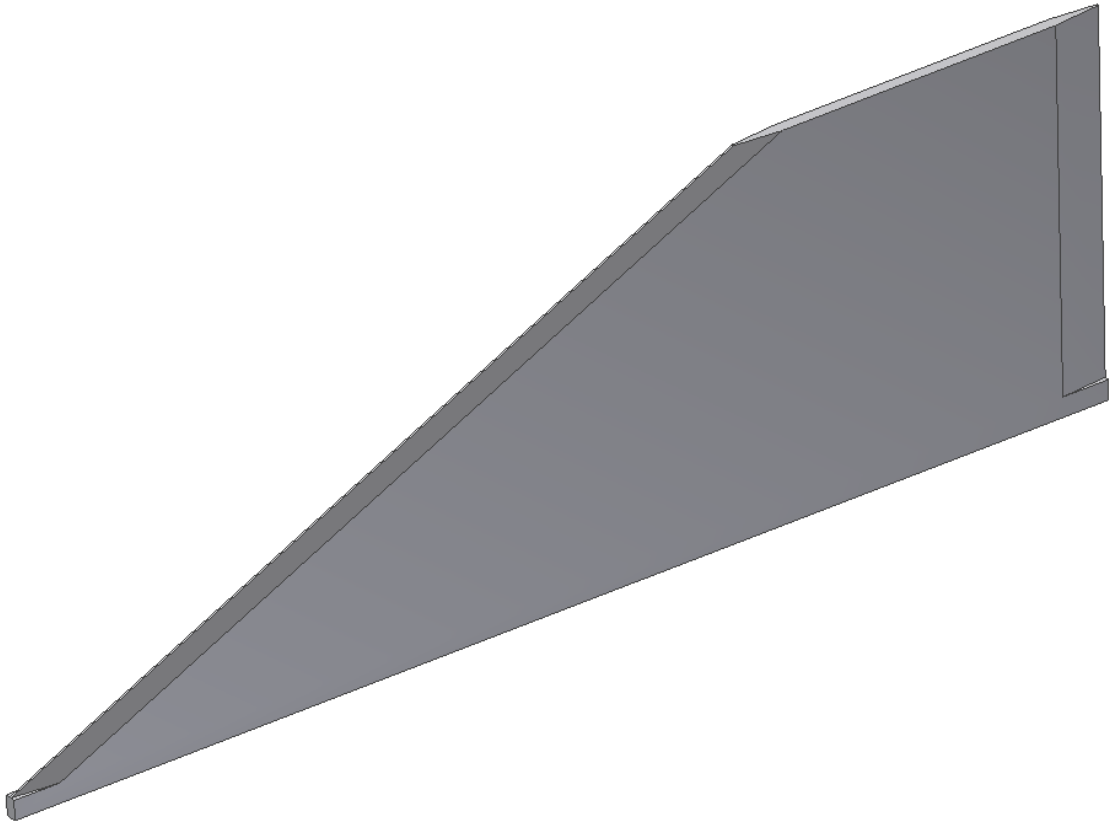

Figure 6-15: CAD rendition of the fin geometry. The hexagonal cross section is apparent.

A FE analysis of the fins was carried out to ensure that they would not yield under the most severe aerodynamic loading conditions expected. The most extreme aerodynamic load was calculated by applying maximal normal-force generating flight conditions. These may only be experienced when the vehicle flies at its maximum speed at the highest pre-stall total angle of attack under maximal atmospheric density conditions (i.e. at sea level). During nominal flight these conditions would never coincide and represented a conservative, extreme worst case scenario. Eq. 5-38 was used to predict this worst case lift coefficient for one fin and the normal force was then calculated using Eq. 5-8.The resulting normal force was found to be 5200 N for a maximum velocity of 600 m/s. This loading was distributed evenly on one side of the fin and the fin base surface was fully-fixed constrained to model static joining to the fin attachment rail.

The fin was meshed using quadratic tetrahedral elements. The maximum von-Mises stress was found to be 199.7 MPa at the aft root chord region, indicating that the worst case aerodynamic loading would not lead to fin failure as aluminium alloy 6082-T6 has a minimum yield strength of 240 MPa. Figure 6-16 shows the FEA predicted von-Mises surface stress distribution on a fin.
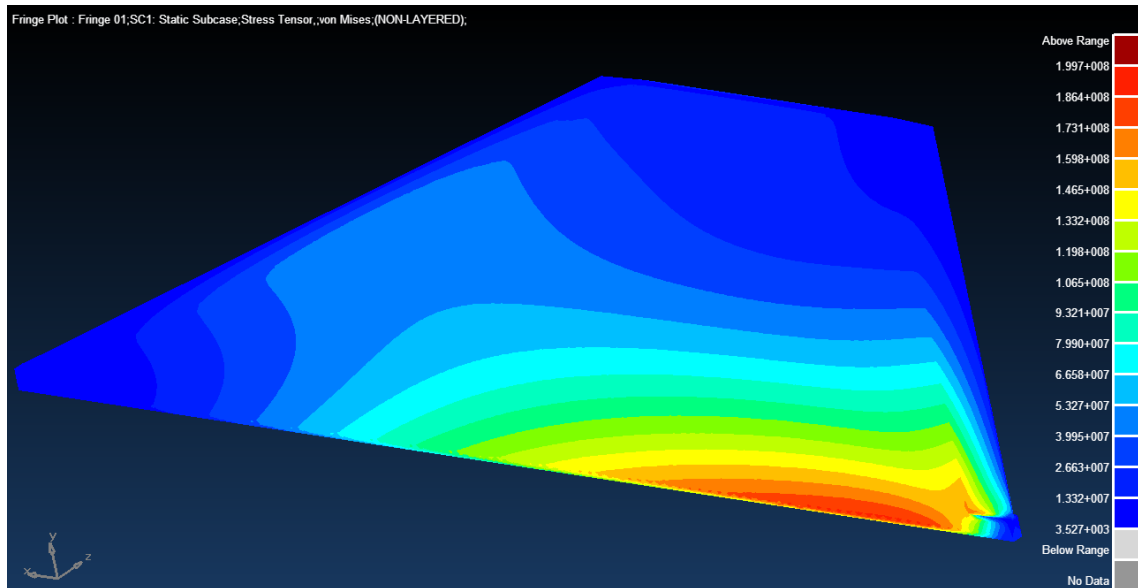

Figure 6-16: MSc SimXpert von-Mises surface stress plot on the fin. The critical failure mode was found to be flutter rather than static aerodynamic lift overload.

Fins may be mounted on sounding rocket fuselages using ingenious attachment techniques. The most suitable method is governed by the materials of the supporting fuselage section, thermo-structural loading conditions and aerodynamic drag considerations. Common techniques on smaller model rockets include the use of angled brackets or slots in the fuselage. The positioning of the Phoenix-1A fins on the PV-1 motor combustion chamber section placed severe constraints on the attachment technique. Any possibility of modifications to the chamber was eliminated due to its severe internal thermal and pressure loads. Therefore, a separate attach structure was needed. The Phoenix-1A fins were thus mounted onto the motor combustion chamber casing using purpose-designed stainless steel mounting rails. The rails were also used to impart the 0.5° canting required on the fins. The stainless steel 431 material was available and was used for its high rigidity and strength properties. The rails were attached using the standard M12 radial bolts also used for the attachment of the PV-1 motor's internal injector bulkhead and nozzle retainer. In addition, the bottom surface of each rail was bonded to the combustion chamber casing using high strength epoxy adhesives. A 0.5° angled slot was CNC machined onto each rail, producing the required cant angle with accuracy. The fin rail geometry

is shown in Figure 6-17. Note the 12 mm bolt holes at either end, used to attach the units to the PV-1 motor combustion chamber casing. Note also the slanted slot in which the fins are fitted, imparting the requisite 0.5° fin cant angles.
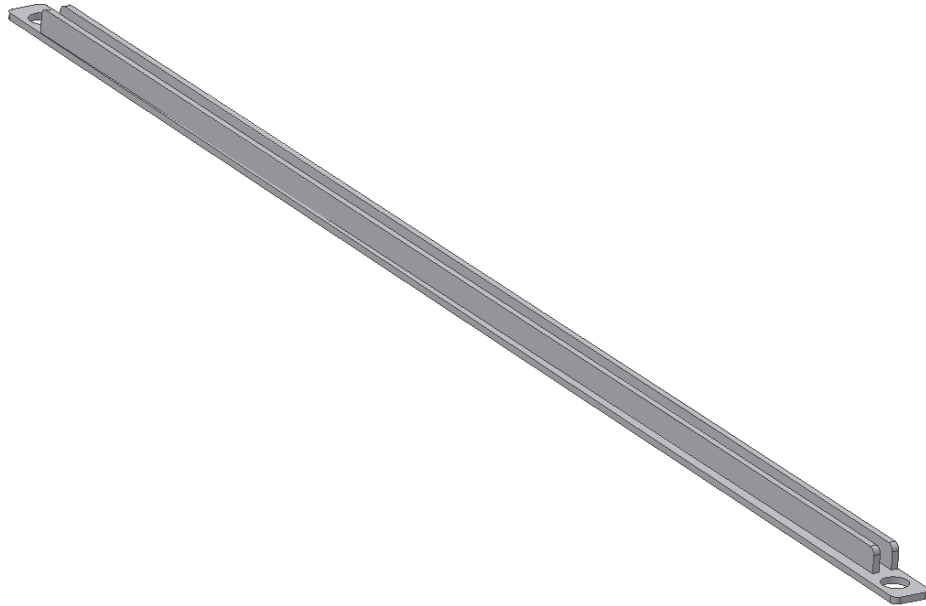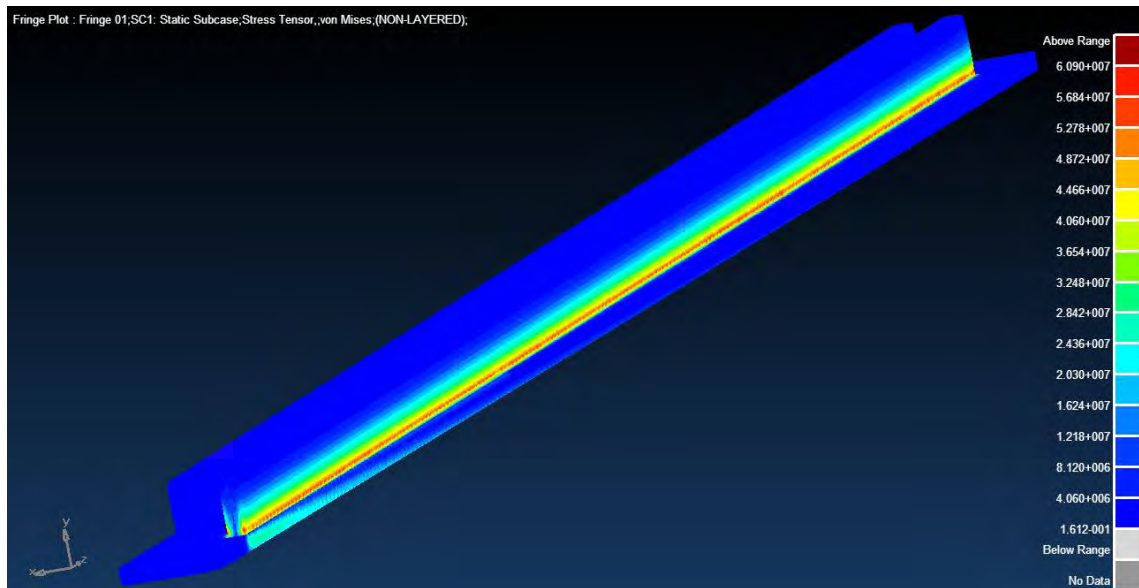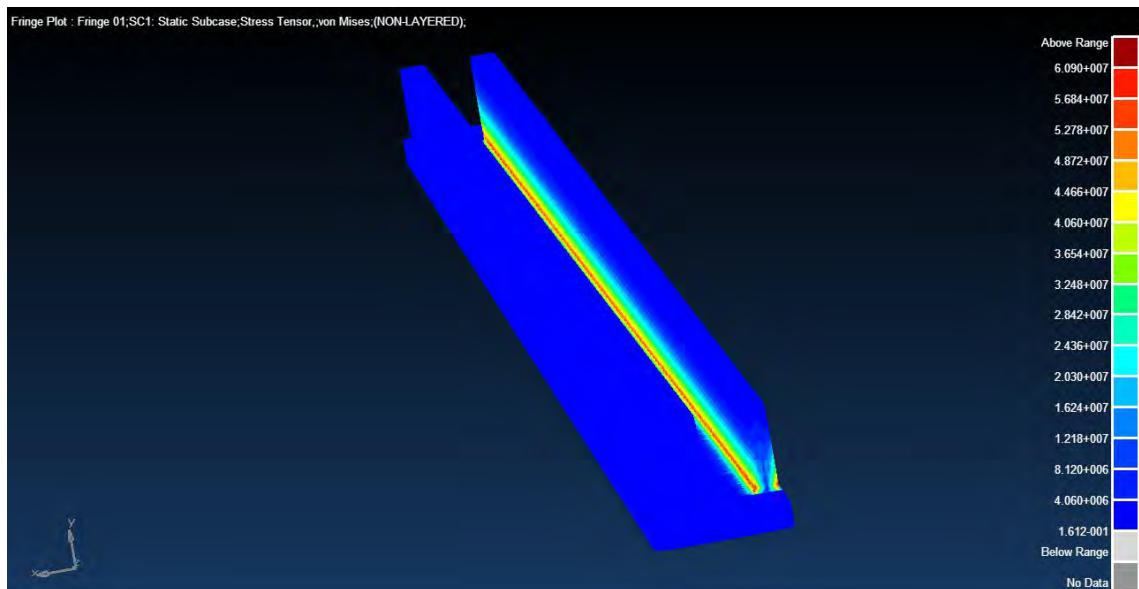

Figure 6-17: CAD rendition of the fin attachment rail geometry.

A FEA on the fin mounting rail verified that the design was suitable. The maximal fin normal force of 5200 N was used to impose worst case loading conditions. The rail model was constrained with fully-fixed constraints on the inner surfaces of the bolt holes at either end. In addition, the bottom surfaces of the rails were also fully-fixed constrained to emulate the adhesive bonding to the outer surface of the motor combustion chamber. The load was applied as a normal distributed force over one of the clot inner wall surfaces, mimicking total transfer of loading form the fin to the rails in a condition of static equilibrium. The FEA result showed a maximum von-Mises stress of 60.9 MPa, indicating a sufficient reserve factor on the rails given the material strength of 300 MPa. Surface von-Mises stress distributions are shown in Figure 6-18. Figure 6-19 shows a photograph of the four fins attached to the PV-1 motor combustion chamber casing using four fin attachment rails and radial bolts. Note the stress concentrations at the slot root on the compressed side and how the radial bolts for the attachment of the fin rails to the casing are also used to attach internal components of the motor such as bulkheads. Each fin was bolted to its fin-rail using 6 equally spaced M4 high tensile bolts, ensuring both shearing and tensile integrity.

(a)

(b)

Figure 6-18: MSc SimXpert von-Mises stress distribution on the surface of the fin attachment rail under lateral lift loading.

Figure 6-19: Assembly of the fins and fin rails on the PV-1 combustion chamber casing, prior to polishing.

6.9 PV-1 Oxidiser Tank Design and Manufacture

The Phoenix-1A PV-1 hybrid motor oxidizer tank is a cylindrical vessel under normally internal pressure. Liquid nitrous oxide is stored in the tank at a pressure of 65 bars. The tank accounts for a large percentage of the total inert mass on the vehicle and hence emphasis was placed on the use of a high specific strength material. The design approach was dictated by the large role the tank plays in determining the vehicle flight performance and the significant safety risk posed by its high internal pressure load. The geometric design was aimed at providing high factors of safety at locations of stress concentrations or loading uncertainty whilst minimising mass by reducing wall material at locations of relatively lower stress.

Whilst the vessel was required to operate under an internal absolute pressure of 65 bars, the filling process required the pre-evacuation of air and the maintenance of a vacuum of before the introduction of high pressure N_2O. Therefore, the vessel was also designed for an external

pressure of one atmosphere against an internal vacuum. The method of [68] demonstrates that the critical shell wall thickness required for cylindrical vessels under internal pressure is the same as for vessels under external pressure, if buckling is not the critical factor. The internal pressure specification of 65 bars would hence be more than sufficient for an external of 1 bar as well. The critical (hoop) stress σ on a cylindrical shell of thickness t and radius r under internal pressure p is given by Eq. 6-7. Note that this approach assumes that the critical failure mode is bending and not buckling

$$t = \frac{pr}{\sigma} \qquad \text{(6-7)}$$

Cylindrical pressure vessels are closed at either end with end-caps referred to as vessel *heads*. These are typically surfaces of revolution with standard profiles. Hemispherical, ellipsoidal, torispherical and flat head profiles are commonly used. Differing profiles are suited to the various loading condition encountered on pressure vessels. The PV-1 oxidiser tank required end-caps that minimised weight as well as overall length. Inspection of the hemispherical vessel wall stress equation (Eq. 6-8) reveals that a smaller end-cap radius induces lower stresses in the end-cap material. Note that flatter end-caps, which tend to conserve total vessel length, require greater wall thicknesses to safely carry the greater wall stresses. This scenario presented a trade-off between size and weight for optimal performance. The torispherical type was chosen for the oxidiser tank as its length may be tuned by varying the ratio of the knuckle radius and crown radius dimensions whilst its geometry is entirely defined using tangentially connected arcs. This head type is thus simple to define accurately and machine using conventional CNC machines and also offers a space savings comparable to flat or convex disc heads without undue stress concentrations. Additionally, all the standard pressure vessel design codes specify formulae for its wall thickness calculations. Figure 6-20 depicts details of certain common pressure vessel head geometries.

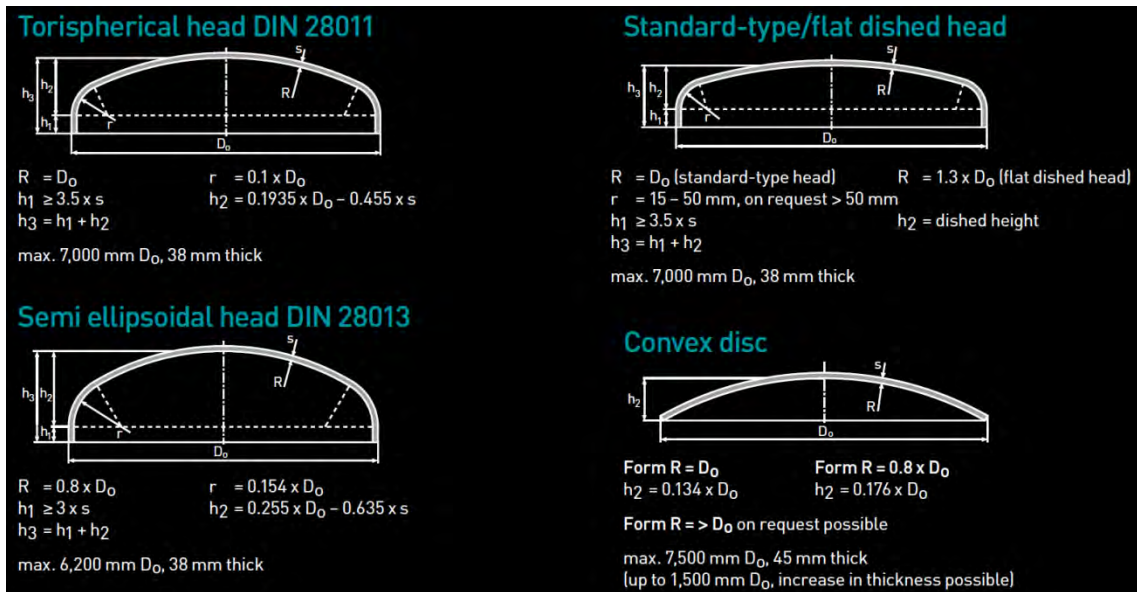$$\sigma = \frac{pr}{2t} \qquad \text{(6-8)}$$

Figure 6-20: Different head types commonly used on pressure vessels, adapted from [69].

The UKZN HYROPS tool was used to evaluate the sensitivity of the altitude performance of the Phoenix-1A to the specific strength of the oxidiser tank shell material. This study used the nominal Phoenix-1A structural configuration with launch elevation angle of 80° under perfect atmospheric conditions. A nominal ramp thrust function of 3750 N was used with a 20 s burn time. The study was thus qualitative rather than quantitative. Table 6-5 summarises the results from this study.

Table 6-5: Apogee performance consequences of oxidiser tank shell material choice

Oxidiser Tank Shell Material	Tank Shell Mass (kg)	Tank Shell Wall Thickness (mm)	Nominal Apogee Altitude (m)
Duplex Stainless Steel 2205	24.16	3.13	12840
Aluminium Alloy 2219 T6	11.47	4.09	16066
Aluminium Alloy 7075 T6	7.96	2.86	17100
Aluminium Alloy 6082 T6	15.80	6.00	14875
Carbon Fibre Epoxy Matrix	5.06	3.20	18008
Titanium Grade 5	5.75	1.30	17786

The material options for the vessel were also constrained by the need for chemical compatibility (inertness) with nitrous oxide in the temperature range of operation. During operation, ambient external temperatures on the vessel would range from 30 °C at launch to negative 60 °C near apogee. Stagnation temperatures up to 200°C would also be experienced for very short periods. The over pressurisation risk posed by the dissociation of nitrous oxide or its vaporisation

warranted appropriate control of the internal tank temperature both on the launch-pad and during flight. However, it was noted that the temperature loading during flight would of a wholly transient nature, with the heat transfer rate through the tank walls being a major factor characterising the structural response and the possibility of nitrous oxide dissociation. A conservative choice of material with respect to both heat transfer properties and thermal stability range was seen as the only practical solution, avoiding an intensive transient heat transfer analysis.

During the material selection and design process, a compromise between safety and performance was maintained by specifying the allowable stress in any portion of the tank to be half the yield strength of the material being considered. This use of an overall stress safety factor of two is consistent with similar practices in the aerospace industry concerning the design of flight-weight pressure vessels [70]. The calculation of the vessel's wall thicknesses and welds was based on the American Society of Mechanical Engineers (ASME) pressure vessel design code [71]. The relative certainty of the loading conditions on the vessel and the transient nature of its loading simplified the overall design process by eliminating corrosion and fatigue considerations. The use of the ASME pressure vessel code ensured adherence to accepted standards with regards to wall thickness calculations, weld designs and welding procedures. In order to preserve the performance of the vehicle, the maximum allowable stress was not limited using the ASME code. The AMSE pressure vessel code specifies the shell thickness t for cylindrical pressure vessels under internal pressure using Eq. 6-9 in terms of the external radius R, allowable stress S, weld efficiency factor E and internal pressure P. The specification of Non-Destructive Testing (NDT) on the welds allowed for a weld efficiency factor of 0.57. This is the weld efficiency value specified by the ASME code for non-destructively tested aluminium alloys in the T6 temper condition for full penetration single-welded butt joints with a backing strip that remains in place after welding [72].

$$t = \frac{PR}{SE + \frac{2P}{5}} \tag{6-9}$$

The wall thickness for the un-welded virgin shell material away from the heat affected zone (HAZ) was thus determined to be 6 mm using a weld efficiency of unity. In order to ensure the structural integrity of the welds and the resulting HAZ, reinforcement was introduced around each circumferential weld in the form of an extra 3 mm of wall thickness. This band of reinforcement was 25 mm wide on each side each weld based on [72]. The circumferential weld preparation was specified with a final depth of 7.5 mm and chamfer angle of 30°. A root gap of 3 mm was used to ensure full penetration bondage between the weld material and adjacent

sections. The Al-4043 Al-Si-Mg filler wire was specified based on recommendations from the literature on the welding of aluminium alloys in the T6 condition [73]. The welds beads were left unaltered on the outer diameter of the welds despite their aerodynamic drag contribution. This ensured additional strengthening of the joints. Figure 6-21 shows a technical drawing of the tank in section with details of the weld design. Note the thickened (9 mm) walls at the weld HAZ. Also note the 7.5 mm weld depth, leaving a 1.5 mm backing plate and a 3 mm flat 'nose' between the chamfers.

The ASME code also specifies a formula (Eq. 6-10) for the wall thickness of a torispherical head with crown radius L and knuckle radius r. The factor M is used to account for stress concentration at the knuckle radius and is read from the relevant table in the ASME code. All other symbols represent the same parameters as in Eq. 6-9. The wall thickness for the oxidiser tank heads was determined to be 9 mm according to the code.

$$t = \frac{PLM}{2SE + P\left(M - \frac{1}{5}\right)} \qquad\qquad M = 1.54 \; for \; \frac{L}{r} = 10 \qquad (6\text{-}10)$$

Non-Destructive Testing (NDT) was performed on the vessel after welding. This included dye-penetration inspections of the welds and hydrostatic pressure testing of the vessel at 80 bars for 15 minutes.
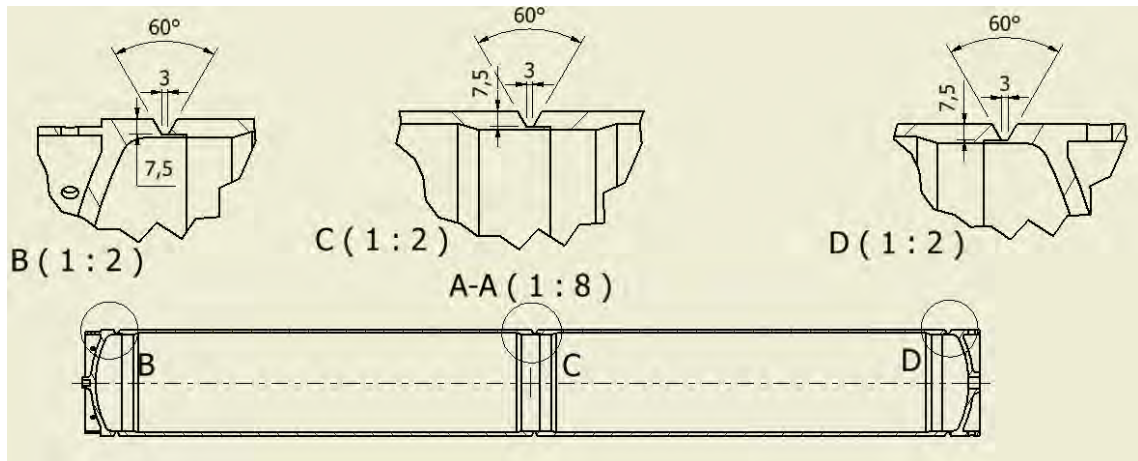

Figure 6-21: Section drawing of the PV-1 oxidiser tank three-section assembly, showing the weld preparation details.

The final design of the Phoenix-1A oxidiser tank was investigated further using FEA. The radial symmetry of the tank geometry about the longitudinal axis and the uniform internal pressure

allowed only a quarter of the geometry to be analysed. Only the heads were investigated as the long central shell section was effectively annular in geometry. The stress distribution in an annular shell under internal pressure has an analytical solution and hence FEA analysis was considered unnecessary. Each of the tank heads was analysed using normal (perpendicular) translational general constraints on all the symmetry planes and the interfacing surface to the tank shell. The loading consisted of the internal pressure of 65 bars. No rotational constraints were applied. Quadratic tetrahedral elements were used with a nominal mesh size of 1 mm for sufficient resolution to capture the expected stress concentration at the knuckle radius. The analyses indicated that maximal stresses in the tank would be acceptable under standard operating conditions. Figure 6-22 and Figure 6-23 show the von-Mises surface stress distributions on the top and bottom tank heads respectively. Note the major stress concentration at the knuckle radius. Note also that the flange is largely stress free. There are also significant stress concentrations at the weld seams, inlet port and near the weld seams.
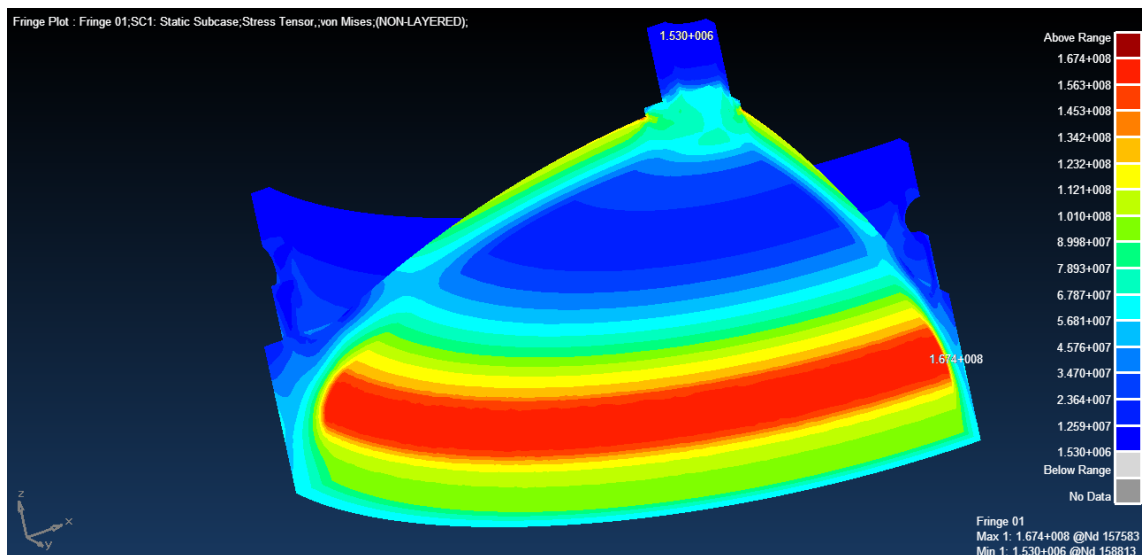

Figure 6-22: MSc SimXpert von-Mises surface stress plot of the PV-1 oxidiser tank's top torispherical head, showing the quarter geometry used to exploit symmetry.
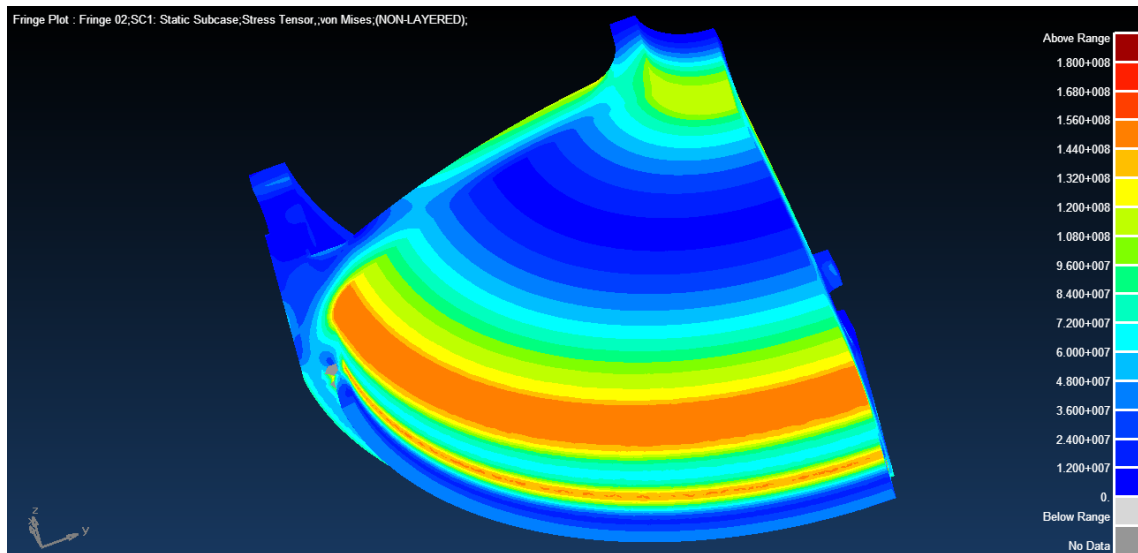
Figure 6-23: MSc SimXpert von-Mises surface stress plot of the PV-1 oxidiser tank's bottom torispherical head, showing the quarter geometry used to exploit symmetry.

The FE analyses revealed that the maximum stresses do indeed occur at the knuckle radii. The top tank head knuckle radius stress was predicted at 167.4 MPa, compared to 156.0MPa for the bottom head. These stresses were found to be higher than expected for a reserve factor of two on the material yield strength, which was 135.0MPa for the aluminium 6082-T6 billet (supplier tested yield strength of 270.0 MPa) used for the tank. However, the reduced reserve factor did not force a modification to the head designs due to their conformance with the ASME pressure vessel code. The final geometry of the tanks is shown in section in Figure 6-24. Note the weld grooves and the wall thickening in the vicinity of the welds for compensating the material weakening in the HAZ. The lower tank head has a port for filling the tank whilst the upper tank head has a protrusion with a 12 mm internal thread for connecting to an eye bolt. The eye bolt was used to tie the lower end of drogue recovery parachute shock cord.

Figure 6-24: CAD cutaway rendition of the PV-1 flight weight oxidiser tank.

The manufacture of the shell was governed by the solid 230 mm diameter billet. The material was procured in this form as tubes with the appropriate dimensions were locally unavailable. The billet was bored to the required thickness profile internally before being turned externally to a diameter of 200 mm. Both external and internal surfaces were given a polished finish to minimise aerodynamic friction drag and ensure uniform propagation of pressure loads. A lathe capable of accurately boring the entire 1600 mm length of the shell was unavailable to the project. The manufacture of the shell was thus completed in 800 mm sections, each of which could bored from either end using boring tools capable of a 400 mm reach. The two sections were then circumferentially welded using a full penetration single-weld butt joint to form the complete1600 mm long shell.

The manufacture of the tank head geometries could be carried out using forging, spin-forming and CNC machining operation. The lack of suitable equipment made forging aluminium 6082-T6 alloy impossible. The heads were also found to be too small for spin-forming using conventional techniques. The heads were thus CNC machined directly from short sections of the same billet which was used for the manufacture of the shell sections. The tank was filled through a reinforced inlet port at the centre of the lower head, threaded to accept a standard tapered ½" NPT fitting. This ensured compatibility with the rest of the oxidiser feed system fuel lines.

The attachment of the tank's adjacent recovery and feed system structures employed radial bolting. The attachment interfaces were designed as flanges onto the tank heads for simplicity

and convenience. A recessed flange was provided on the top head for attachment with the drogue parachute storage bay using eight M8 bolts. The lower tank head was provided with four M12 holes for radial bolting to the support struts used to attach the tank to the motor combustion chamber (refer to section 6.9.2). The tank heads were also used as attachment points for the vehicle's launch lugs. These were attached using the same M12 radial bolts used for the attachment of the tank of the tank to the rest of the aero-structure. The bolt holes on each head were thus accurately aligned prior to tank welding. Figure 6-25 shows in section the attachment of the lugs are the tank heads. Figure 6-26 shows the manufactured oxidiser tank assembled onto the GSE trailer vehicle for static motor firing tests.

Figure 6-25: Quarter section cut-away of the tank, showing the launch lugs (black) fitted onto each end.
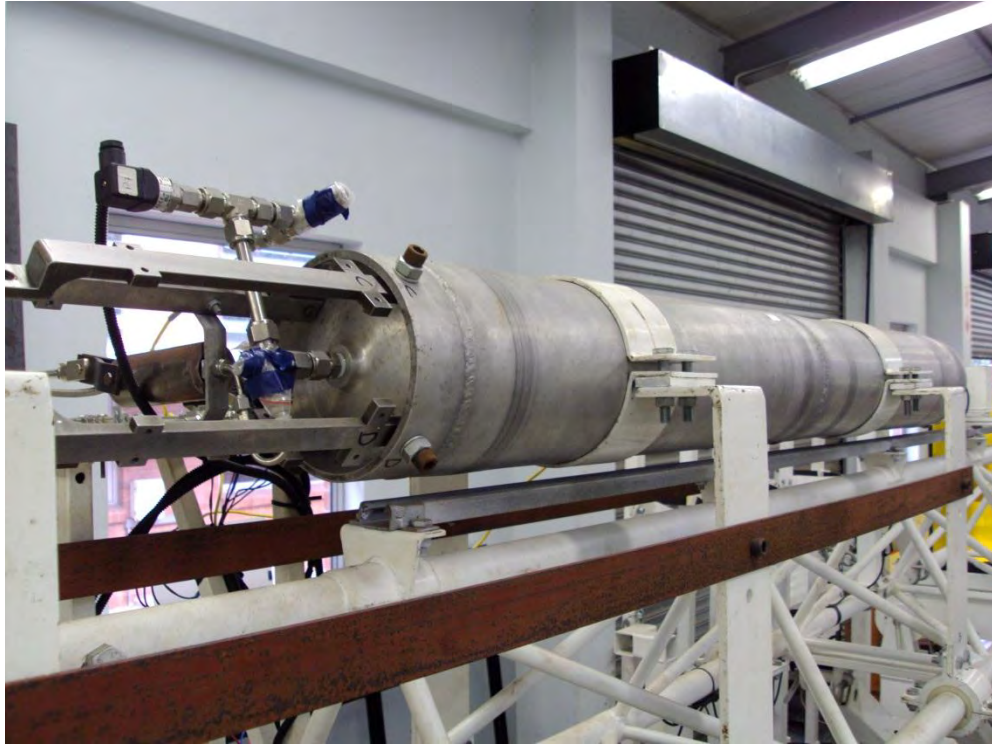
Figure 6-26: The oxidiser tank mounted on the GSE in preparation for ground motor testing.

## 6.10 Design and Manufacture of Internal Supporting Structures

6.10.1 Forward Airframe Bulkheads

Several methods of joining the airframe sections together were evaluated. Four points of attachment existed in the forward section of the Phoenix-1A airframe. The first was the attachment of the internal sleeve (housing) of the drogue parachute bay to the top end of the oxidiser tank. The flight computer bay was joined to the internal sleeve of the main parachute bay as well as the drogue parachute bay. Finally, the nose ogive was attached to the main parachute bay at its forward end. These fixed attachments could be permanent and hence only mechanical fasteners offered practical solutions. The combined wall thickness at the drogue parachute sleeve joint and the oxidiser tank top end was 10 mm and the combined wall thickness was at least 4 mm for the rest of the joints involving any two of the CFRP upper airframe sections.

The pressurisation of the main and drogue parachute bays using carbon dioxide during recovery required the isolation of these bays from and the flight computer bay and the nose ogive. Conversely, the flight computer bay and nose ogive also needed to be sealed against flooding during a sea recovery. These four compartments were separated using cylindrical aluminium

196

bulkheads which also served as supports for the attachment of mechanical fasteners. The choice of material was again dictated by availability and specific strength considerations. The suitable dimensions and relatively superior specific strength of the aluminium 6082-T6 alloy billet which used for the oxidiser tank led to its uses in the forward airframe bulkheads as well.

The bulkheads had a 192 mm nominal diameter due to the 4 mm airframe combined wall thickness and an initial wall thickness of 10 mm was envisaged. Thereafter, linear static FEA was iteratively used to refine the design of the bulkhead geometry. Emphasis was placed on mass reduction by thinning the component in areas of low stress. This resulted in a gradual thickening of the bulkhead towards its centre, carrying the large parachute shock load on the eye-bolt which is attached to the centre of the bulkhead on a threaded M12 hole. The 3D linear static FEA was conducted with the geometry fully fixed constrained on the inner surfaces of the eight radial threaded holes used to attach the bulkheads to adjacent airframe fuselage sections. The combined worst case shock and aerodynamic load of 10 kN was then applied to the central M12 threaded hole inner surface in the axial (body frame x axis) direction. Symmetry was exploited through the use of quarter geometry with normal translational constraints on the symmetry plane surfaces. A fine quadratic tetrahedral mesh was used with a 1 mm element size. The results revealed concentrated von-Mises stress peaks of 189 MPa at the root of each bolt hole. This was deemed acceptable as it was below the 240 MPa design yield strength of the material and the loading was highly conservative. Figure 6-27 shows the von-Mises surface stress distribution from the FEA whilst the full geometry is shown in Figure 6-28 and a photograph of a partially manufactured bulkhead is given in Figure 6-29. The thickening at the centre of the bulkhead diffuses stresses due to parachute shock loading. Note the artificial stress concentration at the central eye-bolt hole for the parachute shock cords. With reference to Figure 2-28, the 12 mm central hole was used to attach eye bolts to which the recovery parachute shock cords were tied. The eight radial holes on the circumference were used to join adjacent tubular composite airframe sections at the bulkhead. The bulkheads were CNC machined and drilled from offcuts of the same aluminium 6082-T6 alloy billet used for the oxidiser tank.
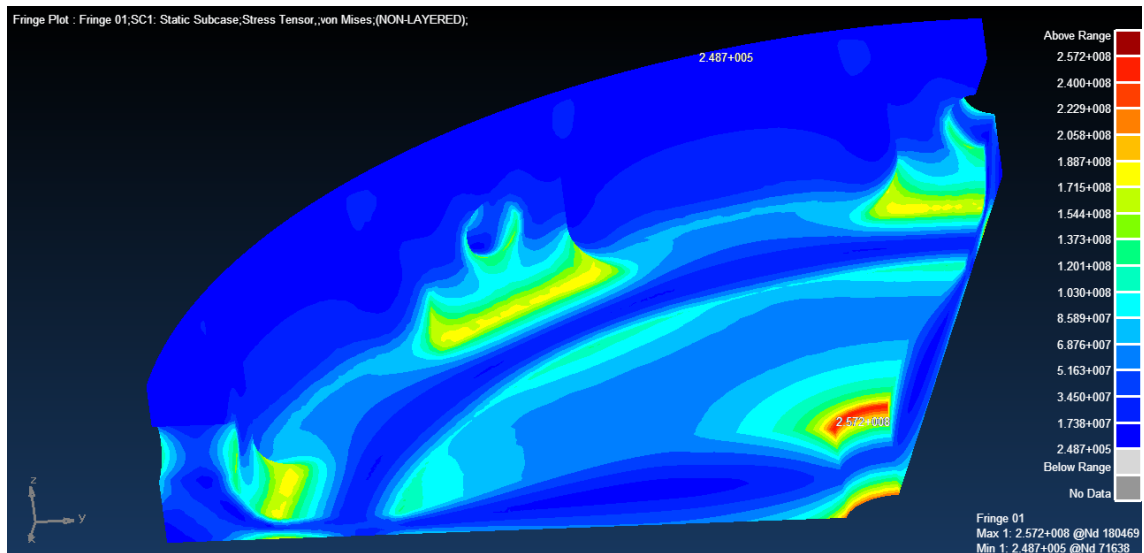
(a)
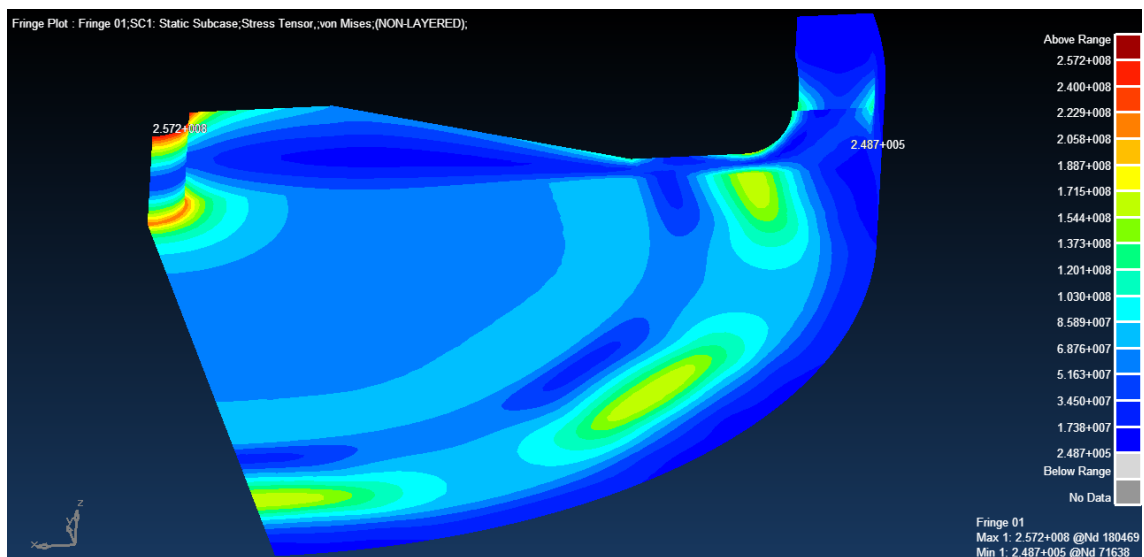
(b)

Figure 6-27: MSc SimXpert von-Mises surface stress plots in the upper airframe bulkhead.
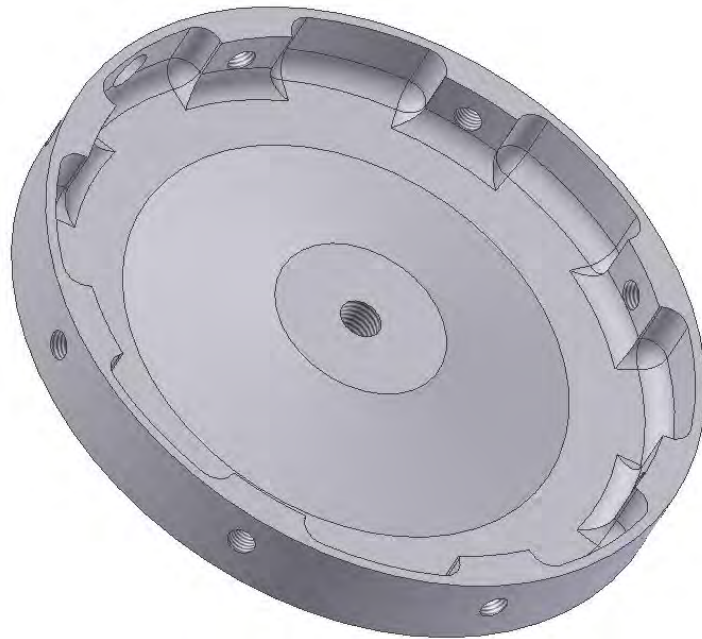
Figure 6-28: CAD rendition of the aluminium alloy 6082-T6 bulkhead geometry, used to separate the various chambers of the forward airframe.

Figure 6-29: A forward airframe bulkhead during manufacture, after CNC milling. The eight radial bolt holes had not been drilled yet. Note the mass reduction at areas of low stress.

6.10.2 Motor Fairing Struts

A mechanical interface between the PV-1 oxidiser tank and oxidiser feed system was required to unite the PV-1 motor's upper section to the PV-1 combustion chamber designed by Genevieve [4], forming the complete PV-1 flight-weight hybrid rocket motor. Four struts were used to form this interface. Struts were chosen over alternative cage or mesh concepts as they allowed for an open frame. Dexterous access to the intricate components of the oxidiser feed system was crucial for assembly purposes. Figure 6-30 shows the mechanical context in which the struts were designed. PV-1 motor components designed by Genevieve [4] are labelled in blue.
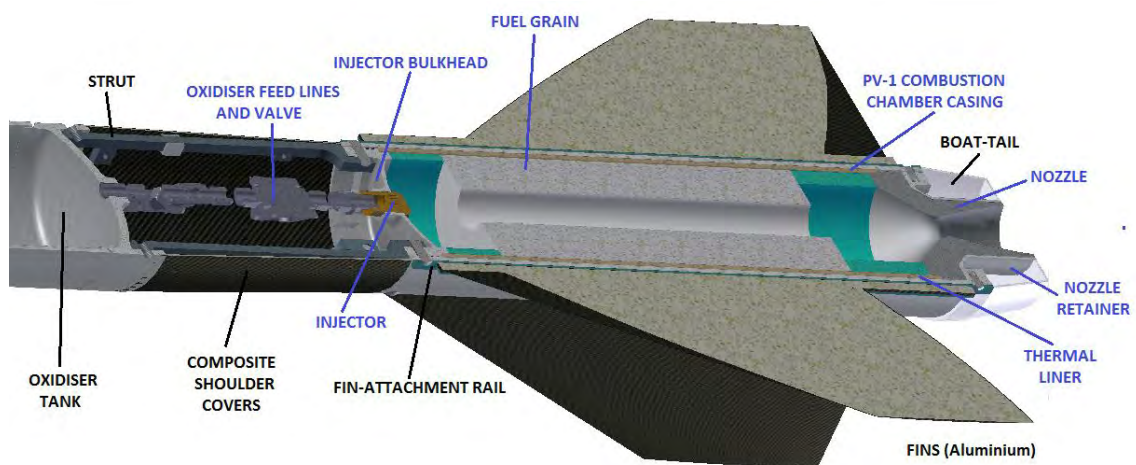
Figure 6-30: CAD assembly cutaway rendition of the rear end of the Phoenix-1A, showing major structural components.

The struts were designed to carry the combined loading from both sections of the vehicle structure they joined.

1) Sum of axial and lateral propulsion (3000 N), aerodynamic (1500 N) and deployment shock loads (5000 N) between the upper and lower parts of the vehicle totalling 9500 N
2) Weight from the oxidiser feed system (60 N)
3) Weight from the enclosing aerodynamic fairing covers (20 N)
4) Lateral reaction from operation of QC system before launch (150 N)

In addition to supporting the above loads, the struts were used to attach and support the aerodynamic fairing composite shells externally as well as the oxidiser feed system's various components internally.

The material selection process favoured higher stiffness and rigidity given the large bending and compressive loads experienced by the struts. However, the locations of the struts below the overall vehicle centre of mass motivated weight reduction due to aerodynamic stability considerations. The geometric design was refined to minimise volume and allow for simplicity of machining. Radii were used to impart strength to critically loaded corners whilst the section thickness was minimised at regions of lower stress. A rendition of the final strut geometry is shown in Figure 6-31. Note the M12 bolt holes at both ends and the horizontal extensions used to support the composite fairing shells (covering the oxidiser feed system internals which were housed in the volume between the struts)

Figure 6-31: CAD rendition of the strut used to interface the oxidiser tank and the combustion chamber casing of the PV-1 flight weight hybrid rocket motor.

The FEA on the struts was carried out by combining the maximum flight and shock loading expected on the struts and applying a quarter of this load on each strut. The strut geometry was modelled directly from the CAD design and was constrained at the lower end bolt hole inner surfaces as would be the case during flight. The total maximum loading on the struts was estimated at 10 kN and the FEA was thus conducted using a 2.5 kN load on each strut. The load was applied in a distributed manner to the inner surface of the upper end bolt hole to emulate load transfer through the rocket airframe. Figure 6-32 shows the FEA von-Mises stress output.

Note small stresses, concentrated near top bolt hole due to local cantilever bending. Axial stresses are very low.
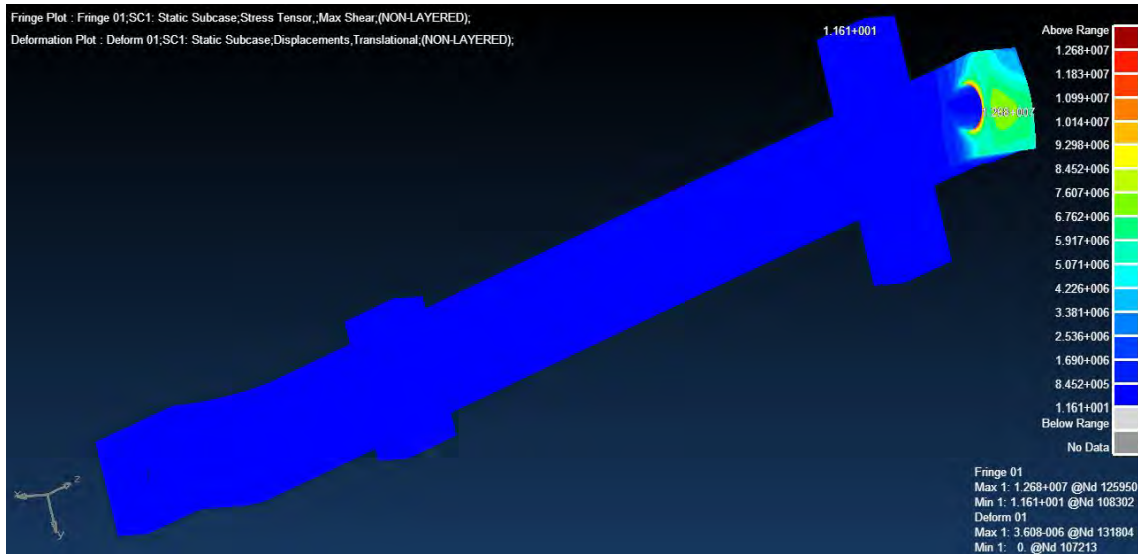
Figure 6-32: MSc SimXpert von-Mises surface stress plots on the struts under worst case loading. The mesh was constrained at the bolt hole at its lower end.

The FEA predicted a maximum von-Mises tensile stress of only 12.68 MPa, which was well below the allowable limit of the material (690 MPa), providing a large reserve factor for additional shock loading. Although this may seem overly conservative, the unpredictable nature of shock loading from high-jerk deceleration made it desirable for the struts to possess a reserve factor well above 10. The struts were also analysed for buckling failure using the Euler criterion [74] and the design was found to be safe due to the high material stiffness and relatively ample cross sectional area. Figure 6-33 shows a photograph of the struts installed on the lower end of the oxidiser tank.
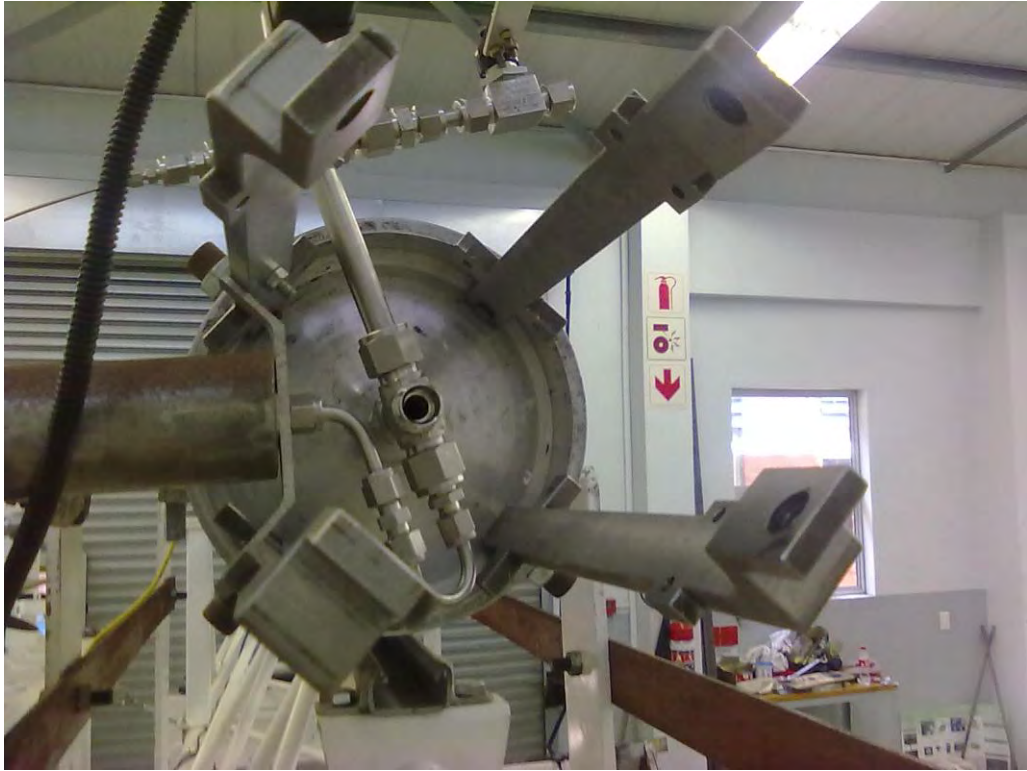
Figure 6-33: The four struts attached to the lower end of the oxidiser tank, shown supporting parts of the oxidiser feed system and ground support equipment.

6.10.3 Flight Computer and Oxidiser Feed System Supports

The flight computer bay requires internal support structures to transfer axial loads and allow for the attachment of otherwise unsupported components such as the flight computers, their power sources and the parachute deployment charges. The need to minimise weight led to the selection of clear polystyrene plate (commercially known as Perspex) as the material of choice for internal supports on the Phoenix-1A. Plate thickness of 10 mm was generally used for supporting sensitive components such as the flight computers and oxidiser feed system servo motor (refer to Chapter 7.2 for details). Secondary supports and attachments utilised 4 mm and 5 mm thick plates for minimising weight. All Perspex components were machined from plating using band-saws and hand-filed for dimensional accuracy.

CHAPTER 7

Phoenix-1A Electro-Mechanical Systems

7.1 Oxidizer Flow Control System

The Phoenix-1A PV-1 hybrid rocket motor employed an electromechanical flow control mechanism to control the flow-rate of oxidizer from the oxidizer tank to the motor combustion chamber. Control over this flow-rate was necessary to facilitate safe remote operation during the motor static testing and launch. The system also offered a potential for thrust throttling during flight. The nitrous oxide line between the oxidizer tank and combustion chamber was fitted with a Swagelok ½ " stainless steel ball valve for the purpose of controlling the oxidizer flow rate. The high starting torque and severe spatial constraints made off-the-shelf solutions either impractical or prohibitively expensive; hence a custom actuation system was designed around the valve. Figure 7-1 shows the structures around which the system was designed. Note the spatial constraints and the need for design for access for assembly and maintenance.
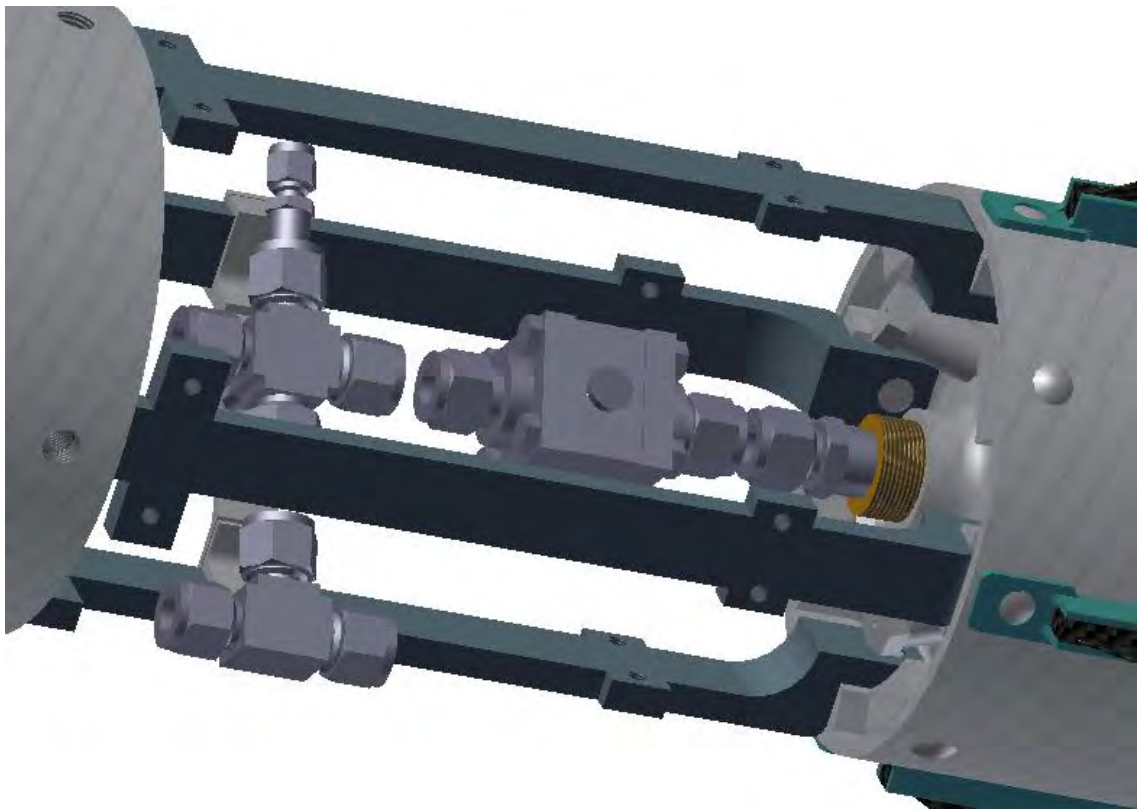

Figure 7-1: Detail CAD rendition of the oxidizer feed system location in the context of the vehicle, showing only the major structures and the plumbing.

The actuation system was envisaged to possess the following characteristics

a) Capacity to open or close the valve under pressure in both standard and emergency conditions

b) Actuation with a speed and delay suitable to the ignition transient of the PV-1 motor

c) Ability to partially open the valve to any fraction required

d) Operability on a power source meeting strict spatial and weight constraints

e) Ease of access for assembly and repairs upon installation on the vehicle

f) Capacity to return the valve to a safe position under failure conditions (power loss, etc.)

g) Controllability by both the GSE (for ground testing) and onboard electronics (for launch)

A Hitec HS 7980 TH high torque servo motor was selected to actuate the oxidizer feed ball valve. The HS 7980 TH servo motor produces 4.4 Nm of torque at its rated operating voltage of 7.4 V. However, the starting torque requirement of the Swagelok ball valve at the operating pressure of 65 bars was 6.7 Nm. A custom made 2:1 ratio stainless steel spur gear set was used to increase the driving torque to the ball valve to 8.8 Nm. The servo motor was powered with a standard 7.4 V two-cell Lithium-Polymer (LiPo) rechargeable battery pack. The operating speed of the servo motor under 7.4 V conditions is 0.22 s / 60°, implying a 0.66 s opening time for a 180° turn on the servo motor and a corresponding 90° turn on the ball valve. The HS 7980 TH servo motor is also digitally programmable for variable speed using the Hitec HPP-21 servo programmer kit, allowing slower speeds in 10 % fractions of full speed. The mechanism is thus pre-adjustable for a wide range of valve opening durations.

This servo motor was controlled using an onboard IC with an Atmel Atmega32 MCU. Control signals sent from the GSE based master control system were processed by the MCU to manage the valve actuation. The Atmega32 is capable of performing logical communication with external devices through its 32 bidirectional I/O ports. These ports may be read or set in sync with the chip's internal clock, which is the default mode of operation. Alternatively, three specific ports may be read asynchronously to trigger (interrupt) event based functions. These interrupt ports were used to trigger the opening and closing of the servo valve. Interrupt functionality may be based on three types of changes on the port designated as the interrupt input.

a) Rising Edge – Only changes from the low voltage (0) state to the high voltage state (1)

b) Falling Edge – Only changes from the high voltage (1) state to the low voltage state (0)

c) Rising and Falling Edge – Any change in voltage state

Each interrupt could in principle be used to trigger two independent functions. The trigger event interrupts the normal execution of instructions on the MCU and gives preference to the function associated with the triggered interrupt. However, the servo valve control systems solely used the rising edge functionality and dedicated each interrupt trigger to a single function. This was a measure taken to provide robustness against oscillatory signal behavior on any one line. Oscillatory signals may be incurred on mechanical switches and is commonly referred to as 'switch bounce'. An added advantage of using the rising edge trigger would be the inability of the GSE to inadvertently change the valve state in the event of a power failure or malfunction on the GSE. In such a situation, the servo would move to its pre-programmed safe position. The same would occur if the PWM signal from the MCU to the servo was lost due to a power failure or malfunction on the MCU itself.

The servo control algorithm was required to operate in two distinct modes, one for static ground testing and the other for flight. For the motor static testing case, the Atmega32 MCU was programmed with two external interrupts, one each for valve opening and valve closing. This allowed direct binary control of the valve from the GSE National Instruments LabView controller. For the vehicle flight testing, the MCU was programmed with a flight sequence. In this mode the external interrupts were programmed to serve as input for launch command as well as an emergency termination signal. During launch, the GSE LabView system would serve only to provide a launch command, after which the GSE would effectively hand over control to the onboard MCU. The MCU would then be programmed to implement the sequence described in Table 7-1.

Table 7-1: Launch sequence description

Time (s) (Launch at $t = 0$)	Event	Actions
$t - 10$	Control passed to MCU	Pre-launch countdown begins
$t - 1$	Oxidizer valve opening	Command servo valve open
$t - 0.75$	Ignition 1	Trigger igniter 1
$t - 0.25$	Ignition 2	Trigger igniter 2
$t = 0$	Flight Takeoff	Start monitoring for flight termination command
$t + 25$	Oxidizer valve closing	Command servo valve close

A single PCB was used to compactly mount the MCU, its supporting electronics and the connectors required for wiring the MCU to the GSE, servo motor and power supplies. This configuration was selected as it did not require the use of different circuits dedicated to static

ground testing or flight testing. Only changes to the MCU's embedded software was necessary to prepare the system for flight. The circuit contained ports for the following:

a) Common grounding for GSE, power sources and servo motor.
b) LabView GSE command signals
c) Power supply for Atmega32 (7.4 V, high current)
d) Power supply for the MCU (4 V, low current)

Switches were also used on the PCB to safe the servo motor and MCU prior to the system being declared safe for static testing or launch. A diagram of the PCB is shown in Figure 7-2. Ports PD2 and PD3 are interrupt inputs. Port 10 is used to supply 5V power to the MCU and port 11 is used to ground the MCU. Note the common grounding and switches for the control of power to the servo motor (7.4 V) and MCU (5V). Jumper wires are denoted by **.

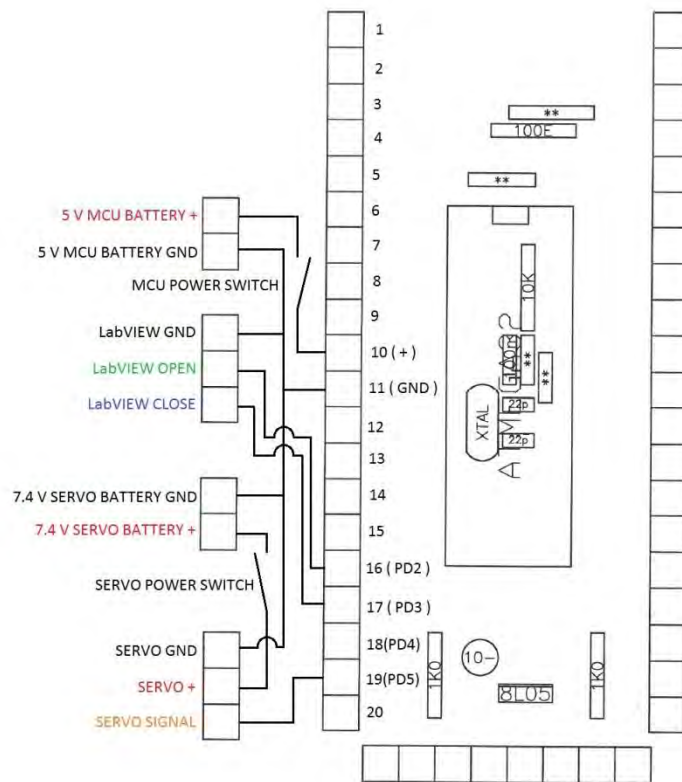Figure 7-2: The servo actuation system MCU PCB layout. The ports denoted PD4 and PD5 are PWM outputs used to control the servo.

The spur gear train used a 40 mm pitch diameter gear with 36 teeth and a 20 mm pitch diameter pinion with 18 teeth. A face diameter of 10 mm was chosen to compromise between space and torque capacity. The gear was keyed directly onto the ball valve actuation shaft and the pinion

was fastened to the servo motor's splined output shaft using a heavy duty Hitec nylon servo horn and an aluminum washer. The gear assembly was manufactured from grade316 stainless steel by a specialist gear machinist and was installed directly onto the threaded actuation shaft of the valve and secured with standard nuts and washers. The pinion was attached onto the servo output shaft using a specially modified Hitec servo horn and a combination of small standard screws and nuts. This was necessary due to the small, propriety profiled, non-standard spline which is machined onto the output shafts of all Hitec servo motors. The Hitec high-strength plastic servo horn was used as an easily available means of interfacing between the special spline profile of the servo and the custom made pinion gear. An additional aluminum washer was necessary to provide flush faces for the interfacing. Four M3 screws with a PCD of 35 mm were used to attach the servo horn to the washer and the pinion gear. Figure 7-3 shows CAD view of the actuation system installed onto the vehicle. Figure 7-4 shows a photograph of the servo motor and ball valve assembly with the protective covers removed.
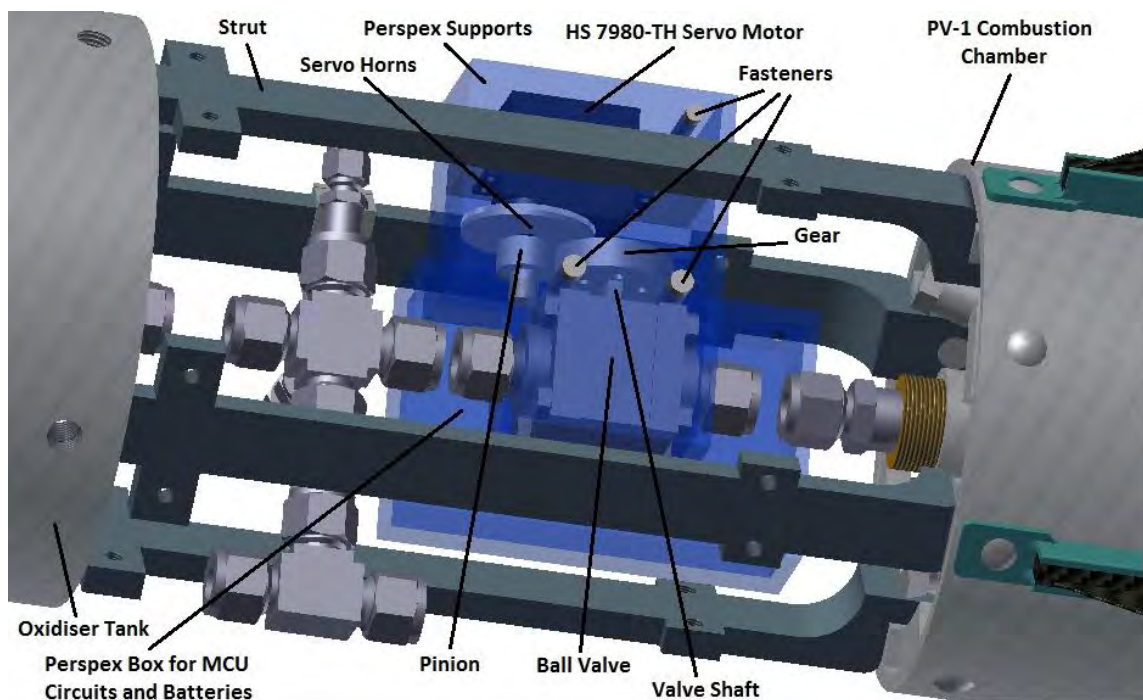

Figure 7-3: CAD assembly rendition of the oxidizer flow control system showing the servo actuation mechanism and the location of the control circuitry and batteries.
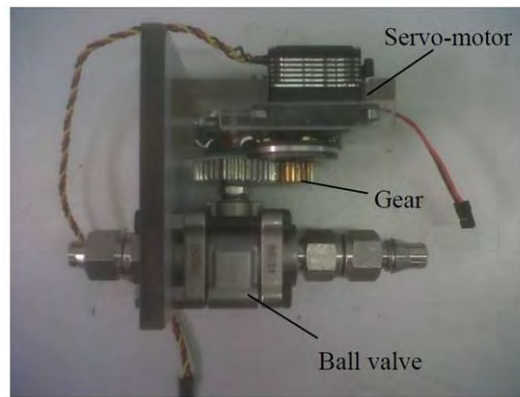
Figure 7-4: Servo valve actuation train, showing the valve, servo motor, gear, pinion, servo horn assembly Perspex brackets for securing the components.

Spatial constraints and the valve actuation loads governed the design and integration of the flow control system's supporting structure into the Pheonix-1A vehicle. As mentioned in Chapter 6, Perspex was chosen as the structural material for its low density, ease of machining, satisfactory structural performance, low cost and availability. The Perspex structural components were designed around the ball valve, servo motor; MCU and battery pack and joined using a combination of standard fasteners and the Tensol Perspex adhesive. The design of the system aimed at satisfying spatial constraints whilst reducing weight and overall complexity.

The servo actuation system was ground tested on several occasions, both in the laboratory and under fully operation conditions during the ground testing of the PV-1. The system was found to be swift and functional. However, it was noted that the servo motor developed a very small but high frequency jittering motion about the commanded position due to its internal electronics being optimized for torque rather than positional accuracy. This effect in turn generated output current fluctuations form the servo battery as the high starting torque of the valve prevented the servo form making small jittering motion against the gear train and the valve shaft. The resultant effect was an extra draught of current and heating of the servo when powered on and held at a single position for extended periods. Another characteristic of the system was the invisibility of the valve shaft to an outside observer and the lack of any digital feedback to the GSE indicating the true position of the shaft. This drawback was deemed significant in the event of an emergency or power failure on the GSE.

7.2 Recovery System

7.2.1 Aspects of Recovery System Design

Reusability in sounding rockets is achieved by including an integral recovery subsystem. The recovery system is tasked with bringing the reusable parts of the vehicle back to the ground relatively undamaged and at an easily accessible location. Recovery mechanisms must decelerate the vehicle to a speed suitable for a safe landing. There are three categories of passive recovery devices commonly used on unguided sounding rockets: parachutes, streamers and fuselage separation. All three approaches rely on aerodynamic drag effects for deceleration.

The instantaneous magnitude of a parachute's decelerating drag force is calculated using the aerodynamic axial force equation (Eq. 5-9). The local atmospheric density determines the effectiveness of any parachute as a function of altitude. The altitude of deployment therefore determines whether terminal velocity may be reached by the system. For most high altitude rockets, terminal velocity is usually attained and the problem reduces to the following aspects:

    a)   Ensuring that the recovery system deploys successfully at the desired flight conditions
    b)   Achievement of a sufficiently low terminal velocity
    c)   Reduction of dispersion (uncertainty) in splashdown location

Parachute recovery systems may use a single or multiple parachutes. The need to minimize drift and reduce splashdown footprint dispersion requires the deployment of the primary parachute at a suitable altitude. This altitude must allow for sufficient descent time for the vehicle to decelerate to the desired splashdown vertical velocity whilst ensuring the wind drift is kept within acceptable limits. However, successful primary parachute deployment cannot take place when the vehicle velocity is too great, due to line shocks and possible entanglement. A small drogue chute is commonly deployed before the main parachute to decelerate the vehicle sufficiently to allow the for a successful main parachute deployment. The primary parachute and drogue parachute combination is known as a dual parachute recovery system although more than one drogue or main parachute may be deployed by larger rockets.

Parachutes may be deployed forward, laterally or rearwards. The deployment direction is important for avoiding unwanted interactions between the parachute canopy and the rest of the airframe, in particular the fins. The orientation of the vehicle during the deployment is used to determine the most suitable deployment direction. Often the most foolproof technique is rearward deployment. However, parachutes are rarely housed near the aft end of sounding

rockets due to the presence of the rocket motor. Drogue parachutes are often deployed near apogee when the vehicle nose is approximately horizontal, in contrast to main parachutes which are deployed with the airframe already separated and in a typically nose down attitude.

Parachutes stored on sounding rockets are folded and stowed so as to minimize space requirements and suitably integrate with other on-board systems. The process whereby parachutes are released and inflated prior to becoming functional is known as parachute deployment. Several categories of mechanical devices may be used to achieve a successful deployment. Pressurization devices increase the pressure in the parachute storage chamber, causing the chamber to expel the parachute through an orifice designed to open at a predetermined pressure. Alternative approaches separate the airframe at the parachute storage location using pyrotechnic or mechanical devices such as explosive bolts or pistons.

An initiator, often a pyrotechnic charge, is needed to provide energy to trigger deployment. Explosive bolts are a popular pyro-mechanical solution to separation and deployment requirements. Pyrotechnic charges are constrained by the availability of sufficient oxygen in the atmosphere. They have another important drawback in that they cause a small explosion when set off, generating heat and releasing kinetic energy in a short space of time. Sensitive equipment in the fuselage must be protected from the effects of the ignition charge. This is commonly achieved using fire-resistant 'wadding-paper' in the model rockets by hobbyists. However, wadding paper is not a highly reliable solution.

During deployment, parachute storage compartments must be designed to open and sufficiently expose the parachute to the atmosphere. The opening action may be driven by either mechanical actuation or internal pressurization. It is usually advantageous to deploy the parachute shroud lines before the canopy to allow for a smoother inflation. A weight or a piston may be used to assist in the complete ejection of the parachute, ensuring a safe inflation away from the rest of the vehicle body.

The choice of deployment mechanism is heavily influenced by cost, complexity, weight and reliability considerations. Mechanical and pressurization deployment mechanisms may be triggered using electronic circuitry or passive sensors. Pre-programmed on-board electronic systems are preferred due to their high degree of reliability and reasonable cost. These circuits are commonly referred to as flight computers and may serve several other logical functions such as stage separation on multistage vehicles. Flight computers are often placed in close proximity to parachute storage compartments to facilitate reliable transmission of deployment signals.

It is possible to deploy several parachutes from a common storage compartment by releasing them in the desired sequence of deployment. Such a compartment needs to be opened to the external atmosphere only for the initial deployment. Subsequent parachutes are stowed until deployment, when the stowing mechanism is removed or destroyed and the parachute becomes free to unfurl and inflate.

Pressurization based deployment systems possess distinct advantages over mechanical deployment systems when employed on smaller sounding rockets. These include lower mechanical complexity and hence lower cost and weight as well as a greater degree of possible redundancy. However, the greater reliability of efficiently designed mechanical systems makes them suitable for larger high altitude sounding rockets where the accurate timing of deployment events is critical to mission success. Space-going sounding rockets with recoverable payload system almost always employ mechanical sophisticated deployment systems to overcome the coupled aerodynamic, thermal and structural complications of atmospheric re-entry.

It is important to note that both the nose and the cylindrical sections of the forward airframe are well suited to storing the parachutes or flight computers. In some designs the entire payload or parts of the payload may be carried in the same compartment as the flight computer. There are thus several possible configurations for the arrangement of components in a dual parachute recovery system. The major components are abbreviated in the summary list below: Main Parachute (MP), Drogue Parachute (DP) and Flight Computers (FC).

1) Separate MP and DP bays on either side of the FC and deployment charges. DP located aft of FC.
2) Separate MP and DP bays on either side of the FC and deployment charges. MP located aft of FC.
3) Single parachute bay. DP placed aft of MP with FC aft of parachute bay.
4) Single parachute bay. MP placed aft of DP with FC aft of parachute bay.
5) Single parachute bay. DP placed aft of MP with FC forward of parachute bay.
6) Single parachute bay. MP placed aft of DP with FC forward of parachute bay.

Option 1 was chosen for the Phoenix-1A based on the need to deploy the relatively large main parachute as far forward of the rest of the vehicle as possible. Option 1 offered more equal distribution of mass, desirable for larger static stability margins. It was also deemed desirable to have the drag force oppose the tendency of the main parachute bay to open under the force generated during drogue parachute deployment.

7.2.2 Shock Chord Dimensioning

The recovery descent using dual parachute deployment results in the vehicle adopting two distinct physical configurations. The first configuration occurs in the time period after the drogue chute deployment event but before the main parachute deployment event. The second configuration occurs from the main chute deployment event to splashdown. Successful recovery requires that during both phases the parachute payload (i.e. vehicle) remain stable and undamaged. It is also desirable to maintain an orientation that minimizes chances of impact on sensitive structural and airframe components during the splashdown. Parts such as the nose tip and fins may be viewed as being more vulnerable as they are structures of low wall thickness and house fragile equipment such as the payload.

The length of shock chord in each parachute compartment and the location of each parachute on the cord determine the relative location of the motor, flight computer bay and nose sections during the recovery phases. These lengths were selected to prevent interference or collision between any two sections of the separated vehicle during recovery. The length of shock chord also determined the maximum relative movement between separated sections during the potentially violent parachute deployment events. A schematic of the various shock-cord lengths and their relation to vehicle structural lengths is shown in Figure 7-5.
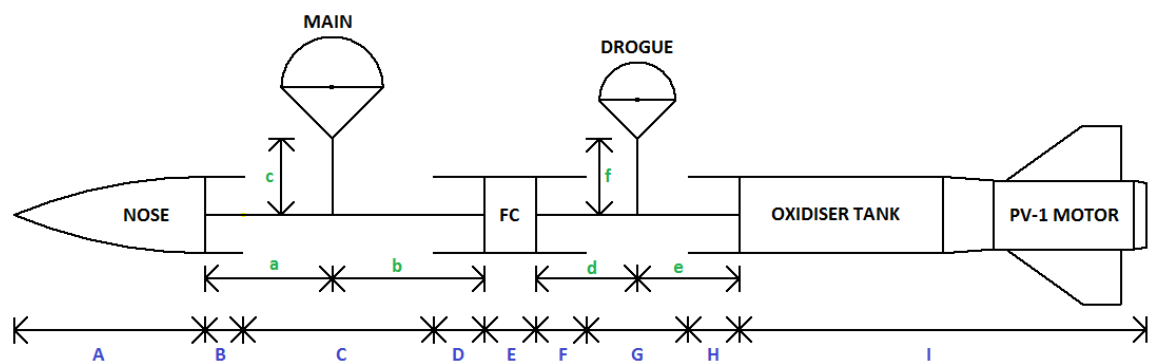
Figure 7-5: Shock cord layout in relation to the parachutes and the distinct vehicle structures. Cord length variables are in green and fixed structural lengths in blue.

With reference to Figure 7-5, the six shock cord section lengths denoted a to f were designed based on the vehicle structural lengths denoted A to I. These lengths would have to be chosen to safely arrange the structural components under two geometric conditions. The first condition arises after drogue parachute deployment but before main parachute deployment. In this case, the combined lengths of the nose (A) and the stowed main parachute and flight computer bays (i.e. the sum of lengths B, D, E and F) would have to be prevented from contact with the rest of

the vehicle (with length the sum of H and I) by making cord length e greater than core length d by at least the sum of A, B, D, E and F. For safety, an additional 500 mm was added. This is conservative as it ignores overlap between the main parachute bay sections with lengths B and D. The second deployment geometry occurs when the main parachute is deployed after drogue parachute deployment. In this case, the nose and upper main parachute bay, with lengths A and B respectively, must be prevented from contact with the rest of the vehicle aft of the main parachute, including the drogue parachute and its associated shock cords. This requirement would be fulfilled by making shock cord length b greater than shock cord length a by at least the sum of lengths A and B. In either case, ample extra cord length would be added to allow for rebound slackening.

7.2.3 Parachute Sizing, Market Survey and Selection

The HYROPS tool could be used to predict the splashdown speed achievable on the Phoenix-1A, given the drag coefficients and effective diameters for both parachutes. The drogue chute deployment delay (post apogee) and the main chute deployment altitude were chosen using engineering judgment to minimize wind drift dispersion. The software was then used to estimate suitable drag coefficients and diameters for each parachute. A market survey of high altitude model rocket parachutes was conducted to match available parachutes to the parachute mass budget and the drag and sizing ranges determined feasible through the HYROPS tool. It was noted that the relatively high apogee altitude made the splashdown speed very sensitive neither to the post-apogee drogue deployment delay nor the main parachute deployment altitude. The parachutes would have sufficient time to reach terminal velocity for even moderate main parachute deployment altitudes in the range of 1000 m to 2500 m. Both drogue and main parachutes were thus expected to contribute significantly to dispersion instead of dispersion being dominated by the slower main parachute. High-power model rocket parachute kit suppliers *SkyAngle*, *Apogee Components* and *The Rocketman* were identified in the United States of America as potential sources of suitable parachutes within the project budget. No local suppliers were located. Prices, shipping costs and suitability to mass and diameter specification led to the selection of *The Rocketman* 7 foot diameter Ballistic Mach II high speed drogue chute and *The Rocketman* 18 foot diameter standard nylon rip-stop main parachute. Both parachutes were of four-lobed star plan-form shape. The 7 foot drogue had a manufacturer tested terminal drag coefficient of 1.29 based on a 7 foot diameter circular reference area whilst the 18 foot main parachute had a manufacturer tested terminal drag coefficient of 2.92, similarly based on a 18 foot diameter circular reference area. The more expensive Ballistic Mach II variety of drogue chute was selected as HYROPS simulation showed a significant residual horizontal velocity in

the region of 150 m/s at apogee for an 80° launch elevation angle. The manufacturer claimed that the Ballistic Mach II variety of drogue parachutes was designed for deployment at supersonic speeds. Figure 7-6 and Figure 7-7 show photographs of the drogue and main parachutes respectively.

Figure 7-6: Seven foot diameter Ballistic Mach II high speed drogue parachute

Figure 7-7: Eighteen foot diameter nylon rip-stop main parachute

7.2.4 Shock Loading Analysis using OSCALC tool

The calculation of the maximum dynamic loading on a parachute shock cord is non-trivial. It is possible to empirically derive estimates based on the vehicle mass and deployment decelerations, as done by the majority of model rocket hobbyists. However, many unrealistic simplifications must be made to use these rules-of-thumb, often leading to large inaccuracies, especially for high altitude, high power sounding rockets with dual parachute recovery systems. The importance of the recovery feature in the Phoenix-1A mission and its reliance on the shock cord necessitated a good evaluation of shock cord suitability and performance. The Opening Shock Calculator (OSCALC) software was identified as a suitable tool designed specifically for the prediction of parachute deployment shock loading characteristics. This tool uses a combination of empirical methods and the momentum-impulse equation to estimate the forces incurred in filling a parachute over a given filling time when the parachute is moving at a given line stretch velocity [75]. The nominal parachute drag coefficient, total mass of vehicle at deployment and the atmospheric density at deployment altitude must also be provided at inputs to the software. Empirical opening shock factors are then used for the calculation of an average opening shock force and corresponding maximum and minimum forces. Figure 7-8 shows a screenshot of the OSCALC tool.

Using the tool, a maximum opening shock load of 4.5 kN was determined for both parachutes under the worst case deployment conditions which occur at sea level. This load was assumed to act axially as the complexities of modeling the exact direction of the opening shock load is beyond the scope of this dissertation. In either case, a worst-case quick inflation time of two seconds was assumed in the absence of any empirical test data. Manufacturer supplied drag coefficients were used. A conservative deployment speed of 75 m/s was used for both the drogue and the main parachutes. The resulting estimates were in agreement with the rule of thumb often used in hobby rocketry stating that the opening shock load is approximately ten times the vehicle weight at deployment. In the OSCALC prediction, the vehicle fully-loaded mass of 95 kg was used despite the nominal deployment weight being 57.5 kg during recovery as all the fuel would have been consumed. These precautions led to a conservative estimate and ultimately a 5 kN opening shock load was specified and used for the structural design as was shown previously in Chapter 6.
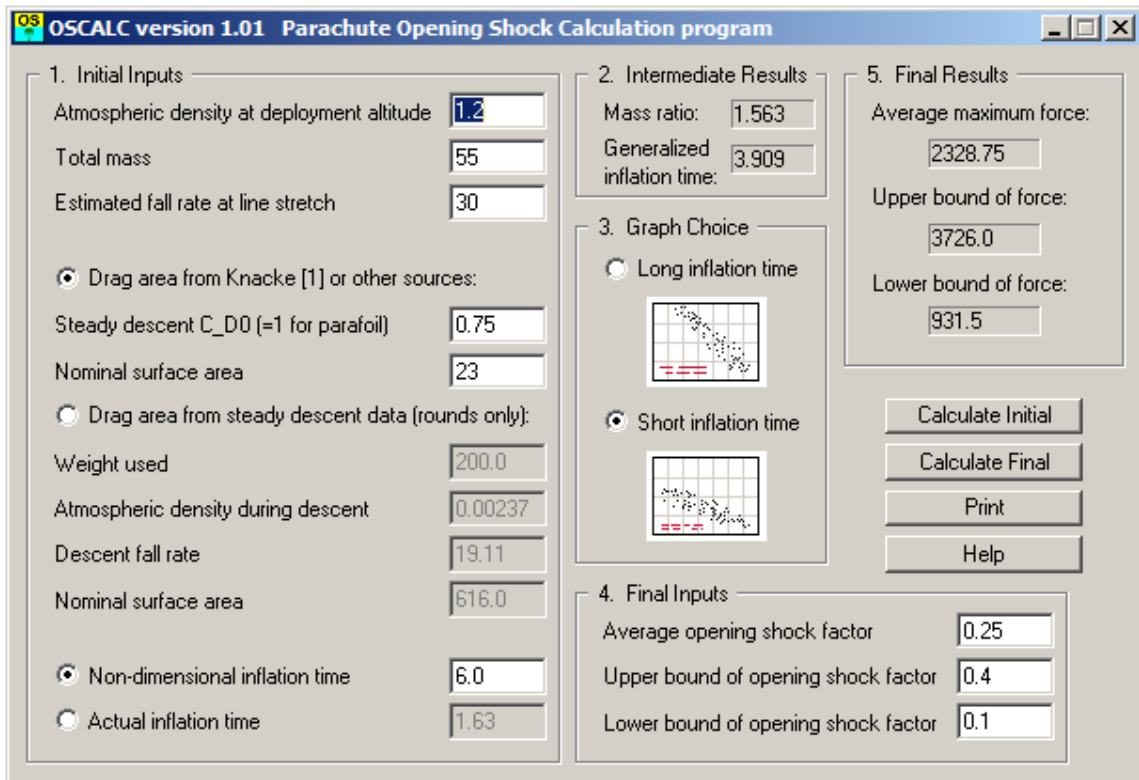
Figure 7-8: Screenshot of the OSCALC software showing typical inputs and outputs. The software may be used with imperial or metric units provided that all inputs are consistent.

7.2.5 Onboard Electronics

The avionics on an unguided sounding rocket may be functionally classed into various components:

1) Recovery system deployment
2) Telemetry
3) Flight termination (a. k. a. Command Destruct)
4) Stage separation management

The single stage Phoenix-1A did not require stage separation mechanisms. However, the flight termination requirement resulted in a similar mechanism being employed.

The successful recovery of the Phoenix-1A depends primarily on the deployment of the recovery parachutes at the appropriate phases of flight. A controlled deployment sequence based on feedback on actual flight conditions is essential for this purpose. Flight computers equipped with barometric and inertial sensors may be used to detect the vehicle altitude, attitude and

acceleration, from which significant flight events may be inferred. The primary function of such circuitry is to use transistor switches to close a high current circuit and supply power from a high amperage battery to the pyrotechnic charge. Metal oxide semiconductor field effect transistors (MOSFET's) are used to enable a low current signal to control a high current signal, allowing embedded digital algorithms to control heavy current devices such as pyrotechnic igniters.

On board micro-controller chips are used to process data from barometric and inertial sensors to sequence parachute deployment, staging and other in-flight procedures on sounding rockets and other high altitude vehicles. A large variety of processors may be used, ranging from inexpensive 8 bit fixed point processors to advanced 32 bit processors capable of real time impact point prediction (IPP) simulations and other advanced navigational tasks. The processor's embedded instruction storage capacity determines the complexity of the control algorithms that may be programmed, whilst the numerical processing capacity determines the accuracy and speed at which data may be sampled and used in the control algorithms. Processor speeds may range from 1 MHz to 40 MHz depending on the onboard cooling available and the frequency of sensor data outputs. Typical data analysis tasks may involve detecting the sharp drop in axial acceleration at stage motor burnout events or the change in the direction of the vertical velocity at or near apogee. Events may also be scheduled based on a pre-programmed timing sequence which itself may be referenced to a flight event. For example, the drogue parachute may be scheduled to deploy 2 seconds after the apogee event whilst the main parachute may be scheduled to deploy another 15 seconds thereafter. Stage separation charges are usually timed after motor burnout events or triggered when specific axial acceleration levels or flight path angles limits are reached. If equipped with a barometer, a flight computer can derive the barometric altitude by comparing the measured atmospheric ambient stagnation pressure to a table of atmospheric pressures as a function of altitude. Such tables must be compact enough to fit in the processor's often limited embedded memory resources. The inertial position and orientation states of the vehicle may be tracked by flight computers fitted with three degree of freedom accelerometers and tri-axial rate gyroscopes. The acceleration outputs may be numerically integrated once to derive the velocity states and again to derive the inertial position. The body rate outputs from the rate gyroscopes must be simultaneously integrated to derive the body orientation for referencing the velocity and position states correctly in inertial coordinates. The mathematical methods of Chapter 3 are directly applicable to this process. The use of a combination of inertial and barometric output altitudes makes flight computers robust to uncertainty effects such as winds and vibration. Winds may negatively affect the barometric altitude whilst vibrations may deteriorate the accuracy of electronic accelerometers and rate gyroscopes.

The Phoenix-1A vehicle solely required the autonomous deployment of its parachutes. The selection and design of the flight computer system was thus based on the need for reliability and safety on the recovery system. The system was designed to be fully redundant with respect to the functioning of all sensors and electronics. This was realized by using two distinct commercially available flight computer systems, each of which featured sensor configurations using both electronic accelerometers and barometric altimeters. Both circuits were wired to simultaneously operate the system. The pyrotechnic triggering outputs for the deployment of each parachute would be wired in parallel with diodes to prevent reverse currents from one circuit damaging the other circuit in the likely event that one flight computer fires a charge before the other.

The G-WIZ HCX 50 is a commercially available high power model rocket flight control device suitable for use at altitudes of up to 70 000 ft. It was chosen as the secondary flight computer on the Phoenix-1A as it was inexpensive and met the specifications for the vehicle. This system uses an on-board single degree of freedom $\pm$ 50 g accelerometer with inertial altitude measurement up to 100000 ft. This is used in conjunction with a barometric altimeter to fire up to four programmable high current pyrotechnic ports. One channel is dedicated to staging at burnout, high altitude drogue parachute deployment and low altitude main parachute deployment each. A freely programmable channel is also reserved for triggering to any detectable flight event. The device is also fitted with a shunt plug to prevent accidental firing of the pyro charges. The device also features an onboard Micro-SD card port, wherein a Micro-SD card is used to record all flight data. The G-WIZ system is provided with FlightView software, capable of programming the unit and downloading recorded flight data to a PC via a USB connection. The device was configured and bench tested using the software and small test charges. The unit weight of only 45 g made the device suitable for a secondary flight computer on a vehicle such as the Phoenix-1A. Based on the HYROPS simulation used for the parachute selections, the drogue chute pyro channel was programmed to fire one second after apogee detection whilst the main parachute was programmed to fire at a barometric altitude of 2000 m. The GWIZ-HCX 50 was powered using an onboard 9 V DC battery stored nearby in the flight computer bay. Figure 7-9 shows a photograph of the GWIZ-HCX 50 printed circuit board with major components labeled.
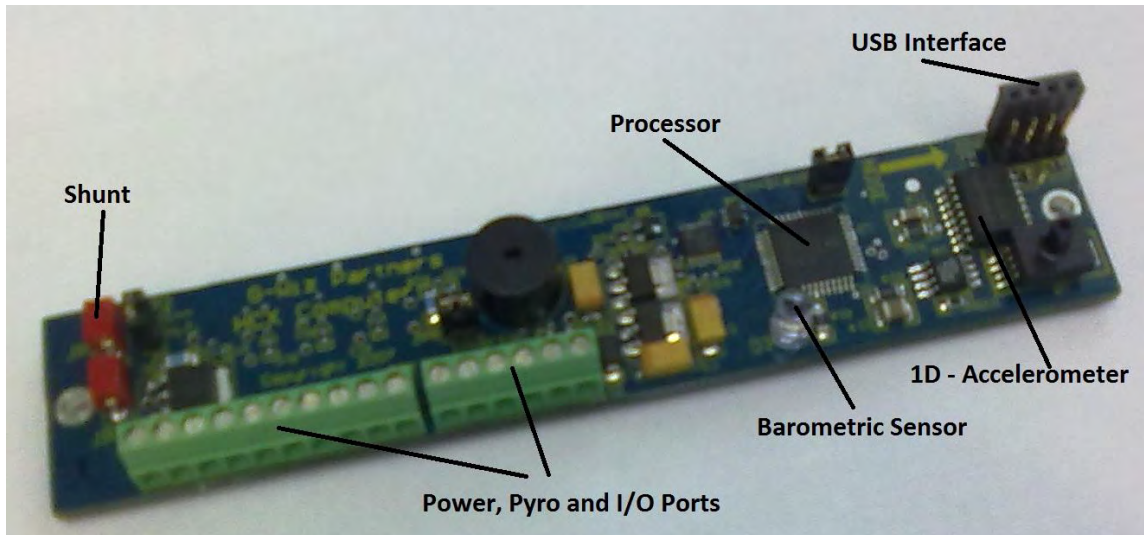
Figure 7-9: The GWIZ-HCX 50 flight computer.

A Black Magic Missile Works – Universal Flight Computer (UFC-4D) flight computer was selected as the primary flight computer for the Pheonix-1A. The device is fully user programmable and offered the user the ability to drive two of its pyrotechnic ignition outputs using logic based on any of the device's detected flight events. It is equipped with a 3 degree of freedom accelerometer and controlled by an 80 MHz, 32-bit ARM Cortex processor, providing 8 digital user I/O channels two high current pyrotechnic channels. This flight computer was at the low-level programmed directly using the Cypress Programmer software development environment corresponding to its Cypress ARM Cortex processor. In addition to flight control, the device also featured an optional 5 Hz GPS unit and 900 MHz, 1 W telemetry unit. However, cost limitations ruled out the purchase of the GPS and telemetry accessories. It was decided that position and velocity measurements from the OTR test range radar would suffice as the flight path tracker and that a less expensive GPS telemetry unit would part of the vehicle payload. The UFC-4D uses a 9 V DC power input, supplied onboard from a standard 9 V battery with a safety switch. Figure 7-10 shows a photograph of the UFC-4D printed circuit board with major components labeled.
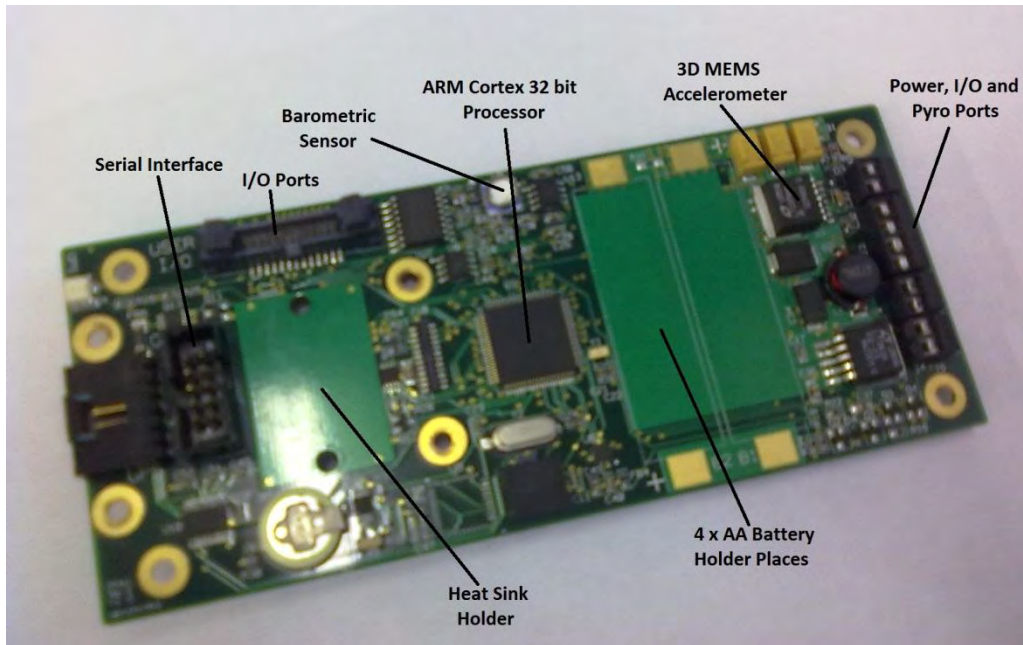
Figure 7-10: The Black Magic Missile Works UFC-4D flight computer.

7.2.6 Rouse Tech CD3 Deployment Hardware

The predicted apogee altitude of the Phoenix-1A, 15000 m, occurs in an atmospheric region where insufficient oxygen density exists for the sustained combustion of black powder charges. Therefore, an alternative system was selected to pressurize the parachute bays and deploy the parachutes. The Rouse Tech CD3 system uses high pressure carbon dioxide cartridges to achieve this. This system was selected as it was well priced, suitably dimensioned and capable of pressurizing both parachute bays on the Phoenix-1A.

The CD3 deployment system consists of a short piston in a cylindrical assembly with a sealed electrically ignited black-powder charge on one side. Electrical ignition of the black powder on the one end of the piston forces it to travel along the cylindrical housing and impact on a canister of compressed carbon dioxide. The impact of the piston (which possesses a sharp point on the canister end) is used to puncture the membrane of the canister and release a sudden charge of carbon dioxide into the parachute bay, causing a large pressurization event. The system possesses the advantage of being to operate at any altitude due to the small amount of air required to ignite the initial black powder charge being sealed within the black powder chamber itself in the piston-cylinder assembly. However, O-rings and high precision threading must be used to ensure that both the piston and the cylinder are sealed and the trapped air does not escape the black powder chamber during the ascent. The CD3 system is supplied with these accessories by its manufacturer. The device is also fitted with a flange for attachment onto

internal bulkheads such that the cylinder is placed in the parachute bay. Once the membrane on the cartridge is punctured, the expanding gases force the piston in the cylinder back to expose holes on the cylinder sided which allow the gases to escape the device and pressurize the parachute bay. Figure 7-11 shows the details of the CD3 device with components separated.
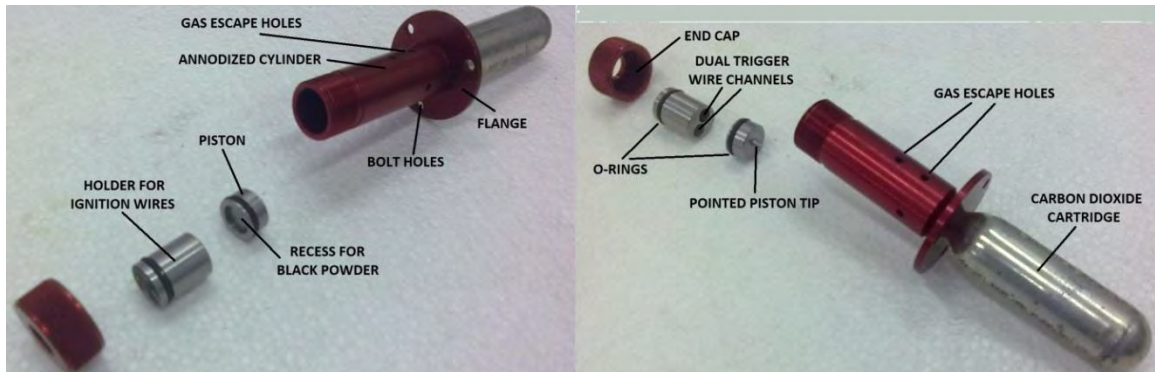

Figure 7-11: Exploded photograph of the CD3 deployment system with major components labeled.

The selection of the compressed carbon dioxide cartridge mass is determined by the diameter and length of the parachute bay in question. A selection chart provided by the manufacturer indicated that the approximately 8" diameter Phoenix-1A would be suited to standard 16 g cartridges for both the roughly 10" long drogue parachute bay and the roughly 12" long main parachute bay. However, sliding friction considerations led to the specification of a 25 g cartridge for the drogue chute bay, as it would have to be forced open under maximum drag resistance conditions. The CD3 system was ground tested for cartridge puncture and found to reliably puncture the cartridge membrane and lead to a sudden increase in local pressure. A few grams of black powder was found to be sufficient.

CHAPTER 8

Concluding Remarks and Future Work

8.1 Discussion and Conclusions

The initiation of the indigenous Phoenix sounding rocket programme has led to research in various technology areas involving aerospace engineering. This work was focused on rocket flight dynamics, sounding rocket systems engineering as well as systems integration. The modelling and simulation aspects of the research has offered useful insights into sounding rocket system behaviour and revealed the key areas which determine their flight performance. Greater confidence in the program outcomes has also been generated.

On a functional level, the HYROPS tool was found capable of simulating the basic six degree of freedom dynamics of a multi-stage sounding rocket when given a low level vehicle design input. The results conformed well to the literature, with deviations lying within the tolerances arising from the design input uncertainties. Apogee altitudes predicted with the tool agreed with the literature to an accuracy of better than 2 %. Aside from this core functionality, more advanced tasks such as orbital motion simulation, parachute recovery simulation and wind modelling was also performed successfully. The tool was capable of quantifying uncertainties arising from subtle effects such as thrust misalignments and winds to a degree impossible with other competing codes. These tasks demonstrated the advantages of integrating the various subsystem models. The inclusion of the genetic algorithm driven optimisation feature and the Monte Carlo uncertainty quantification feature enabled the HYROPS tool to function as a design and analysis tool as well as a simulation tool. Additionally, knowledge of computer graphics, digital data processing and statistical results analysis was used to perform intuitive visualisation of results and the swift generation of high-level vehicle performance statistics. This knowledge was also crucial in making the HYROPS tool more user friendly and robust, ultimately facilitating ease of design for the sounding rocket designer. Unique data structures in the HYROPS code were used to store low-level design details using generic geometric and logical inputs, making the user input, processing, storage and visualisation of vehicle structural and aerodynamic design information more efficient and intuitive. This also had implications in the vehicle optimisation algorithm and the import and export of data to external software.

The HYROPS tool was used to predict the nominal flight performance of the Phoenix-1A sounding rocket design. The predicted apogee altitude of 15000 m was a fundamental indicator

of the suitability of the vehicle's configuration and this had far reaching effects in the structural design of the vehicle and the design of other subsystems such as the recovery system. HYROPS was directly applied to the selection of the recovery parachutes and the selection of a suitable material for the oxidiser tank, demonstrating its usefulness in vehicle subsystems design. Results have also indicated that HYROPS is capable of generating flight planning data of sufficient fidelity for application for flight test permission at test ranges such as the Denel OTR.

The direct outputs from this effort are the HYROPS sounding rocket performance simulation tool and the structural and electro-mechanical design of the Phoenix-1A hybrid sounding rocket. The majority of the vehicle's structural and internal components have also been procured, manufactured and ground tested despite constraints in time, financial resources and access to key materials and manufacturing technologies. An important characteristic of this research effort was the integrated engineering design of various subsystems. Previous researchers had developed sounding rocket propulsion systems, aero-structures and ground support system in a generally decoupled manner. By approaching the problem in a more coupled manner the system complexity was better appreciated, leading to more robust design based on a proactive approach with regards to both performance and safety. This was also a key output from using simulation as a design tool.

In summary, the development and use of the HYROPS software has led to several important conclusions

a) High fidelity flight performance predictions are crucial in understating of sounding rocket technologies, even at the sub-system level

b) Performance predictions are also essential in the iterative design process

c) Meaningful integration of subsystem models into a single framework allows high fidelity system modelling using a reasonable level of engineering effort and computational power

d) The design solution space may be explored using optimisation techniques, greatly reducing the engineering effort at the cost of computational power

e) Mathematical modelling of system uncertainties is a powerful tool in gauging the robustness of the system in complex operating environments

A detailed mechanical engineering design was carried out for the Phoenix-1A vehicle. This mechanical design involved the complementary use of classical engineering design methods, Computer Aided Design (CAD) and established numerical computation techniques such as FEA and CFD. FEA results demonstrated that many of the structural component geometries of the

vehicle could be optimised for weight without compromising on safety factors, whilst CFD results revealed areas where material thermal performance would be critical. These indications could prove useful in the future design of lighter and cheaper sounding rockets. Specific software tools such as RasAero and OSCALC were also used to complement the design and engineering of subsystems where applicable.

Rocket design has a long history and it was apparent from the literature that a working design could be possibly have been obtained by utilising existing knowledge from the fields of missile and projectile design. However, performance predictions from HYROPS and local market surveys revealed that such designs would not be optimal in terms of cost and performance. The reasons for this were noted to be the high degree of coupling between the materials used, aerodynamic performance, thermal stability and structural integrity of a sounding rocket airframe, all of which are in turn coupled to the system cost and operating envelope. Given the aim of developing a cost-effective and reusable vehicle, the design was adapted in many areas to use cost instead of vehicle performance as the measure of success. The process was complicated by the limited material choices and manufacturing process available to the project. These constraints forced the design into a relatively small solution space which afforded little room for optimisation. At a lower level, it was found that commonly available materials and manufacturing techniques could often be used to substitute more exotic technologies by the application of innovative designs. The integration of the externally supplied PV-1 flight motor design into the vehicle mechanical design also forced constraints on certain subsystems. It was observed that a coupled design of the motor and airframe would have reduced or eliminated some of those constraints, allowing for further optimisation.

The technological readiness level (TRL) of the indigenous hybrid sounding rocket concept has been gauged meaningfully by this work, producing a first iteration estimate of the costs, engineering effort and potential pitfalls involved in the local development of this technology. It was apparent that ample room still remains for subsystems optimisations on the Phoenix-1A, which would increase the robustness and feasibility of the vehicle. Such improvements may prove crucial in the economical application of hybrid rocket technology in more advanced systems such as orbital launch vehicles. In summary, it was noted that presently, the local South African industrial base lacks many of the advanced technologies needed for the optimal development and manufacture of state of the art aerospace vehicles. Examples of these include specialised welding technologies, precision manufacture of large pressure vessels using aerospace grade materials and also the capacity to produce precision composite structures for use in supersonic flight conditions.

8.2 Future Work

Through the sounding rocket trajectory activities, a number of underexplored research areas have been identified during this work. The HYROPS simulation tool's internal aerodynamics prediction methods were found to be inadequate in the prediction of the centre of pressure location and the prediction of transonic aerodynamic coefficients in general. The use of more advanced techniques, including numerical methods, from more recent aerodynamic prediction research works would benefit the software by introducing a more accurate aerodynamic model for use with the vehicle optimisation process. The empirical approach to aerodynamics adopted in this work was inherently limited. Future research using a more complete application of CFD and wind tunnel testing would also benefit the general sounding rocket design process greatly, especially with regard to drag minimisation and fin optimisation. The parachute aerodynamic model used in this work was also highly simplistic. Further research into more robust parachute aerodynamic models would ensure that instabilities present in the HYROPS recovery simulations under high gradient wind input could be eliminated. Roll dynamics remains another aspect of the aerodynamic modelling in HYROPS that may benefit from empirical research.

The software architectures built around the structural and aerodynamic models could also be extended to allow for the following

a) Non-linear variation in fuselage radius
b) Alternative fin plan-forms
c) Various fin cross section profiles
d) Tandem (side) boosters
e) Non-hemispherical parachute canopies

The numerical solver used in the HYROPS tool may be improved by the use of variable time stepping. Enhancements involving the switched use of numerical methods of varying order (in simulation time) may make the numerical solution process more efficient in terms of computational resources. Such techniques could also be used to predict instabilities and singularities in the solution in an intelligent manner, leading to a more robust solver. A high altitude atmospheric model and an elliptical geodetic model would also render the software more suitable for orbital simulations.

The structural design of the Phoenix-1A was not optimised fully using the HYROPS optimisation tool due to the presence of severe time constraints. In the future, it would be

beneficial to undertake the design process using the complete design loop as proposed in this work. This would integrate the simulation and thermo-structural analyses completely and would ensure that an optimal design is on the table prior to the search for materials and manufacturing resources. The use of more optimal materials such as aerospace grade aluminium alloy would also benefit the designs of future vehicles. A weakness of the present oxidiser feed system design was noted in the servo valve mechanism. An alternative means of controlling the oxidiser flow without the introduction of a heavy, complex electronically controlled servo valve would increase the system robustness and reliability. Novel solutions could be pursued such as pyrotechnic valves. Additional areas of improvement in the vehicle design could include the elimination of protuberances on the airframe by use of intelligent fastening devices such as V-band joints and radial-axial (radax) joints. A combined FEA of the entire vehicle assembly was omitted in this work, but future designs would benefit from such an analysis as it would reveal the structural interactions between components under flight loading conditions.

At the program level, there remain areas of outstanding research. The completion of the procurement and manufacture processes for the first Phoenix-1A prototype is the immediate goal of the program. Thereafter, the assembly, ground support equipment (GSE) integration and subsystems ground testing phases are the objectives for the near future. A simultaneous flight planning activity using HYROPS is also required before flight testing of the Phoenix-1A at the Denel OTR facility.

REFERENCES

[1] "Sounding Rocket Program Handbook (SRPH)", Suborbital Program and Projects Directorate, Sounding Rocket Program Office, NASA, Goddard Space Flight Center, Wallops Island, VA, United States of America, June 1999

[2] Botma P. J., "The Design and Development of and ADCS OBC for a CubeSat", Master's Thesis, Faculty of Engineering, Stellenbosch University, South Africa, December 2011

[3] "South African National Space Agency (SANSA)", Online, www.sansa.org.za, Accessed 22 November 2012

[4] Genevieve, B., "Development of a Hybrid Sounding Rocket Motor", Master's Thesis, School of Engineering, University of KwaZulu-Natal, South Africa, Submitted, December 2012

[5] Gunther Seibert, "A History of Sounding Rockets and Their Contribution to European Space Research", 1st Ed., European Space Agency Publications Division, The Netherlands, November 2006

[6] "NASA Sounding Rocket Program – Code 810", Online, http://sites.wff.nasa.gov/code810, Accessed 22 November 2012

[7] Barretta, J. et al, "Virginia Tech Sounding Rocket Project", Virginia Polytechnic Institute and State University, Blacksburg, VA, United States of America, 2002

[8] Wheeler, T. et al, "The Pennsylvania State University Student Launch Initiative Preliminary Design Report, 2010 – 2011", Pennsylvania State University, PA, United States of America, December 10, 2010

[9] MIT Rocket Team, "Project AI^{3}R – Aero Ion Infrared Intelligent Rocket", USLI 2012-2013 Preliminary Design Review, Massachusetts Institute of Technology, MA, United States of America, October 29, 2012

[10] Wu, B. et al, "Sub-Orbital Experiments Using Sounding Rockets in Taiwan", National Space Organization (NSPO), Proceedings of the 4th Asian Space Conference, Taipei, Taiwan, October 2008

[11] Amende, A. et al, "University of Washington A. C. E. S. Rocket", University of Washington, Seattle, WA, United States of America, 2009

[12] "Pathfinder II Heavy – Project Technical Report", Embry-Riddle Future Space Explorers and Developers Society, Embry Riddle Aeronautical University, Daytona Beach, FL, United States, 2010

[13] "Stratos II, On Our Way to Space", Delft Aerospace Rocketry Engineering (DARE), Delft University of Technology, Netherlands, Online, projectstratos.nl/wp-content/uploads/sponsor-brochure-Stratos-II-very-small.pdf, Accessed 22 November 2012

[14] Tsohas, J. et al, "Development and Launch of the Purdue Hybrid Rocket Technology Demonstrator", Purdue University, Proceedings of the 45th AIAA/ASME/SAE/ASEE Joint Propulsion Conference and Exhibit, Denver, CO, United States of America, 2-5 August 2009

[15] Doran, E. et al, "Status Update Report for the Peregrine Sounding Rocket Project: Part III", Proceedings of the 45th AIAA/ASME/SAE/ASEE Joint Propulsion Conference and Exhibit, Denver, CO, United States of America, 2-5 August 2009

[16] Tsohas, T., Droppers, L. J. and Heister, S. D., "Sounding Rocket Technology Demonstration for Small Satellite Launch Vehicle Project", Proceedings of the 4th AIAA Responsive Space Conference, Los Angeles, CA, United States of America, April 24-27 2006

[17] "Copenhagen Suborbitals", Online, www.copenhagensuborbitals.com, Accessed 22 November 2012

[18] "HAAS Orbital Rocket Launcher (ARCA)", Online, www.arcaspace.com/images/ Haas_Orbital_Rocket_Launcher.pdf, Accessed 22 November 2012

[19] Linehan, D., "SpaceShipOne: An Illustrated History", 1st Ed., Zenith Press, United States of America, May 15 2008

[20] Grosse, M., "Development Work on a Small Experimental Hybrid Rocket", Proceedings of the 33rd AIAA/ASME/SAE/ASEE Joint Propulsion Conference and Exhibit, Seattle, WA, United States of America, 6-9 July 1997

[21] "Design of Aerodynamically Stabilized Free Rockets", Military Handbook MIL-HDBK-762(MI), Department of Defense, United States of America, 17 July 1990

[22] Newlands, R., "Recovery System Design for Large Rockets", Aspire Space Technical Paper, United States of America, 10 September 2010

[23] Boiffier, J., "The Dynamics of Flight – The Equations", 1st Ed., John Wiley and Sons, Chichester, United Kingdom, 1998

[24] Zipfel, P. H., "Modeling and Simulation of Aerospace Vehicle Dynamics", 2nd Ed., AIAA Educational Series, Reston, VA, United States of America, 2007

[25] Etkin, B., "Dynamics of Atmospheric Flight", 1st Ed., John Wiley and Sons, United States of America, 1972

[26] "Konstantin E. Tsiolkovsky, Genesis Search for Origins", NASA JPL Online Article, genesismission.jpl.nasa.gov/people/biographies/tsiolkovsky.pdf, Accessed 22 November 2012

[27] Gorecki, R. M., "A Baseline 6 Degree of Freedom (DOF) Mathematical Model of a Generic Missile", Defence Science and Technology Report DSTO-TR-0931, Weapons System Division, System Sciences Laboratory, pp. 7-13, July 2003

[28] Khalil, M., Abdalla, H. and Kamal, O., "Trajectory Prediction for a Typical Fin Stabilized Artillery Rocket", Proceedings of the 13th International Conference on Aerospace Sciences & Aviation Technology, ASAT- 13, Military Technical College, Kobry Elkobbah, Cairo, Egypt. May 26 –28, 2009

[29] Jenkins, P. N., "Missile Dynamics Equations for Guidance and Control Modeling and Analysis", DTIC Technical Report RG-84-17, Guidance and Control Directorate, US Army Missile Command, Redstone Arsenal, AL, United States of America, April 1984

[30] James, R. L., Jr., "A Three-Dimensional Trajectory Simulation Using Six Degrees of Freedom with Arbitrary Wind", Technical Note D-641, Langley Research Center, Langley Field, VA, Mar. 1961

[31] McFarland, R. E., "A Standard Kinematic Model for Flight Simulation at NASA AMES", NASA Contractor Report NASA CR-2497, Washington D. C., 1975

[32] Karbon, K. J., "Numerical Methods for Model Rocket Altitude Simulation – A Comparative Study of Accuracy and Efficiency", NAR# 72175, NARAM 40 Research and Development Competition, August 1998

[33] Kyi, Z. H. K., Myint, O. and Aye, K. K., "Mathematical Techniques in Rocket Motion", World Academy of Science, Engineering and Technology 46, 2008

[34] A Saghafi, F. and Khalididelshad, M., "A Monte Carlo Dispersion Analysis of a Rocket Flight Simulation Software", Proceedings of the 17th European Simulation Multi-conference, SCS Europe BVBA, ISBN 3-936150-25-7, pp. 1–7, 2003

[35] Vinh, N. X., "General Theory of Optimal Trajectory for Rocket Flight in a Resisting Medium", Journal of Optimization Theory and Applications, Vol. 11, No. 2, pp. 189–191, 1973

[36] Coburn, N., "Optimum Rocket Trajectories", External Memorandum UMM-48, Aeronautical Research Center, University of Michigan, Ann-Arbor, MI, pp. 3–4, May 1 1950

[37] Roshanian, J. and Keshavarz Z., "Multidisciplinary Design Optimization Applied to a Sounding Rocket", Journal of Indian Institute of Science, Vol. 86, No. 7, pp. 363–375, July-Aug. 2006

[38] Bayley, D. J., "Design Optimization of Space Launch Vehicles Using a Genetic Algorithm", PhD Dissertation, Auburn University, Alabama, United States of America, August 4 2007

[39] Bairstow, B. K. et al, "Multi-objective Optimization of Two-Stage Rockets for Earth-To-Orbit Launch", Proceedings of the 47th AIAA/ASME/ASCE/AHS/ASC Structures, Structural Dynamics and Materials Conference, Newport, RI, United States of America, 1-4 May 2006

[40] Picone, J. M., Hedin A. E. and Drob D. P., "NRLMSISE-00 Empirical Model of the Atmosphere: Statistical Comparisons and Scientific Issues", Journal of Geophysical Research, NASA Goddard Space Flight Center, Greenbelt ML, United States of America, 2001

[41] Johnson, D. L., Roberts, B. C. and Vaughan, W. W., "Reference and Standard Atmosphere Models", Proceedings of the 13th Conference on Applied Climatology and the 10th Conference

on Aviation, Range and Aerospace Meteorology, Portland, OR, United States of America, 13-16 May 2002

[42] Jaffe, S. C., "Diagnosing Inter-model variability of Northern Hemisphere Jet Stream Portrayal in 17 CMIP3 Global Climate Models", PhD Thesis, University of Wisconsin Madison, United States of America, 2012

[43] Gage, S., "Creating a Unified Graphical Wind Turbulence Model from Multiple Specifications", Proceedings of the AIAA Modeling and Simulation Technologies Conference and Exhibit, Austin, TX, United States of America, 11-14 August 2003

[44] Weise, T., "Global Optimization Algorithms – Theory and Application", 2nd Ed., E-Book, 2009, Online, www.it-weise.de, Accessed 22 November 2012

[45] Eshelman L.J. & Schaffer J.D. (1993), "Real-coded genetic algorithms and interval schemata", in D. Whitley (Ed.), "Foundation of Genetic Algorithm II", pp. 187-202 Chapter 4, 1993

[46] Minor, L. G., "General Purpose Six Degree of Freedom Terminal Homing Missile Simulation Program", Technical Report RE-72-16, U. S. Army Missile Command, Redstone Arsenal, AL, United States of America, 31 August 1972

[47] Zipfel, P. H., "CADAC: Multi-use Architecture for Constructive Aerospace Simulations", Journal of Defense Modeling and Simulation (JDMS): Applications, Methodology, Technology, XX(X) pp. 1–17, The Society for Modeling and Simulation International, 2011

[48] Niskanen, S., "Development of an Open Source Model Rocket Simulation Software", Masters Thesis, Dept. of Computational Science and Engineering, Helsinki University of Technology, Helsinki, Finland, 2009

[49] United States Geological Survey (USGS), Global Land Survey , 2002, NASA Earth Observer 1 (EO-1) Advance Land Imager (ALI), 10 m scene "EO1A17408420 02172110KX", USGS, Sioux Falls, South Dakota, United States of America, 2009

[50] "Municipal Demarcation Board (South Africa)", Online, www.demarcation.org.za, Accessed 18 January 2010

[51] Jenkins, R. B., "Nike Apache Performance Handbook", NASA Technical Note D 1699, Goddard Space Flight Center, ML, United States of America, 1963

[52] Dembrow, D. W. and Jamieson, L. B., "Comparison of Theoretical with Actual Nike-Apache Sounding Rocket Performance", NASA Technical Report, United States of America, 1963

[53] Curtis, H., "Orbital Mechanics for Engineering Students", 1st Ed., Elsevier, Norfolk, United Kingdom, 2005

[54] "Big Desktop Images", Online, hea-www.harvard.edu/~fine/images/desktops/F-16XL-WindTunnel.jpg, Accessed 22 November 2012

[55] Hoak, D. E. and Finck, R. D., "USAF Stability and Control DATCOM", MacDonnell Douglas Aircraft Corporation, Wright Patterson Air Force Base, OH, United States of America, April 1978

[56] Rogers, C. E. and Cooper, D., "Rogers Aeroscience RASAero Aerodynamic Analysis and Flight Simulation Program – User's Manual", Version 1.0.0, Rogers Aeroscience, Lancaster, CA, United States of America, 2008

[57] Maple, C. G., and Synge, J. L., "Aerodynamic Symmetry of Projectiles", Quarterly of Applied Mathematics, Vol. 6, pp. 315-366, Jan. 1949

[58] Hopkins, F. J., "A Semi-empirical Method for Calculating the Pitching Moment of Bodies of Revolution at Low Mach Number", NACA RM A51C14, 1951

[59] Nielsen, J. N., "Missile Aerodynamics", 1st Ed., McGraw-Hill, York, PA, United States of America, 1960

[60] Allen, H. J. and Perkins, E. W., "A Study of Effects of Viscosity on Flow Over Slender Inclined Bodies of Revolution", NACA Technical Report TR 1048, 1951

[61] Diederich, F., "A plan-form parameter for correlating certain aerodynamic characteristics of swept wings", NACA Technical Note - TN-2335, 1951

[62] "Mach 1 on Mid-Power", Online, mcfisher.0catch.com/other/mach1/mach1.htm, Accessed 22 November 2012

[63] "The Descriptive Geometry of Nose Cones", Gary A. Cromwell Sr., 1996, Online, projetosulfos.if.sc.usp.br/artigos/NoseCone_EQN2.pdf, Accessed 01 June 2010

[64] Spreiter, J. R., "On the Range of Applicability of the Transonic Area Rule", NACA Technical Note 3673, Ames Aeronautical Laboratory, CA, United States of America, May 1956

[65] Spiegel, M. et al, "Tetrahedral vs. polyhedral mesh size evaluation on flow velocity and wall shear stress for cerebral hemodynamic simulation", Computer Methods in Biomedics and Biomedical Engineering, pp. 1-14, 2010

[66] Theodersen, T., "General Theory of Aerodynamic Instability and the Mechanism of Flutter", Report No. 496, in "Classical Aerodynamic Theory", compiled by Jones, R. T., NASA Report RP-1050, Ames Research Center, CA, United States of America, December 1979

[67] Martin, D. J., "Summary of Flutter Experiences as a Guide to the Preliminary Design of Lifting Surfaces on Missiles", NACA Technical Note 4197, Langley Field, VA, United States of America, February 1958

[68] Annaratone, D., "Pressure Vessel Design", 1st Ed., Springer-Verlag, Heidelberg, Germany, 2007

[69] "Competence and Innovation: Weisstaler Boedenpresswerke", Online Brochure, www.scribd.com/doc/67163532/flyer-7000-en.pdf, Accessed 22 November 2012

[70] Musgrave, G. E., Larsen, A. and Sqobba, T., "Safety Design for Space Systems", 1st Ed., Butterworth-Heinemann, United Kingdom, pp. 640-641, 31 March 2009

[71] Megysey, E. F., "Pressure Vessel Handbook", 12th Ed., Pressure Vessel Publishing Inc., Tulsa, Oklahoma, United States of America, 1973

[72] Missori S. and Sili A., "Mechanical Behavior of 6082-T6 Aluminum Alloy Welds", Metallurgical Science and Technology, Vol. 18, No. 1, pp. 12-18, 2000

[73] Kolarik, L. et al, "Weldability Test of Precipitation Hardenable Aluminium Alloy EN AW 6082 T6", Dept. of Mechanical Engineering, Czech Technical University, Prague, MM Science Journal, July 2011

[74] Gere, J. M. and Goodno, B. J., "Mechanics of Materials", 8th Ed., Cengage Learning, United Kingdom, 2012

[75] "OSCALC", Opening Shock Calculator Program, Software Package, Ver. 1.01, Parks College Parachute Research Group, Saint-Louis University, Saint-Louis, MO, United States of America, 2006

[76] Mayo, E. E., Weisskopf G. A. and Hutton, C. I., "Nike Tomahawk Nose Optimization Studies", NASA Goddard Space Flight Center, Greenbelt, Maryland, United States of America, November 1965

APPENDICES

Appendix A1: Analytical Formulae for the Physical Properties of Some Geometries

A1.1 Moments of Inertia Annuli

$$I_{XX} = \frac{1}{2}\pi\rho L(r^4 - (r-t)^4)$$

$$I_{YY} = I_{ZZ} = \frac{\pi\rho L}{12}\left(3(r^4 - (r-t)^4) + L^2(r^2 - (r-t)^2)\right)$$

(A-1)

A1.2 Truncated Cones and Hollowed Truncated Cones

The mass of a truncated cone is simply the mass of the un-truncated cone minus the sum of the truncated portion

$$m = \frac{\pi\rho L}{3}\left(r_b^2 + r_b r_t + r_t^2\right)$$

(A-2)

Let H be the height of the full (un-truncated) cone

$$H = L + \frac{Lr_t}{r_b - r_t}$$

The center of mass x coordinate is the given using the principle of substitution as

$$R_x = \frac{\left(\frac{H}{4}\frac{\pi\rho H r_b^2}{3}\right) - \left(\left(L + \frac{H-L}{4}\right)\frac{\pi\rho(H-L)r_t^2}{3}\right)}{\frac{\pi\rho}{3}(Hr_b^2 - (H-L)r_t^2)}$$

(A-3)

The moments of inertia are similarly calculated by subtracting the property of a cone of height H from that of the truncated cone, as in Eq. A-4.

$$I_{XX} = \frac{3\pi\rho}{10}\left(\left(\frac{H}{3}r_b^4\right) - \left(\frac{(H-L)}{3}r_t^4\right)\right)$$

$$I_{YY} = I_{ZZ} = \frac{3}{5}\left(\left(\frac{\pi\rho H r_b^2}{3}\right)\left(\frac{r_b^2}{4} + H^2\right) - \left(\frac{\pi\rho(H-L)r_t^2}{3}\right)\left(\frac{r_t^2}{4} + (H-L)^2\right)\right)$$

(A-4)

The mass, center of mass and moment of inertia of a hollowed truncated cone with wall thickness t is calculated by subtracting the respective properties of a truncated cone with length L, base radius $r_b - t$ and top radius $r_t - t$ from the properties of the standard truncated cone described above. The principle of substitution is used to calculate the center of mass using the negative mass concept, where the local reference is the base of the truncated cone.

A1.3 Center of Mass and Moment of Inertia of a Set of Four Trapezoidal Flat Fins

The x coordinate of the center of mass of a set of four planar trapezoidal fins, referenced to the trailing edge root, is given by Eq. A-5. The center of mass lies on the body frame x axis due to tetragonal symmetry.

$$R_x = \frac{(2C_r + C_t)(C_r - C_t - 2w) + 3C_r(C_r + C_t)}{6(C_r + C_t)}$$

(A-5)

The moment of inertia of a set of four thin trapezoidal fin set is given by Eq. A-6, referenced to the trailing edge fin root location on the body frame x axis.

$$I_{XX} = \frac{\rho t s^3}{3}(C_r + 3C_t) + \left(\frac{4\rho(C_r + C_t)st}{2}\right)r_t^2$$

$$I_{YY} = I_{ZZ} = \frac{s\rho t}{3}\left(4(C_r - w)^3 - (C_r - w - C_t)^3 + \frac{C_r^4 - 4C_r(C_r - w)^3 + 3(C_r - w)^4}{w}\right)$$

(A-6)

A1.4 Tangent Ogives and Hollowed Tangent Ogives

Mayo *et al* [76] present an appendix containing the rather involved functional relations between the dimensions and the physical properties of a tangent ogive. The mass of a tangent ogive is given by Eq. A-7.

$$m = 8\rho\pi r^3\left(f\left(f^2 + \frac{1}{4}\right)^2 - \frac{f^3}{3} - \left(f^2 - \frac{1}{4}\right)\left(f^2 + \frac{1}{4}\right)^2 \sin^{-1}\left(\frac{f}{f^2 + \frac{1}{4}}\right)\right)$$

(A-7)

where the ogive fineness ratio f is given by

$$f = \frac{L}{2r}$$

The x coordinate of the center of mass of a tangent ogive is given (in terms of the mass) by Eq. A-8.

$$R_x = \frac{16\pi\rho r^4}{m}\left[\frac{1}{2}f^2\left(f^2+\frac{1}{4}\right)^2 - \frac{1}{12}f^4\right.$$

$$-2\left(f^2-\frac{1}{4}\right)\left(f^2+\frac{1}{4}\right)^2\left[\frac{1}{2}f\sin^{-1}\left(-\frac{f}{f^2+\frac{1}{4}}\right)-\frac{1}{3}\left(f^2+\frac{1}{4}\right)\right]$$

$$\left.+2\left(f^2-\frac{1}{4}\right)^2\left[-\frac{\left(f^2-\frac{1}{4}\right)^2}{3}-\frac{f^2}{2}\right]+\frac{1}{3}f^2\left(f^2-\frac{1}{4}\right)^2\right]$$

(A-8)

The longitudinal moment of inertia of a tangent ogive is given by Eq. A-9. The lateral moment of inertia is ignored as it a complex function which yields small values for thin walled nose ogives with large fineness ratios.

$$I_{YY} = I_{ZZ} = \frac{32\pi\rho r^5}{3}\left(f^3\left(f^2+\frac{1}{4}\right)^2 - \frac{f^5}{30}+\frac{4f}{3}\left(f^2+\frac{1}{4}\right)^3\left(f^2-\frac{1}{4}\right)-\frac{5f}{6}\left(f^2-\frac{1}{4}\right)^4\right.$$

$$-\left[\frac{5f^2}{4}\left(f^2-\frac{1}{4}\right)+\frac{1}{4}\left(f^2-\frac{1}{4}\right)^3\right]\left[f\left(f^2-\frac{1}{4}\right)+\left(f^2+\frac{1}{4}\right)^2\sin^{-1}\left(\frac{f}{f^2+\frac{1}{4}}\right)\right]$$

$$\left.+\frac{f^3}{3}\left(f^2-\frac{1}{4}\right)^2\right)$$

(A-9)

In a similar fashion to the hollowed truncated cone, the physical properties of a hollowed ogive with wall thickness is given by subtracting the properties of a tangent ogive with base radius and length from the properties of the standard tangent ogive described above. Again, the center of mass with respect to the local origin (i.e. base of the tangent ogive) is calculated using the principle of substitution.